EXPERIMENTAL AND NUMERICAL STUDIES ON TWO-DIMENSIONAL GRAVITY CURRENTS IN A HORIZONTAL CHANNEL

Thesis by

Wingsiu Richard Chan

In Partial Fulfillment of the Requirements

for the Degree of

Doctor of Philosophy

California Institute of Technology

Pasadena, California

1993

(Defended November 11, 1992)

ACKNOWLEDGEMENTS

The author would like to thank his thesis advisor, Professor Edward E. Zukoski, for his unfaltering support throughout the progress of this research project. Through his encouragement and enthusiasm, Professor Zukoski was able to provide vital guidance in the direction of this research. His insight in the experimental field proved to be instrumental in the completion of this project.

The author would also like to thank Professor Toshi Kubota for his invaluable contributions to this research project. His patience and well-timed advice were essential to the progress of this research. His in depth knowledge of a broad range of scientific topics also contributed greatly in various portions of this research project, especially in the modeling effort and the subsequent numerical technique used in this project.

The author would like to acknowledge Professor James Knowles, Professor Frank Marble and Professor Rolf Sabersky, who spent their precious time on the thesis committee. The author would also like to acknowledge Professor Anthony Leonard for his advice in choosing the numerical technique used in this research project. Discussions with fellow graduate students Dr. Ian Waitz, Dr. Joseph Yang and Mr. Moon-Tai Yeung also yielded fruitful results in this area. Mr. Yeung and Mr. Thomas Zsak also provided much needed assistance in the experimental effort in this project.

The author would also like to acknowledge the faculty members of the Department of Mechanical Engineering and of GALCIT for their constructive criticism during the progress of this research. The author would also like to thank many of the staff members, especially Ms. Dorothy Eckerman and Ms. Connie Yehle, for their generous assistance. The author was indebted to Mr. Tom Welmers for his assistance in solving both hardware and software problems that the author encountered during the computational phase of the research, and Mr. Larry Frazier, Mr. Alan Goudey, and Mr. George Lundgren for their assistance in the construction of the pieces of experimental apparatus.

The author would also like to acknowledge the financial support by Grant number 60NANB9D0958 from the National Institute of Standards and Technology, with Dr. L. Cooper as the contract monitor.

ABSTRACT

The objective of this investigation is to examine the behavior of two-dimensional gravity currents, especially as applied to the spreading of smoke, generated from a room fire, along a long corridor. Both experimental and numerical techniques were used to provide a model that can adequately explain and predict the behavior of a gravity current under certain boundary conditions.

A series of experiments was carried out to study the effects of Reynolds number on gravity currents in a horizontal water channel. Measurements of the time varying front position, velocity profile of the following current, and the depth of a gravity current were made using either dyed liquids or hydrogen bubble technique. Quantitative results were shown to agree with previously published results. A model was put forth to bridge the gap between the existing models for an inertia-buoyancy dominated gravity current and a viscous-buoyancy dominated one. Comparison between the experimental results and numerical results obtained from the model proved that the model can adequately explain the behavior of the phenomenon.

A second series of experiments was conducted to investigate the behavior of gravity currents in an inclined channel. The quantitative results obtained were less scattered than those obtained in previous research. The gravity current was found to be unsteady in a horizontal channel, while a channel with an angle of inclination of one degree was found to produce a steady flow behind the front of the gravity current. The change of the gravity currents from an unsteady to a steady nature due to the change in the inclination of the channel was found to be gradual and much less abrupt than assumed in previous studies.

TABLE OF CONTENTS

LIST OF FIGURES

LIST OF TABLES

NOMENCLATURE

c_1 Proportionality constant which is related to the increase in depth with time in equation (2.4)

C_D Drag coefficient due to stress at the lower boundary

d_{ref} Characteristic length scale, $(Q^2/g')^{1/3}$

Fr Froude number, $\frac{V_f}{g' h_1}$

g Acceleration due to gravity

g' Reduced gravity, $\frac{\rho_w - \rho_a}{\rho_a} g$

H Channel height

h Depth of a gravity current at any position x and time t

h_0 Initial depth of a gravity current just behind the head

h_1 Head height of a gravity current

h_2 Mean height of the first wave of the reflected bore of a gravity current

h_3 Maximum height of the first wave of the reflected bore of a gravity current

h_4 Depth of gravity current just upstream of the reflected bore

K Constant used to start solution as defined in equation (3.6c)

k Constant used in the model as defined in equation (3.4e)

L Length of bottom wall of the channel

n Exponent related the front position to time

p Pressure of the current at location (x,y) and time t

p_H Pressure at y = H

p_0 Pressure at y = 0

P_{ref} Characteristic pressure, $\rho_a U_{ref}^2$

$P_{99\%}$ Position at which the front velocity first attains 99% of that of the constant front speed

Q Volumetric discharge rate per unit width of the channel

R Arbitrary variable to demonstrate discretization in the Lax method

R_1 Alternative length scale, $\frac{Q^5}{g' \nu_w^3}^{1/3} = d_{ref} Re$

Re	Reynolds number, Q/ν_w
$Re_{x'}$	Reynolds number based on x', $\frac{U_w x'}{\nu_w}$
$Re_{\delta'}$	Reynolds number based on δ', $\frac{U_w \delta'}{\nu_w}$
Ri	Richardson number, $g' h/U_w^2$
S	$U_w h + U_a (H - h)$
S_2	Shape factor, used by Britter and Linden (1980)
t	Time after start of discharge
t_0	Time at which the front of a current arrives at a particular location
t_{ref}	Characteristic time scale, $(Q/g'^2)^{1/3}$
U_a	Velocity of ambient fluid at location x and time t
U_{ref}	Characteristic velocity scale, $(Q\, g')^{1/3}$
U_w	Free-stream velocity of the current at location x and time t
u	Horizontal velocity of the fluid at location (x,y) and time t
u_h	Horizontal velocity of the current at y = h
u_w	Horizontal velocity of the current at location (x,y) and time t
V_f	Constant front speed of a gravity current
V_j	Velocity of the internal jump
V_r	Constant speed of the reflected bore of a gravity current
v	Vertical velocity of the fluid at location (x,y) and time t
v_H	Velocity of the fluid at y = H
v_h	Vertical velocity of the current at y = h
v_0	Velocity of the fluid at y = 0
w_0	Length of inlet in bottom wall through which discharge enters channel
w_1	Length of outlet in the top wall through which excess fluid is displaced from the channel
x	Distance from the leading edge of the bottom wall of the channel
x'	Distance upstream from the front of a gravity current
x_f	Instantaneous position of the front of a gravity current
$\dot{x}_f$	Instantaneous velocity of the front of a gravity current
x_j	Position of the internal jump
x_r	Instantaneous position of the reflected bore
x_t	Distance from source at which velocity of front starts to decrease

in a horizontal channel, also known as transition position

x_t Distance from source at which velocity of front starts to decrease in an inclined channel, also known as transition position

y Vertical distance from the bottom wall

z Characteristic length scale in model, defined by $\frac{x}{w_0}$

α Fraction of current fluid withdrawn at the head

β Factor that represents loss of fluid at the front, used by Grundy and Rottman (1986)

$\Delta\rho$ Difference between the working fluid and the ambient fluid, $\rho_w - \rho_a$

δ Boundary layer thickness at the bottom wall

δ' Displacement thickness of the boundary layer

γ Ratio of the velocity of the fluid on the streamline that stagnates at the front of the current to the mean velocity of the following flow

θ Angle of inclination of the channel

θ' Momentum thickness of the boundary layer

θ_c Critical angle at which a gravity current changes from unsteady to steady

ν_a Kinematic viscosity of the ambient fluid

ν_r Ratio between kinematic viscosity of the ambient fluid and that of the working fluid

ν_w Kinematic viscosity of the current

ρ Density of the fluid at location (x,y) and time t

ρ_a Density of ambient fluid

ρ_r Ratio between the density of the ambient fluid and that of the working fluid

ρ_w Density of working fluid

τ Characteristic time scale in model, defined by t

τ_0 Initial time to start computation of gravity current

τ_1 Time to start viscous solution in the computation

Superscript

$( )^*$ Quantities which are made dimensionless by dividing by the corresponding scaling parameter.

Superscript

$( )_i$	Value of quantity when it first appears
$( )_f$	Value of quantity at the front of the gravity current
i_K	Grid number of the current front
j	Number for time step

CHAPTER 1

INTRODUCTION

1.1 An introduction to gravity currents

When a fluid is introduced into an environment of a different density, it will spread under the influence of its own buoyancy forces due to gravity. When light fluid is discharged into heavier fluid it rises to the surface and then spreads along the surface, driven by the horizontal pressure gradient due to the density difference. Similarly, the discharge of a heavy fluid into a less dense environment results in a current spreading on the bottom of the light fluid reservoir. This type of fluid motion is known as a gravity current. The density difference between the fluids may be due to dissolved material, temperature differences, or suspended particles.

Gravity currents, also known as density currents, are frequently encountered in both natural and artificial situations. While thunderstorm outflows, growth of lava domes and avalanches are widely known natural examples of gravity currents, waste water discharge into rivers, oil spill in the ocean, accidental release of toxic industrial gases, and the motion of smoke, generated in accidental fires, along the ceiling of a corridor are just a few of the important and practical examples of man-made gravity currents.

Gravity currents are characterized by a raised head with abundance of mixing between the fluids at the front, followed by a shallower flow behind. An example of a gravity current is shown in Figures 1.1a through Figure 1.1d. These pictures were taken near the inlet by releasing salt solution into a channel filled with fresh water. Due to the density difference between the two fluids, the gravity current of salt solution, which is the dark blue fluid in the figures, spreads along the bottom of the channel. For presentation purposes, the currents are shown upside-down to illustrate smoke movement in a corridor. The head of a gravity current is characterized by an overhang of fluid called the nose at the front. A shifting pattern of lobes and clefts develop at the front of a current due to the no-slip condition imposed by the rigid surface, while billows resembling those due to Kelvin-Helmholtz instability appear in the shear zone at the rear part of the head. Considerable amount of mixing can also be seen to occur in this area.

The mixed fluid is left behind the advancing head, and is shown as the light blue-colored fluid in Figures 1.1a through Figure 1.1d. This mixed fluid is swept along by the current. This is evident by observing the decrease in depth of the light blue-colored layer from Figure 1.1b to Figure 1.1c. Thus, the average velocity in a gravity current behind the head must be greater than the velocity of the advancing front in order to make up for the loss of fluid at the head. By comparing Figures 1.1b and 1.1c, the current thickness can be observed to have increased significantly with time even before the arrival of the bore shown in Figure 1.1c. This bore results from the reflection of the current by the downstream end wall, and is roughly twice the height of the current just upstream of it. The reflected bore is also wavy in nature, as shown in Figure 1.1d.

The same current is shown in Figure 1.2a to be approaching the downstream end wall. Figures 1.2b and 1.2c show how the current hits the end wall, reflects from the wall and advances upstream in the form of a bore. By comparing Figures 1.2c and 1.2d, it is observed that the waviness downstream of the bore subsides after some time, but the thickness of the current downstream of the bore does not change significantly with time.

The objective of the present investigation is to gain a better understanding of some of the characteristics of gravity currents which may be useful to the development of models for smoke movement in hallways. Although corridors are in general considered as horizontal, a 20 cm difference in height at the two ends of a corridor that is 20 m long yields an angle of 0.5^{o} for the ceiling. It will be shown later that the characteristics of a gravity current in a horizontal channel differs significantly from those of a gravity current in a slightly inclined duct. As a result, considerations will be given to both gravity currents on a horizontal boundary and gravity currents on a slope.

1.2 Previous research

Since gravity currents are related to so many different natural and man-made phenomena, they have many practical applications. As a result, a large volume of literature exists on the studies of gravity currents. J. E. Simpson first authored a short review of the research conducted on gravity currents (Simpson, 1982) and then later wrote a book with more details of the research performed on gravity currents and internal bores (Simpson, 1987). The book by Simpson contains one of the best collections of

photographs and illustrations that qualitatively describes the various details of gravity currents, especially the billows and the lobes and clefts of the head at the front of the currents.

1.2.1 A brief review of research conducted on gravity currents with continuous release in a horizontal channel

By applying Bernoulli's theorem, in its form applicable to steady irrotational flows, von Karman (1940) obtained the following relationship between the propagating velocity of the current, V_f, the depth of the current, h, the acceleration due to gravity, g, the density of the current, ρ_w, and that of the ambient fluid, ρ_a, for a two-dimensional gravity current:

$$V_f = \sqrt{2 \frac{\rho_w - \rho_a}{\rho_a} g h} . \qquad (1.1)$$

In this study by Karman, the head height is assumed to be the same as the depth of the following current, and is also at the same time much smaller than the depth of the ambient fluid.

The same result was later derived by Benjamin (1968) in his study of the properties of steady, inviscid gravity currents by imposing an overall balance of momentum fluxes against buoyancy forces in the flow of an air cavity into a horizontal channel filled with water. Gravity currents in a channel of limited depth was also considered. The Froude number of the front decreased from $\sqrt{2}$ when h/H = 0 to $1/\sqrt{2}$ when h/H = 0.5 according to the expression

$$\frac{V_f}{\sqrt{g' h}} = \sqrt{\frac{(H-h)(2H-h)}{H(H+h)}} \qquad (1.2a)$$

where g' is the reduced gravity and H is the depth of the channel. The reduced gravity is defined as

$$g' = \frac{\Delta\rho}{\rho_a} g \qquad (1.2b)$$

where $\Delta\rho = \rho_w - \rho_a$. (1.2c)

Note that equation (1.2a) is equivalent to equation (1.1) when the channel height, H, is much larger than the height of the current, h. Benjamin's theory was found to be in good agreement with the experiments performed by Zukoski (1966).

For a heavy, two-dimensional gravity current flowing beneath a lighter fluid, the driving gravity force can only be balanced by the inertial force as long as the shear-layer thickness and the boundary-layer thickness are small when compared with the current thickness, h,. Using dimensional analysis, the characteristic length was found to be $d_{ref} = (Q^2/g')^{1/3}$, the characteristic time is $t_{ref} = (Q/g'^2)^{1/3}$ and the characteristic velocity is $U_{ref} = (g' Q)^{1/3}$. where Q is the volumetric influx rate of the current fluid per unit width of the channel. These characteristic scales were used by Chen (1980), Didden and Maxworthy (1982), and others. If the head height, h_1, is the same as the height of the following current, h, dimensional analysis will reproduce equation (1.1) except for the proportionality constant which must be determined empirically.

On the other hand, when the viscous drag becomes the dominant retarding force balancing the buoyancy force, the length of the current is given by $x_f \sim (g' Q^3/\nu_w)^{1/5} t^{4/5}$ instead (Didden and Maxworthy 1982 and Huppert 1982), which implies that the front velocity of the current decreases with time. In the expression above, ν_w is the kinematic viscosity of the current, x_f is the position of the front, and t is the time from the start of the influx. By order of magnitude arguments, Didden and Maxworthy showed that the total viscous drag of a bottom current is determined by the bottom stress only for $t \gg t_{ref}$. Moreover, Huppert proposed that viscous effects become important after approximately 0.4 (t_{ref} Re), where $Re = Q/\nu_w$ is the influx Reynolds number.

Chen (1980) analytically matched the inertia-buoyancy regime and the viscous-buoyancy regime to find the position of the transition between the two regimes, x_t, assuming an abrupt change from one regime to the other. It was proposed that $x_t = 0.133 R_1$ where $R_1 = (d_{ref} Re)$, and is supported by the experiments of Chobotov (1987) at $Re \cong 1000$. However, closer examination of the experimental results of Wood (1965) shows considerable variation at other Reynolds numbers.

For over a decade, Keulegan performed a series of experimental studies on both lock exchange flows and flows with continuous discharge to determine the front velocity. Keulegan (1946) found that the front velocity is constant and proportional to the characteristic velocity, U_{ref}, when viscous force is small. Keulegan (1958) also found that the front velocity was not constant when the density ratio of the two fluids is close to unity or, more precisely, when $g' < 20$ cm/s^2. For 20 cm/s^2 < g', Chobotov (1987) obtained reasonable agreement between gravity current experiments with heat transfer and a model with the steady-state approximation.

It was noticed that the density within the current is constant and the interface between the current and the ambient fluid is rather thin, about 10% of the current thickness, h. As a result, vertical mixing and diffusion of solute is important only in this relatively narrow interfacial layer. Delichatsios (1990) also pointed out that in smoke movement along the ceiling, no entrainment was observed to occur in the following flow. This is because the shear is zero near the top of the layer (Ellison and Turner 1959), and there is little transfer of fluid across the interface.

It was noticed by Middleton (1966) that the head height of a current remained constant for a long time, and Wood (1965) found that the ratio of the head height to the depth of the layer just behind the head was 1.8. However, Keulegan (1958) observed a value of 2.16. This discrepancy is due to the turbulent nature of the head and the presence of the mixed layer of fluid on top of the following flow. As a result, large errors exist for the measurements of both the head height and the depth of the current just behind the head. In addition, it was noticed that the flow of dense fluid behind the head is maintained against friction by a small slope in the density surface (Simpson and Britter 1979 and Chobotov 1987). However, no extensive quantitative information is available.

The shape and the motion of the head has been the subject of ongoing research since it is different from the following flow. The interface between the two fluids at the head of a gravity current is a typical frontal zone. That means the interface is a region in which a high density gradient is maintained even though there is intense motion and mixing (Simpson 1982). Simpson (1969) noted that the flow to the rear of the head is turbulent but its general shape remains steady. The foremost point of the head was slightly elevated above the surface since less dense fluid was overrun by the current, and the height of the nose is roughly 13% of the head height (Simpson and Britter 1979). There is intense mixing between the two fluids near the leading edge of the gravity

current, the mixed fluid being left behind the head and on top of the following gravity current. The mixing results from a shear instability between the two fluids complicated by the gravitational instability of less dense fluid near the bottom surface overrun by the head. Studies with dye tracers led to conclusion that the depth of the overrun less dense fluid is very small, about a tenth of the height of the foremost point of the head, and the flux of light fluid flowing under the head is estimated to be of the order of 0.01 of the flux of light fluid involved in mixing at the top of the head. Although the momentum exchange of this overrun light fluid as it passes through the head is insignificant when compared to other momentum changes near the head, this fluid is responsible for the lobe and cleft formation seen in most gravity currents (Simpson 1972). Bulges are swept away backwards from the front of the head and form billows which roll up. The disturbances increase in size, eventually breaking down into irregular motion. In growth they look like Kelvin-Helmholtz billows. In addition, measurements from streak photographs (Simpson and Britter 1979) gave a ratio of flow speed to front speed of about 1.3.

When the overrunning of less dense fluid is suppressed, the lobe and cleft structure disappears and regular billows can be seen forming on the leading edge of the head which has a slope of about 40^{o}. This was experimentally accomplished by Britter and Simpson (1978), who brought the head of the gravity current to rest on the fixed part of the floor of a tank by means of an opposing flow, while the floor of the tank was in the form of an endless moving belt. The velocity gradients at the floor ahead of the gravity current were thus reduced, and an inviscid gravity current with mixing was formed. In such an experiment, the foremost point of the gravity current head was on the floor, the flow was nearly two-dimensional, and more distinct billows could be seen. It was also estimated that the Richardson number across the shear layer was less than 0.01, and thus the density interface was very sharp. The average velocity of the flow behind the head of the current was about 22% faster than the velocity of the advancing front.

1.2.2 A brief review of research conducted on gravity currents with continuous release in an inclined channel

At slopes greater than about 0.5^{o}, the combination of the buoyancy force and the streamwise component of the gravitational force is large enough to overcome frictional

effects and entrainment drag. Thus, a steady head velocity results. The propagating velocity of the front of a gravity current on a slope is constant as long as its depth is small when compared to the channel height. It is proportional to the characteristic velocity, U_{ref}, at large Reynolds numbers although the proportionality constant still depends on the angle of inclination, θ (Britter and Linden 1980). Middleton (1966) found that the proportionality constant increases with slope for small slope. This is in sharp contrast to a horizontal gravity current, in which the balance of forces cannot be struck, the supply of denser fluid from behind the head diminishes continually owing to the diminishing fluid pressure-head, and so the front velocity will always slow down. The transition from the unsteady to the steady currents occurs at an angle which depends on the coefficient of friction at the bottom wall (Britter and Linden 1980).

The entrainment rate of a current falls off rapidly as the layer Richardson number, Ri, increases and is negligible when Ri is more than 0.8, regardless of θ (Ellison and Turner 1959). Since the Richardson number increases when θ decreases, the amount of entrainment decreases dramatically at small slopes. As a result, entrainment is only negligible at slopes of less than a couple of degrees.

In contrast to the head of a horizontal current, the head of a gravity current in an inclined channel increases in size as it travels down a slope, due to both direct entrainment into the head itself and addition of fluid from the following flow. The direct entrainment increases with increasing slope and accounts for one-tenth of the growth of the head at 10 degrees and about two-thirds at 90 degrees (Britter and Linden 1980). The effect of entrainment is seen in the measurements of the growth of the head height with distance down the slope. On contrary, for a horizontal current there is virtually no mixing in the flow behind the head and any mixed fluid produced at the head itself is left behind and above the following current as the current moves forward.

Middleton (1966) also suggested that an increase in slope does not affect the velocity of the head per se, but it results in a greater velocity in the following current and therefore in a greater supply of denser fluid into the head. The size of the head therefore increases, and the velocity also increases until a new equilibrium is set up between the size and velocity of the head. As a result, at a given discharge, increase in the slope produces a decrease in the thickness of the following flow and a corresponding increase in the average velocity in the current. At the same time it produces an increase in the

thickness of the head and a corresponding but smaller increase in the velocity of the head.

On the other hand, Wood (1965) and Britter and Linden (1980) observed that as the slope increases the head tends to have a steeper leading edge and the length of the head tends to shorten. When the slope tends to zero, Middleton (1966) found that the head is of a constant size and the layer behind it is of a constant depth.

1.3 Objective of the present study

The objective of the present study is to better understand gravity currents as applied to motion of smoke, generated in accidental fires, along the ceiling of a long corridor. This is schematically shown in Figures 1.3a through 1.3g, which is a reproduction of Figures 1.6a through 1.6g of Chobotov (1987). For an accidental fire in a room connected to a long corridor as shown in Figure 1.3a, the toxic, heated smoke generated by the fire will rise to the ceiling. It will entrain air and fill the room from the ceiling downwards. When the layer of smoke is deep enough, it will spill over the soffit and into the corridor, as shown in Figure 1.3b. Due to the density difference between the heated smoke and the cooler ambient air, the smoke layer will spread at a velocity V_f in the form of a gravity current, as shown in Figure 1.3c. If the flow rate, and thus the Froude number, of the current is large enough, an internal jump will appear, as shown in Figure 1.3d. When the front of the current hits the end of the corridor, it will reflect and advance in the form of a bore at a speed of V_r, as shown in Figures 1.3e and 1.3f. Finally, as shown in Figure 1.3g, the reflected bore will eventually reach the burn room, the waviness of the bore will subside, and the whole layer will grow deeper with time.

Although it was pointed out that a large body of literature exists for gravity currents in a horizontal channel, none of them has bridged the gap between the inertia-buoyancy regime and the viscous-buoyancy regime, nor does any of them give quantitative information about the depth of the current between the two regimes. It has been pointed out by Chen (1980) and others that a gravity current has a steady front velocity and a constant current depth in the inertia-buoyancy regime and a retarding front velocity and a growing current thickness in the viscous-buoyancy regime. Since smoke movement in a long corridor, which is the main objective in this research, may experience both regimes in practice, it is of great interest to find out whether the

transition from one regime to the other is gradual or abrupt. It is also important to obtain quantitative information concerning the depth and the velocity of gravity currents so that a model which is valid for both regimes can be proposed. Since the flow is unsteady in the viscous-buoyancy regime, the model for a heat-transferring gravity current proposed by Chobotov (1987) can be improved if the steady-state approximation used by Chobotov can be waived. As a result, it is advantageous to build a model that is valid for both regimes by first considering an adiabatic, viscous gravity current in a horizontal channel. A successful model for adiabatic gravity currents can then serve as the basis for a model for heat-transferring gravity currents.

As a result of the above reasons, experimental results will be presented in Chapter 2 to supply quantitative information about the time varying front position, the transition position between the two regimes, the growth in current thickness, and the velocity profile of a current. It should be pointed out that in the experiments conducted in this study, the fluid of the current was always introduced normal to the streamwise direction into the ambient environment. This was done both to ensure that there was no initial streamwise momentum and that the volume of the fluid in the current was always the same as the total amount of influx, since there was neither a strong internal jump nor turbulent mixing near the inlet. This method of introduction of the current fluid is thus very different from that used by numerous other researchers (Wilkinson 1970 and Chobotov 1987). In those studies, the fluid of the current was injected in the streamwise direction through a slot into the ambient environment, usually accompanied by a strong internal jump and turbulent mixing near the inlet due to the initial streamwise momentum. As a result, the volume of the fluid in a current in those cases was larger than the total amount of influx because of entrainment and mixing at the jump. Due to these differences, the velocity profile in the current, the spreading rate of the front of the current and the depth of the current may strongly depend on the method of introduction of the current fluid, and caution must be used when comparing the results from the various studies.

Equipped with the new quantitative information from Chapter 2, a model for an adiabatic, viscous gravity current will be developed in Chapter 3 by first considering inviscid gravity currents and then viscous ones. Experiments concerning gravity currents in an inclined duct will be briefly discussed in Chapter 4, together with some discussions on the transition from an unsteady gravity current in a horizontal channel to the steady case in a sloped channel. Finally, concluding remarks will be given in Chapter 5.

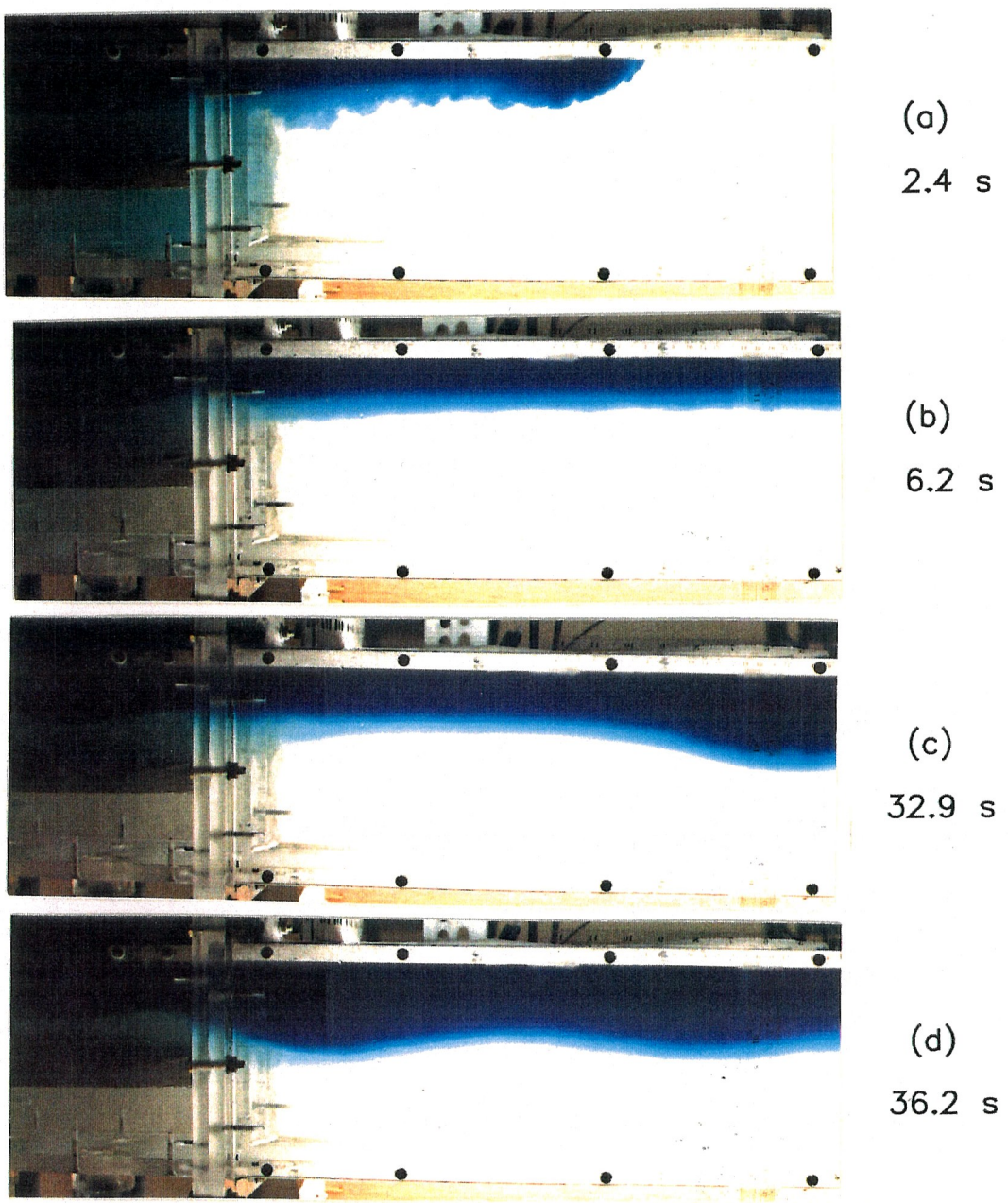

Figure 1.1 Development of gravity current over time near the inlet.

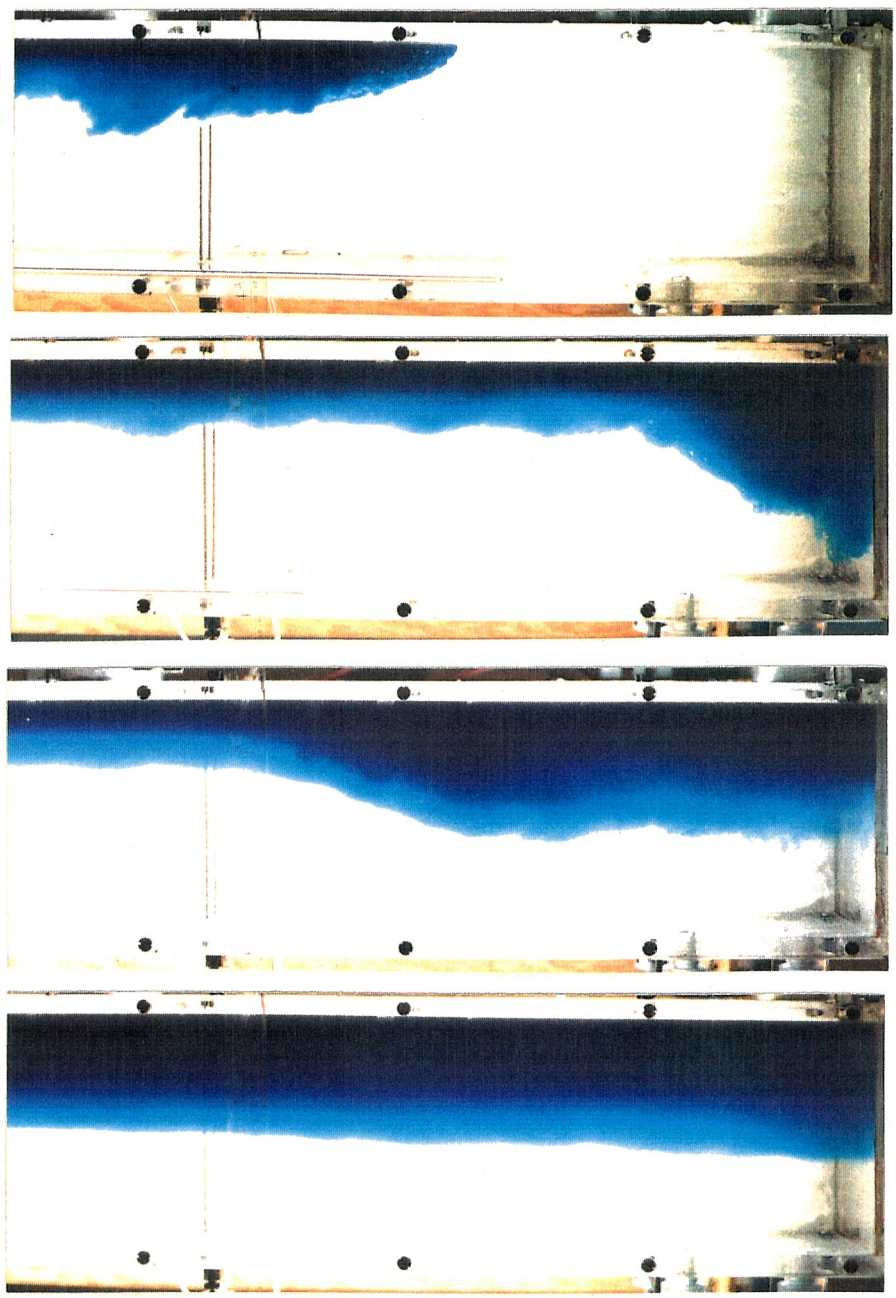

Figure 1.2 Formation of the reflected bore at the downstream end wall.

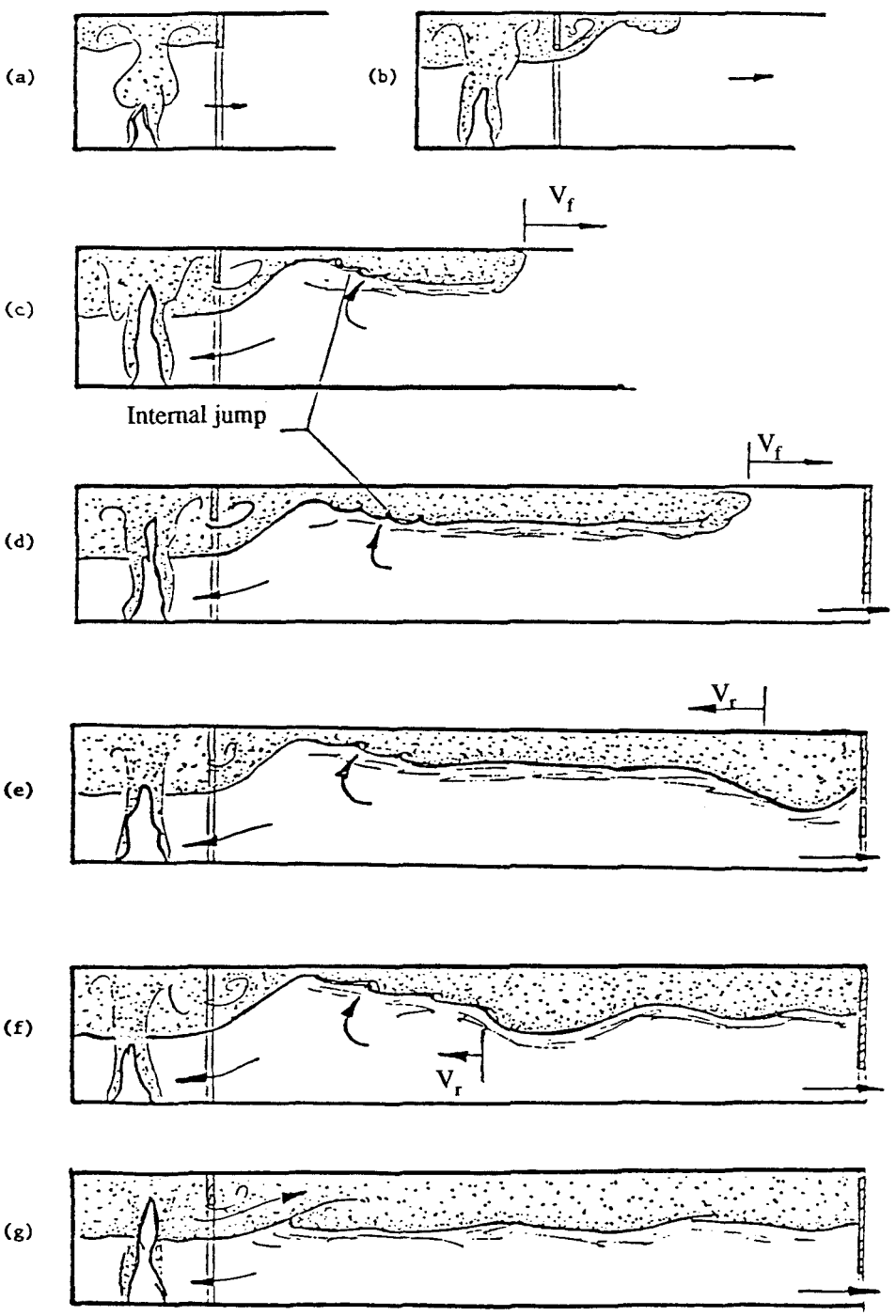

Figure 1.3 Motion of smoke in a long corridor of a burning building.
[Reproduced from Figure 1.6 of Chobotov (1987)]

CHAPTER 2

EXPERIMENTAL STUDIES ON GRAVITY CURRENTS IN A HORIZONTAL CHANNEL

2.1 Introduction

For a dense gravity current spreading over a horizontal bottom boundary in a less dense environment, the front of the current is much deeper than the following current, and is commonly known as the head. There is intense motion and mixing at the head, although a high density gradient is still maintained. The foremost point of the head is slightly elevated above the surface, and is commonly known as the nose. The mixing between the two fluids at the head of the current is the result of gravitational instabilities on the bottom and shear instabilities on the top, and the mixed fluid is left behind the head and above the following current. However, there is virtually no mixing between the following current and the ambient fluid nor between the current and the mixed fluid left behind by the head. Since there is no streamwise gravitational component, the friction on the current is only counteracted by the buoyancy force. As a result, the depth of the current must continue to increase in order to supply enough pressure head to overcome the viscous drag, and thus the velocity of the head decreases with time. Experiments were performed in the present study to investigate this effect. The experimental set-up and procedures for the present study on gravity currents in a horizontal channel will be described in Section 2.2. The results from relevant experiments concerning the front velocity of gravity currents will be discussed in Section 2.3. Quantitative measurements of current depth in a horizontal channel will be reported in Section 2.4. Section 2.5 will be devoted to experiments using hydrogen bubbles as the flow visualization aid. Finally, some measurements of the density of the current will be discussed in Section 2.6.

2.2 Experimental set-up

A schematic diagram of the experimental set-up is shown in Figure 2.1. Before each experiment, food-grade salt or sugar was first mixed with water in a big tank to form salt or sugar solution. The density and kinematic viscosity of this solution, which will also be referred to as the working fluid, were then measured by a hydrometer with

resolution of 0.0005 g/cm^3 and by a calibrated viscometer, respectively. The specific gravity of the working fluid varied from 1.02 to 1.15. The solution was then pumped through a calibrated flow meter which was accurate up to 6 cm^3/s. This flow meter measured the volumetric flow rate of the working fluid and was regulated by a valve.

The working fluid was then introduced into a long rectangular duct filled with either fresh water, salt solution or sugar solution, commonly known as the ambient fluid. The ambient fluid had a lower density than the working fluid. The channel was 277 cm long with a square cross-section of length 15 cm on each side. The length of the channel could be extended to either 343 cm or 409 cm by attaching one or more ducts of the same cross-section at the downstream end of the channel. The walls of the channel was built with half-inch thick plexiglass, and the channel rested on top of a steel brace structure. This structure could be adjusted so that the angle of inclination of the channel to the horizontal could be easily changed. Measurement of the angle was performed by using a gunner's quadrant, which was accurate to within 0.02 degree.

There was a 12.7 cm long opening on the bottom wall at one end of the channel which served as the inlet for the working fluid to enter the duct. This end is also referred to as the upstream end. The opposite end of the channel is referred to as the downstream end. The side wall through which the observations were made is referred to as the front side wall, while the other side wall is referred to as the rear side wall. Due to the opening in the bottom wall at the upstream end, the bottom wall was about 264 cm long even though the channel length was 277 cm. In addition, there were four valves, each connected to half-inch plastic tubes, installed on the top of the duct at the upstream end. Four similar valves were also installed at the downstream end. By controlling these valves, ambient fluid displaced by the working fluid could be removed at either the upstream end or the downstream end, or both.

The influx rate of working fluid was maintained at a constant level in order to provide a continuous and steady supply of working fluid. The working fluid entered the duct first through a two-inch diameter plastic tube and then through a 21 cm long, 15 cm wide, and 12 cm deep entrance section which was mounted on the floor of the duct and was filled with a plastic, wool-like material. The working fluid was supplied through the bottom wall into the channel in a direction normal to the bottom wall of the channel. The above precautions helped to provide a uniform velocity profile when the working fluid was introduced through the bottom wall into the channel. This also removed

streamwise momentum of the working fluid, and ascertained that the volume of the current is the same as the volume of working fluid introduced. As a result, the forces on the fluid downstream of the inlet were strictly due to buoyancy and viscous effects. It should again be pointed out that due to the lack of initial streamwise momentum, there was no strong internal jump nor turbulent mixing at the inlet. As a result, caution should be used when comparing results of this study with those of other studies in which the working fluid was injected through a slot in the streamwise direction into the ambient fluid. In those cases, a strong internal jump and turbulent mixing were usually observed due to the initial streamwise momentum of the current.

A splitter plate was placed above the inlet region to prevent any incoming working fluid from exiting the upstream exit due to the pressure field produced by the excess ambient fluid leaving the duct. As a precaution to avoid any mixing between the ambient fluid and the working fluid before an experiment, the working fluid was introduced into the inlet region at a very low flow rate. Once the working fluid had reached the floor level, the influx rate was suddenly increased to the desired value of the experiment and was maintained at a constant value throughout the experiment.

When the heavier working fluid was introduced into the channel filled with a lighter ambient fluid, it spread along the bottom of the channel due to buoyancy forces. The layer of working fluid is also known as a gravity current. The edge of the bottom wall at the upstream inlet is known as the leading edge, and is used as the reference position to identify the streamwise position of a location along the channel. The leading edge is also simply referred to as the 'source' for convenience. Since the salt solution, the sugar solution, and fresh water are all transparent, dye or hydrogen bubbles had to be used as the flow visualization technique so that the working fluid could be distinguished from the ambient fluid and be monitored.

Color video cameras with VHS format were used to record the progress of each experiment. The front position of the current, which is the farthest point of the layer of working fluid from the leading edge of the bottom wall of the channel, could then be determined by analyzing the recorded tapes. In addition, the depth of the current and the velocity of the fluid inside the current could also be found by the flow visualization techniques mentioned earlier. The procedures and the results for the measurement of each of the above parameters will be described in the following sections.

2.3 Measurements of the front position of the current

2.3.1 Experimental procedures

As mentioned in Section 2.2, salt or sugar solution was mixed with extra concentrated Kriegrocine blue powder before each experiment for visualization purpose. One teaspoon of the powder was enough to give one hundred liters of salt or sugar solution a dark blue color. A tape measure with resolution of 1 mm was secured on the side of the duct to show the distance of all locations from the leading edge of the bottom wall.

A video camera was mounted on a wooden block with wheels. This device was then placed on a track that ran parallel to the side walls of the channel and was placed at the same height as the bottom of the channel. The camera could then be moved along the track with minimal effort. At the same time, the camera was focused on the front of the gravity current through the front side wall of the channel as the current spread along the channel. This set-up allowed the video camera to record the time varying front position of the current with minimal interruption.

In addition, the video camera has a timer that is accurate to one-hundredth of a second. This timer was turned on before each experiment, and the time elapsed during the experiment was recorded on each video frame for reference. By noting the time elapsed and the corresponding front position, the time varying front position of the current could be found.

When the current hit the wall at the downstream end of the channel, it reflected from the wall and moved in the upstream direction in the form of a bore. However, since the features of the front of the reflected bore is not as distinctive as the front of the current, it is hard to record the front position of the bore using the tape measure that was attached to the side of the duct. Instead, vertical markers were attached to the side of the channel at regular intervals. As a result, by recording the passage of the reflected bore at the markers, together with the corresponding elapsed time, the time varying position of the reflected bore advancing in the upstream direction could be found.

2.3.2 Experimental results

As described in the last section, the front position of a gravity current was recorded for various elapsed time from the start of the experiment. Figure 2.2 shows an example of how the front position of the current, x_f, in Test 604 changes with time, t. The front speed of the current accelerates through an initial stage at the start of the experiment. The front then travels at a constant speed, V_f. This is known as the principal stage (Chen 1980), and is also known as the inertia-buoyancy dominated regime. After a sufficiently long time, the flow is dominated by viscous and buoyancy forces only. This stage of the current is known as the final stage or the viscous-buoyancy dominated regime, and the front speed undergoes constant deceleration. The presence of the three stages does not depend on whether the excess fluid is removed through the valves at the upstream end of the channel, which is simply referred to as the case of a gravity current in a channel with an upstream exit, or through the valves at the downstream end of the channel, which is referred to as the case of a gravity current in a channel with a downstream exit.

It should be noted that in the case of a channel with an upstream exit, the ambient fluid is at rest in the section not yet reached by the moving front (Keulegan, 1958). The ambient fluid above the current is moving in the upstream direction at the same volumetric flow rate as the influx because the two fluids are incompressible, and any excess fluid must be displaced from the channel. On the other hand, in the case of a channel with a downstream exit the ambient fluid downstream of the front is moving downstream at the same rate as the influx. However, the ambient fluid above the gravity current in this case hardly moves, since entrainment from the ambient fluid into the current is negligible.

Figure 2.3 reveals that the deceleration process found in the final stage of a current agrees with the proposed behavior of $x_f^* \sim t^{*4/5}$ (Chen, 1980), where the length scale, d_{ref}, and time scale, t_{ref}, used to obtain these non-dimensional quantities are the same as those introduced in Section 1.2. The non-dimensional transition position at which the gravity current started to change from an inertia-buoyancy dominated regime to a viscous-buoyancy dominated regime, x_t^*, was indicated in Figure 2.3. This transition position was recorded for each experiment.

The non-dimensional constant front speed, V_f^*, in the present study is shown as a function of Reynolds number, Re, in Figure 2.4. The reference velocity scale, U_{ref}, used to normalize V_f was introduced earlier in Section 1.2. Keulegan (1958) observed that the decrease in the salinity of the front with travel is small when the source salinity is large. This is because some of the mixed fluid left behind by the head is entrained into the current just behind the head and causes gradual dilution of the fluid in the head. For reduced gravity, g', less than 20 cm/s^2, the front velocity fluctuates as well as decreases very quickly with distance from the source. The same phenomenon was also observed in the present study. As a result, the data presented in this investigation will be limited to 20 cm/s^2 < g'. It was found that V_f^* increases with Re when Re < 1000 in a channel with an upstream exit. The variation of V_f^* was also found to be large within this range of Reynolds number. This variation in V_f^* can be attributed to the changes in the non-dimensional channel height, H^*, and the non-dimensional inlet length, w_0^*. The combined effects of H^* and w_0^* on V_f^* will be discussed in detail in Chapter 3.

On the other hand, this variation decreased dramatically with increasing Re. The average value of V_f^* for 1000 < Re was found to be 0.89 ± 0.02 in this case. It is interesting to note that although the average value of V_f^* found in the present study is larger than the average value of 0.70 found by Keulegan (1946) and smaller than the value of 1.06 found by Wood (1965), it is approximately the average of the two.

It should be noted that the working fluid used by Wood (1965) was injected in the streamwise direction into the ambient fluid through a slot. Thus, there was initial streamwise momentum, and the flow was not subjected only to buoyancy force when it first started. As a result, the quantitative results obtained by Wood are expected to be different from those in the present investigation. On the other hand, the specific dimensions of the apparatus used by Keulegan (1946) were not disclosed. Thus, no arguments can be put forth to explain the discrepancy between the experimental results obtained by Keulegan and the present study, although it is suspected that the geometry of the channel, especially the length of the inlet, is the primary reason behind this discrepancy. Details on how the geometry of the channel affects the front speed will be discussed in Chapter 3.

Using the value of the non-dimensional head height, h_1^*, found in the present study, $h_1^* = 1.59 \pm 0.19$, shown later in Section 2.4.2, the average Froude number of the

head, $Fr = \frac{V_f}{\sqrt{g' h_1}}$, was found to be 0.706 in this study. Keeping in mind the uncertainty in the measurement of h_1*, this result is in good agreement with the experimental results obtained by Keulegan (1958), who found that for 840 < Re, Fr = 0.705, and Middleton (1966), who found that Fr = 0.66 at Re = 2500.

It should be noted that the variation in V_f* for Re < 1000 is due to changes in the non-dimensional channel height, H*, and the non-dimensional inlet length, w_0*. Since the geometry of the channel, H and w_0 in particular, are fixed in the experiments, the ratio H*/w_0* is a constant. It was found that at a fixed Re, V_f* decreases with increasing H*. It will be shown in Chapter 3 that this result agrees with the model to be presented in that chapter. According to that model, V_f* increases with H* but decreases with w_0*. It will be shown in Chapter 3 that w_0* has a larger impact on V_f* than H*. As a result, for a fixed ratio of H*/w_0*, w_0* increases when H* increases, and thus V_f* decreases with increasing H*.

The non-dimensional constant front speed for gravity currents in a horizontal channel with a downstream exit is also shown in Figure 2.4. As in the case of an upstream exit, the value of V_f* does not appear to depend strongly on Re for 1000 < Re. The average value of V_f* in this case is 0.90 ± 0.04, which is within one standard deviation of the value for the case of an upstream exit. As a result, it is concluded that within the range of the parameters used in the present experimental study, the value of V_f* does not depend significantly on the exit condition. This observation also agrees with that of Keulegan (1946), who found that when the opposing ambient velocity is less than 30% of the current velocity, the current velocity in such a case is larger than 99% of the current velocity in a stationary ambient environment.

Figure 2.5 shows the position of the reflected bore, x_r, in Test 237 as a function of time from start, t. As indicated in the last section, the number of data points which could be taken for the position x_r was restricted by the number of markers placed along the channel as well as the ability to record the passage of the reflected bore at the specific markers. As a result, the number of data points that were taken in each experiment for x_r was much less than that for the front position of the current, x_f. However, it can be observed in Figure 2.5 that the velocity of the reflected bore was fairly constant for most of the time as the bore advanced in the upstream direction. Figure 2.6 shows the non-

dimensional speed of the reflected bore, V_r^*, as a function of Reynolds number. From the figure, the non-dimensional speed of the reflected bore does not vary significantly with Reynolds number. For 1000 < Re in a channel with an upstream exit, $V_r^* = 0.74 \pm 0.04$. For the lone experiment in a channel with a downstream exit, it was found that $V_r^* = 0.76$, which agrees with the result found for gravity currents in a channel with an upstream exit. Note that the speed of the reflected bore is 83% of the speed of the constant front speed of the gravity current, which is in good agreement with the result obtained by Heskestad and Hill (1987) for smoke movement in a long corridor.

As mentioned earlier, the transition position at which the gravity current changed from an inertia-buoyancy dominated regime to a viscous-buoyancy dominated regime, x_t, was recorded for each experiment. The value x_t/R_1, where $R_1 = Q^2/[(g' Q)^{1/3}\nu_w]$, is shown in Figure 2.7 as a function of Reynolds number. Chen (1980) proposed that the ratio x_t/R_1 has a constant value of 0.133 regardless of the Reynolds number for a plane gravity current with continuous release. However, it can be seen in Figure 2.7 that x_t/R_1 is instead a decreasing function of Re. This discrepancy is due to the assumption by Chen (1980) that a current changes abruptly from an inertia-buoyancy regime to a viscous-buoyancy regime, while in the present experiments, the transition from one regime to another is more gradual as observed in Figure 2.2. For 1000 < Re, the data points from the experiments was found to congregate along a line with a slope of -1 in the logarithmic-logarithmic plot. This suggests that if the value of (x_t/R_1)Re is plotted against Re instead, it would be constant for 1000 < Re. Since by definition $Re = Q/\nu_w$, the parameter $(x_t/R_1)Re = x_t/d_{ref} = x_t^*$. As a result, the corresponding plot of x_t^* as a function of Re is shown in Figure 2.8. The variation of the value of x_t^* at a fixed value of Re is significant for small Reynolds number, and x_t^* increases with increasing H^*. The reasons used earlier to explain the variation in V_f^* may also be valid in this case. The effects of the three-dimensional front and of the side walls may also have significant impact on the variation of the value of x_t^* when Re < 1000. For 1000 < Re, however, the variation of x_t^* is less significant, and it was found that $x_t^* = 88 \pm 11$.

2.3.3 Experimental errors

Since the tape measure used to identify positions along the channel has a resolution of 1 mm, the experimental error due to this measurement is less than about 0.1% in general and is negligible compared to the distance travelled by the current front.

On the other hand, although the hydrometers used to measure fluid densities are accurate up to 0.0005 g/cm^3, any error in the density measurements is magnified because it is not the fluid densities but the difference in the densities that is important, since it is this difference in densities that provides the driving buoyancy forces. As a result, the errors in density measurements may contribute to relatively large errors. For example, at a reduced gravity of g' = 20 cm/s^2, the error due to density measurements can be up to 5%. Therefore, all experiments were carried out at 20 cm/s^2 < g'.

Another major source of error is the flow rate regulated by the flow meter. As was mentioned in Section 2.2, the flow meter can be accurate up to 6 cm^3/s. As a result, the percentage error increases with decreasing flow rate. For example, at Re = 1000, Q $\cong$ 10 cm^2/s. Since the channel width is 15 cm, the percentage error due to the error in measurement is up to 4%. Thus, for experiments with small values of Q, a smaller flow meter which has a higher resolution of 1.5 cm^3/s was used.

Fortunately, owing to the cube root in the expression for the velocity scale, U_{ref}, the actual contributions by the errors in the measurements of g' and Q to the experimental errors in front position measurements are reduced. For example, a 3% error in g' will only lead to roughly a 1% error in the front velocity.

However, the error introduced in the starting process is intangible. It was described in Section 2.2 that the working fluid was initially introduced at a very slow rate to prevent premature mixing. The supply was then increased suddenly to the desired value when the working fluid had reached the floor level. Since the valve to the flow meter was manually controlled, repeatability of the process was less than desirable.

It should also be pointed out that the influence of this error in the determination of the constant front speed is minimal. This is because initial effects are not important during the principal stage which is dominated by inertia and buoyancy forces.

2.4 Measurements of the depth of the current

2.4.1 Experimental procedures

As mentioned in Section 2.3.1, the salt or sugar solution which served as the working fluid was mixed with extra concentrated Kriegrocine blue powder before each experiment for visualization purpose. Although one teaspoon of the powder was enough for one hundred liters of the solution for the purpose of identifying the front of the current, the mixed layer between the working and the ambient fluid was not well illustrated. An additional teaspoon of the Kriegrocine powder solved this problem. The mixed layer could then be seen in a faint blue color, while the current was represented by a dark blue color. Moreover, fluorescent lights were lit behind the rear side wall of the channel to enhance the contrast of the color of the fluids inside the duct. The interface between the current and the mixed layer was then well illustrated. However, by changing the amount of dye used per liter of solution, the darkness of the color of the mixed layer could be changed. As a result, the darkness of the color of the mixed layer would not provide accurate quantitative information of the concentration of solute in the layer. Samples drawn from the mixed layer, using the technique which will be described in Section 2.6.1, revealed that the density difference between the mixed layer and the ambient fluid was less than 20% of the density difference between the working fluid and the ambient fluid.

Video cameras were again used to record each experiment. However, instead of being deployed on movable tracts and allowed to follow the front of the current, each camera was left stationary and allowed to focus on a fixed position of the channel throughout an experiment. As a result, the depth of the current at various locations along the channel could be recorded simultaneously. Transparent rulers with resolution of 1 mm were secured vertically on the channel at the locations of interest to provide reference length scales on the recorded video frames. By noting the changes in the depth of the current at a fixed position along the channel with time elapsed, as discussed in Section 2.3.1, the time history of the depth of the current at a specific distance from the source could be found. In the present study, experiments were only carried out in a channel with an upstream exit.

2.4.2 Experimental results

As described in the last section, the current thicknesses at various locations were recorded when an experiment was carried out. Figure 2.9 shows an example, Test 604, of the changes in the non-dimensional depth of the current, h*, at x* = 37 as non-dimensional time, t*, progressed. The first spike of the curve represents the raised head of the gravity current when the front arrived. The depth of the following flow was shallower than the maximum head height. The depth of the following current then increased with time, first very rapidly but then at a diminishing pace. At $t^* \cong 700$, the depth of the current suddenly increased at a rapid rate. This second rapid increase in h* represents the arrival of the reflected bore. The subsequent fluctuations of the depth of the current signify the wavy nature of the reflected bore.

After the front had just passed a specific location, the depth of a gravity current increased rapidly. This rate of growth in thickness decreased considerably thereafter until the arrival of the reflected bore. If this increase in depth is due to the increase in the displacement thickness of the boundary layer that results strictly from the advancing front of the current, the solution for the Blasius problem can be used. The displacement thickness, δ', at a distance x' from the leading edge of a flat plate in Blasius problem, was given in White (1986) to be

$$\frac{\delta'}{x'} = \frac{1.72}{\sqrt{Re_{x'}}} \tag{2.1}$$

where $Re_{x'}$ is the Reynolds number based on x', a uniform free-stream velocity, U_w, and the kinematic viscosity of the current, ν_w. If a transformed coordinate which travels with the front of the current is used, it is obvious that the displacement thickness at the front of the current behaves like that at the leading edge of a flat plate. Using the assumption that the velocity in the fluid is fairly constant and not significantly different from that of the front velocity, it can be deduced from equation (2.1) that

$$\delta' \cong 1.72 \sqrt{\nu_w (t - t_0)} \tag{2.2}$$

where t_0 is the time when the front of the current arrived at the location of interest. If the increase in depth of the current at a specific location over time was strictly due to the

increase in boundary layer thickness due to the advancing front, equation (2.2) can be rewritten as

$$h^* \cong h_0^* + 1.72\sqrt{t^* - t_0^*} \tag{2.3}$$

where h_0^* is the initial current depth just after the head had passed that location. Equation (2.3) represents the model first proposed by Chobotov (1987) to explain the growth in current thickness. However, it will be shown in Chapter 3 that an alternative model better explains the phenomenon.

Figure 2.10 shows the experimental data from Test 329. The non-dimensional depth of the gravity current at $x^* = 26$ in that experiment was plotted against the non-dimensional time from start, t^*. A curve was fitted to the data points after the head had passed but before the arrival of the reflected bore. The following equation was used for the curve fit:

$$h^* \cong h_0^* + c_1\sqrt{t^* - t_0^*}\,. \tag{2.4}$$

The deviation of the data points from the fitted curve is less than the experimental error due to the measuring techniques. If the argument above is valid, the value of c_1 should be 1.72. Note also that in addition to the non-dimensional initial current depth, h_0^*, other symbols were also defined in Figure 2.10. The non-dimensional head height is denoted by h_1^*, while h_3^* represents the non-dimensional maximum height of the first wave of the reflected bore. The non-dimensional depth of the current just before the arrival of the reflected bore is denoted by h_4^*. Since the amplitude of the wave of the reflected bore was large in some experiments, h_2^*, which is defined as the non-dimensional mean height of the first wave, may be more meaningful in comparing results of different experiments.

The non-dimensional initial current depth, h_0^*, obtained by equation (2.4) from various experiments was found not to depend significantly on the Reynolds number. It is shown in Figure 2.11 as a function of the non-dimensional distance from the leading edge, x^*. Despite the scattering of the data points as a result of the curve fit, h_0^* clearly decreases with increasing value of x^* according to the expression $h_0^* = -1.4\text{x}10^{-3}\ x^* + 0.85$. Due to the vast number of data points being used in obtaining the least square

curve, shown as the dashed line in the figure, the position of the line does not change significantly even if the few data points which deviate greatly from the least square fit were excluded.

In contrast to the behavior of h_0*, the constant for the curve fit in equation (2.4), c_1, does not depend on x*. Figure 2.12 shows the value of c_1 as a function of Reynolds number. The value of c_1 is governed by the expression $c_1 = 5.9 \times 10^{-4}$ Re + 0.91. Since it was determined that $c_1 = 1.72$ if the increase in depth of the current is strictly due to the increase in boundary layer thickness resulting from the advancement of the front of the current, it is concluded that other factors must also play major roles in the spatial and temporal changes in h*. These factors will be studied in Chapter 3, and it will be shown that the most prominent factor is the growth in boundary layer thickness from the leading edge of the bottom wall.

When the depth of a gravity current at various locations were recorded as time progressed, the current thickness at a specific time at the various locations could be obtained. Figure 2.13 shows an example of the variation of the depth of a gravity current with the distance from the leading edge at non-dimensional time t* = 200. The depth of the current dropped rapidly between the upstream end wall and the leading edge of the bottom wall of the duct. The current developed a weak internal jump just downstream of the leading edge of the bottom wall, and then the depth of the current continued to decrease. This decrease in h* with respect to x* was due to the continual increase in the boundary layer thickness in the current, together with the decrease in the fluid velocity at any spatial location with time. This will be further discussed in Chapter 3.

Although the head height, h_1, is not well defined due to the turbulent mixing of ambient and working fluids in the head as shown in Figure 1.1a, an attempt was made to investigate the dependency of h_1 on x* or Re. Figure 2.14 shows the non-dimensional head height, h_1*, as a function of x*. It can be observed that h_1* depends on x* only weakly, if at all, for $15 < x^* < 150$. The average value of h_1* found in the present study is 1.59 ± 0.19. No dependency of h_1* on Re was observed. It can also be shown that h_1* has at most a very weak dependency on the channel height, H*, for $5 < H^* < 12$, or alternatively, for $0.11 < h_1^*/H^* < 0.36$. The ratio between the head height and the depth of the following current, h_1^*/h_0^*, can be deduced from the results presented above. The average value of h_1^*/h_0^* increases from 1.93 at x* = 20 to 2.48 at x* = 150. This is in

good agreement with the average value of 2.16 found by Keulegan (1958) and not far from the value of 1.8 given by Wood (1965). This is also in good agreement with the experimental results obtained by Simpson and Britter (1979), although they plotted the results as a function of h_0^*/H^* instead of x^*, which is a more fundamental parameter.

On the other hand, the non-dimensional mean height of the first wave of the reflected bore, h_2^*, displays a decreasing trend with respect to increasing non-dimensional distance from the source, x^*, in Figure 2.15. The value of h_2^* can be given by the expression $h_2^* = -3.4 \times 10^{-3} x^* + 2.43$, which is represented by the dashed line in the figure. It can also be shown that h_2^* is at most a very weak function of H^* within the range $5 < H^* < 15$. Alternatively, the non-dimensional maximum height of the first wave of the reflected bore, h_3^*, can also be used as the means to characterize the reflected bore. As shown in Figure 2.16, h_3^* is also a decreasing function of x^*, and is given by the expression $h_3^* = -4.0 \times 10^{-3} x^* + 2.66$, which is represented by the dashed line in Figure 2.16. No significant dependence of either h_2^* or h_3^* on Re can be observed.

The variations of h_2^* and h_3^* are direct consequences of the decreasing depth of the current, h^*, as a function of the distance downstream of the leading edge, x^*. When the reflected bore advanced upstream, it acted as if it was moving up a slope. As a result, the total height of the reflected bore increased when it moved toward the upstream end of the duct. However, by observing the mean amplitude of the reflected bore, $h_2^* - h_4^*$, at various locations, x^*, it was noticed that $h_2^* - h_4^*$ is at most a very weak function of x^*. Its dependency on x^* can be described by the expression $h_2^* - h_4^* = -3.0 \times 10^{-4} x^* + 0.77$ and is only one-tenth of the dependency of h_2^* on x^*. On the other hand, as shown in Figure 2.17, $h_2^* - h_4^* = 1.1 \times 10^{-4}$ Re $+ 0.53$, which is represented by the dashed line in the figure. Although the coefficients in the two expressions for $h_2^* - h_4^*$ in terms of x^* and in terms of Re are similar, the range of Re is roughly two orders of magnitude as that of x^*. As a result, the value of $h_2^* - h_4^*$ depends strongly on Re but at most weakly on x^*.

A similar observation was made on the amplitude of the reflected bore, $h_3^* - h_4^*$. Its value shows a similarly very weak dependency on x^*, and can be described by the expression $h_3^* - h_4^* = -3.0 \times 10^{-4} x^* + 1.01$. On the other hand, it can be related to the Reynolds number by the expression $h_3^* - h_4^* = 2.0 \times 10^{-4}$ Re $+ 0.51$, which is shown as the dashed line in Figure 2.18.

2.4.3 Effects of the interfacial shear on a gravity current

Figure 2.19 shows the time varying non-dimensional depth of two gravity currents at $x^* = 27$ with Re = 1250, $d_{ref} = 1.87$ cm, and $t_{ref} = 0.173$ s. The only difference in the two experiments is between the kinematic viscosities of the ambient fluids used in the experiments. Although the kinematic viscosity of the ambient fluid in one of the two experiments is more than double that in the other experiment, the depths of the two currents were found to be within experimental error of each other. As a result, it is concluded that the interfacial shear does not contribute strongly to the continual increase in the thickness of a gravity current, and thus can be ignored in the modelling effort to be presented in Chapter 3.

However, the spreading rates of the same two currents were found to be different. The gravity current in the less viscous ambient environment was found to have a constant front speed, V_f^*, that is 6% larger than that in the experiment with a more viscous ambient fluid, as shown in Figure 2.20. It is thus concluded that shear between the head and the ambient fluid slightly affects the propagation speed of the front. However, since it was shown in Figure 2.19 that the depth of the current at any specific position was not affected, it can be concluded that the contribution of the moving front to the boundary layer thickness is at most important only to the region of the current close to the front. It will be shown in the model to be presented in Chapter 3 that the continuous increase in the thickness of a gravity current is due to the need of a growing pressure head that is needed to overcome the ever increasing drag on the bottom wall and is not due to a boundary layer growing from the front of the current. The conclusion above is thus in good agreement with the results obtained from the model.

2.4.4 Experimental errors

Experimental errors involved in current depth measurements are larger than those in front velocity measurements primarily because the distance travelled by a current is two orders of magnitude larger than the current depth. As a result, an error of 1 mm in depth measurement will typically represent an error of 5%.

In addition, the effects of the random errors in the front position measurements are reduced because a linear least square fit was used over a large number of points to obtain the constant front speed. On the other hand, there is no such advantage in dealing with the random errors in the current depth measurements.

Finally, the effects of an error in Q are doubled in the depth measurements when compared to the front position measurements because the length scale, d_{ref}, depends on $Q^{2/3}$ while the velocity scale, U_{ref}, only depends on $Q^{1/3}$.

2.5 Measurements using hydrogen bubble technique

2.5.1 Experimental procedures

In some experiments, the working fluid was not mixed with a dye before it was used. Instead, hydrogen bubbles were generated during those experiments for flow visualization purposes. To generate the hydrogen bubbles, a tungsten wire with a diameter of one-thousandth of an inch was placed normal to the flow direction in the channel at a fixed position from the leading edge of the bottom wall and midway between the front and rear side walls to minimize any effects due to the side walls. One end of the wire was connected to an electronic circuitry which supplied square electrical pulses of 2.5V ± 2.5V across the electrodes. This circuitry was identical to the one developed by Miller (1987), who gave a comprehensive description of the circuitry. The tungsten wire served as the cathode of the circuit. A conducting rod was placed far downstream of the tungsten wire in the channel. It was connected to the other end of the circuit and served as the anode. The working fluid then closed the circuit. A more general description on the utilization of hydrogen bubbles as a flow visualization aid can be found in Schraub et al. (1965).

During half of the cycle of a square electrical pulse, the voltage between the electrodes was non-zero. Electrolysis thus occurred around the tungsten wire, and hydrogen bubbles were formed. These bubbles were then swept away from the wire by the moving fluid in the gravity current. Since the size of a bubble is of the same order as the diameter of the wire, and the vertical velocity of a bubble induced by buoyancy forces increases with increasing bubble diameter, the diameter of the tungsten wire must

be small in order to obtain good quantitative results. When the vertical velocity of a bubble is small when compared to the horizontal velocity of the current fluid around the bubble, the bubble will be moving practically at the same speed as the surrounding fluid and can thus serve as a marker of the motion of the fluid. As a result, a thin tungsten wire of one-thousandth of an inch diameter was used to generate small bubbles, so that the bubbles could serve as accurate markers of the motion of the current, and in turn good quantitative data about the velocity profile of the gravity current could be obtained.

During the second half of the cycle of the square electrical pulse, the voltage across the electrodes dropped to zero, no bubbles were generated during this period of time. By supplying continuous square electrical voltage pulses, sheets of bubbles were formed intermittently. As a result, the time varying velocity profile of a gravity current at a specific location could be found by first measuring the distance between the positions of the leading edges of two bubble sheets at each of several vertical distances from the bottom wall and then multiplying this distance by the frequency of the electrical pulses. This was achieved by digitizing a single video frame and then recording the light intensity of the pixels in an array. Since hydrogen bubbles reflect more light than the working fluid, the leading edge of a bubble sheet at any particular distance from the bottom wall could be found automatically by locating the position of the large gradient of light intensity in the array.

As in previous experiments, the experiments involving the hydrogen bubble technique were recorded by video cameras, and experiments were carried out only in a channel with an upstream exit. The reference lengths on the video frame in the normal and streamwise directions were predetermined by placing an object of known dimensions inside the channel filled with the ambient fluid before an experiment. A sheet of light originating from a point source was shone in a plane parallel to the streamwise direction, through the bottom wall of the channel, onto the bubbles in order to provide the contrast necessary for good video records of the bubbles. It was observed that when salt solution was used as the working fluid, most of the bubbles were generated inside the current because salt solution is much more conductive than fresh water, the fluid most often used as the ambient fluid. This is illustrated in Figure 2.21a.

Due to the difference in refractive index between the working fluid and the ambient fluid, most of the light was reflected or refracted from the interface. Only a small amount of the light could penetrate the interface undisturbed and illuminate the

bubbles in the layer of ambient fluid. As a result, good quantitative measurements on the velocity profile of the layer of ambient fluid could not be obtained simultaneously with measurements on the velocity profile of a gravity current.

It was described earlier that mixed fluid was left behind the head and on top of the current. Inside the mixed layer, the speed of the fluid in the streamwise direction decreased from that of the current fluid to zero with increasing distance from the bottom wall. The speed of the fluid then increased with distance away from the bottom wall until it matched the speed of the layer of ambient fluid and moved in the opposite direction to that of the current. As a result, the speed of the fluid inside the mixed layer was smaller than that in the current and might not be large when compared to the vertical velocity of the bubbles due to buoyancy. As a result, the vertical velocity of the bubbles might not be negligible. The bubbles could not serve as accurate markers of the fluid, and thus quantitative data could not be obtained. However, valuable qualitative information could still be obtained from the motion of the bubbles in this layer, as well as in the layer of ambient fluid. For example, it was observed that none of the bubbles penetrated from the ambient layer through the interface into the current. It is thus concluded that no fluid is entrained from the ambient layer into the current, which is in good agreement with Ellison and Turner (1959).

There are times, after the head had passed but before the arrival of the bore, when the boundary layer was lifted from the bottom wall. An example of this phenomenon is shown in Figure 2.21b. However, the boundary layer reattaches very quickly, usually within 0.1 s. A rough estimate of the Reynolds number, $Re_{\delta'}$, based on the displacement thickness, δ', for the particular example shown in Figure 2.21b was found to be about 300. This value is much lower than the critical Reynolds number at which transition occurs (Schlichting 1968). As a result, it is concluded that this lifting of the boundary layer is not due to turbulence. Instead, it may be due to unstable disturbances, which was discussed by Schlichting.

On the other hand, the boundary layer is shown in Figure 2.21c to separate at the arrival of the reflected bore. In this figure, reversal of flow direction can be seen near the bottom wall. This presents a problem to the model to be shown in Chapter 3, which uses an integral method. Nevertheless, except for some secondary flows, the fluid downstream of the reflected bore can be assumed to have stopped moving in the horizontal direction.

An unexpected benefit that accompanied the problem regarding the change in refractive index across the interface was the availability of quantitative information about the position of the interface. As mentioned earlier, a significant amount of the light was refracted from the interface. Due to the three dimensionality and waviness of the interface, some of the light refracted from the interface was focused and thus bright spots were formed. As a result, the interface was recorded on each video frame as a bright but yet thin stripe. By noting the distance of this stripe from the bottom wall, the time varying depth of the current at a fixed position could be accurately determined.

2.5.2 Experimental results

In the experiments in a channel with an upstream exit, it was noticed that the ambient fluid was quiescent before the arrival of the front of the gravity current. This is in good agreement with the observations of Keulegan (1958). Both the ambient fluid and the working fluid were found to be near quiescent downstream of the reflected bore. It was also found that the zero velocity point, the point at which the flow was neither moving upstream nor downstream, lay above the current. The portion of the flow in the shear layer at which the largest velocity gradient occurred was observed to be above the gravity current. This is supported by Figure 2.22, which shows the velocity profile at $x^* = 52$ and $t^* = 126$ for Test 395 with Re = 2105. A boundary layer was observed to exist at the bottom wall, and the estimated thickness of the boundary layer is denoted by δ. The interface between the current and the ambient fluid was at $y^* \cong 1.03$, where y^* is the non-dimensional distance above the bottom wall. By definition, the interface height is identical to the depth of the current, h^*. The flow is uniform between the interface and the boundary layer. The uniform velocity in this portion of the flow is denoted as the current velocity, U_w^*. Since the velocity gradient at the interface is small when compared to that at the bottom wall, the viscous drag due to the interfacial shear is not significant when compared to the viscous drag due to the boundary layer at the bottom wall. This observation supports the conclusion drawn in Section 2.4.3, which stated that interfacial shear contributed little to the growth in current thickness.

As mentioned in the last paragraph, the non-dimensional depth of the current, h^*, is by definition identical to the interface height. The value of h^* at $x^* = 52$ in Test 395, using hydrogen bubbles as the flow visualization aid, was determined for various time.

This time varying non-dimensional depth of the current was then compared in Figure 2.23 to that obtained in Test 329, which was conducted under very similar conditions but in which Kriegrocine blue dye was used as the flow visualization aid. The values of h* in the two tests are observed to be within experimental errors. As a result, it is concluded that both hydrogen bubbles and blue dye can serve as flow visualization aids and can provide good quantitative information for the determination of h*.

Figure 2.24 shows both the time varying non-dimensional depth of the current in Test 395 as well as the corresponding non-dimensional boundary layer thickness, δ^*. The boundary layer thickness was observed to fluctuate during the experiment. This fluctuation might have been caused by neutral disturbances (Schlichting 1968). It might also have been caused by the presence of longitudinal convection cells similar to those observed by Chobotov (1987) in the thermal boundary layer of a gravity current with heat transfer to the boundary. In addition, each value of δ^* was obtained by observation from a velocity profile plot similar to Figure 2.22. As a result, the error introduced in the estimation of the boundary layer thickness is not negligible. Nevertheless, the figure shows that the value of δ^* at $x^* = 52$ fluctuated around 0.25 long after the head had passed. If the boundary layer is developed strictly from the moving front according to equation (2.4), the boundary layer thickness should have kept rising with time. As a result, the development of the boundary layer had to be due to the leading edge of the bottom wall of the channel. However, in a steady, uniform flow as in the Blasius problem, the value of δ^* would be 0.75, which is much larger than the measured value in the experiment. It will be shown in Chapter 3 that the effects of the increasing current depth, h*, and the correspondingly decreasing current velocity, U_w^*, combined to keep the boundary layer thickness at the lower measured value. Since the boundary layer thickness is not an ever increasing function of time, the continuous increase in h* at a location x* must be a combination of the increase in δ^* at the particular location and the ever increasing pressure head needed to overcome the increasing drag on the bottom wall downstream of x*.

The corresponding non-dimensional uniform velocity of the current, U_w^*, found in Test 395 is shown in Figure 2.25 as a function of non-dimensional time, t*. The current velocity decreased continuously with time following the expression $U_w^* = -1.3 \times 10^{-3}\, t^* + 1.13$. Since the front of the current was found in Section 2.3.2 to spread at a non-dimensional speed of 0.89, the fluid near the front of the current was

overtaking the front of the current and mixed with the ambient fluid. The mixed fluid was then left behind the head and on top of the following current. According to the above expression, the velocity of the fluid just behind the head was 18% faster than the front speed in this particular experiment, and is in good agreement with the results of Britter and Simpson (1978).

2.5.3 Experimental errors

In the experiments using hydrogen bubbles as the flow visualization aid, each video frame was digitized and the light intensity recorded. Each pixel represents roughly 0.018 cm in the horizontal dimension and 0.014 cm in the vertical dimension. As a result, the location of a position can be measured accurately. This is illustrated by the excellent agreement between the current depth measured using this technique and that using the blue dye as the flow visualization aid.

On the other hand, since the fluid in the boundary layer moves at a very low speed, the bubbles may not represent accurate markers of the flow field, as discussed in Section 2.5.1. As a result, caution must be used in interpreting results related to the boundary layers.

In addition, the results concerning the boundary layer thickness as shown in Figure 2.24 was manually determined by observing velocity profiles similar to that in Figure 2.22. As a result, the random error in the determination of the boundary layer thickness will be significant. The periodical lifting of the boundary layer may also contribute to the fluctuation of the experimental data deduced using this measuring technique.

It was also mentioned in Section 2.5.1 that velocity profiles were obtained by observing the distance between the leading edges of two consecutive bubble sheets. Due to an uneven light source and the scatter of light by the bubbles, the light intensity at the edge of a bubble sheet has a lower gradient with respect to streamwise distance than desirable. In addition, the leading edge was determined automatically by software using a pre-determined threshold of light intensity. As a result, the velocity profiles deduced are not as smooth as the raw data shown in Figure 2.21a.

2.6 Measurements of fluid densities

2.6.1 Experimental procedures

In two experiments, the supply of working fluid into the channel was stopped as soon as the front of the current hit the wall at the downstream end of the channel. After the resulting wavy motion of the interface had subsided, the thicknesses of the layer of ambient fluid, the mixed layer, and the layer of working fluid were measured and the volume of each layer was deduced. Samples of fluids were taken from the three layers. The density of each sample was then measured by a calibrated hydrometer. These data provided valuable information about the amount of mixing during the experiment.

2.6.2 Experimental results

It was found that in each of the two experiments, the density of the fluid sample taken from the layer of ambient fluid was, within the accuracy of the hydrometer, the same as the original density of the ambient fluid. Similarly, the density of the sample taken from the layer of working fluid was the same as the density of the working fluid introduced into the channel. However, density measurement on the sample taken from the mixed layer revealed that its density was between those of the ambient fluid and the working fluid. In the two different experiments, the density differences between the mixed fluid and the ambient fluid were 8% and 18%, respectively, of the corresponding density differences between the ambient fluid and the working fluid. Since the density of the fluid inside the current was the same as the density of the working fluid introduced, most, if not all, of the salt in the mixed layer was due to mixing at the front of the current and was not due to interfacial mixing or diffusion. As a result, by assuming a value of roughly 0.7 for the non-dimensional initial current depth, h_0^*, throughout the experiments, it was deduced that the fluid velocities just behind the front of the currents were 16% and 17% faster than the respective velocities of the front of the currents. This result is in good agreement with the result obtained in the hydrogen bubble experiments described in Section 2.5.2.

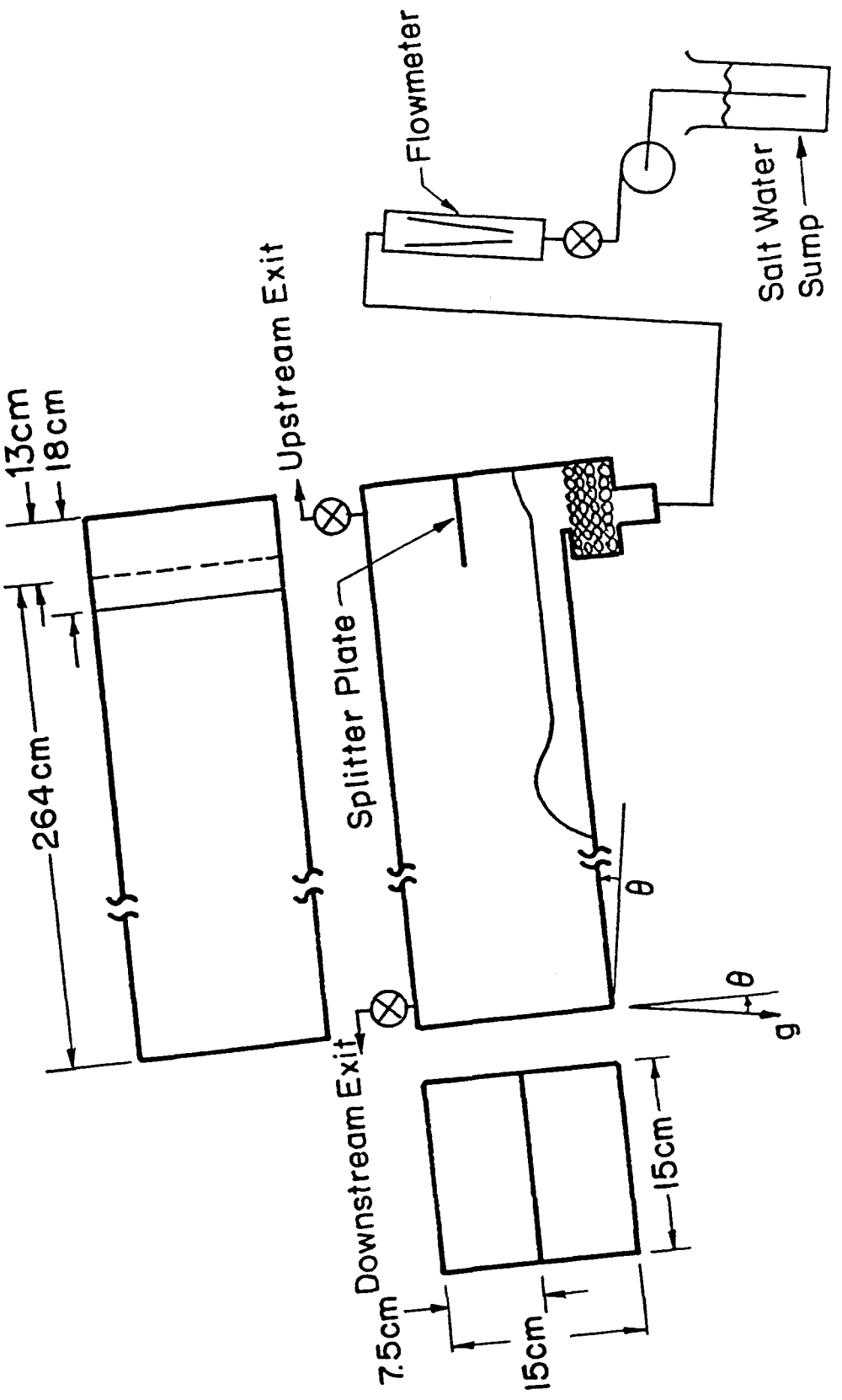

Figure 2.1 Schematic diagram of gravity current experimental apparatus.

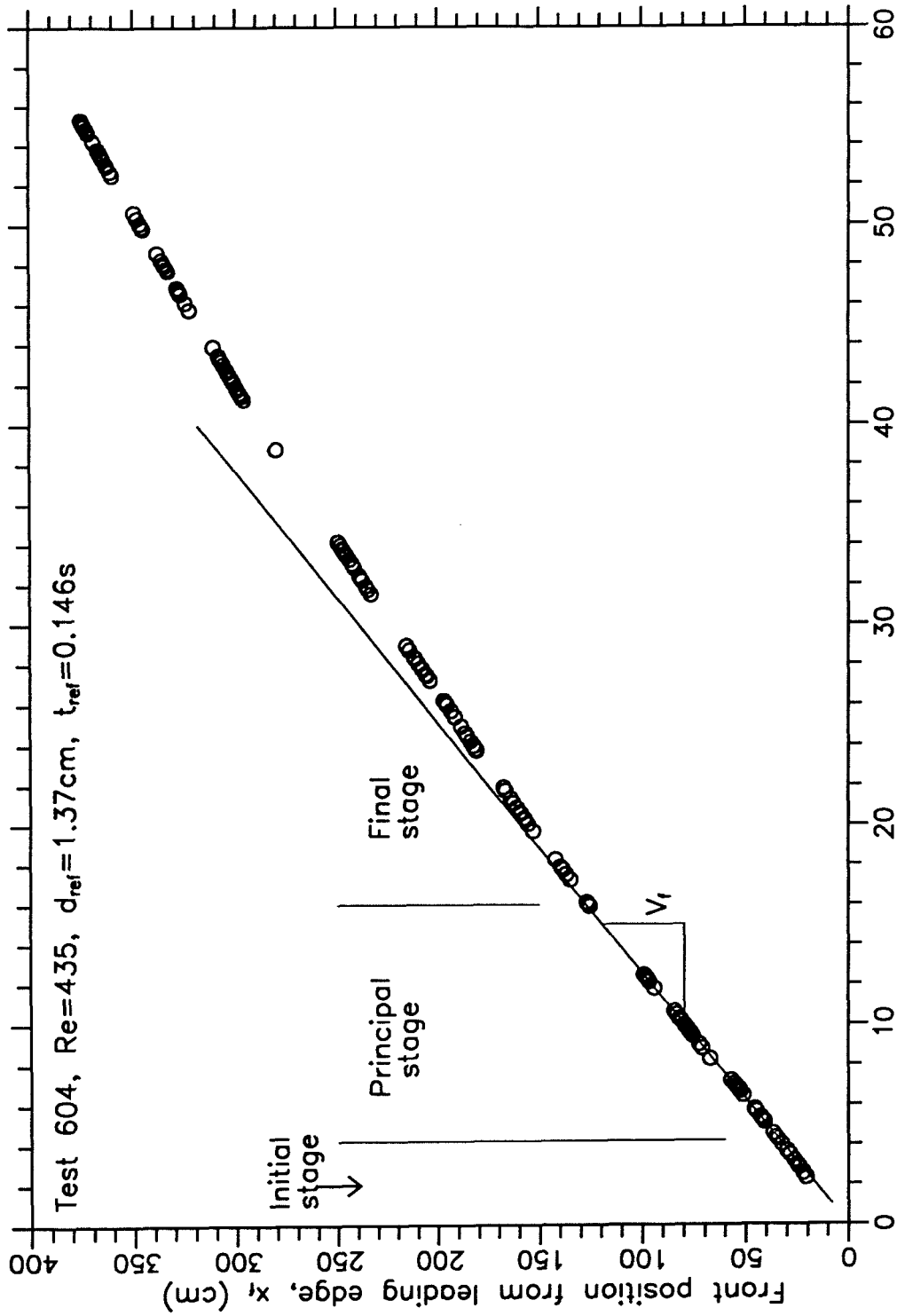

Figure 2.2 Front position from the leading edge as a function of time.

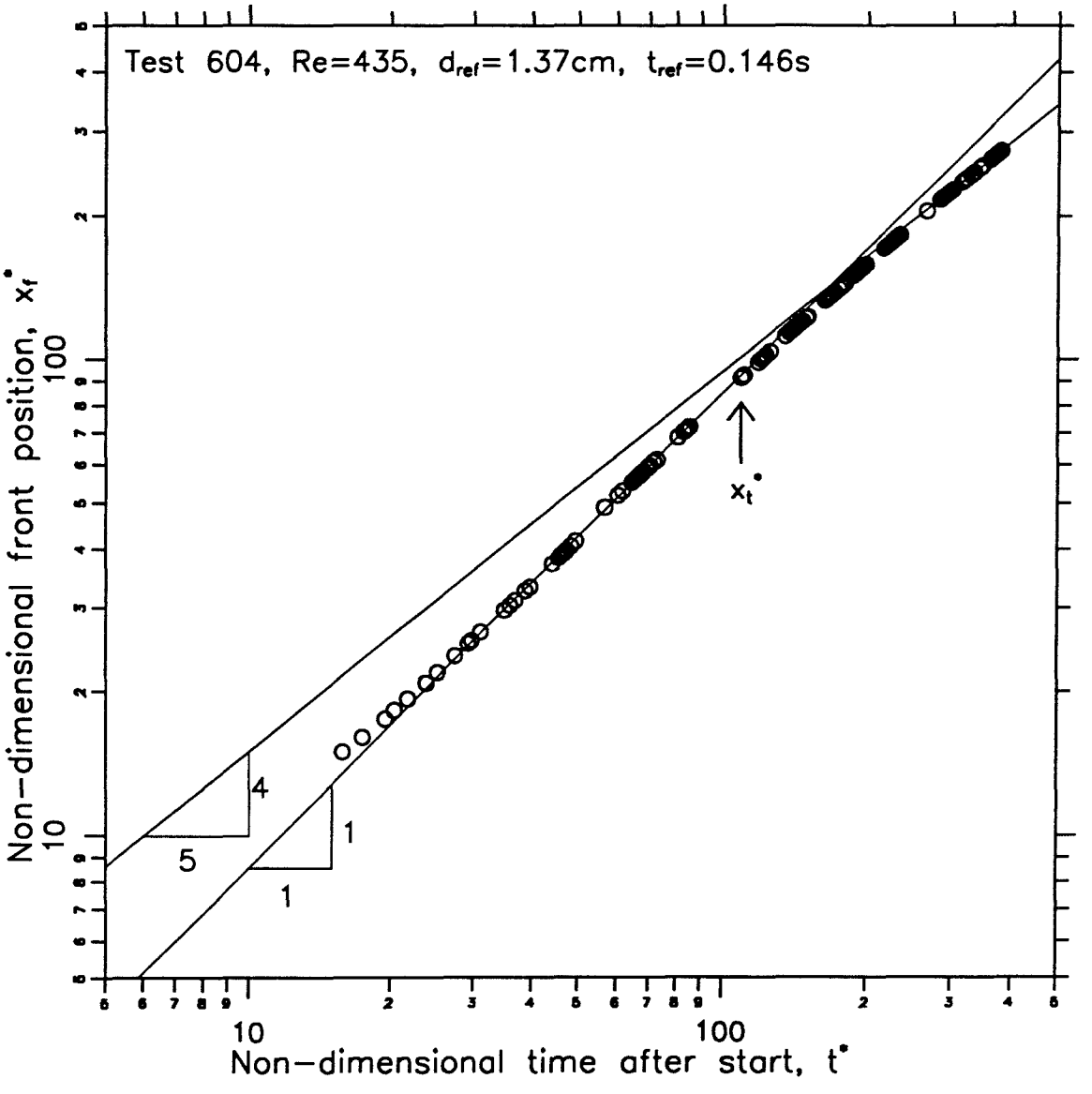

Figure 2.3 Front position from source as a function of time.

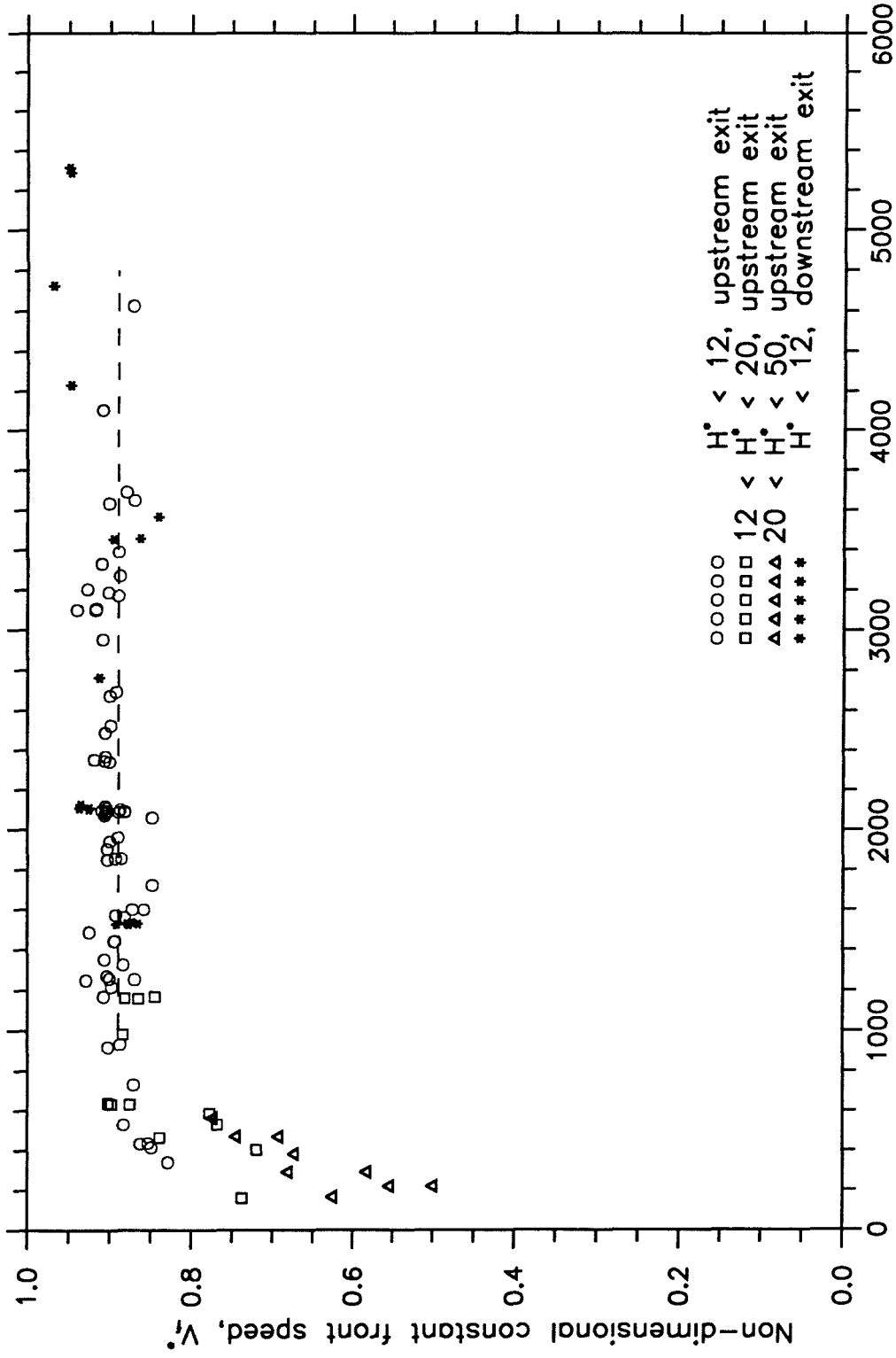

Figure 2.4 Constant front speed in a horizontal duct as a function of Reynolds number.

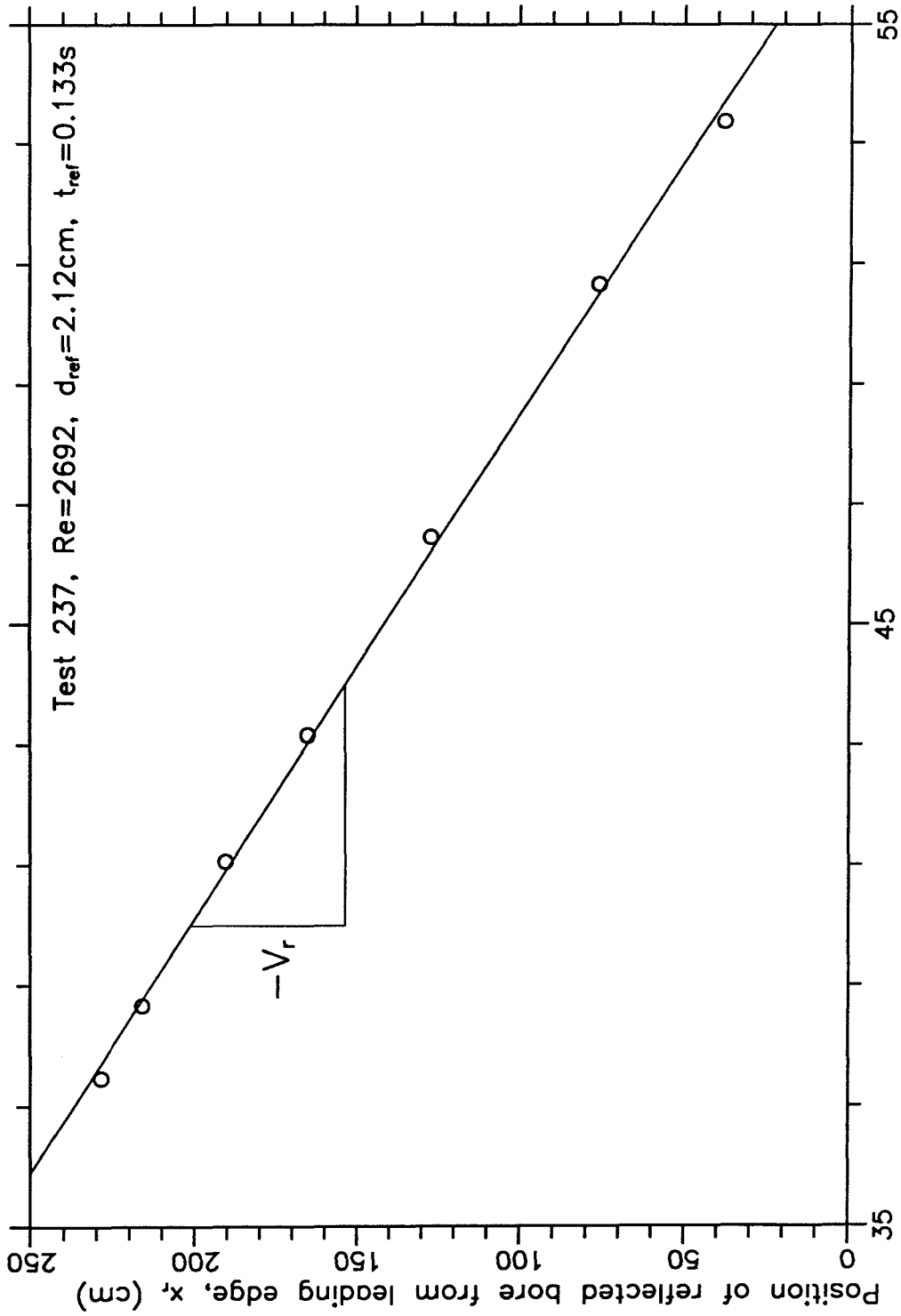

Figure 2.5 Position of reflected bore from leading edge as a function of time.

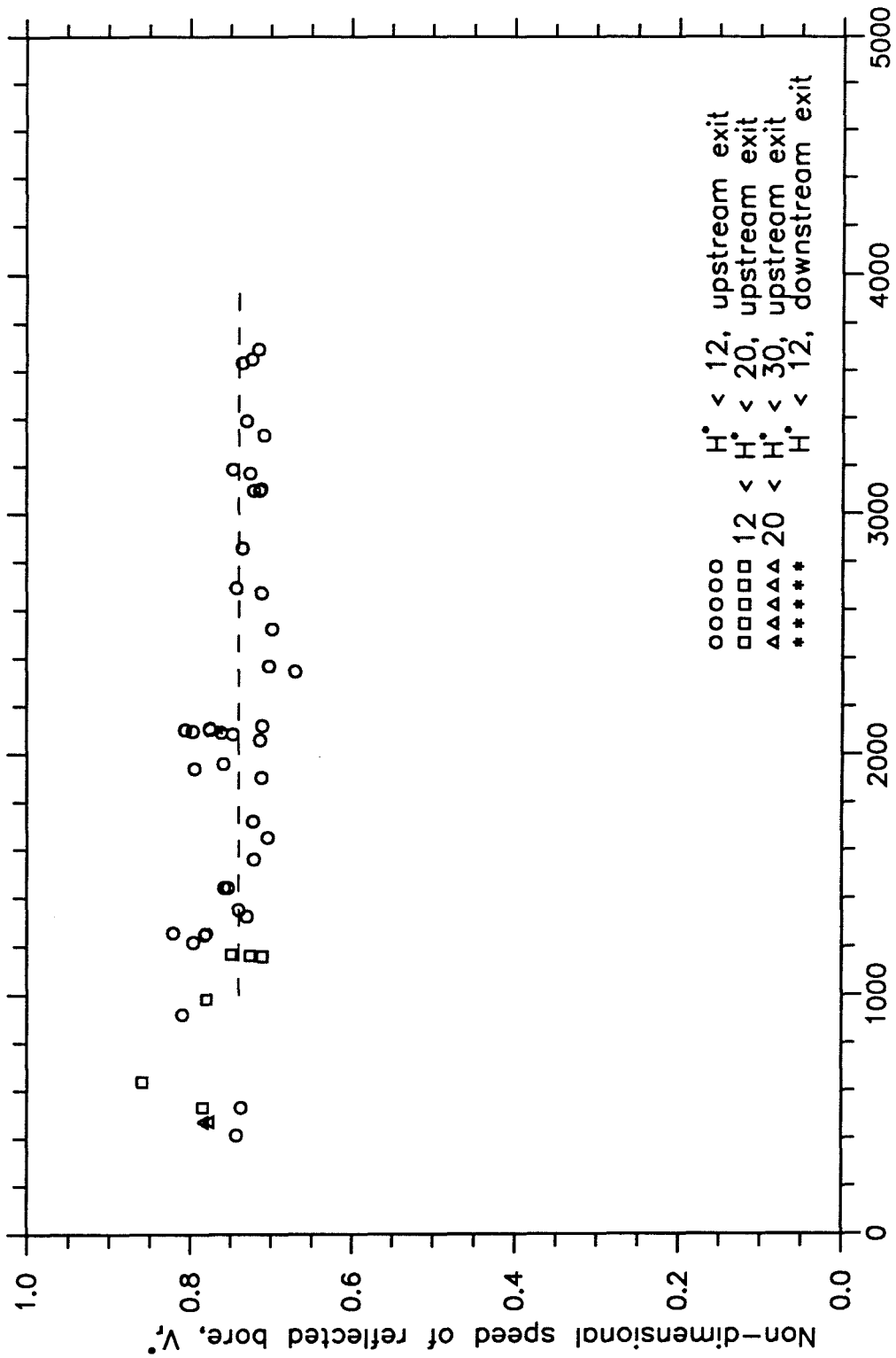

Figure 2.6 Speed of reflected bore as a function of Reynolds number.

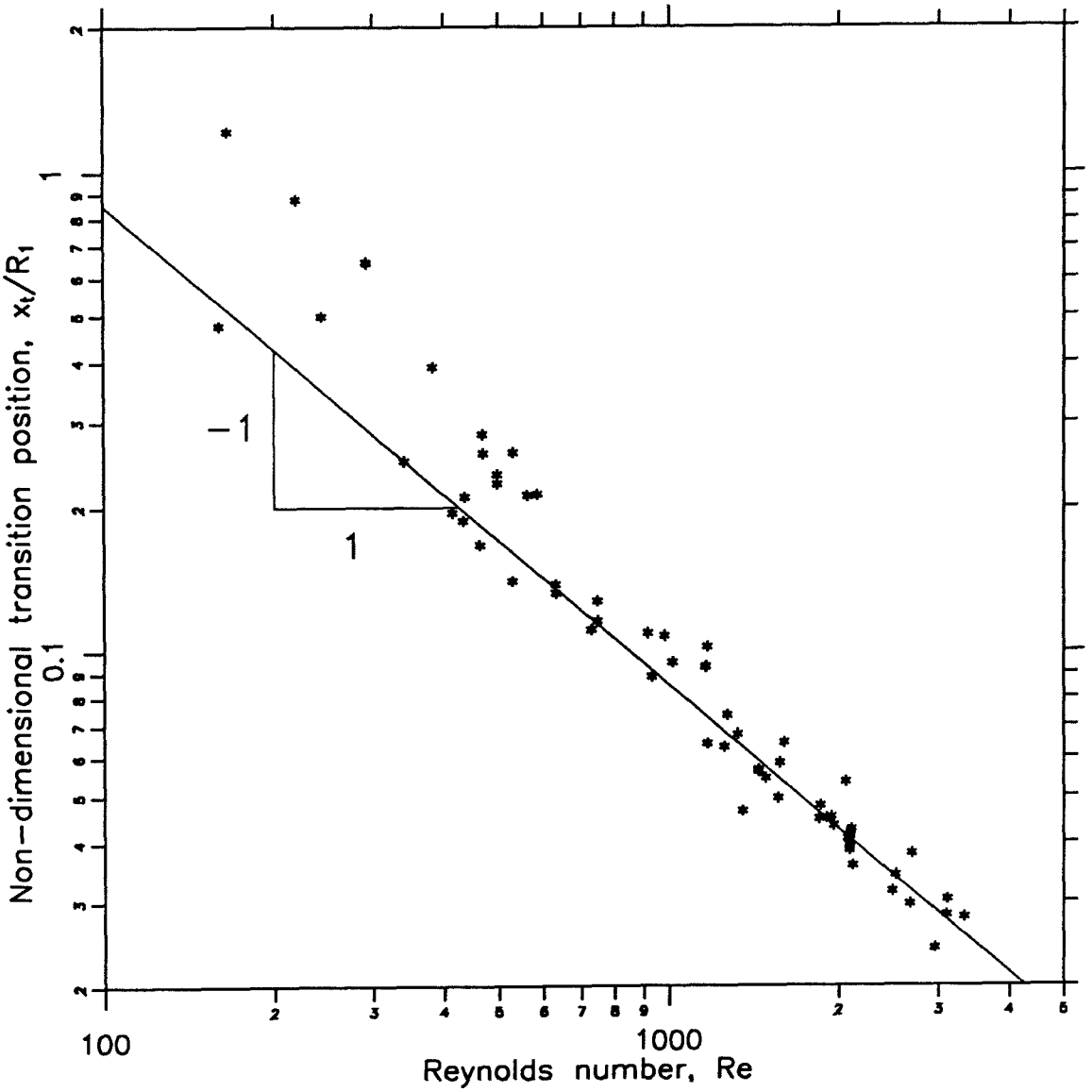

Figure 2.7 Transition position as a function of Reynolds number.

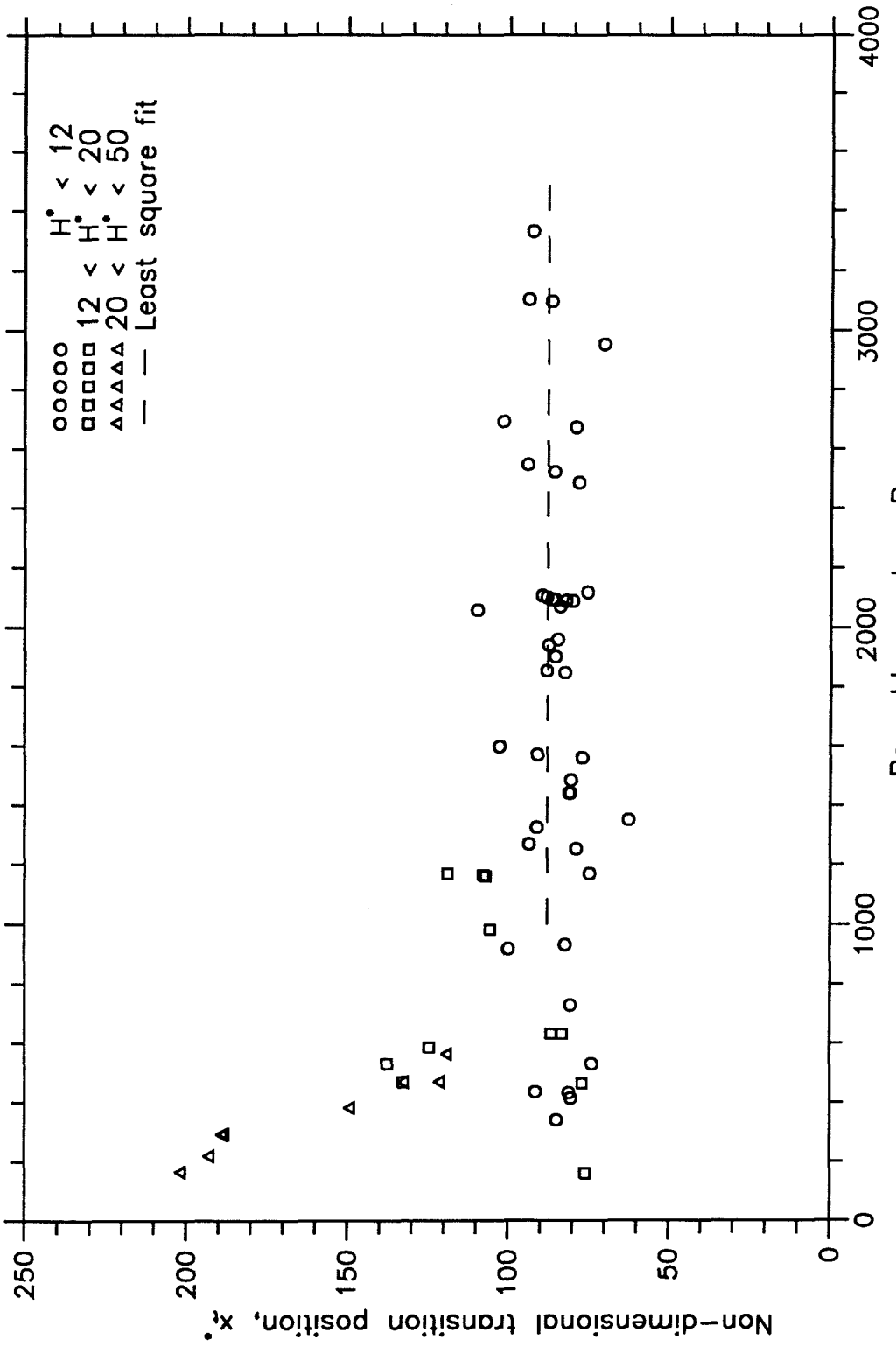

Figure 2.8 Transition position as a function of Reynolds number.

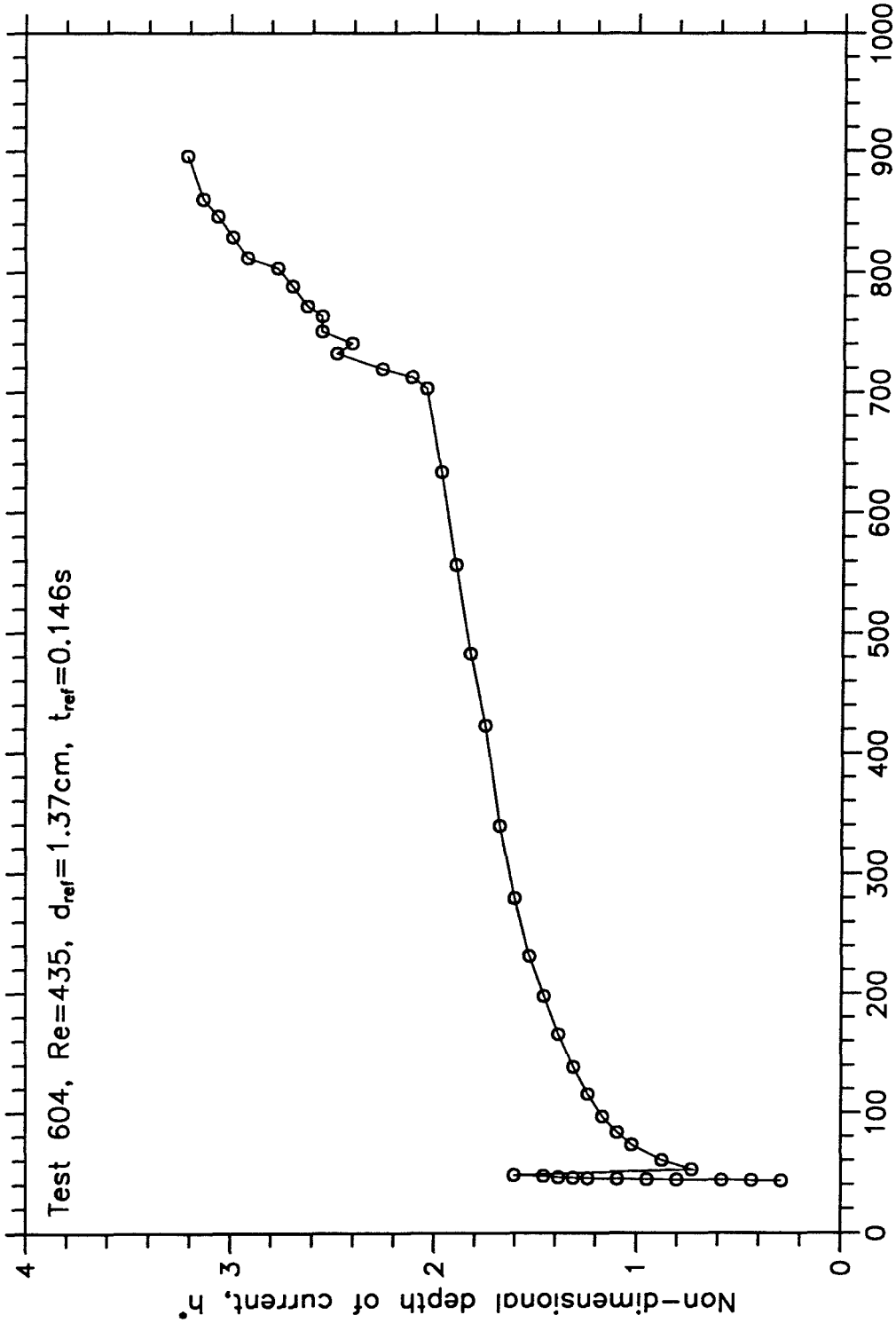

Figure 2.9 Depth of current at $x^*=37$ as a function of time.

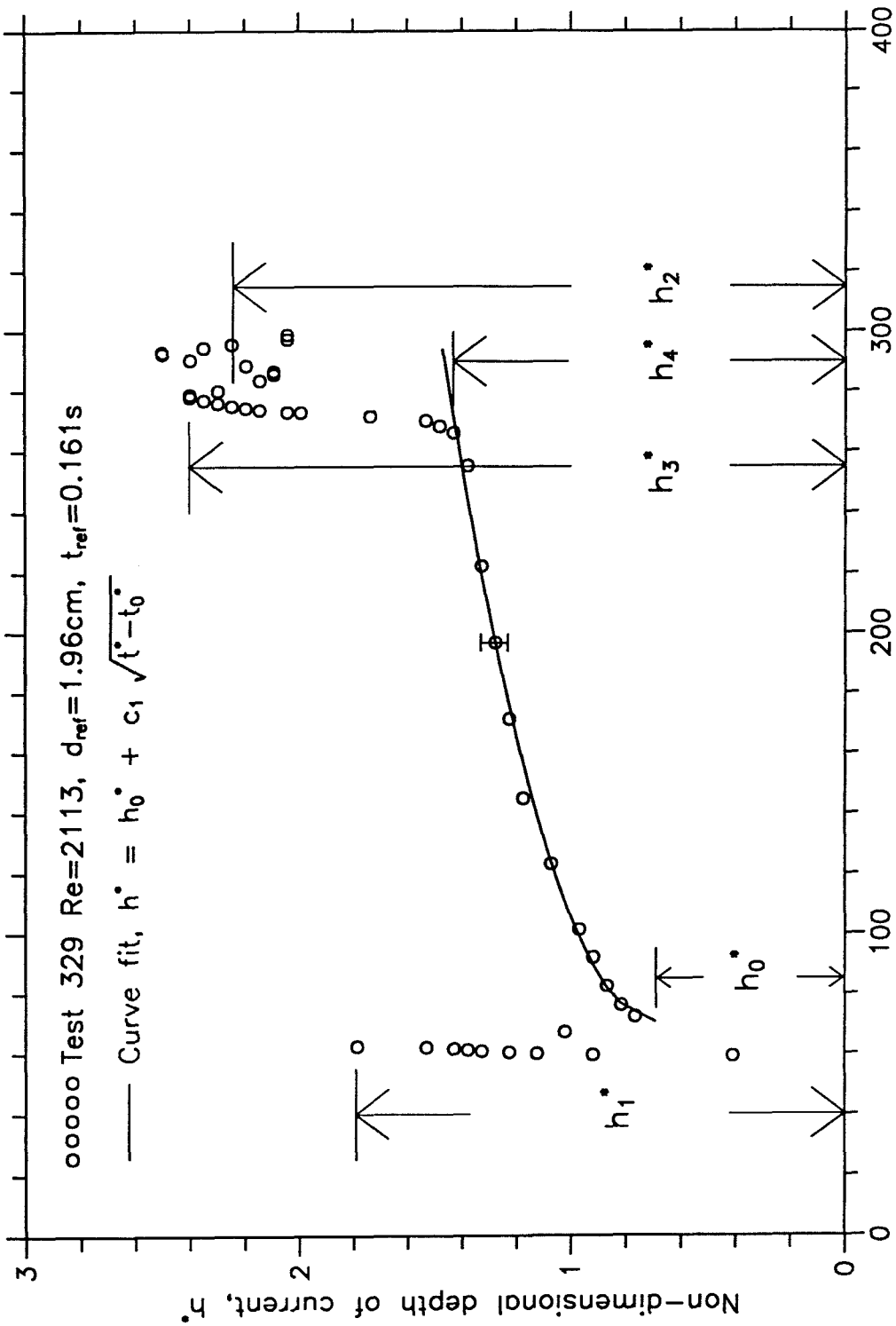

Figure 2.10 Depth of current at x^*=26 as a function of time.

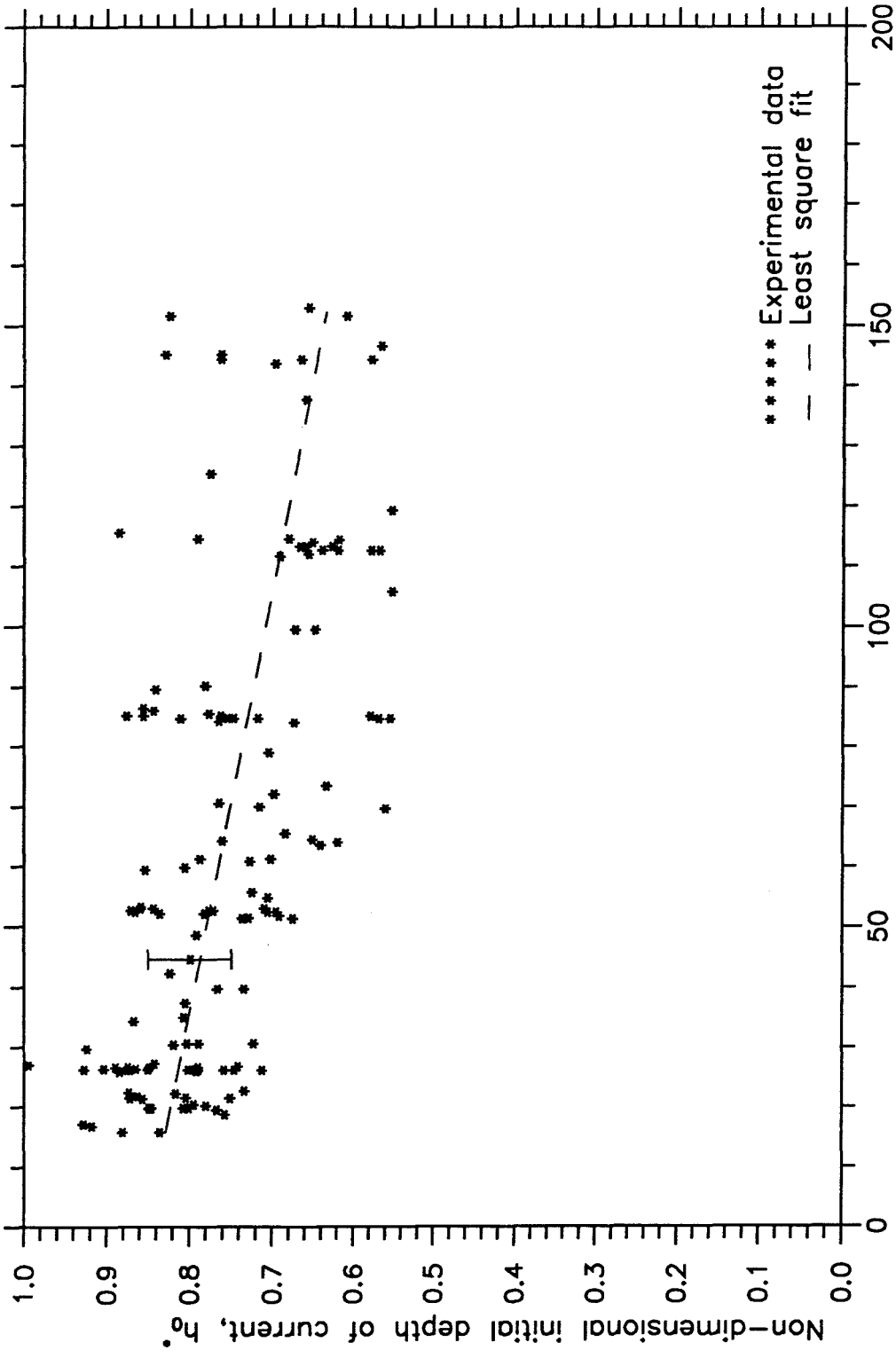

Figure 2.11 Initial depth of current as a function of distance from the leading edge.

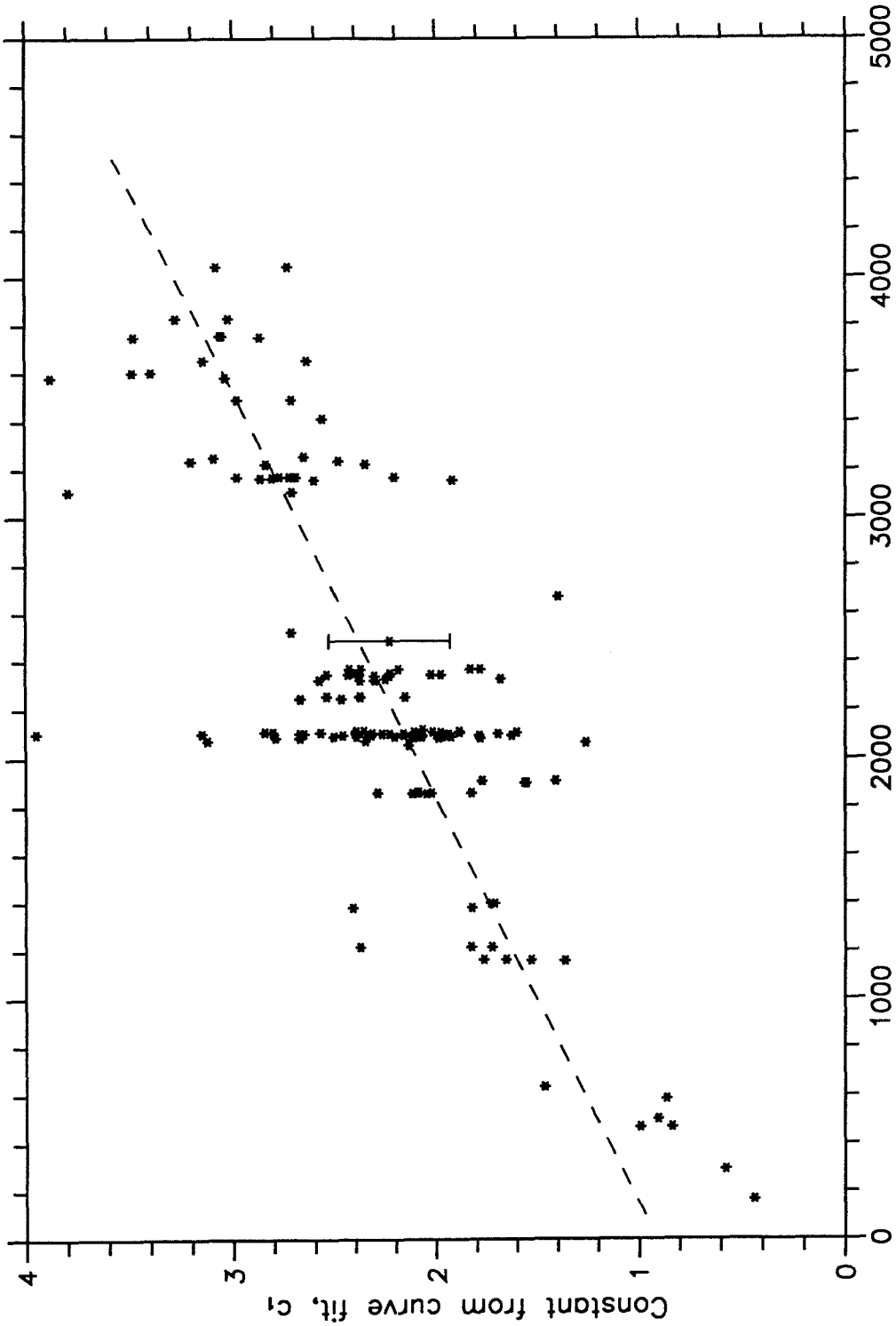

Figure 2.12 Constant from curve fit as a function of Reynolds number.

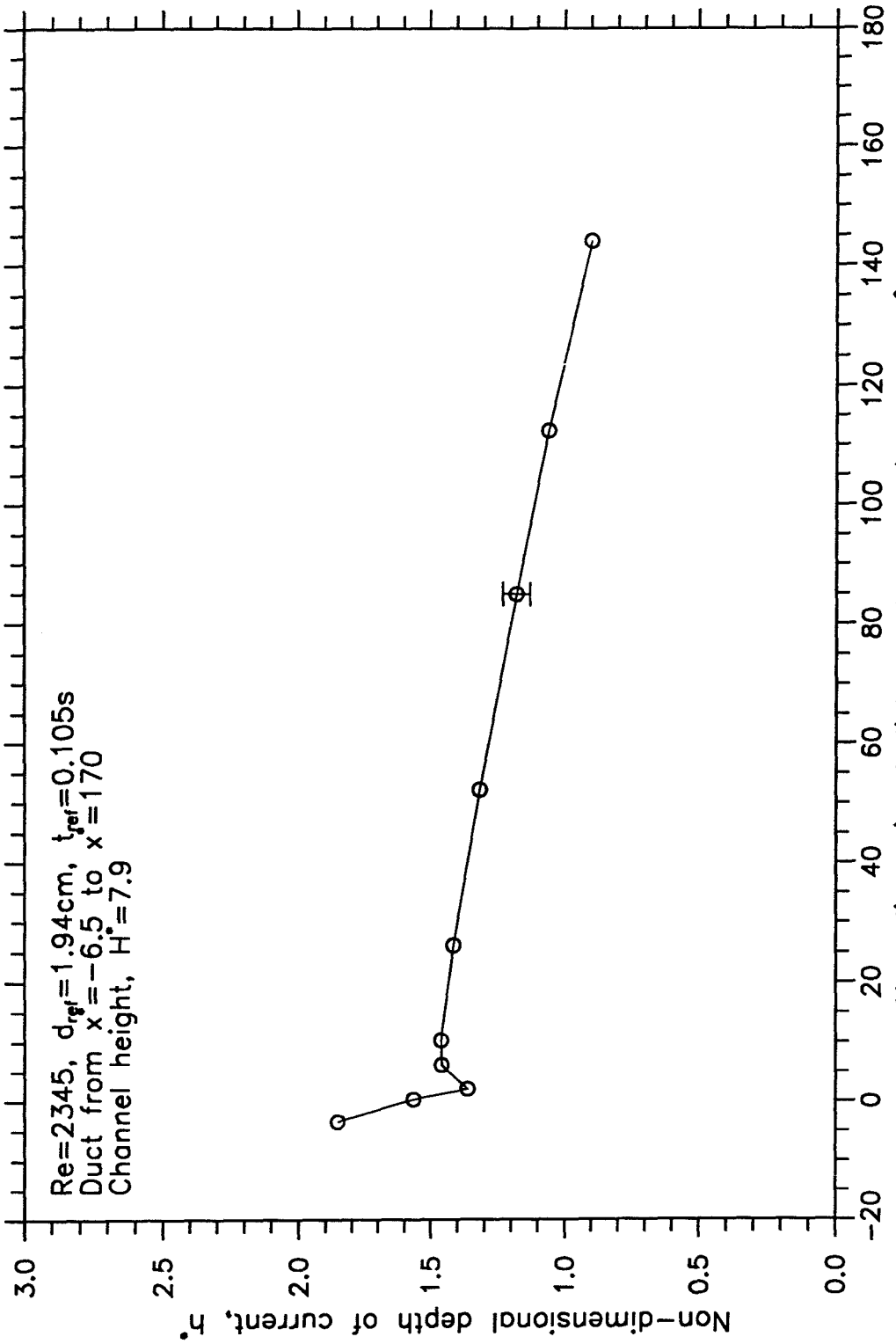

Figure 2.13 Depth of current as a function of distance from the leading edge, t*=200.

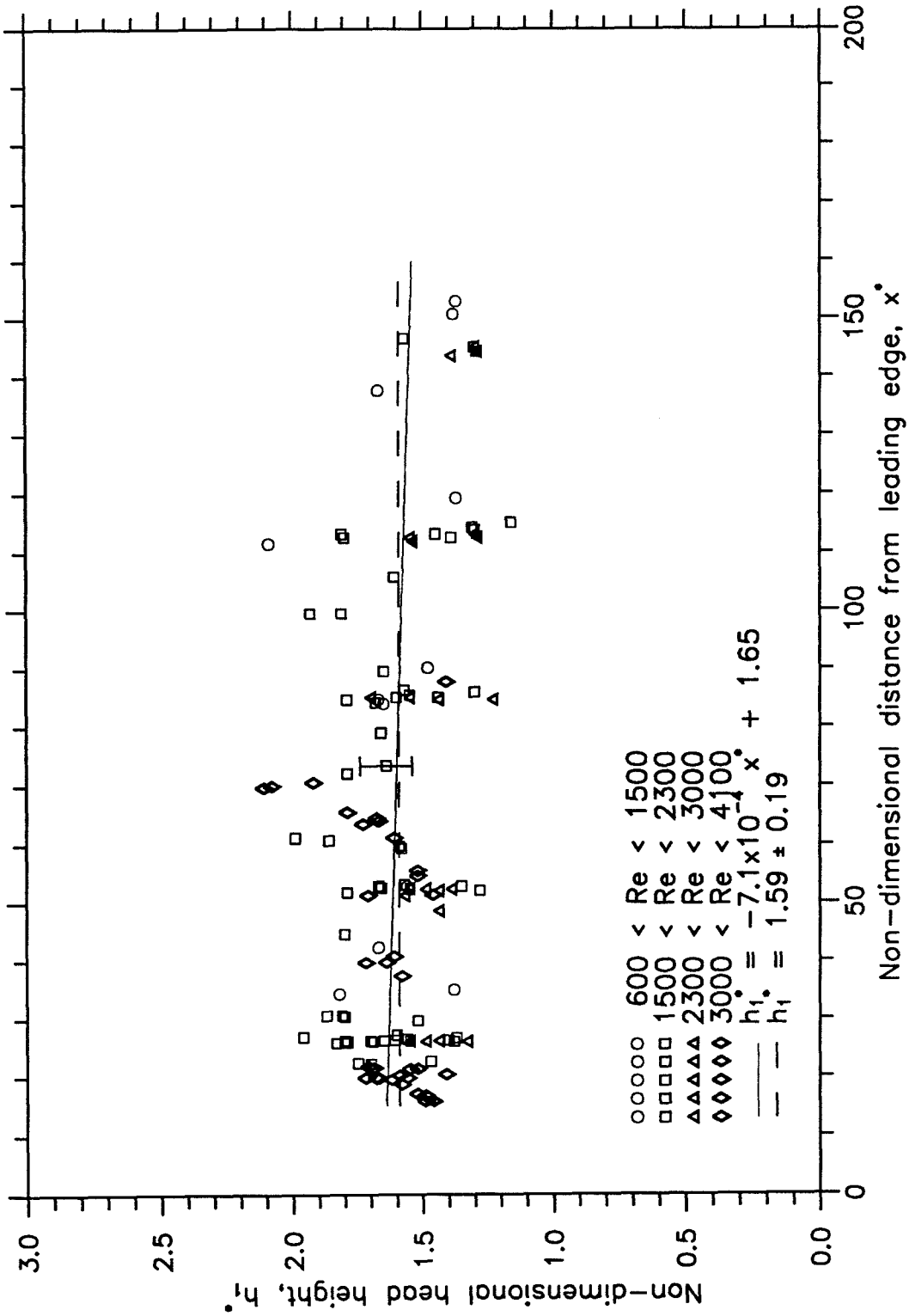

Figure 2.14 Head height as a function of distance from the leading edge.

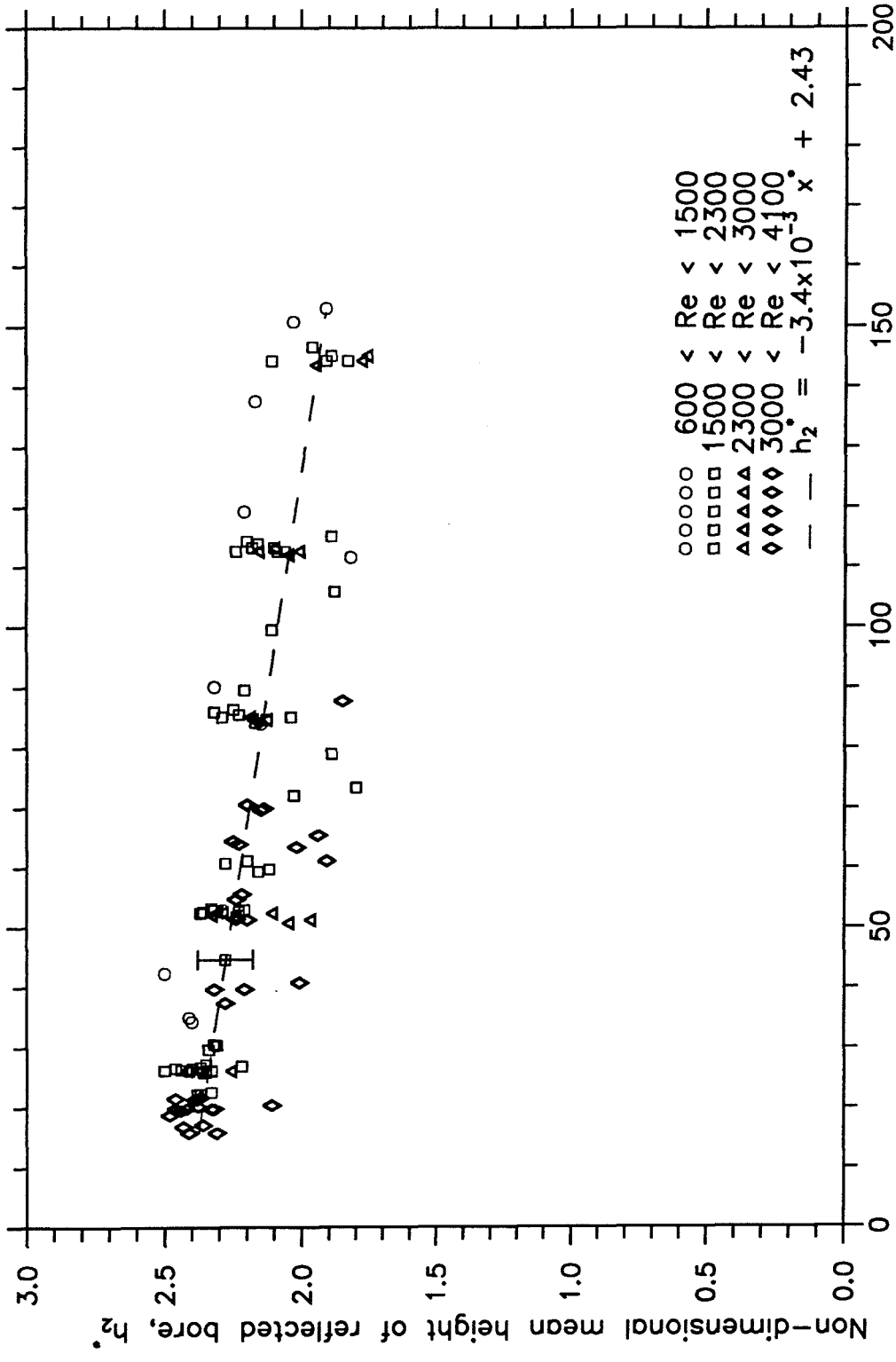

Figure 2.15 Mean height of the first wave of the reflected bore as a function of the distance from the leading edge.

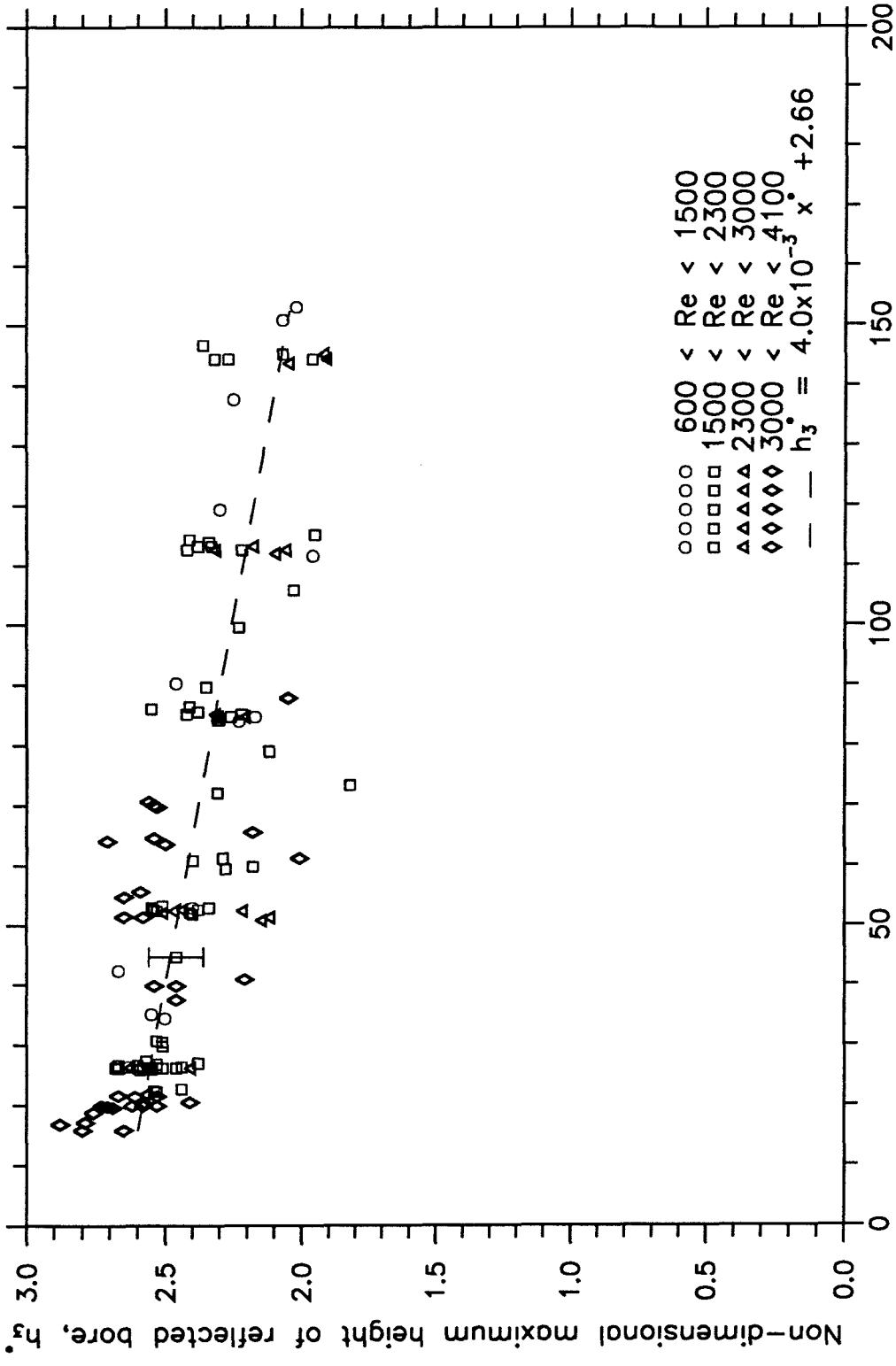

Figure 2.16 Maximum height of the first wave of the reflected bore as a function of the distance from the leading edge.

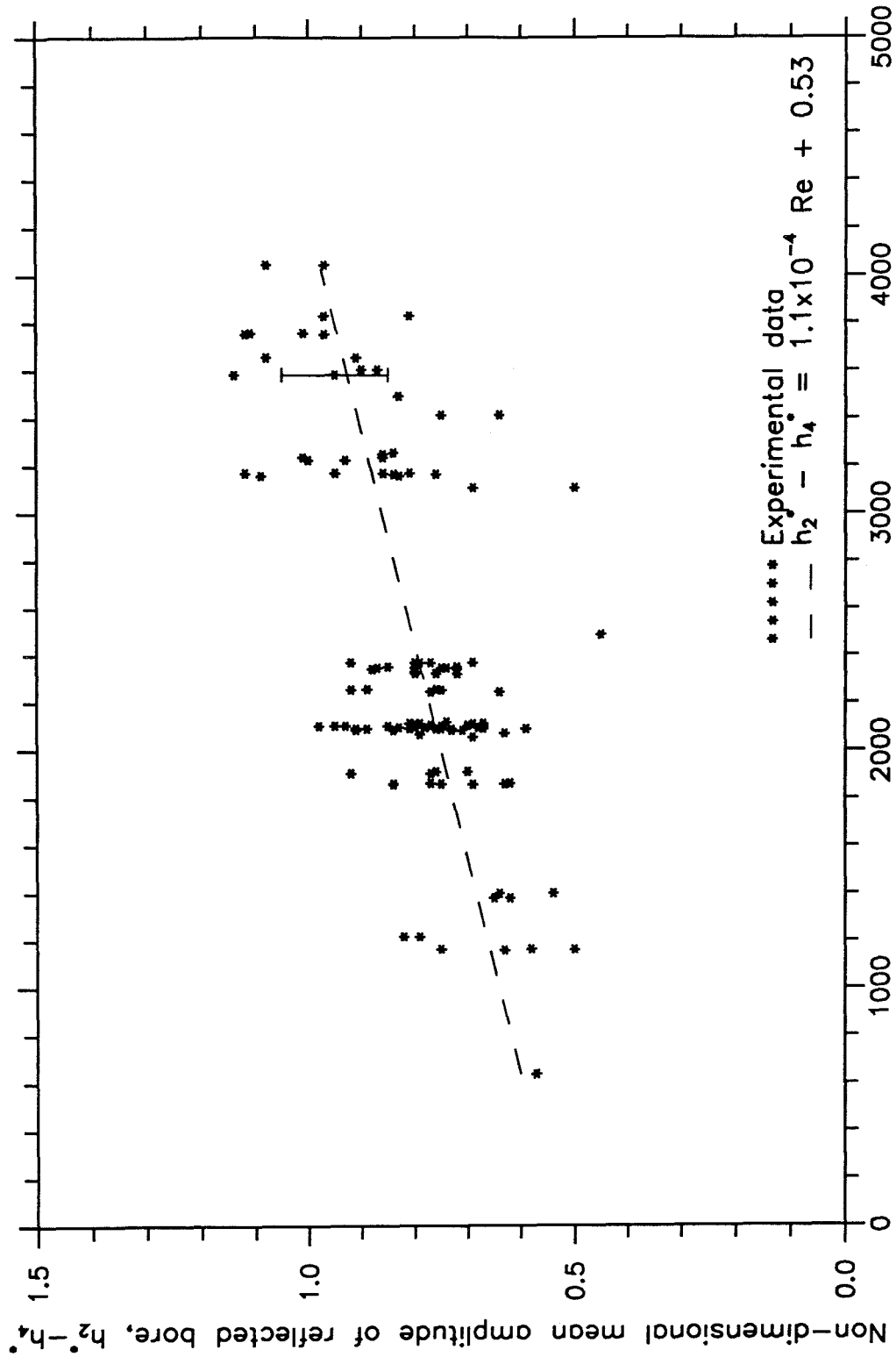

Figure 2.17 Mean amplitude of reflected bore as a function of Reynolds number.

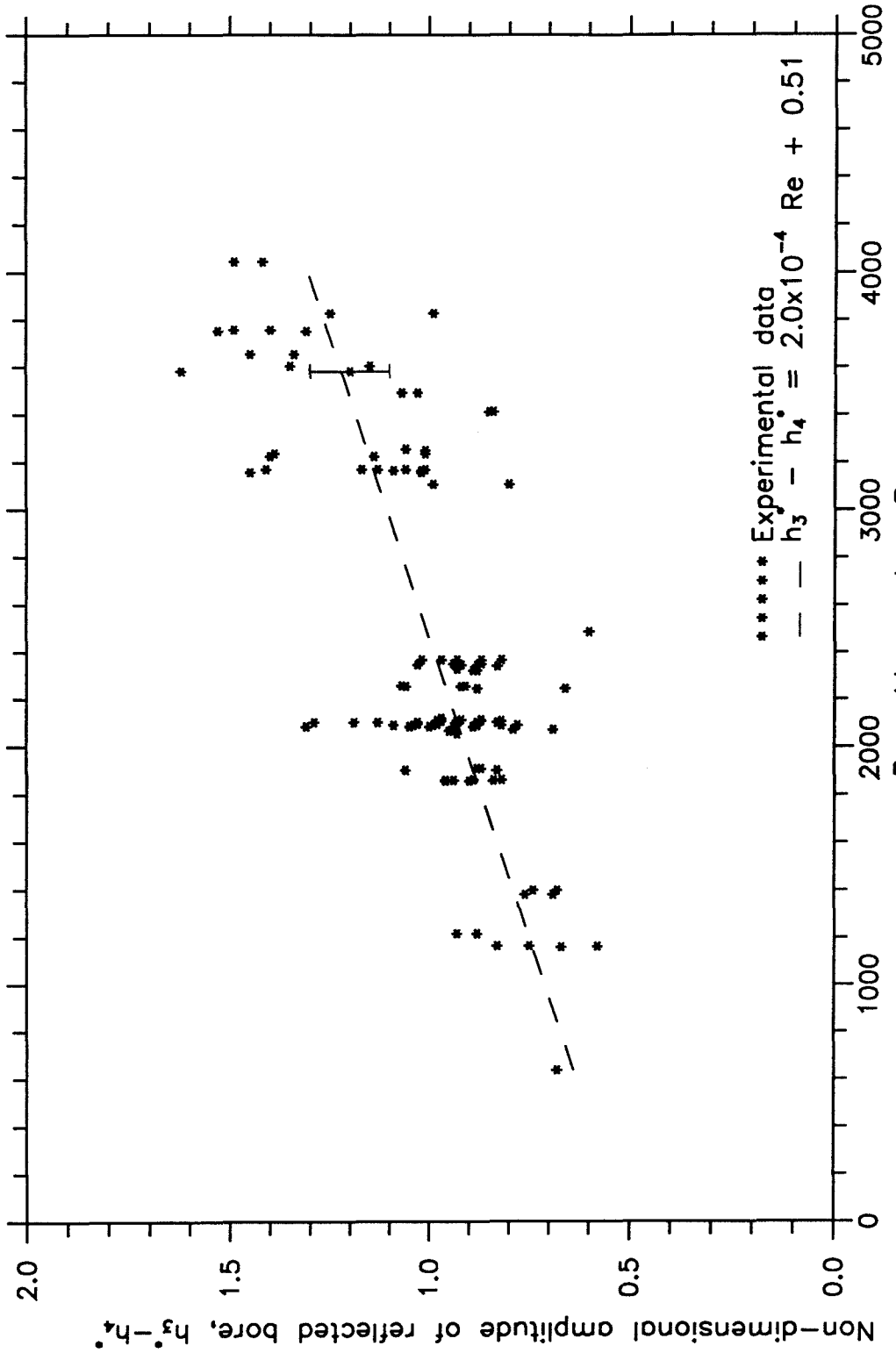

Figure 2.18 Amplitude of the reflected bore as a function of Reynolds number.

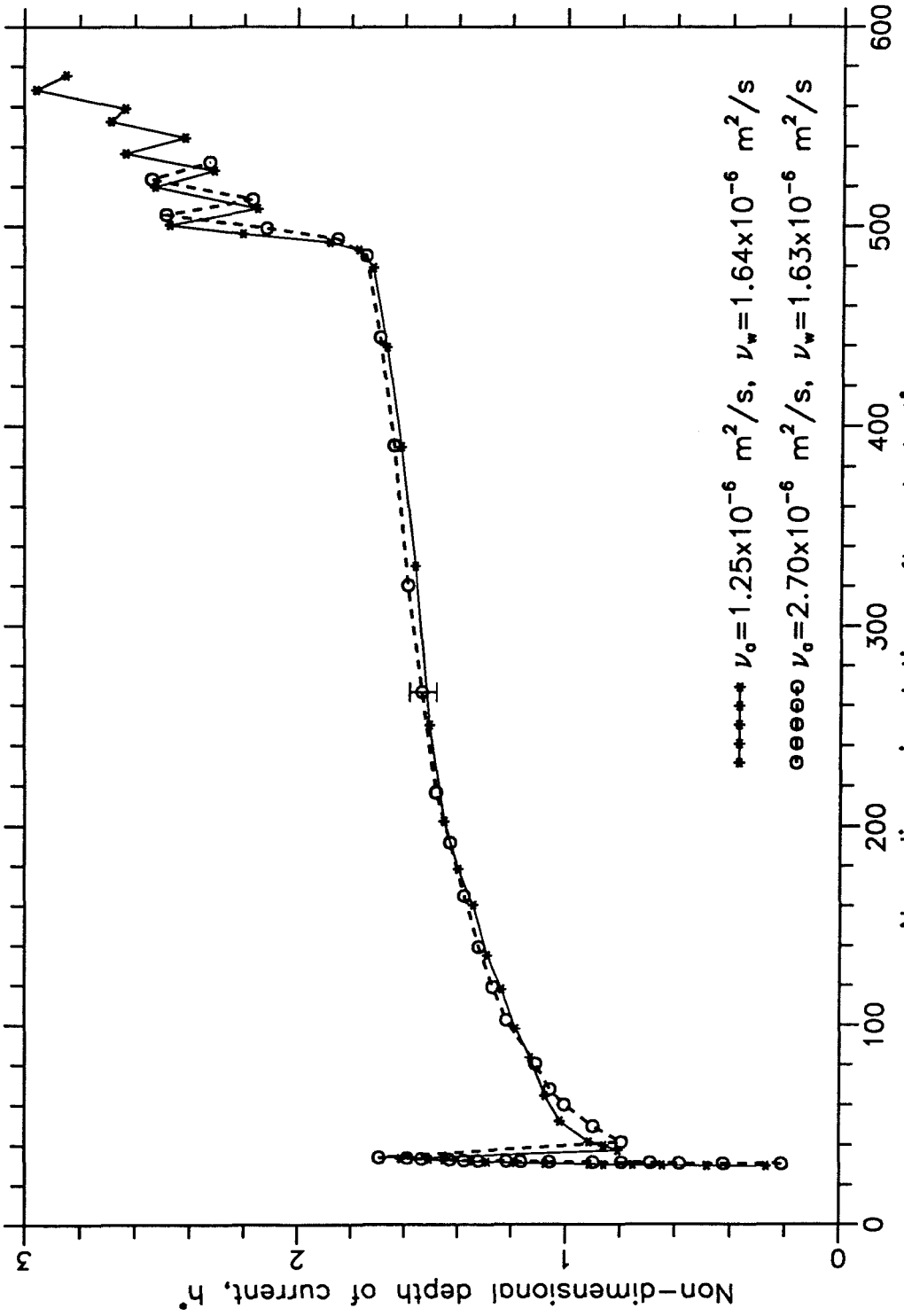

Figure 2.19 Depth of current at x^*=27, with Re=1250, as a function of time.

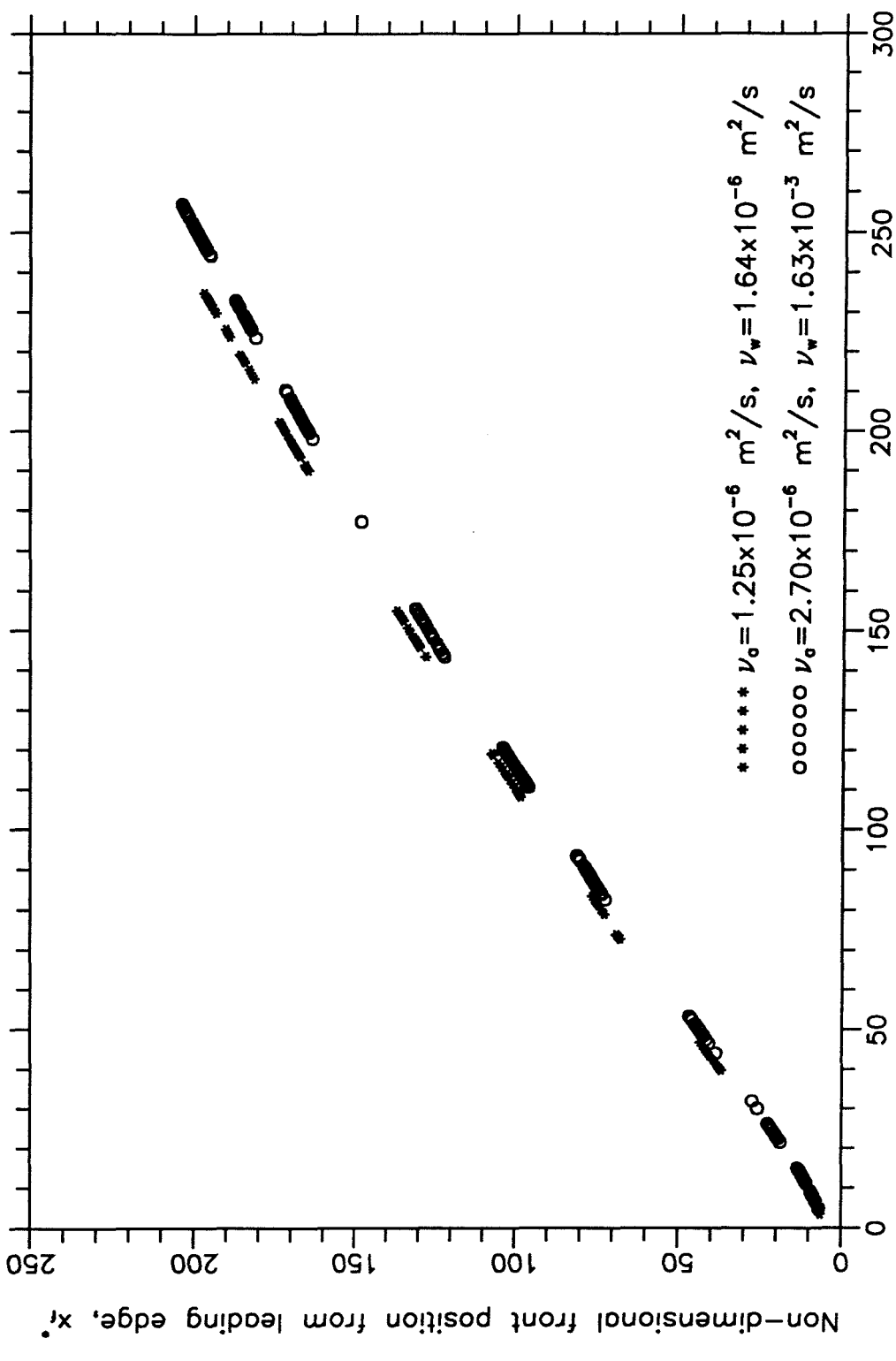

Figure 2.20 Front position from the leading edge, with Re=1250, as a function of time.

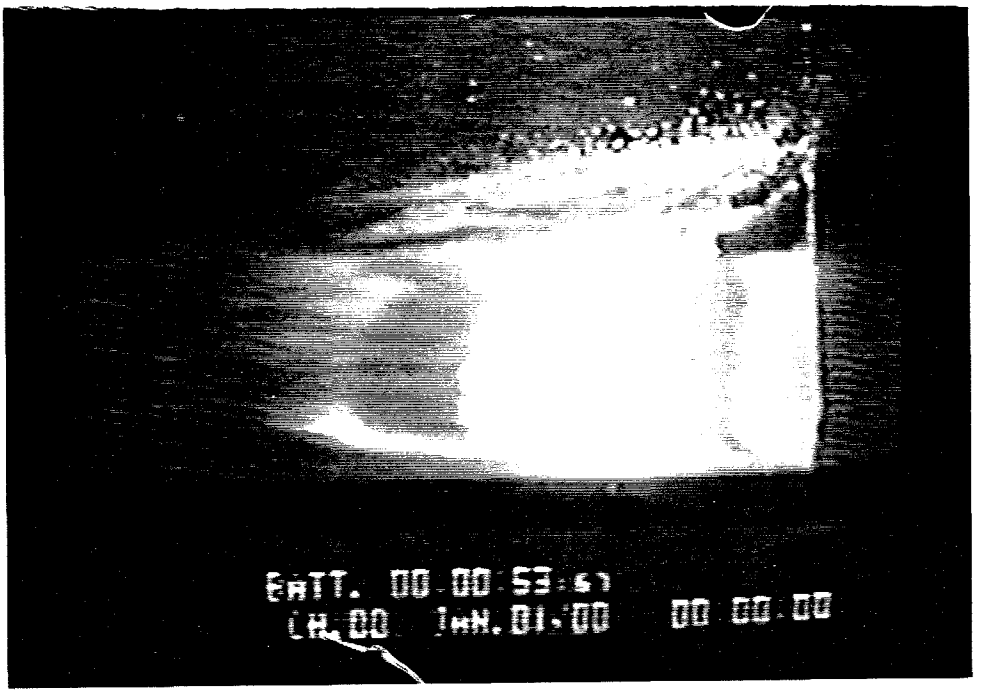

Figure 2.21a Hydrogen bubbles as the flow visualization aid.

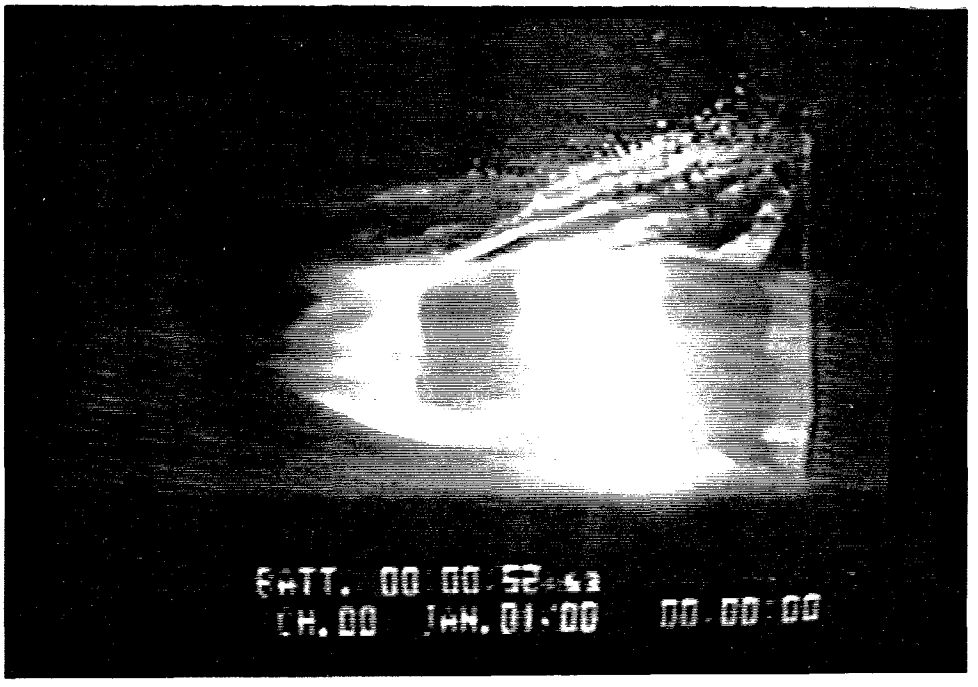

Figuare 2.21b Lifting of boundary layer.

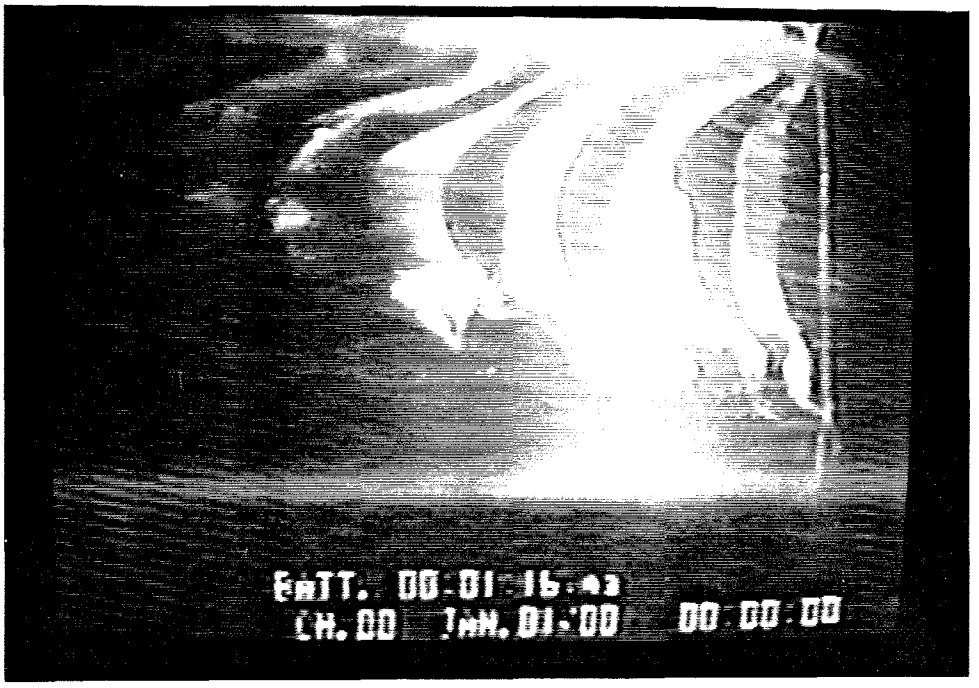

Figure 2.21c Separation of boundary layer at the arrival of the reflected bore.

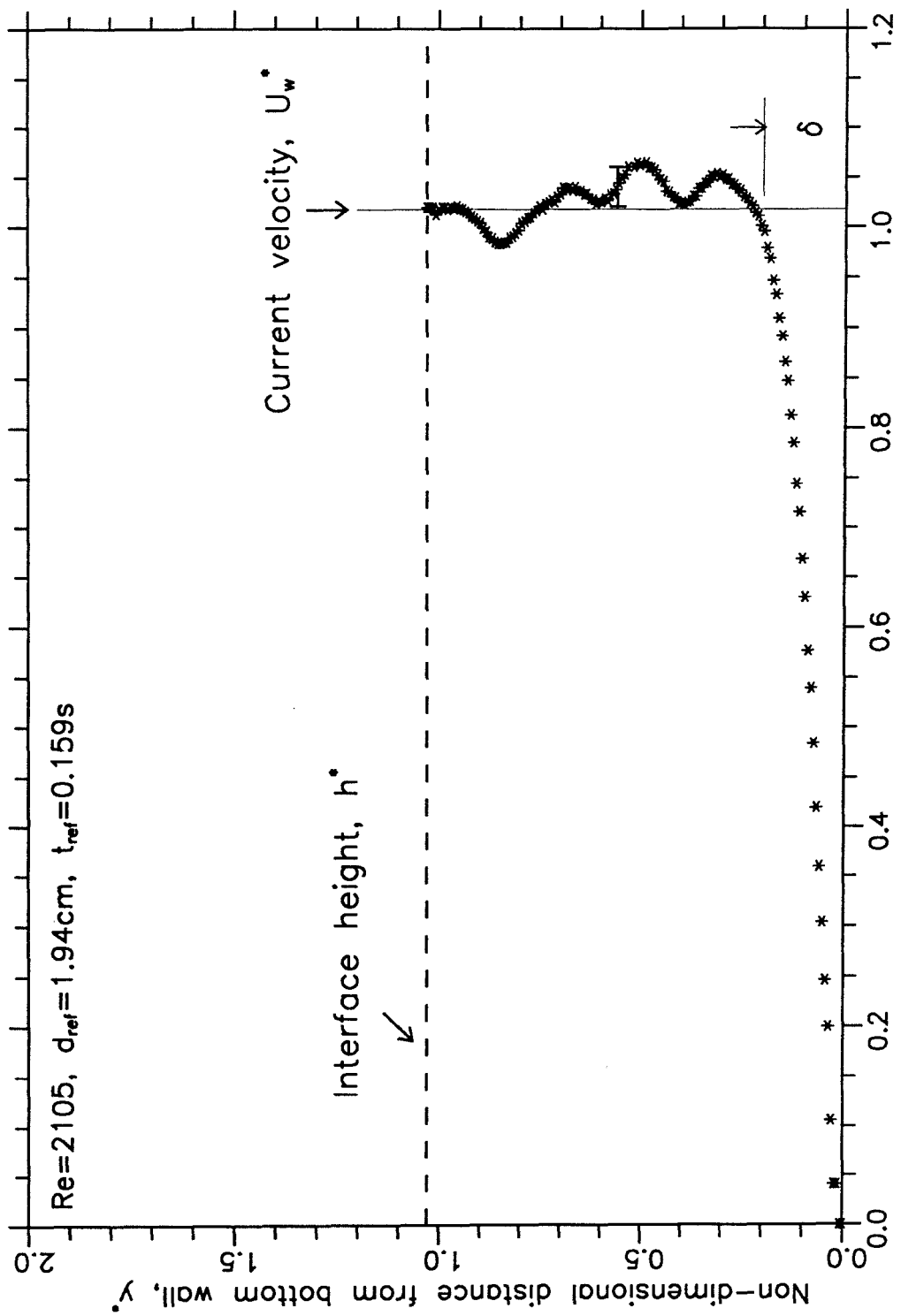

Figure 2.22 Velocity profile at x^*=52 from the leading edge, with t^*=126.

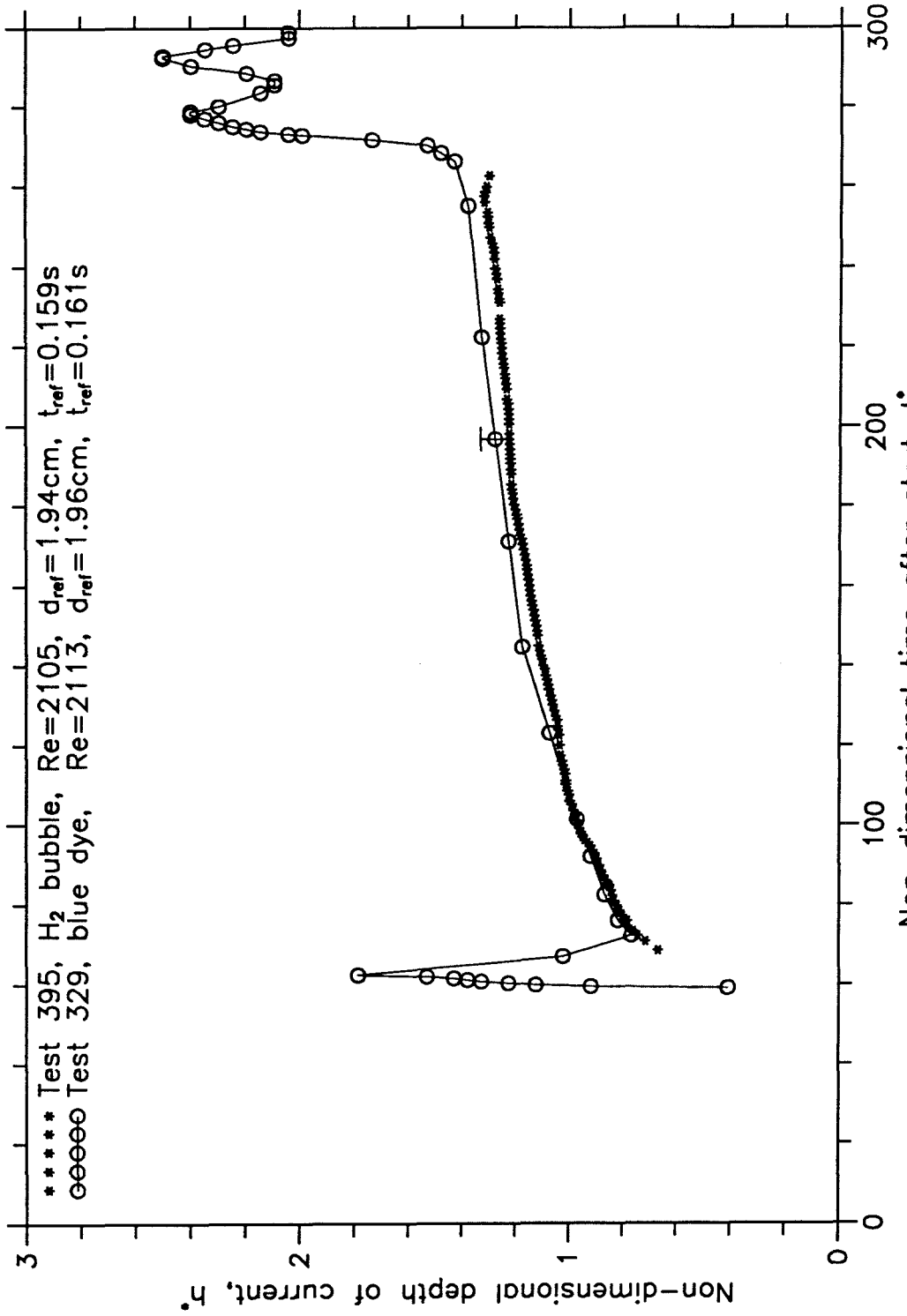

Figure 2.23 Comparison of experimental results using different flow visualization techniques at $x^*=52$.

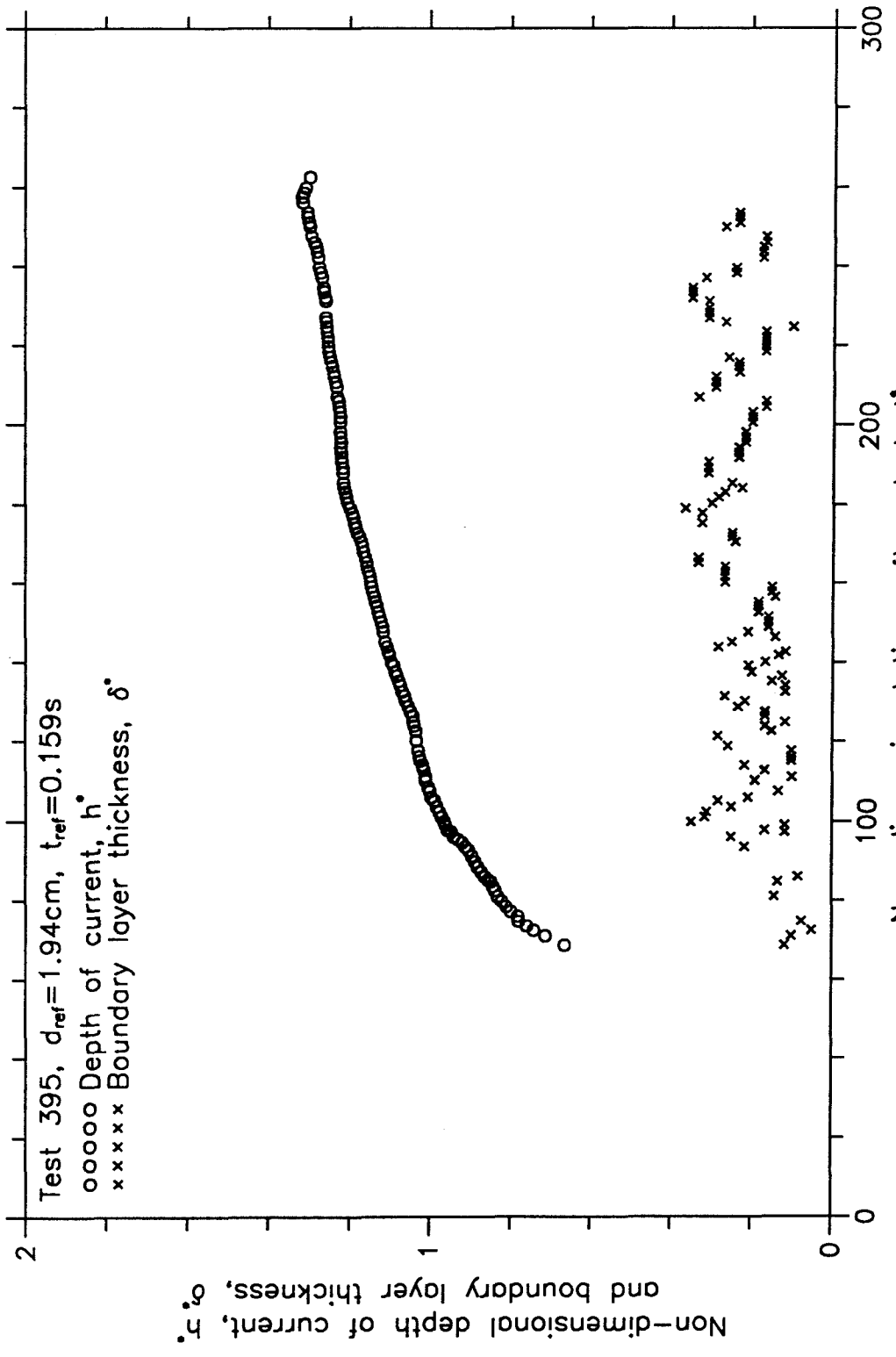

Figure 2.24 Depth of current and boundary layer thickness as a function of time at x^*=52 with Re=2105.

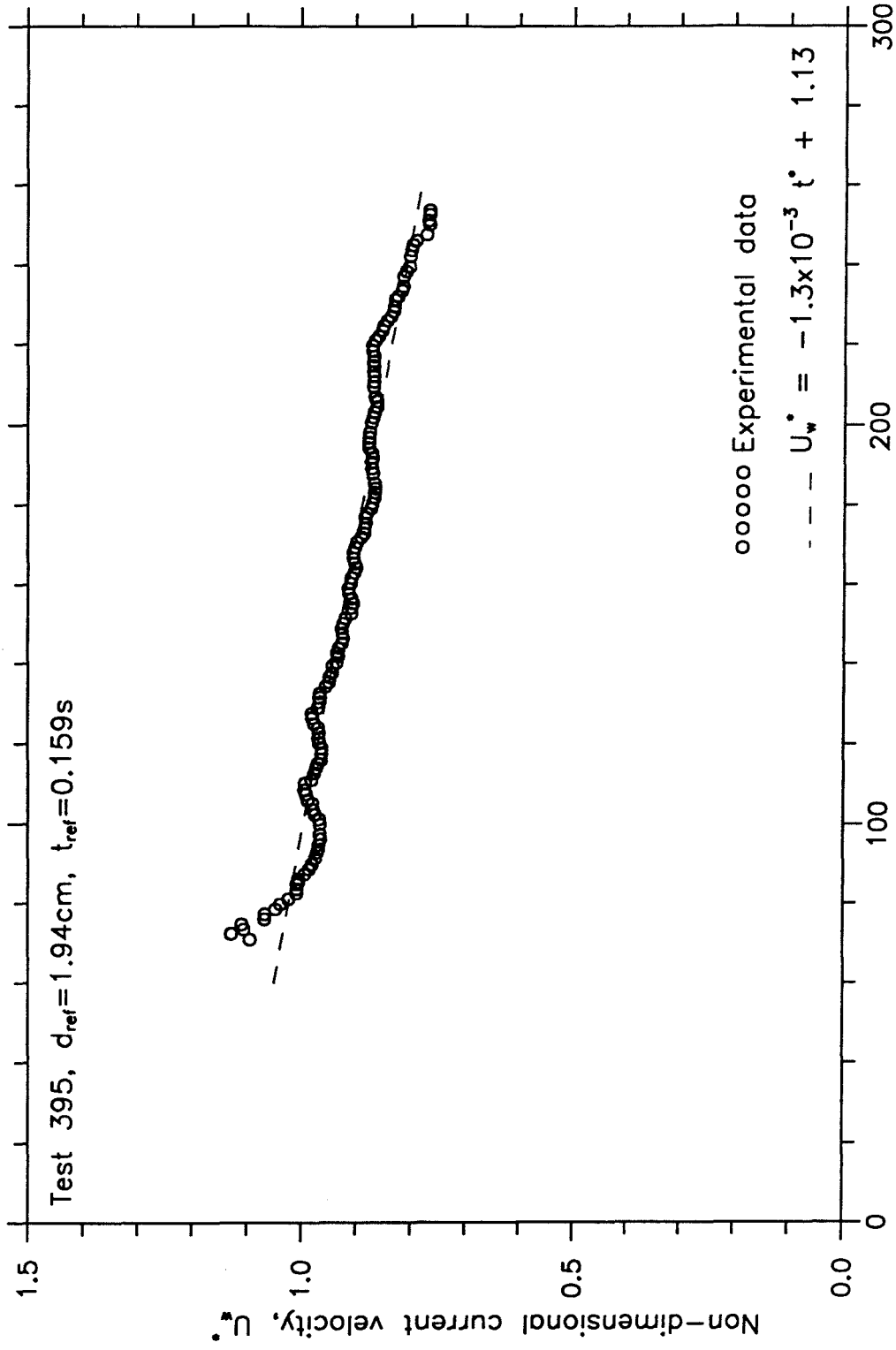

Figure 2.25 Velocity of current at x^*=52 as a function of time, with Re=2105.

CHAPTER 3

MODELING OF ADIABATIC GRAVITY CURRENTS IN A HORIZONTAL CHANNEL

3.1 Introduction

When a fluid is introduced into an ambient fluid of lower density, it will flow underneath the ambient fluid due to gravity. This flow of one fluid into another fluid of different density is known as a gravity current. Gravity currents are so frequently encountered that one may overlook their presence. They occur both naturally and artificially. Examples of gravity currents include sea-breeze fronts, avalanches, oil spill in the ocean, waste water discharge in a river, and smoke movement in a corridor.

In this investigation, a model is presented for gravity currents in a horizontal channel in order to better understand smoke movement in a corridor. To avoid various complicated problems arising from a heat-transferring gravity current, an adiabatic model is developed in which the effects of heat transfer are neglected. By first understanding the role of each parameter with the absence of heat transfer, this model can then form the basis for a more comprehensive model for a heat-transferring gravity current.

3.2 Description of the model

In this adiabatic model for gravity currents, an enclosed horizontal channel is filled with an ambient fluid of density ρ_a. A heavier fluid of density ρ_w is introduced vertically upward against gravity at a volumetric influx rate per unit width Q. It passes through a rectangular opening, referred to as the inlet, of length w_0 in the floor of the channel. The channel has a total length of $L+w_0$ with a squared cross-sectional height H. The heavier fluid, which is also known as the working fluid, will spread away from the inlet along the bottom wall of the channel due to the density difference between the two fluids. This layer of working fluid, referred to as the gravity current, will attain a depth h, a free-stream velocity or uniform velocity U_w, and a boundary layer thickness δ, due to the drag on the bottom wall. The farthest downstream location of the current, x_f, also

known as the front of the current, advances downstream at a velocity $\dot{x}_f$, which is also known as the front velocity or front speed. Moreover, the flow in this model is assumed to be incompressible. As a result, ambient fluid must be displaced from the channel at the same volumetric flow rate as the influx of the working fluid. This excess fluid is removed through a rectangular opening known as the outlet, of length w_1, on the top wall of the channel at the same end from which the working fluid is introduced. This end of the channel will be referred to as the upstream end, while the opposite end of the channel is known as the downstream end. The ambient fluid is assumed to be quiescent far away from the approaching gravity current (Keulegan, 1958), but it is assumed to be moving with a uniform velocity U_a, called the ambient velocity, at streamwise locations where the front of the current has already passed. A schematic diagram of the channel is shown in Figure 3.1. Note that all the depths and velocities associated with the fluids are functions of both time and spatial positions.

Since the width of the channel is constant and the influx and outflow conditions can be assumed to be uniform across the width of the channel, the flow can be assumed to be two-dimensional when the effects on the flow due to the side walls of the channel are small. As shown in Figure 1.1a and Figure 1.2a, the billows and the lobes and clefts observed by Simpson (1969) are very complicated. To simplify the modelling effort, they are left out of the model. However, it will be shown that their absence does not alter the essence of the flow. As a result, the partition between the front of the current and the ambient fluid is sharp and vertical. A rectangular coordinate system (x,y) is then sufficient to identify spatial positions in the channel. The x-coordinate is measured in the streamwise direction from the leading edge of the bottom wall of the channel, while the y-coordinate is measured vertically upward from the bottom wall. This coordinate system is illustrated in Figure 3.1. The working fluid is being introduced into the channel at a volumetric flow rate per unit width Q. The density of the working fluid and that of the ambient fluid are ρ_w and ρ_a, respectively, with $\rho_a < \rho_w$. The corresponding kinematic viscosities are ν_w and ν_a, respectively. The acceleration due to gravity is denoted by g.

Entrainment is assumed to be negligible in this model because of the stably stratified configuration. This assumption is made plausible by a number of experiments such as those of Ellison and Turner (1959). Diffusion across the interface is also assumed to be negligible. Although these assumptions are valid when both the working

and the ambient fluids are liquids, they might have to be modified when the fluids are gases because the Schmidt numbers for liquids are about three orders of magnitude larger than those for gases. The Schmidt number is defined as the kinematic viscosity of a fluid divided by the diffusion coefficient of the same fluid. Since the kinematic viscosities of gases are roughly ten times larger than those of liquids while the diffusion coefficients of gases are roughly ten thousand times larger than those of liquids, the Schmidt numbers for liquids are about three orders of magnitude larger than those for gases.

These points are made clear by considering the following example. For a 100 kW fire in a room connected to a 2 m wide corridor, the volumetric flow rate of smoke per unit width of the corridor, Q, was found to be roughly 10^4 cm^2/s (Chobotov 1987). Assuming a bulk overheat of 50 K for the heated smoke, the reduced gravity, g', is 165 cm/s^2 and the kinematic viscosity of the smoke, ν_w, is about 0.2 cm^2/s. As a result, the input Reynolds number of the current, $Re = Q/\nu_w$, is roughly $5x10^4$. In addition, the length scale, d_{ref}, the time scale, t_{ref}, and the velocity scale, U_{ref}, for the gravity current as defined in Section 1.2 are 85 cm, 0.72 s, and 118 cm/s, respectively. As a result, if the length of the corridor, L, is 40 m, the non-dimensional corridor length, L*, is about 47, and the current is either inertia-buoyancy dominated or at most in the beginning of the transition to the viscous-buoyancy regime. The total non-dimensional time for the front of the gravity current to reach the downstream end wall of the corridor and for the reflected bore to reach the fire room is therefore less than 100.

To look at the diffusive flux across the interface in the example mentioned above, the effects of the horizontal motion of the fluids are neglected to simplify the analysis. The Schmidt number of the heated smoke is assumed to be about 0.7. As a result, the concentration of the smoke gases at a non-dimensional depth of 0.07 below the interface is found to be 10% of that in the current, while the mass fraction of the smoke that has crossed the interface is only 0.7% of the total mass in the current.

This result is not very different from that of a case with the same non-dimensional input parameters but with both fluids being liquids. The Schmidt number in that case is about 1000, and the non-dimensional depth above the interface at which the concentration of the current fluid is at least 10% of that in the current is only $1.8x10^{-3}$, while the mass fraction of the current fluid crossing the interface is only 0.02%.

On the other hand, the length scale, d_{ref}, involved with the fire example is large. If the corridor has a total height of 3 m, the height at which the concentration of the smoke gases is at least 10% of that in the current is roughly 2 m above the ground, and may thus affect the ability of people to escape from the burning building. As a result, the availability of a model that can adequately model both the spreading rate of the smoke and the depth of the smoke layer is crucial for fire safety purposes.

It is further assumed in this model that the depth of the ambient layer is much larger than that of the current. Thus, the velocity of the ambient fluid is much smaller than that of the current. As a result, the viscous drag on the top wall can be ignored.

Finally, the shear stress at the interface is assumed to be small when compared to the drag due to the bottom boundary layer. This assumption is supported by the experimental results presented in Section 2.4.3 and 2.5.2 for the case with both fluids being liquids. Moreover, by comparing results obtained by Lock (1951) for a laminar shear layer and the Blasius solution for a boundary layer on a semi-infinite flat plate, the shear stress at the interface of a laminar shear layer can be shown to be about 23% of the laminar frictional stress on the bottom wall, regardless of the working fluid. Therefore, it is assumed that viscous effects are only important in the lower boundary layer in this model.

From the above descriptions, the input parameters of interest to the model are Q, g, ρ_a, ρ_w, and ν_w. From these parameters, the reference length scale, d_{ref}, time scale, t_{ref}, and velocity scale, U_{ref}, of the flow can be shown by dimensional analysis (Chen 1980 and Didden and Maxworthy 1982) to be

$$d_{ref} = \left(\frac{Q^2}{g'}\right)^{1/3} \tag{3.1a}$$

$$t_{ref} = \left(\frac{Q}{g'^2}\right)^{1/3} \tag{3.1b}$$

and $$U_{ref} = \frac{d_{ref}}{t_{ref}} = (Q\, g')^{1/3}\ ; \tag{3.1c}$$

where, g', the reduced gravity, is defined as

$$g' = \left(\frac{\Delta\rho}{\rho_w}\right) g \tag{3.1d}$$

where $\Delta\rho = \rho_w - \rho_a$. (3.1e)

The reduced gravity is a measure of the effective gravitational or buoyancy force in the flow. Although different ways of defining the reduced gravity have been used (Britter and Linden 1980; Alavian 1986; and Oh 1983), the reduced gravity is not sensitive to the definition when $\Delta\rho \ll \rho_a$, in which case the Boussinesq approximation can be used. Although there are four physical lengths w_0, w_1, L, and H, present in this model, none of them is the appropriate reference length scale. This is because buoyancy forces, which are the driving forces in this phenomenon, are not represented in any one of the four lengths. As a result, the length scale d_{ref}, which takes into account of the buoyancy effect, is used. However, it will also be shown that these physical lengths do affect the solutions as expected.

The non-dimensional groups formed by the input parameters are the Reynolds number, Re, the density ratio of the fluids, ρ_r, and the ratio of the kinematic viscosities, ν_r, where

$$Re = Q/\nu_w \tag{3.1f}$$

$$\rho_r = \rho_a/\rho_w \tag{3.1g}$$

and $\nu_r = \nu_a/\nu_w$. (3.1h)

Since only viscous effects on the bottom wall are considered important to the current depth and the kinematic viscosity of the ambient fluid has at best a very weak effect on the front velocity, as was shown in Section 2.4.3, the ratio of kinematic viscosities can be assumed to play no role in this model. This assumption is supported by the experimental result shown in Figure 2.19 and Figure 2.20. The effects of the density ratio between the two fluids are retained in this model. However, it does not play a

significant role when it is close to unity and when Boussinesq approximation can be used.

Although the model appears upside-down when compared to a schematic diagram of smoke movement in a corridor, the result is directly applicable to that phenomenon when the scaled values of the parameters are comparable and when the assumptions described are valid.

In order to better understand the role of each of the above named parameters, the solution of the simplest model is first sought. Additional parameters are then introduced so that their significance can be revealed. The order in which the various models are to be presented is:

Section 3.3. Inviscid gravity currents in a channel of infinite depth;

Section 3.4. Inviscid gravity currents in a channel of finite depth;

Section 3.5. Viscous gravity currents in a channel of infinite depth;

Section 3.6. Viscous gravity currents in a channel of finite depth.

3.3 Inviscid gravity currents in a channel of infinite depth

3.3.1 General description of the model

In this model, a gravity current is assumed to be inviscid. All length scales are assumed to be small when compared to the channel height. The derivation of the governing equations, boundary conditions and initial conditions is detailed in Appendix A. For convenience, the following co-ordinate transformation is used:

For $-w_0^* \le x^* \le 0$, $\tau^* = t^*$ (3.2a)

and $$z^* = \frac{x^*}{w_0^*} .$$ (3.2b)

For $0 \le x^* \le x_f^*$, $\tau^* = t^*$ (3.2c)

and $$z^* = \frac{x^*}{x_f^*(t^*)}\,;$$ (3.2d)

in which the ( )* quantities are normalized by the appropriate combinations of the length scale, the time scale, and the velocity scale.

The governing partial differential equations, the boundary conditions, and the initial conditions derived in Appendix A are shown below.

Governing equations:

For $-1 \le z^* \le 0$, $$\frac{\partial h^*}{\partial \tau^*} + \frac{1}{w_0^*}\frac{\partial}{\partial z^*}(U_w^* h^*) = v_0^*$$ (3.3a)

and $$\frac{\partial U_w^*}{\partial \tau^*} + \frac{1}{w_0^*}\frac{\partial}{\partial z^*}\left[\tfrac{1}{2}(U_w^*)^2 + h^*\right] = 0\,.$$ (3.3b)

For $0 \le z^* \le 1$, $$\frac{\partial h^*}{\partial \tau^*} - \frac{z^* \dot{x}_f^*}{x_f^*}\frac{\partial h^*}{\partial z^*} + \frac{1}{x_f^*}\frac{\partial}{\partial z^*}(U_w^* h^*) = v_0^*$$ (3.3c)

and $$\frac{\partial U_w^*}{\partial \tau^*} - \frac{z^* \dot{x}_f^*}{x_f^*}\frac{\partial U_w^*}{\partial z^*} + \frac{1}{x_f^*}\frac{\partial}{\partial z^*}\left[\tfrac{1}{2}(U_w^*)^2 + h^*\right] = 0\,.$$ (3.3d)

The influx velocity, v_0^*, that appears in equations (3.3a) and (3.3c) is shown in Appendix A to be a function of the co-ordinate z^*, and is given by

$$v_0^*{}_{(z^*)} = \frac{1}{(1-\frac{1}{2}k)}\frac{1}{w_0^*} \qquad \text{for } -1 \le z^* \le -k$$ (3.4a)

$$v_0^*{}_{(z^*)} = \frac{1}{(1-\frac{1}{2}k)}\frac{1}{w_0^*}\left(\frac{z^*}{-k}\right) \qquad \text{for } -k \le z^* \le 0$$ (3.4b)

and $v_0^*{}_{(z^*)} = 0$ for $0 \le z^* \le \frac{L^*}{w_0^*}$ (3.4c)

where $0 < k < 1$, and $k \cong 0$.

Boundary conditions:

At $x^* = -w_0^*$, $z^* = -1$, $\frac{\partial h^*}{\partial z^*} = 0$ (3.5a)

and $U_w^* = 0$. (3.5b)

At $x^* = 0$, $z^* = 0$, $h^*_{(z^*=0^-)} = h^*_{(z^*=0^+)}$ (3.5c)

$$\frac{1}{w_0^*}\frac{\partial h^*}{\partial z^*}(z^*=0^-) = \frac{1}{x_f^*}\frac{\partial h^*}{\partial z^*}(z^*=0^+) \quad (3.5d)$$

$$U_w^*{}_{(z^*=0^-)} = U_w^*{}_{(z^*=0^+)} \quad (3.5e)$$

and $$\frac{1}{w_0^*}\frac{\partial U_w^*}{\partial z^*}(z^*=0^-) = \frac{1}{x_f^*}\frac{\partial U_w^*}{\partial z^*}(z^*=0^+)\,. \quad (3.5f)$$

At $x^* = x_f^*$, $z^* = 1$, $\dot{x}_f^* = (1 - \alpha)U_w^*$ (3.5g)

and $$U_w^* = \sqrt{\frac{h^*}{\frac{1}{2} - \alpha}}\,. \quad (3.5h)$$

Also, $$x_f^* = \int_0^{\tau^*} \dot{x}_f^*\, d\tau^* \quad (3.5i)$$

and $$h^*_{i_K,j+1} = h^*_{i_K,j} + \frac{\tau^*_{j+1} - \tau^*_j}{\tau^*_j - \tau^*_{j-1}}(2h^*_{i_K-1,j} - h^*_{i_K-2,j-1} - h^*_{i_K,j}) \quad (3.5j)$$

in which the present time step is represented by the subscript j in equation (3.5j), and the spatial node at $z^* = 1$, or equivalently $x^* = x_f^*$, is denoted by the subscript i_K. In equation (3.5h), α is a constant and is derived from $(\alpha U_w^* h^*)_{x=x_f}$, the rate of volumetric loss of working fluid per unit width at the front of the current. This is achieved by putting a sink of strength $\alpha U_w^* h^*$ at the front of the current. Note also that equation (3.5h) is identical to the result obtained by Benjamin (1968) if $\alpha = 0$.

After the current is allowed to spread for a prolonged period, the front of the current will eventually hit the end wall. A reflected bore will advance in the upstream direction, as schematically shown in Figure 3.2. Since a distinct front no longer exists, equations (3.5g) through (3.5j) are no longer valid. As shown in Appendix A, they must be replaced by the following boundary conditions:

At $z^* = 1$,
$$\frac{\partial h^*}{\partial z^*} = 0 \qquad (3.5k)$$

$$U_w^* = 0 \qquad (3.5l)$$

$$\dot{x}_f^* = 0 \qquad (3.5m)$$

and
$$x_f^* = L^* . \qquad (3.5n)$$

Initial conditions:

At time $\tau^* = \tau_0^* > 0$ where $\tau_0^* \cong 0$, it is shown in Appendix A that:

For $-1 \le z^* < 0$,
$$h^* = v_{0(z^*)}^* \tau_0^* \qquad (3.6a)$$

and
$$U_w^* = 0 . \qquad (3.6b)$$

For $0 \le z^* \le 1$,
$$h^* = v_{0(z^* = -k)}^* \tau_0^*/K \qquad (3.6c)$$

and
$$U_w^* = \sqrt{\frac{h^*}{\frac{1}{2} - \alpha}} \qquad (3.6d)$$

where K is an arbitrarily large number and $\tau_0^* \equiv 0$. For large τ^* compared to τ_0^*, the solution was found to be independent of K and τ_0^*, as shown later in Section 3.3.7. Using equations (3.5g) and (3.5i), the velocity and position of the front at $\tau^* = \tau_0^*$ can then be found and be used as initial conditions.

Numerical method is needed to help in solving the system of equations described above. After many methods were tried, the Lax method (Press et al. 1986) was adopted because it provides stable solutions in spite of the fact that it is numerically dissipative. In addition, the errors introduced by numerical dissipation can be minimized by carefully selecting the time step and spatial resolution used in the computation. If i denotes the local spatial node, and j denotes the present time, the Lax method discretizes the spatial and temporal gradients of an arbitrary variable R* as follows

$$\frac{\partial R^*}{\partial z^*} = \frac{R^*_{i+1,j} - R^*_{i-1,j}}{z^*_{i+1} - z^*_{i-1}} \tag{3.7a}$$

$$\frac{\partial R^*}{\partial \tau^*} = \frac{R^*_{i,j+1} - \frac{1}{2}(R^*_{i+1,j} - R^*_{i-1,j})}{\tau^*_{j+1} - \tau^*_j}. \tag{3.7b}$$

A computer program was written in Fortran to solve the above system of equations. The program was executed by a DEC Vaxstation 3600 with VMS Version 5.5. Twenty-one sets of parameters were chosen to test the present model. They are listed in Table 3.1.

Case number	w_0^*	α	L^*	τ_0^*	K
1.1	3	0.0	450	10^{-3}	10^3
1.2	6	0.0	450	10^{-3}	10^3
1.3	12	0.0	1500	10^{-3}	10^3
1.4	18	0.0	1500	10^{-3}	10^3
1.5	24	0.0	1500	10^{-3}	10^3
1.6	6	0.05	450	10^{-3}	10^3
1.7	6	0.10	450	10^{-3}	10^3
1.8	6	0.15	450	10^{-3}	10^3
1.9	6	0.20	450	10^{-3}	10^3
1.10	6	0.225	450	10^{-3}	10^3
1.11	6	0.25	450	10^{-3}	10^3
1.12	6	0.30	450	10^{-3}	10^3
1.13	6	0.35	450	10^{-3}	10^3
1.14	6	0.40	450	10^{-3}	10^3
1.15	6	0.45	450	10^{-3}	10^3
1.16	6	0.0	150	10^{-3}	10^3
1.17	6	0.0	150	10^{-2}	10^3
1.18	6	0.0	150	10^{-3}	10^2
1.19	24	0.10	1500	10^{-3}	10^3
1.20	24	0.20	1500	10^{-3}	10^3
1.21	24	0.25	1500	10^{-3}	10^3

Table 3.1 **Cases investigated for inviscid gravity currents in a channel of infinite depth.**

The output from each computation includes:

1. The time varying volume of working fluid in the gravity current and the corresponding time varying volume of working fluid lost through the sink at the front of the current.

2. Time varying front position and time varying front velocity of the working fluid.

3. Depth and velocity of the layer of working fluid at given times as functions of distance from the leading edge of the bottom wall of the channel.

4. Time varying depth and time varying velocity of the layer of working fluid at given distances from the leading edge of the bottom wall of the channel.

From Table 3.1, it is evident that the different numerical test cases were chosen to show the respective effects of w_0*, α, L*, τ_0* and K. Cases 1.1 to 1.5 were chosen to show the effects of w_0*. Cases 1.6 to 1.15, and also Cases 1.19 to 1.21 were chosen to reveal the effects of α. Finally, Cases 1.16 to 1.18 were chosen to show the effects of L*, τ_0*, and K, respectively.

3.3.2 Estimation of errors in the computation

The computed volume of the layer of working fluid is a measure of the error in the computation. Since there is no mixing in the model, the volume of working fluid in the layer computed plus the amount of working fluid lost through the sink at the front of the current must be the same as the volume of working fluid introduced into the channel if no numerical error was introduced. However, due to numerical dissipation, numerical errors are unavoidable. The computed volume per unit width of the layer of working fluid in the current for Case 1.7 is shown in Figure 3.3 as an example. In the figure, the combined non-dimensional volume per unit width of the working fluid in the layer plus the amount of fluid lost through the sink is represented by the dotted line against time, while the total non-dimensional volume of working fluid introduced through the inlet per unit width is represented by the solid line. By comparing the two lines, it is evident that although there is error in the computed volume, this error is less than half a percent. In

each of the cases considered, the time step and spatial resolution were carefully selected so that the error in the combined volume of working fluid does not exceed 1%.

3.3.3 General description of the solutions

In addition to the combined volume of the current as mentioned in Section 3.3.2, other variables were also recorded at various times to help understand the evolution of the solutions. Two of these variables are the depth of the current, h*, and the velocity of the fluid, U_w*, as functions of distance from the leading edge of the bottom wall at a given time. Case 1.2 is used as an example in Figures 3.4a and 3.4b to reveal the changes of h* and U_w* as functions of distance from the leading edge at non-dimensional times t* = 25, 225, 425, and 625. In each of the two figures, the curve is bounded by a vertical solid line on the left side. This line represents the location of the upstream end wall of the channel, while the downstream end wall of the channel coincides with the vertical axis on the right hand side of the graph.

From Figure 3.4a, it is obvious that a significant amount of fluid is accumulated above the inlet to build up the pressure head needed to drive the current in the downstream direction. As a result, the depth of the current drops rapidly in the streamwise direction near the inlet. However, away from the inlet, the current depth is not a strong function of the streamwise position until the arrival of the bore that results from the reflection of the front at the downstream end wall, as evident by comparing the two curves representing t* = 225 and 425. As a result, the front speed remains constant for this part of the flow phenomenon. It is also obvious that the depth increases with time at a fixed streamwise position, for example, by comparing the curves for various times at x* = 50.

Moreover, it can be seen from Figure 3.4a that as the depth of the layer decreases with distance away from the inlet, it reaches a minimum and then increases slightly before attaining a constant value. This minimum depth represents an internal jump. This internal jump travels in the downstream direction at a constant speed V_j*, which is different from the front velocity after a starting regime. It should also be noted that due to the dissipative nature of the numerical scheme being used, the jump is smeared, and it looks more like a "hump" then an abrupt jump.

Figure 3.4a also shows that the depth, h*, is roughly tripled after the front of the current has hit the end wall at the downstream end and moves in the upstream direction in the form of a bore. It is apparent that the depth of this bore is not a strong function of its position. By recording the position of the bore at various times, the instantaneous speed of the reflected bore can be deduced. It was found that this speed is constant when the bore is travelling within the section of the channel where the depth of the current is constant. It was also found that this speed increases when the bore reaches the section near the inlet where the depth of the current is decreasing rapidly in the streamwise direction. However, in spite of the rapid changes in speed in this section of the channel, it was found that h* attains a similar value at all positions that the bore has passed, even though the change in h* with streamwise position in this section is large before the arrival of the bore. Hereafter, unless it is stated otherwise, when the constant speed of the reflected bore, V_r*, is mentioned, it refers to the speed of the bore in the section of the flow in which it propagates with a constant speed.

The corresponding velocity of the fluid in the current, U_w*, at various times increases with distance near the inlet, as shown in Figure 3.4b, but remains constant far away from the inlet. This result, together with the dependence of the depth on the streamwise position, satisfies the equation of mass conservation as required. After the front hits the end wall, the velocity of the fluid downstream of the reflected bore vanishes, while the velocity at a position upstream of the bore is unaffected. The velocity of the working fluid at a fixed location decreases with time before the bore arrives. This supports the observation earlier in this section that the corresponding depth increases with time.

Two other variables of interest are the front position, x_f*, and the front velocity, $\dot{x}_f$*, of the current. Case 1.2 is again used as an example to show the changes in x_f* and $\dot{x}_f$* as functions of time in Figures 3.5a and 3.5b, respectively. In these figures, it can be seen that the front velocity increases slowly with time when the current first started to spread downstream. This stage of the phenomenon is called the initial stage (Chen 1980). After achieving a speed of roughly 1.2, the acceleration stops, and the front then moves at a constant speed until it hits the wall at the downstream end of the channel. This stage of the flow is called the principal stage. The constant speed in this stage is denoted as V_f*. After the current hits the end wall, it reflects from the wall as a bore which moves in the upstream direction.

As was discussed earlier in this section, the internal jump advances downstream at a speed that is different from the front velocity. The position of this jump, x_j^*, in Case 1.2 is plotted against time in Figure 3.6a. It can be seen from the figure that the rate of advance of this position decreases with time in the beginning before achieving a constant speed, V_j^*. After a long time, the rate of advance again starts to decrease until the arrival of the reflected bore, at which time the internal jump vanishes. Moreover, direct comparison of Figure 3.5a and Figure 3.6a shows that V_f^* is roughly three times as large as V_j^*.

The position of the reflected bore as a function of time for Case 1.2 is shown in Figure 3.6b. It can be seen that the bore advances upstream at a constant speed, V_r^*, right after the front of the current hits the downstream end wall, as described earlier. The speed then increases when the bore is near the inlet, at which the depth of the current is decreasing rapidly away from the inlet.

Figure 3.7a shows the Froude number of the current, $U_w/\sqrt{g' h}$, or equivalently, $U_w^*/\sqrt{h^*}$ in the current at $t^* = 25$, 225, 425, and 625. It can be seen that the Froude number at a particular time increases from zero at the upstream end wall to a maximum of roughly 1.5, before it dips slightly and maintains a constant value at roughly 1.4. This is again in good agreement with Benjamin (1968), who suggested that the Froude number for an inviscid gravity current in a channel of infinite depth with no mixing is $\sqrt{2}$.

However, in Figure 3.7b, the Froude number relative to the speed of the internal jump is shown as a function of distance from the inlet at $t^* = 225$. It can be seen that this relative Froude number increases with downstream position until it is larger than unity, and then it drops to slightly below unity before achieving a constant value, signifying the presence of a weak internal jump. In both Figures 3.7a and 3.7b, the vertical line on the left-hand side represents the upstream end wall of the channel, while the downstream end wall is represented by the vertical axis on the right-hand side of the graph, as explained earlier in this section.

Finally, Figure 3.8a illustrates the increase in depths as functions of time for the locations $x^* = -6$ and 50, again using Case 1.2 as an example. It can be seen that at each of the two locations, the depth, h^*, increases rapidly with time soon after the front has

passed, but the rate of increase drops quickly, and the depth of the current remains roughly constant thereafter. The accompanying Figure 3.8b shows the corresponding velocity of the layer of working fluid, U_w^*. It can be seen that when the head first passed the location $x^* = 50$, U_w^* jumps to about 1.2. It then decreases slowly with time. It should be noted that $x^* = -6$ in this particular case corresponds to the location of the upstream wall, and U_w^* at this location is always zero, as evident in Figure 3.8b in which the dashed line representing this velocity coincides with the line representing $U_w^* = 0$ at all time. This is in agreement with equation (3.5b), which stated that the velocity at the upstream end wall must be zero at all times.

3.3.4 Effects of the length of the inlet, w_0^*, on the solutions

Figure 3.9a shows the non-dimensional front positions, x_f^*, versus the non-dimensional time from start, t^*, for Cases 1.1, 1.3, and 1.5, while Figure 3.9b shows the corresponding non-dimensional front velocity $\dot{x}_f^*$ versus time for each of the same three cases. The curves for Cases 1.3 and 1.5 were drawn only up to $x_f^* = 450$ in the two figures for illustrative purposes, even though they extend well beyond the stated positions. Although the three cases have different L^* in addition to different w_0^*, it will be shown in a later section that L^* does not affect the values of x_f^* because the front of the current in each case had not reached the downstream end wall within the time period shown in the figure. As a result, the difference in the three curves can only be attributed to their difference in w_0^*. From the figures, it can be seen that the front velocity in each case accelerates during the initial stage from zero to a steady velocity of about 1.2. This velocity then remains constant throughout the principal stage. In addition, one of the effects of w_0^* on the solution in each case is the total time taken by this acceleration process. It is obvious from the figures that a channel with a longer w_0^* requires a longer time and distance to complete the initial stage.

Results from cases 1.1 through 1.5 reflect the effects of the inlet length when there is no loss of working fluid through the sink at the front of the current. In Figure 3.10a, the non-dimensional constant front speed, V_f^*, and the non-dimensional constant speed of the reflected bore, V_r^*, are shown as functions of the non-dimensional inlet length, w_0^*. It is obvious that neither V_f^* nor V_r^* depends on w_0^*. In addition, V_f^* has a value of about 1.2 while the value of V_r^* is roughly half as large. It can be shown by

using conservation equations of mass and momentum that this is in agreement with the observation in Section 3.3.3 that the value of h* at a position at which the reflected bore has passed is three times as large as its value before the arrival of the reflected bore.

Furthermore, it was shown in Figures 3.9a and 3.9b that although all the cases eventually reach the same non-dimensional constant front speed, the amount of time taken to complete the initial stage are different for cases with different w_0*. As a result, the front position of the current when the constant front speed is reached is different for each case. To compare the different cases, a new length parameter $P_{99\%}$ is defined as the front position of the current at which the non-dimensional front velocity, $\dot{x}_f$*, first attains 99% of the value of the non-dimensional constant front speed, V_f*. Figure 3.10b shows that the ratio $P_{99\%}$*/w_0* is independent of the non-dimensional inlet length, w_0*.

Another parameter of interest is the non-dimensional position of the internal jump, x_j*. Although the ratio x_j*/x_f* in a specific case changes with time, Figure 3.11a reveals that the ratio between the non-dimensional position at which the internal jump first appears and the corresponding non-dimensional front position of the current, $(x_j*/x_f*)_i$, does not depend on the non-dimensional inlet length, w_0*. In addition, the non-dimensional constant speed of the internal jump, V_j*, is also independent of the inlet length, as evident from Figure 3.11b.

Some other effect of w_0* on the solutions are shown in Figures 3.12a and 3.12b. Figure 3.12a shows the current depth as a function of distance from the leading edge of the bottom wall at t* = 275 for Cases 1.1, 1.3, and 1.5. This figure reveals that the fluid spreads farther in a given time for a channel with a shorter w_0*. This is because in non-dimensional terms, more fluid is required to fill the layer of working fluid above the inlet when the inlet is longer, and thus less fluid was made available to spread the current when it started. As a result, the front of this current lags behind that in a channel with a shorter inlet, even though the front in each case will eventually achieve a similar speed after the section above the inlet reaches equilibrium, as was the case in Figure 3.12a. This also explains the longer time required for the initial stage of a longer inlet, as mentioned earlier in this section. The depth of the current far away from the inlet is also very similar for each of the three cases. This is in agreement with the present model, because equations (3.5g) and (3.5h) suggest that when the front speeds are similar, the current depths at the front should also follow suit.

Finally, it should also be noted that w_0* does not have a lasting effect on h* at a given non-dimensional location, x*. This is illustrated in Figure 3.12b. In this figure, the current depth is shown as a function of time at x* = 50 for Cases 1.1, 1.3, and 1.5. It is obvious from the figure that the front of the current in Case 1.1, which has the shortest w_0*, arrives earlier than that in Case 1.5, which has the longest w_0*. This is in agreement with the conclusion drawn earlier in this section. However, after t* ≅ 300, it is observed that there is no apparent difference in the current depth for the three cases.

3.3.5 Effects of the rate of loss of working fluid at the front of the current, α, on the solutions

The rate of volumetric loss of working fluid per unit width at the front of the current, αU_w*h*, has a profound effect on the solution. According to equation (3.5h), an increase in α will give rise to a lower value of non-dimensional constant front speed, V_f*, when α is small. This is illustrated in Figures 3.13a and 3.13b. Figure 3.13a shows the non-dimensional front position, x_f*, as a function of the non-dimensional time after start, t*, for Cases 1.2, 1.7, and 1.9, which correspond to values of α at 0, 0.1, and 0.2 respectively. Figure 3.13b reveals the corresponding non-dimensional time varying front velocities. Shortly after the flow has started, the fluid velocity at the front is small. The effect of the loss of fluid at the front is thus minimal. However, as the front velocity increases, the rate of volumetric loss of working fluid at the front also increases. Moreover, the rate of loss of fluid also increases with the value of α for the same fluid velocity at the front of the current. Hence, the constant front speed decreases for increasing value of α for small values of α.

However, it can also be seen from Equations 3.5g and 3.5h that the front speed will instead begin to increase as α approaches 0.5. The constant front speed is shown in Figure 3.14a as a function of α. It can be seen that V_f* decreases with increasing α up to a value of α of roughly 0.3. When the value of α is further increased, the value of V_f* also increases instead. In addition, the constant speed of the reflected bore, V_r*, also decreases with increasing α for α smaller than 0.3. For α larger than 0.3, V_r* does not achieve a constant value for a sufficiently long enough time, and thus is not shown in the

figure. It is also observed that the values of V_f* and V_r* are independent of w_0* for a given value of α.

Figure 3.14b shows the effects of α on the front position at which the front velocity first attains 99% of the constant front speed, $P_{99\%}$*. In this figure the ratio $P_{99\%}$*/w_0* is shown as a function of α. It can be seen from the figure that the value of $P_{99\%}$*/w_0* decreases with increasing value of α until the value of α is about 0.4. Then, the value of $P_{99\%}$*/w_0* increases with increasing value of α. It is also observed from the figure that the value of $P_{99\%}$*/w_0* is independent of the value of w_0* for a given value of α.

The value of α also has a significant effect on the current depth at the front, $(h^*)_f$. Figure 3.15a shows the value of $(h^*)_f$ as a function of w_0* for $\alpha = 0$, while Figure 3.15b shows the value of $(h^*)_f$ as a function of α. Although the value of $(h^*)_f$ is independent of w_0* for a given α, as shown in Figure 3.15a, Figure 3.15b shows that it decreases with increasing α. This can be explained simply by noting that when more fluid is lost through the front of the current, the amount of fluid left in the layer of working fluid near the front of the current is reduced. As a result, the depth at the front of the current decreases with increasing rate of loss of fluid.

Finally, the constant speed of propagation of the internal jump, V_j*, is shown as a function of the rate of loss of working fluid at the front, α, in Figure 3.16a. From the figure, V_j* increases with increasing α. It should be noted that two methods were used to determine the location of the internal jump. The first method is to use the point of minimum depth of the current. This method works well up to a value of α at about 0.2. For a value of α above 0.2, the jump is so weak that a large error will be present when the location of the jump is determined by this method. The second method is to use the local maximum of the second derivative. This method does not only compare favorably with the first method for small α, it also provides reasonable values for the location of the internal jump for α of up to 0.35, beyond which a internal jump could not be identified. Furthermore, Figure 3.16b also illustrates the same trend for the ratio of the constant speed of propagation of the internal jump and the constant front speed as a function of α.

3.3.6 Effects of the length of the channel, $L^*+w_0^*$, on the solutions

The non-dimensional length of the channel, $L^*+w_0^*$, has no effects on the solution before the front of the current hits the end wall. This is demonstrated in Figure 3.17a, in which the current depth as a function of x^* at $t^* = 125$ is shown for Cases 1.2 and 1.16. The two cases have identical input parameters, including w_0^*, except L^* and thus $L^*+w_0^*$. It is obvious that the two solutions are identical at $t^* = 125$. However, due to the difference in L^* in the two cases, the front of the current in Case 1.16 hits the end wall before $t^* = 175$, while that in Case 1.2 hits the end wall after $t^* = 175$. As a result, when the current depths of the two cases at $t^* = 175$ are shown in Figure 3.17b, it can be seen that the front in Case 1.2 is still spreading in the downstream direction, while that in Case 1.16 has already hit the downstream end wall, tripled its depth, and its reflected bore is moving in the upstream direction. In the two figures, the short vertical line on the left-hand side of each curve again represents the upstream end wall of the channel, while the line on the right hand side of the curve at $t^* = 175$ for Case 1.16 represents its downstream end wall.

3.3.7 Effects of the parameters τ_0^* and K on the solutions

The effects of the parameters τ_0^* and K are illustrated in Figures 3.18a and 3.18b. Figure 3.18a shows the current depth as a function of distance from the leading edge at $t^* = 125$ for Cases 1.16 and 1.17. The parameters used in these two cases are identical except for the value of τ_0^*, which is 10^{-3} in Case 1.16 and 10^{-2} in Cases 1.17. It can be observed from the figure that the value of τ_0^* does not have a significant effect on the solutions when $t^* \gg \tau_0^*$. Finally, Figure 3.18b illustrates the current depth as a function of distance from the leading edge at $t^* = 125$ for Cases 1.16 and 1.18. Again, the parameters used in these two cases are identical except that in Case 1.16 the value of K is 10^3, while in Case 1.18 the value of K is 10^2. From the figure, it can be observed that when the value of K is large, it does not play a prominent role in the solutions.

3.4 Inviscid gravity currents in a channel of finite depth

3.4.1 General description of the model

In addition to the parameters discussed in the last section, there are other variables which affect the solution significantly when the channel depth is finite. In this section, the effects of these variables are going to be investigated.

The motion of the layer of ambient fluid is no longer negligible, as assumed in the previous model presented in Section 3.3. Since the channel depth is limited at H, the depth of the layer of ambient fluid is only the difference between the channel depth, H, and the depth of the gravity current, h. It can be obtained readily by inspection once h is found. On the other hand, the velocity of the fluid in this layer, U_a, cannot be found by inspection. Furthermore, when U_a is not identically zero, the pressure gradient on the top wall, $\partial p_H/\partial x$ does not vanish. As a result, the conservation equations for mass and momentum for the layer of ambient fluid must also be used. Due to the presence of the term p_H in the conservation equations, a reference pressure is required. This reference pressure, P_{ref}, can be defined as

$$P_{ref} = \rho_a U_{ref}^2 \,. \tag{3.8}$$

Note that the definition of the reference pressure will not affect the solutions.

Using the same transformation of the independent variables as described by equations (3.2a) through (3.2d), the governing equations, the boundary conditions and the initial conditions for an inviscid gravity current in a channel of limited depth are shown in Appendix B to be:

Governing equations:

For $-1 \le z^* \le 0$,

$$\frac{\partial h^*}{\partial \tau^*} + \frac{1}{w_0^*}\frac{\partial}{\partial z^*}(U_w^* h^*) = v_0^* \tag{3.9a}$$

$$\frac{1}{w_0^*}\frac{\partial}{\partial z^*}[U_w^* h^* + U_a^*(H^* - h^*)] = v_0^* - v_H^* \tag{3.9b}$$

and $$\frac{\partial}{\partial \tau^*}(U_w^* - \rho_r U_a^*) + \frac{1}{w_0^*}\frac{\partial}{\partial z^*}\left[\frac{1}{2}(U_w^*)^2 - \frac{1}{2}\rho_r (U_a^*)^2 + h^*\right] = 0 . \quad (3.9c)$$

For $0 \le z^* \le 1$, $$\frac{\partial h^*}{\partial \tau^*} - \frac{z^* \dot{x}_f^*}{x_f^*}\frac{\partial h^*}{\partial z^*} + \frac{1}{x_f^*}\frac{\partial}{\partial z^*}(U_w^* h^*) = v_0^* \quad (3.9d)$$

$$\frac{1}{x_f^*}\frac{\partial}{\partial z^*}[U_w^* h^* + U_a^*(H^* - h^*)] = v_0^* - v_H^* \quad (3.9e)$$

and $$\frac{\partial}{\partial \tau^*}(U_w^* - \rho_r U_a^*) - \frac{z^* \dot{x}_f^*}{x_f^*}\frac{\partial}{\partial z^*}(U_w^* - \rho_r U_a^*) + \frac{1}{x_f^*}\frac{\partial}{\partial z^*}\left[\frac{1}{2}(U_w^*)^2 - \frac{1}{2}\rho_r (U_a^*)^2 + h^*\right] = 0 . \quad (3.9f)$$

The outflow velocity, v_H^*, that appears in equations (3.9b) and (3.9e) is shown in Appendix B to be a function of the co-ordinate z*. It can be expressed as

$$v_H^*{}_{(z^*)} = \frac{1}{w_1^*} \qquad \text{for } -1 \le z^* \le -\left(1 - \frac{w_1^*}{w_0^*}\right) \quad (3.10a)$$

and $$v_H^*{}_{(z^*)} = 0 \qquad \text{for } -\left(1 - \frac{w_1^*}{w_0^*}\right) \le z^* \le \frac{L^*}{w_0^*} . \quad (3.10b)$$

Boundary conditions:

At $z^* = -1$, $$\frac{\partial h^*}{\partial z^*} = 0 \quad (3.11a)$$

$$U_w^* = 0 \quad (3.11b)$$

and $$U_a^* = 0 . \quad (3.11c)$$

At $z^* = 0$, $$h^*_{(z^*=0^-)} = h^*_{(z^*=0^+)} \quad (3.11d)$$

$$\frac{1}{w_0^*}\frac{\partial h^*}{\partial z^*}(z^*=0^-) = \frac{1}{x_f^*}\frac{\partial h^*}{\partial z^*}(z^*=0^+) \tag{3.11e}$$

$$U_w^*{}_{(z^*=0^-)} = U_w^*{}_{(z^*=0^+)} \tag{3.11f}$$

$$\frac{1}{w_0^*}\frac{\partial U_w^*}{\partial z^*}(z^*=0^-) = \frac{1}{x_f^*}\frac{\partial U_w^*}{\partial z^*}(z^*=0^+) \tag{3.11g}$$

and $$\frac{1}{x_f^*}\frac{\partial}{\partial z^*}[U_w^* h^* + U_a^*(H^* - h^*)]_{(z^*=0)} = v_0^*{}_{(z^*=0)} - v_H^*{}_{(z^*=0)} . \tag{3.11h}$$

At $z^* = 1$, $$\dot{x}_f^* = (1 - \alpha)\, U_w^* \tag{3.11i}$$

$$U_w^* = \sqrt{\frac{h^*}{(\frac{1}{2} - \alpha) + \rho_r \frac{h^*}{H^* - h^*}(1 - \alpha) + \frac{1}{2}\rho_r (\frac{h^*}{H^* - h^*})^2}} \tag{3.11j}$$

and $$U_a^* = -\frac{h^*}{H^* - h^*} U_w^* . \tag{3.11k}$$

Also $$x_f^* = \int_0^{\tau^*} \dot{x}_f^*\, d\tau^* \tag{3.11l}$$

and $$h^*{}_{i_K,j+1} = h^*{}_{i_K,j} + \frac{\tau^*_{j+1} - \tau^*_j}{\tau^*_j - \tau^*_{j-1}}(2h^*{}_{i_K-1,j} - h^*{}_{i_K-2,j-1} - h^*{}_{i_K,j}) . \tag{3.11m}$$

Note that equation (3.11j) is slightly different from the result of Benjamin (1968), since Benjamin was studying the motion of an air cavity in a liquid, and there is no spatial gradient for P_H in the current in that case. However, for the extreme cases when $h = 0$ and when $h = H$, the results for the two cases are identical.

As described in Section 3.3.1, after the front of the current has hit the downstream end wall, equations (3.11i) through (3.11m) are replaced by the following equations:

At $z^* = 1$, $$\frac{\partial h^*}{\partial z^*} = 0 \qquad (3.11n)$$

$$U_w^* = 0 \qquad (3.11o)$$

and $$U_a^* = 0 . \qquad (3.11p)$$

Also $$\dot{x}_f^* = 0 \qquad (3.11q)$$

and $$x_f^* = L^* . \qquad (3.11r)$$

Initial conditions:

At time $\tau^* = \tau_0^* > 0$ where $\tau_0^* \cong 0$, it is shown in Appendix B that:

For $-1 \leq z^* < 0$, $$h^* = v_0^*{}_{(z^*)}\, \tau_0^* \qquad (3.12a)$$

$$U_w^* = 0 \qquad (3.12b)$$

and $$U_a^* = 0 . \qquad (3.12c)$$

For $0 \leq z^* \leq 1$, $$h^* = v_0^*{}_{(z^* = -k)}\, \tau_0^*/K \qquad (3.12d)$$

$$U_w^* = \sqrt{\frac{h^*}{\frac{1}{2} - \alpha}} \qquad (3.12e)$$

and $$U_a^* = - \frac{h^*}{H^* - h^*} U_w^* . \qquad (3.12f)$$

The velocity and the position of the front at $\tau^* = \tau_0^*$ can then be deduced from equations (3.11i) and (3.11l), respectively.

The Lax method was again used to obtain solution for this model. In addition, the spatial gradient in equation (3.9b) can be evaluated by

$$\frac{\partial S^*}{\partial z^*} = \frac{S^*_{i,j} - S^*_{i-1,j}}{z^*_i - z^*_{i-1}} \tag{3.13a}$$

and the spatial gradient in equation (3.9e) can be evaluated by

$$\frac{\partial S^*}{\partial z^*} = \frac{S^*_{i+1,j} - S^*_{i,j}}{z^*_{i+1} - z^*_i}\ ; \tag{3.13b}$$

where $$S^* = U_w{}^* h^* + U_a{}^* (H^* - h^*)\ . \tag{3.13c}$$

Thirteen sets of parameters were selected to test the present model. They are listed in Table 3.2.

Case number	$w_0{}^*$	α	H^*	$w_1{}^*$	L^*	ρ_r
2.1	6	0.0	7.5	0.48	450	0.925
2.2	12	0.0	7.5	0.48	1500	0.925
2.3	24	0.0	7.5	0.48	1500	0.925
2.4	6	0.0	15	0.48	450	0.925
2.5	6	0.0	30	0.48	450	0.925
2.6	6	0.0	7.5	0.12	450	0.925
2.7	6	0.0	7.5	1.92	450	0.925
2.8	6	0.0	7.5	0.48	450	1.000
2.9	6	0.0	7.5	0.48	450	0.850
2.10	6	0.10	7.5	0.48	450	0.925
2.11	6	0.20	7.5	0.48	450	0.925
2.12	24	0.10	7.5	0.48	1500	0.925
2.13	24	0.20	7.5	0.48	1500	0.925

Table 3.2 Cases investigated for inviscid gravity currents in a channel of finite depth.

From Table 3.2, it is evident that Cases 2.1 through 2.3 were selected to show the importance of w_0* to an inviscid gravity current in a horizontal channel of finite depth. In addition, Cases 2.4 and 2.5 were chosen to illustrate the effects of H*, while Cases 2.6 and 2.7 were chosen to reveal the effects of the outlet length, w_1*. Moreover, Case 2.8 and 2.9 were selected to examine the influence of the ratio between the density of the ambient fluid and that of the working fluid, ρ_r. Note that ρ_r does not affect the solutions in a channel of infinite depth. Furthermore, Cases 2.10 through 2.13 were chosen to study the effects of α. Finally, the effects of L*, τ_0* and K were found to be the same as those in the previous model, and will not be further discussed in this section.

3.4.2 Estimation of errors in the computation

As in the cases for inviscid gravity currents in a channel of infinite depth, the time step and spatial resolution for the present model were carefully selected so that the error in the accumulated volume of working fluid in each case is less than 1%.

3.4.3 General description of the results and solutions

The front position and the front velocity of the current in this model are found to be similar to those found in the previous model. Their differences due to different input and geometrical parameters will be discussed in later sections. The depth and the velocity of the layer of working fluid for this model are also very similar to those presented for the previous model. The differences due to a finite channel height will be discussed in a later section.

On the other hand, the velocity of the layer of ambient fluid does not vanish in this model. In Figure 3.19a the velocities of the two fluid layers for Case 2.1 are shown as functions of distance from the leading edge at various times. By comparing Figure 3.19a with Figure 3.4b, it is obvious that the velocity of the layer of working fluid calculated in the present model is similar to that in the previous model at a given time. It should also be noted that the scale on the y-axis in the two figures are different, and caution must be used when comparing the two figures. In the present model, the non-

dimensional velocity of the ambient fluid, U_a^*, above the current does not vanish at any time. Instead, it takes on a negative value at all time. Physically, it means that while the layer of working fluid is spreading downstream, the ambient fluid above the current is moving in the upstream direction, and is being displaced through the outlet at the upstream end. This is in agreement with the continuity equations in Section 3.4.1, equations (3.9b) and (3.9e). In this specific example, the magnitude of the velocity of the ambient fluid is only about 10% of that of the working fluid. This magnitude is a function of the channel height, H*. It will be shown in Section 3.4.6 that the magnitude of the velocity of the ambient fluid decreases with increasing channel height, and it tends to be zero when the channel height is much larger than the other length scales. In that case it is equivalent to the result of an inviscid gravity current in a channel of infinite depth.

The pressure on the top wall of the channel, p_H, is also non-zero in the present model. Using equation (B.6c) in Appendix B, p_H^* can be found once the velocity of the ambient fluid is known. This pressure for Case 2.1 is shown in Figure 3.19b as a function of distance from the leading edge at various times. This figure shows that when the front is advancing in the downstream direction, p_H^* decreases very quickly with increasing distance from the upstream end wall. It then retains a nearly constant value at the streamwise locations that the front of the current has already passed. For positions downstream of the front, p_H^* is constant but with a much larger value, as is evident by the rapid increase in the value of p_H^* at the position of the front of the current at the various times. However, after the front hits the downstream end wall, the situation changes. Since the return bore moves in the upstream direction and the velocities of both the ambient and the working fluids downstream of the bore vanish, the pressure on the top wall downstream of the bore is constant but at a value lower than that upstream of the bore. This is illustrated in Figure 3.19b at $t^* = 425$ and $t^* = 625$. The vertical line bounding each curve on the left-hand side in Figures 3.19a and 3.19b again represents the location of the upstream end wall of the channel, while the downstream end wall in each figure coincides with the vertical axis on the right-hand side of the graph.

3.4.4 Effects of the length of the inlet, w_0^*, on the solutions

The conclusion drawn for the previous model that the fluid spreads farther in a given time for a channel with a smaller inlet is also valid for this model. This is revealed in Figures 3.20a and 3.20b. Figure 3.20a shows the non-dimensional current depth as a

function of the distance from the leading edge at t* = 275 for Cases 2.1 through 2.3. It can be deduced from the figure that the fluid in a channel with a smaller w_0* spreads farther than that in a channel with a larger w_0*. In addition, the current depths far downstream from the leading edge are the same for the three cases. The vertical line on the left hand side of each curve in Figure 3.20a represents the location of the upstream end wall of the respective channel.

On the other hand, as in the case of inviscid gravity currents in a channel of infinite depth, the length of the inlet does not have a lasting effect on h* at a given non-dimensional location, x*. This is illustrated in Figure 3.20b. In this figure, the current depth as a function of time at x* = 50 for the same three cases mentioned in the last paragraph are shown. The front of the current in Case 2.1, which has the shortest w_0*, can be observed to arrive earlier at x* = 50 than that in Case 2.3, which has the largest w_0*. This supports the conclusion drawn in the last paragraph that the front of a current in a channel with a shorter w_0* spreads farther at a given time. However, after t* $\cong$ 350, there is no apparent difference in the current depths for the three cases. As a result, it is concluded that the effects of w_0* on h* in the model for inviscid gravity currents in a channel of finite depth are at best only temporary.

3.4.5 Effects of the rate of loss of working fluid at the front of the current, α, on the solutions

As described in Section 3.3.5, the rate of volumetric loss of working fluid per unit width at the front of the current, αU_w*h*, has a profound impact on the solution. Figure 3.21a shows the effects of α on the non-dimensional constant front speed, V_f*, and the non-dimensional constant speed of the reflected bore, V_r*. Both speeds decrease with increasing value of α, but they are independent of the non-dimensional inlet length, w_0*. Figure 3.15b illustrates a similar effect of α on $(h^*)_f$.

3.4.6 Effects of the channel height, H*, on the solutions

Similar to the other length parameters, the non-dimensional height of the channel, H*, also affects the spreading of the layer of working fluid. If the channel height is large

when compared to the other length scales, the relative motion of the ambient fluid is minimal. As a result, the effort required to displace this fluid is also negligible. On the other hand, when the channel height becomes smaller, the excess ambient fluid that is being displaced through the outlet is required to move faster in the upstream direction to maintain the same volumetric flow rate as the influx. A larger pressure head is thus required to accelerate this ambient fluid. As a result, the front velocity of the layer of working fluid decreases with decreasing channel height. This is illustrated in Figure 3.22a, which shows the non-dimensional current depth as a function of the non-dimensional distance from the leading edge at $t^* = 275$ for Cases 2.1, 2.4, and 2.5. It can be deduced from this figure that the working fluid spreads farther at a given time in a deeper channel. In addition, there is no difference in the current depths near the inlet in the three cases. However, while the front speed decreases with increasing channel height away from the inlet, the corresponding current depth increases to satisfy continuity. Moreover, the differences between the currents with $H^* = 7.5$ and $H^* = 15$ are much larger than those between $H^* = 15$ and $H^* = 30$.

Similarly, Figure 3.22b compares the non-dimensional current depth in Case 1.1, which has an equivalent of an infinite channel height, and Case 2.5, which has a channel height of $H^* = 30$. By comparing Figure 3.22a and Figure 3.22b, it is observed that the differences between the currents in Figure 3.22a with $H^* = 15$ and $H^* = 30$ are similar to those between $H^* = 30$ and an infinite H^*. As a result, it can be concluded that the effect of H^* is less prominent when it is large when compared to the other length scales, and it was found that the effects of H^* are insignificant when $H^* > 60$.

The channel height also has a large effect on the non-dimensional velocity of the layer of ambient fluid, U_a^*. This is illustrated in Figure 3.23a, which shows the non-dimensional velocity of the ambient fluid as a function of the non-dimensional distance from the leading edge at $t^* = 275$ for Cases 2.1, 2.4, and 2.5. The magnitude of the velocity of ambient fluid is shown to decrease with the channel height. When $H^* = 30$, as in Cases 2.5, U_a^* is less than 0.04, which is much smaller than the magnitude of the non-dimensional velocity of the working fluid, which typically has an order of magnitude of unity. This figure thus supports the argument that the effects of H^* are not significant when $H^* > 60$.

The non-dimensional current depth at $x^* = 50$ for each of the above three cases is shown as a function of time in Figure 3.23b. Although the current depths of the three

cases are different just after the head has passed the location $x^* = 50$, there is no apparent difference in the depths after $t^* \cong 200$.

Finally, Figure 3.24a shows the non-dimensional constant front speed and the non-dimensional constant speed of the reflected bore as functions of the inverse of the non-dimensional channel height, $1/H^*$. A value of $1/H^* = 0$ represents an infinitely deep channel. While the value of V_f^* decreases with increasing $1/H^*$, the corresponding V_r^* increases with increasing $1/H^*$. The changes in both speeds are less than 7% for the range of $1/H^*$ shown. However, according to Figure 3.24b, there is no clear indication that the ratio $P_{99\%}^*/w_0^*$ is a function of $1/H^*$.

3.4.7 Effects of the length of the outlet, w_1^*, on the solutions

The effects of the non-dimensional length of the outlet, w_1^*, are revealed in Figures 3.25a and 3.25b. In Figure 3.25a, the non-dimensional depth of the current is shown as a function of the non-dimensional distance from the leading edge at $t^* = 275$ for Cases 2.6 and 2.7. The input parameters for the two cases are identical except that the non-dimensional length of the outlet, w_1^*, in Case 2.7 is sixteen times as long as that in Case 2.6. There is no apparent difference in the current depths of the two cases. As a result, it can be concluded that the outlet length does not have a major impact on the solution.

Moreover, the effects of w_1^* on the non-dimensional constant front speed, V_f^*, and the non-dimensional constant speed of the reflected bore, V_r^*, are not significant. This is revealed in Figure 3.25b, which shows V_f^* and V_r^* as functions of w_1^*. It is observed that neither of the two speeds depends on w_1^* for the range of w_1^* being considered.

3.4.8 Effects of the density ratio between the ambient fluid and the working fluid, ρ_r, on the solutions

Figure 3.26a shows that there is no apparent difference between the depth of a gravity current at $t^* = 275$ with a density ratio between the ambient fluid and the working fluid, ρ_r, of 0.850 and one with $\rho_r = 1.000$. Figure 3.26b further reveals that the density

ratio does not have a large influence on the non-dimensional constant front speed, V_f^*, and the non-dimensional constant speed of the reflected bore, V_r^*. It is thus concluded that the density ratio between the two fluids does not have a significant impact on the solution for the range of ρ_r being considered. This range of density ratio is the same as that found in the experiments carried out in this study and shown earlier in Chapter 2.

3.5 Viscous gravity currents in a channel of infinite depth

3.5.1 General description of the model

A model for inviscid gravity currents in an infinitely deep horizontal channel was presented in Section 3.3 and a model for inviscid gravity currents in a horizontal channel with limited depth was discussed in Section 3.4. These models are valid when the effects on a gravity current due to the viscous drag exerted by the bottom wall are small when compared to the buoyancy forces. As a result, the models are not valid when the viscosity is very large, or when the channel is very long. In the second case, although the flow can be treated as inviscid in the beginning, viscous drag due to the bottom wall increases with time. Thus, the viscous drag cannot be neglected after a sufficiently long time.

In this section, a model will be presented to describe the behavior of a viscous gravity current in a channel of infinite depth. The behavior of a viscous gravity current in a channel of finite depth will be treated in Section 3.6. The other assumptions stated in Appendix A are still assumed to be valid in this section. For example, the effects due to interfacial shear are assumed to be small when compared to those due to the viscous drag on the bottom wall.

Since the velocity profile of the current, $u = u(t,x,y)$, is not known in this model, there are more unknowns to be solved than equations available. As a result, von Karman's momentum-integral theory is used to obtain an approximate solution. Although the result is only an approximation, White (1986) described the method as "startlingly accurate."

The velocity profile inside the current can be assumed to have a cubic shape. The resulting velocity profile which satisfies the boundary conditions can be written as

$$\frac{u}{U_w} = \frac{3}{2}\frac{y}{\delta} - \frac{1}{2}\left(\frac{y}{\delta}\right)^3 . \tag{3.14}$$

As a result, the displacement thickness, δ', and the momentum thickness, θ', which are defined as

$$\delta' = \int_0^{\delta} \left(1 - \frac{u}{U_w}\right) dy \tag{3.15a}$$

and

$$\theta' = \int_0^{\delta} \frac{u}{U_w}\left(1 - \frac{u}{U_w}\right) dy \tag{3.15b}$$

can then be evaluated using equation (3.14). They are related to the boundary layer thickness, δ, by the following equations

$$\delta' = \frac{3}{8}\delta \tag{3.16a}$$

and

$$\theta' = \frac{39}{280}\delta . \tag{3.16b}$$

The velocity gradient that is needed to evaluate the stress on the bottom wall can also be written in terms of δ:

$$\left.\frac{\partial u}{\partial y}\right|_0 = \frac{3}{2}\frac{U_w}{\delta} . \tag{3.17}$$

Thus, using the reference length, time, and velocity scales as defined in Section 3.2, together with the transformation of the independent variables as described by equations (3.2a) through (3.2d), the governing partial differential equations, the boundary conditions and the initial conditions are shown in Appendix C to be:

Governing equations:

For $-1 \le z^* \le 0$, $$\frac{\partial h^*}{\partial \tau^*} + \frac{1}{w_0^*}\frac{\partial}{\partial z^*}\left[U_w^*\left(h^* - \frac{3}{8}\delta^*\right)\right] = v_0^* \tag{3.18a}$$

$$\frac{\partial U_w^*}{\partial \tau^*} + \frac{1}{w_0^*}\frac{\partial}{\partial z^*}\left[\frac{1}{2}(U_w^*)^2 + h^*\right] = 0 \tag{3.18b}$$

and $$\delta^* = 0\,. \tag{3.18c}$$

For $0 \le z^* \le 1$, $$\frac{\partial h^*}{\partial \tau^*} - \frac{z^*\dot{x}_f^*}{x_f^*}\frac{\partial h^*}{\partial z^*} + \frac{1}{x_f^*}\frac{\partial}{\partial z^*}\left[U_w^*\left(h^* - \frac{3}{8}\delta^*\right)\right] = v_0^*; \tag{3.18d}$$

when $\delta^* < h^*$, $$\frac{\partial U_w^*}{\partial \tau^*} - \frac{z^*\dot{x}_f^*}{x_f^*}\frac{\partial U_w^*}{\partial z^*} + \frac{1}{x_f^*}\frac{\partial}{\partial z^*}\left[\frac{1}{2}(U_w^*)^2 + h^*\right] = 0 \tag{3.18e}$$

and $$\frac{\partial}{\partial \tau^*}[(\delta^*)^2] - \frac{z^*\dot{x}_f^*}{x_f^*}\frac{\partial}{\partial z^*}[(\delta^*)^2] + \frac{13}{35}\frac{U_w^*}{x_f^*}\frac{\partial}{\partial z^*}[(\delta^*)^2] + \frac{52}{35}\frac{(\delta^*)^2}{x_f^*}\frac{\partial U_w^*}{\partial z^*} - 2\frac{1}{x_f^*}\frac{(\delta^*)^2}{U_w^*}\frac{\partial h^*}{\partial z^*} = \frac{8}{Re}; \tag{3.18f}$$

while for $\delta^* = h^*$, $$\frac{\partial U_w^*}{\partial \tau^*} - \frac{z^*\dot{x}_f^*}{x_f^*}\frac{\partial U_w^*}{\partial z^*} + \frac{1301}{2800}\frac{1}{x_f^*}\frac{\partial}{\partial z^*}[(U_w^*)^2] + \left[\frac{8}{5} + \frac{213}{1400}\frac{(U_w^*)^2}{h^*}\right]\frac{1}{x_f^*}\frac{\partial h^*}{\partial z^*} = -\frac{12}{5}\frac{1}{Re}\frac{(U_w^*)^2}{h^*} \tag{3.18g}$$

and $$\delta^* = h^*\,. \tag{3.18h}$$

The Reynolds number, Re, was defined earlier in equation (3.1f) of this chapter.

Boundary conditions:

At $z^* = -1$, $$\frac{\partial h^*}{\partial z^*} = 0 \tag{3.19a}$$

$$U_w^* = 0 \tag{3.19b}$$

and $$\delta^* = 0\,. \tag{3.19c}$$

At $z^* = 0$, $$h^*_{(z^*=0^-)} = h^*_{(z^*=0^+)} \tag{3.19d}$$

$$\frac{1}{w_0^*}\frac{\partial h^*}{\partial z^*}(z^*=0^-) = \frac{1}{x_f^*}\frac{\partial h^*}{\partial z^*}(z^*=0^+) \tag{3.19e}$$

$$U_w^*{}_{(z^*=0^-)} = U_w^*{}_{(z^*=0^+)} \tag{3.19f}$$

$$\frac{1}{w_0^*}\frac{\partial U_w^*}{\partial z^*}(z^*=0^-) = \frac{1}{x_f^*}\frac{\partial U_w^*}{\partial z^*}(z^*=0^+) \tag{3.19g}$$

and $$\delta^* = 0\,. \tag{3.19h}$$

At $z^* = 1$, $$\delta^* = 0 \tag{3.19i}$$

$$\dot{x}_f^* = (1 - \alpha)\, U_w^* \tag{3.19j}$$

and $$U_w^* = \sqrt{\frac{h^*}{\frac{1}{2} - \alpha}}\,. \tag{3.19k}$$

Also $$x_f^* = \int_0^{\tau^*} \dot{x}_f^*\, d\tau^* \tag{3.19l}$$

and $$h^*_{i_K,j+1} = h^*_{i_K,j} + \frac{\tau^*_{j+1} - \tau^*_j}{\tau^*_j - \tau^*_{j-1}}\left(2h^*_{i_K-1,j} - h^*_{i_K-2,j-1} - h^*_{i_K,j}\right)\,. \tag{3.19m}$$

After the front of the current hits the downstream end wall, it was shown in Appendix C that equations (3.19i) through (3.19m) must be replaced by the following boundary conditions:

At $z^* = 1$, $$\frac{\partial h^*}{\partial z^*} = 0 \qquad (3.19n)$$

$$U_w^* = 0 \qquad (3.19o)$$

and $$\frac{\partial \delta^*}{\partial z^*} = 0 \,. \qquad (3.19p)$$

Also $$\dot{x}_f^* = 0 \qquad (3.19q)$$

and $$x_f^* = L^* \,. \qquad (3.19r)$$

Initial conditions:

At time $\tau^* = \tau_0^* > 0$ where $\tau_0^* \cong 0$, it is shown in Appendix C that:

For $-1 \le z^* < 0$, $$h^* = v_0^*{}_{(z^*)}\, \tau_0^* \qquad (3.20a)$$

$$U_w^* = 0 \qquad (3.20b)$$

and $$\delta^* = 0 \,. \qquad (3.20c)$$

For $0 \le z^* \le 1$, $$h^* = v_0^*{}_{(z^* = -k)}\, \tau_0^*/K \qquad (3.20d)$$

$$U_w^* = \sqrt{\frac{h^*}{\frac{1}{2} - \alpha}} \qquad (3.20e)$$

and $$\delta^* = 0 \,. \qquad (3.20f)$$

The velocity and the position of the front at $\tau^* = \tau_0^*$ can then be deduced from equations (3.19j) and (3.19l), respectively. In addition, it was found that equation (3.18f) will give rise to numerical instability when τ^* is not large when compared to τ_0^*. On the other hand, if equation (3.20f) was used in place of equation (3.18f) until $\tau^* = \tau_1^*$, where τ_1^*

$\gg \tau_0^*$, then the solution was found to be stable. For large τ^* compared to τ_1^*, the solution will be shown to be independent of τ_1^*.

The Lax method was again used to obtain solution for this model. Nineteen sets of parameters were selected to test the present model. They are listed in Table 3.3.

Case number	w_0^*	α	Re	L^*	τ_0^*	τ_1^*	K
3.1	6	0.0	200	450	10^{-3}	10	10^3
3.2	6	0.0	500	450	10^{-3}	10	10^3
3.3	6	0.0	1000	450	10^{-3}	10	10^3
3.4	6	0.0	2000	450	10^{-3}	10	10^3
3.5	6	0.0	5000	450	10^{-3}	10	10^3
3.6	12	0.0	200	1500	10^{-3}	10	10^3
3.7	12	0.0	1000	1500	10^{-3}	10	10^3
3.8	12	0.0	5000	1500	10^{-3}	10	10^3
3.9	24	0.0	200	1500	10^{-3}	20	10^3
3.10	24	0.0	1000	1500	10^{-3}	20	10^3
3.11	24	0.0	5000	1500	10^{-3}	20	10^3
3.12	6	0.1	200	450	10^{-3}	10	10^3
3.13	6	0.2	200	450	10^{-3}	10	10^3
3.14	6	0.1	1000	450	10^{-3}	10	10^3
3.15	6	0.2	1000	450	10^{-3}	10	10^3
3.16	6	0.1	5000	450	10^{-3}	10	10^3
3.17	6	0.2	5000	450	10^{-3}	10	10^3
3.18	6	0.0	1000	300	10^{-3}	10	10^3
3.19	6	0.0	1000	450	10^{-3}	20	10^3

Table 3.3 Cases investigated for viscous gravity currents in a channel of infinite depth.

From Table 3.3, it is obvious that Cases 3.1 through 3.5 were selected to study the effects of the Reynolds numbers. Cases 3.6 through 3.11 were chosen to study the effects of the inlet length, w_0*, while Cases 3.12 through 3.17 were selected to show the influence of α. Finally, Case 3.18 and Case 3.19 would reveal the effects of L* and τ_1*, respectively.

3.5.2 Estimation of errors in the computation

The computed volume of the layer of working fluid in each case again provides a measure of the error due to numerical dissipation. In most of the present cases, the time step and spatial resolution were carefully selected so that the error in the accumulated volume of working fluid of each case is less than 3%. However, Case 3.9 is an exception. The error in the volume of working fluid in that case reaches 8%, due to both the low Reynolds number, Re and the large inlet length, w_0*. As a result, an improvement in the numerical scheme is necessary to study very low Reynolds number flows in a channel with a large inlet length.

3.5.3 General description of the results and solutions

The non-dimensional current depth and the non-dimensional velocity of the layer of working fluid as functions of the non-dimensional distance from the leading edge of the bottom wall at times t* = 25, 225, 425, and 625 for Case 3.4 with Re = 2000 are shown in Figures 3.27a and 3.27b to illustrate the differences between an inviscid gravity current and a viscous one. In Figure 3.27a, it can be seen that the depth of a viscous gravity current decreases continuously with distance from the leading edge at a particular time, and the depth of the current at a fixed position increases with time due to viscous effects. This is in contrast with Figure 3.4a, which shows that the depth of an inviscid current far away from the leading edge is constant for a given time, and this depth is also constant for various times at a fixed position until the arrival of either the internal jump or the reflected bore, whichever comes first. According to the present model, the depth of a viscous gravity current at a fixed position which is downstream of the reflected bore increases with time, while that obtained from the inviscid model remains constant with time, as shown in Figures 3.4a.

A related difference between the solutions obtained from the two models can also be observed in the velocity of the layer of working fluid. In Figure 3.27b, it can be seen that the velocity of the layer of working fluid with viscous effects increases with distance from the leading edge at any given time until the location is near the front of the current or near the reflected bore. On the other hand, the velocity of this layer at a fixed position decreases with increasing time. This is in sharp contrast to that of an inviscid gravity current. The velocity of the layer of working fluid in an inviscid current far away from the leading edge was shown in Figure 3.4b to be constant with both time and position until the arrival of the reflected bore.

It can also be deduced from these two figures that the front of an inviscid gravity current spreads downstream faster than that in a viscous one. However, the reflected bore in an inviscid gravity current can be observed to travel upstream slower than that in a viscous one. Finally, the velocity in the layer of working fluid in a viscous gravity current at a fixed position drops sharply after the reflected bore passed that position. Although this velocity decreases continually with distance at a given time, it nevertheless has a magnitude of up to 10% of that upstream of the bore. This contributes to the increase in the depth of the layer downstream of the bore with time, as discussed in the previous paragraph. On the other hand, it can be seen in Figures 3.4 that the velocity downstream of the bore in an inviscid gravity current is negligible, and thus the corresponding current depth remains constant with time. The vertical line bounding each curve on the left-hand side in Figures 3.27a and 3.27b again represents the upstream end wall of the channel, while the downstream end wall coincides with the vertical axis on the right-hand side in each figure.

Figure 3.28a reveals the changes in the boundary layer thickness in the layer of working fluid as a function of distance from the leading edge at times $t^* = 25$, 225, 425, and 625, again using Case 3.4 as an example. The boundary layer due to the leading edge can be regarded as a steady boundary layer. Its changes with time are due to the changes in the velocity in the layer of working fluid. On the other hand, the boundary layer caused by the advancing front of the current grows quickly with distance away from the front at a given time, and it moves downstream along with the front. As a result, the portion of the current with the boundary layer caused by the leading edge of the bottom wall increases continuously with time, as can be deduced by comparing the curves representing the boundary layer thickness at the various times. However, after the

front of the current has hit the wall at the downstream end of the channel, the picture becomes very different. As was discussed in Figure 3.27b, the velocity suffers a large drop downstream of the bore, and the boundary layer should separate in practice, as shown in Figure 2.21c. Since the present model uses an integral approach, the separation of the boundary layer could not be attained. Instead, the model provides an approximate solution that satisfies the conservation equations of mass and momentum. As a result, the boundary layer thickness downstream of the bore can be seen to increase sharply.

Figure 3.28b further illustrates the effects described in the last paragraph. The solid curves in the figure represent the depth of the current at times $t^* = 225$ and 425, while the dashed lines represent the corresponding boundary layer thickness. Before the front of the current hits the downstream end wall, it can be observed from the figure that the boundary layer thickness increases with distance downstream from the inlet until it occupies the whole depth of the current. In addition, the boundary layer thickness increases sharply downstream of the reflected bore, as described in the last paragraph, and occupies the thickness of the whole layer in that portion of the current. As mentioned in the last paragraph, this is due to the inability of the present model to handle the boundary layer in this particular case. The vertical line bounding each curve on the left-hand side again represents the position of the upstream end wall of the channel.

An important feature of the present model is shown in Figure 3.29a. This figure shows the non-dimensional depth of the current and the non-dimensional boundary layer thickness at $x^* = -6$ and $x^* = 50$ as a function of the non-dimensional time for Case 3.4. By comparing this figure with Figure 3.8a, it can be seen that at $x^* = -6$, which is the position of the upstream end wall, the depth of an inviscid gravity current does not increase with time, while that in a viscous current increases continuously with time even though the bottom wall does not exist in this portion of the channel. The dashed line, which represents the corresponding boundary layer thickness at $x^* = -6$, coincides with the x-axis. As a result, the boundary layer thickness in this portion of the channel is zero. It can thus be concluded that the increase in current depth is strictly due to the increase in boundary layer thickness downstream of $x^* = -6$. At $x^* = 50$, the viscous effects are even more profound. It is observed that the depth of a viscous gravity current increases at a much larger rate with time than that obtained from the inviscid model. This can be attributed to the increase in boundary layer thickness with distance from the leading edge in the viscous model. The current with an increasing boundary layer thickness is analogous to having an inviscid flow, but with a bottom wall of the shape of the

displacement thickness. The flow has to overcome this sloping bottom wall that increases with time and distance, and an ever increasing pressure head is needed to drive the flow at a given position. In addition, the boundary layer at a fixed position was found in Figure 3.29a to remain roughly constant with increasing time after an initial period during which it increases rapidly with time. As a result, it can be deduced that the increase in the depth of the current at a fixed position is not only due to the increase in the boundary layer thickness at the location of interest, but also due to the increase in the boundary layer thickness downstream of that position.

The boundary layer in a viscous current is thus similar to the boundary layer thickness obtained in the Blasius problem with the leading edge of the bottom wall being analogous to the leading edge of a flat plate in the Blasius problem, except for the decrease in velocity in the layer of working fluid with time. However, the boundary layer thickness in the Blasius problem with similar conditions can be deduced to attain a value of 0.8, while the boundary layer thickness in the present model attains only about half that value. This discrepancy can be attributed to both the decreasing fluid velocity and increasing current depth at that location.

The accompanying Figure 3.29b shows the corresponding non-dimensional velocity of the layer of working fluid in Case 3.4 at $x^* = 50$ as a function of the non-dimensional time from start. Since the velocity at the upstream end wall is always zero, it is represented by the dashed line that coincides with zero velocity at all time. The non-dimensional velocity of the fluid at $x^* = 50$ is about 1.5 just after the front of the current has passed. It then decreases continuously thereafter. When the reflected bore arrives at $t^* \cong 970$, the velocity suffers a sharp drop. According to Figure 3.27b, this velocity will attain a value of about 10% of that before the arrival of the bore.

Furthermore, the front position and the front velocity of a viscous gravity current are found to be different from those in an inviscid one. The front position of Case 3.3 is illustrated in Figure 3.30a. while the corresponding front velocity is shown in Figure 3.30b. The front position of the current in Figure 3.30a can be seen to go through the same accelerating initial stage and the stage of constant spreading rate, referred to as the principal stage in Section 3.3.3, as in the case of an inviscid current. After $t^* \cong 130$, however, the spreading rate of the front decreases with time. This decrease in front speed is due to the viscous drag exerted by the bottom wall on the current, as is evident from the continuous increase in the boundary layer thickness with time in Figure 3.28a.

Chen (1980) referred to this stage of decreasing front speed as the final stage. The position of the front at which the front velocity starts to decrease is denoted by x_t, and it was experimentally shown to exist earlier in Section 2.3.2. It will also be referred to as the transition position, since the front velocity changes from a constant speed to an ever decreasing one while the current changes from an inertia-buoyancy regime to a viscous-buoyancy regime. The above observation can also be seen in Figure 3.30b. It should be noted that the kinks observed in Case 3.3 are due to changes in the grid size used during computation to minimize the computational time and resources needed, and not due to physical reasons. These kinks will become smaller with increasing resolution. However, it was found that the increase in accuracy does not justify the extra computational time needed for an increase in resolution. As a result, the resolution was not increased to minimize the kinks.

Figure 3.31 shows an interesting effect of the Reynolds number. It was established by Benjamin (1968) that the front of an inviscid current spreads at a constant rate, while Huppert (1982) and Didden and Maxworthy (1982) established that the front of a current spreads at a rate such that $x_f \propto t^{4/5}$ in the viscous-buoyancy regime. In Figure 3.31, the non-dimensional front position of the current in Case 3.1 is shown as a function of the non-dimensional time in logarithmic scales. It can be seen from the figure that when t* is small, the flow behaves as if it is inviscid, and the front advances at a constant rate as predicted by Benjamin. However, at $t^* \cong 100$ in this particular case, the spreading rate becomes proportional to $t^{4/5}$ as predicted for a gravity current dominated by viscous and buoyancy forces. This is in good agreement with the experimental results presented earlier in Section 2.3.2. As a result, it is concluded that although numerous assumptions and approximations are used in this viscous model, it nevertheless captures the essence of the phenomenon.

Furthermore, it was shown in Section 3.3.3 that the speed of a reflected bore is constant until the bore is near the inlet. In Figure 3.32, it is shown that the viscous model provides a different result. Since the depth of a viscous current is an ever decreasing function with respect to x*, the speed of the reflected bore is an increasing function when it advances upstream. As a result, the magnitude of the slope of the plot in Figure 3.32, which shows the non-dimensional position of the reflected bore, x_r^*, as a function of t* for Case 3.1 increases continuously with time. This is not in good agreement with the experimental results shown earlier in Section 2.3.2. The discrepancy can be attributed to

the inability of this model to handle the separating boundary layer of the bore, as well as other factors present in the experiments. As a result, quantitative information about the speed of the reflected bore will not be pursued any further in this model.

3.5.4 Effects of the Reynolds number, Re, on the solutions

The Reynolds number, Re, has a profound impact on the solutions. This is illustrated by comparing the non-dimensional time varying front position of Cases 3.3 and 3.5 as a function of the non-dimensional time in Figure 3.33a. In Figure 3.33a, it can be seen that the spreading rate increases with increasing Reynolds number. In addition, Figure 3.33b, which compares the front velocity of the same two cases, reveals that the transition position, x_t, also increases with increasing Reynolds number. In Case 3.3, when Re = 1000, it was observed that $x_t^* \cong 130$ and $V_f^* \cong 1.14$. On the other hand, when Re = 5000 it was observed that $x_t^* \cong 242$ and $V_f^* \cong 1.19$ in Case 3.5. Note that it was shown in Section 3.3.4 that an inviscid gravity current with similar conditions yields $V_f^* \cong 1.23$. Thus, it can be concluded that the flow at a higher Reynolds number behaves more like an inviscid flow, as expected.

Figure 3.34a further illustrates this change in the non-dimensional transition position, x_t^*. It is observed from the figure that the non-dimensional transition position increases with increasing Reynolds number. Thus, its occurrence is due to viscous effects. However, it was also shown in Section 2.3.2 that in the experiments conducted, x_t^* decreases with Reynolds number when Re < 1000, and x_t^* is roughly constant for 1000 < Re. This discrepancy is due to the three-dimensional effects at the front of the current owing to the overrun of ambient fluid. Since it was shown in Section 3.4.3 that the current depth results from the boundary layer thickness developed from the leading edge, this discrepancy in x_t^* will not prevent the model from capturing the essence of the phenomenon. As a result, quantitative evaluation of x_t^* will not be pursued hereafter.

Similarly, Figure 3.34b shows the corresponding changes in $P_{99\%}^*/w_0^*$. It can be seen that $P_{99\%}^*/w_0^*$ is also influenced by viscous effects, and it increases with increasing Reynolds number. The rate of increase of $P_{99\%}^*/w_0^*$ slows down considerably with increasing Reynolds number. Thus, it will not increase indefinitely with increasing Reynolds number. This agrees with the result shown in Figure 3.10b,

which shows that the ratio $P_{99\%}^*/w_0^*$ will attain a value of about 9 for an inviscid gravity current. However, since this ratio does not appear to have a large effect on the solution, it will not be pursued any further.

As mentioned earlier in this section, the non-dimensional constant front speed, V_f^*, increases with increasing Reynolds number. This is illustrated in Figure 3.35a. For Re < 1000, the rate of increase in V_f^* with Reynolds number is large. However, when the Reynolds number is sufficiently large, the rate of increase is reduced, and the value of V_f^* tends to that of an inviscid gravity current, which is shown as the dashed line in the figure.

The depth of current at the front, $(h^*)_f$, in the principal stage also exhibits a similar behavior as V_f^*. In Figure 3.35b, it can be seen that $(h^*)_f$ increases rapidly with Reynolds number for small Reynolds numbers, but the rate of increase slows down considerably when the Reynolds number is sufficiently large. The value of $(h^*)_f$ for a large Reynolds number is also close to that of an inviscid gravity current, which is shown in the figure as a dashed line. Hence, it supports the conclusion that at higher Reynolds numbers, the flow behaves like an inviscid gravity current.

Figures 3.36a and 3.36b further illustrate this fact. Figure 3.36a shows both the non-dimensional current depth and the non-dimensional boundary layer thickness at $t^* = 225$ for Case 3.3 with Re = 1000, and compares them with the depth of a corresponding inviscid current. Similarly, Figure 3.36b shows the non-dimensional current depth and the non-dimensional boundary layer thickness at $t^* = 225$ for Case 3.5, which has a Reynolds number of 5000 and again compares them to the corresponding depth of an inviscid gravity current. Note that for an inviscid current, the boundary layer thickness is always zero. From the figures, it can be seen that a current with a lower Reynolds number develops a much thicker boundary layer, and the corresponding current depth at a fixed position at a given time must then be deeper to overcome the thicker boundary layer downstream of that particular location. It can also be observed from the figures that, as a result from the argument above, a current with a higher Reynolds number will resemble an inviscid gravity current more than that with a lower Reynolds number.

3.5.5 Effects of the length of the inlet, w_0*, on the solutions

As in previous models, the fluid in the present viscous model spreads farther in a given amount of time for a channel with a shorter inlet, w_0*. This is shown in Figures 3.37a and 3.37b. In Figure 3.37a, the non-dimensional front position as a function of the non-dimensional time for Cases 3.3, 3.7, and 3.10 are shown. It is observed that the initial acceleration stage is longer for the current with a longer inlet. Figure 3.37b is even more illustrative. The non-dimensional front velocity of each of the same three cases is shown as a function of the non-dimensional time. It can be seen that the front velocity of each case has a similar initial stage during which the front velocity accelerates quickly. The principal stage that follows has a constant front velocity, which is followed by the stage with decelerating front velocity. It is obvious that a longer inlet requires a longer initial stage, but the decelerating stage does not strongly depend on w_0*, as is evident by the overlapping of the three curves that represent the three different cases at $200 < t^*$. Due to this longer initial stage, by the time the current in a channel with a longer inlet starts to approach the value of the constant front speed the boundary layer is already well developed, and the fluid that is available at the front of the current is less than that of a current with a shorter inlet. As a result, the constant front speed that can be attained by a longer inlet is less than that achievable by a shorter inlet before the start of the decelerating stage.

The argument put forth earlier in this section that a larger constant front speed can be achieved by a shorter inlet is further supported by Figure 3.38, which shows the non-dimensional constant front speed, V_f*, as a function of Reynolds number, Re, for cases with w_0* = 6, 12, and 24. From the figure, it is evident that at low Reynolds numbers, the decelerating stage starts early, and thus the constant front speed that can be achieved by a long inlet is much smaller than that which can be achieved by a short inlet. On the other hand, when the Reynolds number is large, the deceleration stage starts later, and the constant front speed that can be achieved is less sensitive to the inlet length. In addition, the constant front speed at very large Reynolds number approaches that of an inviscid gravity current, which is shown as the dashed line in the figure. The value of V_f* for an inviscid gravity current was shown in Section 3.3.4 to be independent of w_0*.

Finally, the non-dimensional current depth and the non-dimensional boundary layer thickness as a function of the non-dimensional distance from the leading edge at t* = 275 and Re = 1000 for w_0* = 6 and w_0* = 24 are compared in Figure 3.39a. From the

figure, it can be seen that the differences in h* and in δ^* at the same t* are small when x* is small, but the differences increase with increasing x*. On the other hand, Figure 3.39b shows that the differences in h* and in δ^* at a fixed x* decrease with increasing t* for the same two cases. For sufficiently large t*, there is no significant difference in h* and in δ^* at $x^* = 50$ and $Re = 1000$ between the two cases.

3.5.6 Effects of the rate of loss of working fluid at the front of the current, α, on the solutions

Figure 3.40 shows the non-dimensional time varying front position for Cases 3.3, 3.14, and 3.15. These three cases have identical conditions except for the rate of loss of working fluid at the front of the current, α. It is observed that the initial acceleration stage does not strongly depend on α. However, the spreading rate of the front decreases with increasing α in both the principal stage and the decelerating stage. This is better illustrated in Figure 3.40b, which shows the non-dimensional time varying front velocity of the same three cases. It can be seen that the front velocity in each case has a similar initial stage during which the front velocity accelerates quickly. The principal stage that follows has a constant front velocity, which is then followed by the final stage. It is obvious that the initial stage is independent of α, as is evident by the overlapping of the three curves when t* is small. However, it can also be seen that the non-dimensional constant front speed that can be achieved by a large α is smaller than that by a smaller α. This is because the fluid that is available at the current front is less in a current with a larger α. Finally, it can be seen that contrary to the effects of w_0^*, the curves do not coincide in the final stage for the three cases. Instead, they are roughly parallel to each other.

The non-dimensional current depth and the non-dimensional boundary layer thickness as functions of the non-dimensional distance from the leading edge at $t^* = 275$ and $Re = 1000$ for $\alpha = 0.0$ and 0.2 are compared in Figure 3.41a. The differences in h* and in δ^* are negligible when x* is small, but they increase with increasing x*. Furthermore, Figure 3.41b shows that the differences in h* and in δ^* at $x^* = 50$ decreases with increasing t* for the same two cases. At $t^* \cong 300$, there is no apparent difference in h* nor in δ^* between the two cases.

Finally, Figure 3.42 shows the non-dimensional constant front speed, V_f^*, as a function of Reynolds number, Re, for cases with α = 0.0, 0.1, and 0.2. From the figure, it is apparent that the constant front speed that can be achieved by a larger α is smaller than that which can be achieved by a smaller α. Regardless of the Reynolds number, the variation in the constant front speed due to α does not appear to be very sensitive to Re. In this aspect, the effect of α on the solution is different from that of w_0^*.

3.5.7 Effects of the channel length, $L^*+w_0^*$, on the solutions

The non-dimensional length of the channel, $L^*+w_0^*$, again shows no effects on the solution before the front of the current hits the end wall. This is demonstrated in Figure 3.43a, which shows the non-dimensional current depth, h*, as a function of the non-dimensional distance from the leading edge, x*, at t* = 225 for Cases 3.3 and 3.18. These two cases have identical input parameters except for L*, and thus $L^*+w_0^*$. The solutions at t* = 225 are identical for the two cases.

However, due to the difference in L*, the front of the current in Case 3.18 hits the end wall before t* = 375, and that in Case 3.3 hits the end wall after t* = 375. As a result, when the non-dimensional current depths at t* = 375 for the two cases are shown in Figure 3.43b, it can be seen that the front in Case 3.3 is still spreading in the downstream direction, while that in Case 3.18 has already hit the end wall, and the reflected bore is moving in the upstream direction. In Figures 3.43a and 3.43b, the short vertical lines at the both sides of each curve again represent the upstream and the downstream end walls of the channel.

3.5.8 Effects of τ_1^* on the solutions

As described in Section 3.5.1, the flow in each of the cases tested with this model was assumed to be inviscid until $t^* = \tau_1^*$, so that a stable solution could be obtained. The effects of τ_1^* on the solution are revealed in Figures 3.44a and 3.44b. Figure 3.44a shows the non-dimensional current depth and the non-dimensional boundary layer thickness at t* = 375 as functions of the non-dimensional distance from the leading edge of the bottom wall for Cases 3.3 and 3.19. It should be noted that the parameters in the

two cases are identical except that $\tau_1^* = 10.0$ in Case 3.3 and $\tau_1^* = 20.0$ in Case 3.19. It is observed from Figure 3.44a that the difference in τ_1^* does not have a profound effect on h^* nor on δ^* at $t^* = 375$. In addition, Figure 3.44b shows the non-dimensional current depth and the non-dimensional boundary layer thickness at $x^* = 50$ as functions of time from start for the same two cases. The differences between the two cases are minimal at best, as is evident from the coincidence of the two solutions shown in the figure. As a result, it is concluded that the effects of τ_1^* are insignificant when $t^* \gg \tau_1^*$.

3.6 Viscous gravity currents in a channel of finite depth

3.6.1 General description of the model

In this section, a model will be presented to describe the behavior of a viscous gravity current in a channel of finite depth. Unlike the model for inviscid gravity currents in a channel of finite depth as presented in Sections 3.4 nor that for viscous gravity currents in a channel of infinite depth in Section 3.5, this model is merely a collection of the features already presented in the earlier models and does not contain any additional features. Other assumptions made in the earlier models are still assumed to be valid in the present model. The interfacial shear and the viscous force being exerted on the ambient fluid by the top wall of the channel are assumed to be small when compared to the viscous force being exerted on the current by the bottom wall.

Using the transformed z^*-τ^* co-ordinates, the governing equations, the boundary conditions, and the initial conditions are shown in Appendix D to be:

Governing equations:

For $-1 \le z^* \le 0$,
$$\frac{\partial h^*}{\partial \tau^*} + \frac{1}{w_0^*}\frac{\partial}{\partial z^*}(U_w^* h^*) = v_0^* \qquad (3.21a)$$

$$\frac{1}{w_0^*}\frac{\partial}{\partial z^*}[U_w^* h^* + U_a^*(H^* - h^*)] = v_0^* - v_H^* \qquad (3.21b)$$

$$\frac{\partial}{\partial \tau^*}(U_w^* - \rho_r U_a^*) + \frac{1}{w_0^*}\frac{\partial}{\partial z^*}[\tfrac{1}{2}(U_w^*)^2 - \tfrac{1}{2}\rho_r (U_a^*)^2 + h^*] = 0 \qquad (3.21c)$$

and $$\delta^* = 0\,. \qquad (3.21d)$$

For $0 \le z^* \le 1$,

when $\delta^* < h^*$, $$\frac{\partial h^*}{\partial \tau^*} - \frac{z^* \dot{x}_f^*}{x_f^*}\frac{\partial h^*}{\partial z^*} + \frac{1}{x_f^*}\frac{\partial}{\partial z^*}[U_w^*(h^* - \tfrac{3}{8}\delta^*)] = v_0^* \qquad (3.21e)$$

$$\frac{1}{x_f^*}\frac{\partial}{\partial z^*}[U_w^*(h^* - \tfrac{3}{8}\delta^*) + U_a^*(H^* - h^*)] = v_0^* - v_H^* \qquad (3.21f)$$

$$\frac{\partial}{\partial \tau^*}(U_w^* - \rho_r U_a^*) - \frac{z^* \dot{x}_f^*}{x_f^*}\frac{\partial}{\partial z^*}(U_w^* - \rho_r U_a^*) + \frac{1}{x_f^*}\frac{\partial}{\partial z^*}[\tfrac{1}{2}(U_w^*)^2 - \tfrac{1}{2}\rho_r (U_a^*)^2 + h^*] = 0 \qquad (3.21g)$$

and $$\frac{\partial}{\partial \tau^*}[(\delta^*)^2] - \frac{z^* \dot{x}_f^*}{x_f^*}\frac{\partial}{\partial z^*}[(\delta^*)^2] + \frac{13}{35}\frac{U_w^*}{x_f^*}\frac{\partial}{\partial z^*}[(\delta^*)^2] + 2\frac{(\delta^*)^2}{U_w^*}\frac{\partial U_w^*}{\partial \tau^*} - 2\frac{(\delta^*)^2}{U_w^*}\frac{z^* \dot{x}_f^*}{x_f^*}\frac{\partial U_w^*}{\partial z^*} + \frac{122}{35}\frac{(\delta^*)^2}{x_f^*}\frac{\partial U_w^*}{\partial z^*} = \frac{8}{Re}\,; \qquad (3.21h)$$

and for $\delta^* = h^*$, $$\frac{\partial h^*}{\partial \tau^*} - \frac{z^* \dot{x}_f^*}{x_f^*}\frac{\partial h^*}{\partial z^*} + \frac{1}{x_f^*}\frac{\partial}{\partial z^*}[U_w^*(h^* - \tfrac{3}{8}\delta^*)] = v_0^* \qquad (3.21i)$$

$$\frac{1}{x_f^*}\frac{\partial}{\partial z^*}[U_w^*(h^* - \tfrac{3}{8}\delta^*) + U_a^*(H^* - h^*)] = v_0^* - v_H^* \qquad (3.21j)$$

$$\frac{\partial}{\partial \tau^*}\left[U_w^*\left(h^* - \frac{3}{8}\delta^*\right) - \rho_r U_a^* h^*\right]$$

$$- \frac{z^* \dot{x}_f^*}{x_f^*}\frac{\partial}{\partial z^*}\left[U_w^*\left(h^* - \frac{3}{8}\delta^*\right) - \rho_r U_a^* h^*\right]$$

$$+ \frac{1}{x_f^*}\frac{\partial}{\partial z^*}\left[(U_w^*)^2\left(h^* - \frac{18}{35}\delta^*\right)\right] - \frac{\rho_r U_a^* h^*}{x_f^*}\frac{\partial U_a^*}{\partial z^*}$$

$$- \frac{\rho_r U_a^*}{x_f^*}\frac{\partial}{\partial z^*}\left[U_w^*\left(h^* - \frac{3}{8}\delta^*\right)\right] + \frac{h^*}{x_f^*}\frac{\partial h^*}{\partial z^*} = \frac{3}{2}\frac{1}{Re}\frac{U_w^*}{\delta^*} \qquad (3.21k)$$

and $\delta^* = h^*$. (3.21l)

Boundary conditions:

At $z^* = -1$, $\dfrac{\partial h^*}{\partial z^*} = 0$ (3.22a)

$U_w^* = 0$ (3.22b)

$U_a^* = 0$ (3.22c)

and $\delta^* = 0$. (3.22d)

At $z^* = 0$, $h^*_{(z^*=0^-)} = h^*_{(z^*=0^+)}$ (3.22e)

$$\frac{1}{w_0^*}\frac{\partial h^*}{\partial z^*}(z^*=0^-) = \frac{1}{x_f^*}\frac{\partial h^*}{\partial z^*}(z^*=0^+) \qquad (3.22f)$$

$U_w^*{}_{(z^*=0^-)} = U_w^*{}_{(z^*=0^+)}$ (3.22g)

$$\frac{1}{w_0^*}\frac{\partial U_w^*}{\partial z^*}(z^*=0^-) = \frac{1}{x_f^*}\frac{\partial U_w^*}{\partial z^*}(z^*=0^+) \qquad (3.22h)$$

$$\frac{1}{x_f^*}\frac{\partial}{\partial z^*}\left[U_w^*\left(h^* - \frac{3}{8}\delta^*\right) + U_a^*\left(H^* - h^*\right)\right]_{(z^*=0)}$$
$$= v_0^*{}_{(z^*=0)} - v_H^*{}_{(z^*=0)} \qquad (3.22i)$$

and $\delta^* = 0$. (3.22j)

At $z^* = 1$, $\delta^* = 0$ (3.22k)

$$\dot{x}_f^* = (1 - \alpha) U_w^* \tag{3.22l}$$

$$U_w^* = \sqrt{\frac{h^*}{(\frac{1}{2} - \alpha) + \rho_r \frac{h^*}{H^* - h^*} (1 - \alpha) + \frac{1}{2} \rho_r (\frac{h^*}{H^* - h^*})^2}} \tag{3.22m}$$

and $$U_a^* = - \frac{h^*}{H^* - h^*} U_w^* \, . \tag{3.22n}$$

Also $$x_f^* = \int_0^{\tau^*} \dot{x}_f^* \, d\tau^* \tag{3.22o}$$

and $$h^*_{i_K,j+1} = h^*_{i_K,j} + \frac{\tau^*_{j+1} - \tau^*_j}{\tau^*_j - \tau^*_{j-1}} (2h^*_{i_K-1,j} - h^*_{i_K-2,j-1} - h^*_{i_K,j}) \, . \tag{3.22p}$$

As in the previous models, after the front of the current has hit the downstream end wall, equations (3.22l) through (3.22p) must be replaced by the following equations

At $z^* = 1$, $$\frac{\partial h^*}{\partial z^*} = 0 \tag{3.22q}$$

$$U_w^* = 0 \tag{3.22r}$$

$$U_a^* = 0 \tag{3.22s}$$

and $$\frac{\partial \delta^*}{\partial z^*} = 0 \, . \tag{3.22t}$$

Also $$\dot{x}_f^* = 0 \tag{3.22u}$$

and $$x_f^* = L^* \, . \tag{3.22v}$$

Initial conditions:

At time $\tau^* = \tau_0^* > 0$ where $\tau_0^* \cong 0$, it is shown in Appendix D that:

For $-1 \leq z^* < 0$,

$$h^* = v_0^*{}_{(z^*)}\, \tau_0^* \tag{3.23a}$$

$$U_w^* = 0 \tag{3.23b}$$

$$U_a^* = 0 \tag{3.23c}$$

and

$$\delta^* = 0\,. \tag{3.23d}$$

For $0 \leq z^* \leq 1$,

$$h^* = v_0^*{}_{(z^* = -k)}\, \tau_0^*/K \tag{3.23e}$$

$$U_w^* = \sqrt{\frac{h^*}{(\frac{1}{2} - \alpha) + \rho_r \frac{h^*}{H^* - h^*}(1 - \alpha) + \frac{1}{2}\rho_r (\frac{h^*}{H^* - h^*})^2}} \tag{3.23f}$$

$$U_a^* = -\frac{h^*}{H^* - h^*}\, U_w^* \tag{3.23g}$$

and

$$\delta^* = 0\,; \tag{3.23h}$$

where K is an arbitrarily large number as discussed in previous models. The velocity and position of the front at $\tau^* = \tau_0^*$ can then be found using equations (3.22l) and (3.22o). In addition, it was found that equation (3.21h) will give rise to numerical instability when τ^* is not large when compared to τ_0^*. If equation (3.23h) was used in place of equation (3.21h) until $\tau^* = \tau_1^*$, where $\tau_1^* \gg \tau_0^*$, then the solution was found to be stable. For large τ^* compared to τ_0^* and τ_1^*, the solution was found to be independent of K, τ_0^* and τ_1^*.

The Lax method was again used to obtain solutions for this model due to the reasons previously stated. Forty-nine sets of parameters were chosen to test the present model. These sets of parameters are listed in Table 3.4.

Case number	w_0*	α	Re	H*	w_1*	L*	ρ_r
4.1	3	0.0	200	7.5	0.24	150	0.925
4.2	3	0.0	500	7.5	0.24	150	0.925
4.3	3	0.0	1000	7.5	0.24	150	0.925
4.4	3	0.0	2000	7.5	0.24	150	0.925
4.5	3	0.0	5000	7.5	0.24	150	0.925
4.6	6	0.0	200	7.5	0.24	150	0.925
4.7	6	0.0	500	7.5	0.24	150	0.925
4.8	6	0.0	1000	7.5	0.24	150	0.925
4.9	6	0.0	2000	7.5	0.24	150	0.925
4.10	6	0.0	5000	7.5	0.24	150	0.925
4.11	12	0.0	200	7.5	0.24	150	0.925
4.12	12	0.0	500	7.5	0.24	150	0.925
4.13	12	0.0	1000	7.5	0.24	300	0.925
4.14	12	0.0	2000	7.5	0.24	300	0.925
4.15	12	0.0	5000	7.5	0.24	600	0.925
4.16	24	0.0	200	7.5	0.24	150	0.925
4.17	24	0.0	500	7.5	0.24	150	0.925
4.18	24	0.0	1000	7.5	0.24	300	0.925
4.19	24	0.0	2000	7.5	0.24	300	0.925
4.20	24	0.0	5000	7.5	0.24	600	0.925
4.21	6	0.0	200	15	0.24	150	0.925
4.22	6	0.0	500	15	0.24	150	0.925
4.23	6	0.0	1000	15	0.24	150	0.925
4.24	6	0.0	2000	15	0.24	300	0.925
4.25	6	0.0	5000	15	0.24	300	0.925

Case number	w_0*	α	Re	H*	w_1*	L*	ρ_r
4.26	6	0.0	200	30	0.24	150	0.925
4.27	6	0.0	500	30	0.24	150	0.925
4.28	6	0.0	1000	30	0.24	150	0.925
4.29	6	0.0	2000	30	0.24	300	0.925
4.30	6	0.0	5000	30	0.24	300	0.925
4.31	6	0.1	200	7.5	0.24	150	0.925
4.32	6	0.2	200	7.5	0.24	150	0.925
4.33	6	0.1	1000	7.5	0.24	150	0.925
4.34	6	0.2	1000	7.5	0.24	150	0.925
4.35	6	0.1	5000	7.5	0.24	300	0.925
4.36	6	0.2	5000	7.5	0.24	300	0.925
4.37	6	0.0	200	7.5	0.48	150	0.925
4.38	6	0.0	200	7.5	1.20	150	0.925
4.39	6	0.0	1000	7.5	0.48	150	0.925
4.40	6	0.0	1000	7.5	1.20	150	0.925
4.41	6	0.0	5000	7.5	0.48	300	0.925
4.42	6	0.0	5000	7.5	1.20	300	0.925
4.43	6	0.0	200	7.5	0.24	150	0.80
4.44	6	0.0	200	7.5	0.24	150	1.00
4.45	6	0.0	1000	7.5	0.24	150	0.80
4.46	6	0.0	1000	7.5	0.24	150	1.00
4.47	6	0.0	5000	7.5	0.24	300	0.80
4.48	6	0.0	5000	7.5	0.24	300	1.00
4.49	6	0.0	1000	7.5	0.24	300	0.925

Table 3.4 Cases investigated for viscous gravity currents in a channel of finite depth.

Case 4.1 through Case 4.20 were selected to show the effects of the non-dimensional inlet length, w_0*, at various Reynolds numbers, Re. Case 4.21 through Case 4.30 were chosen to reveal the influence of the non-dimensional channel height, H* on the solutions at various Reynolds numbers. Similarly, Case 4.31 through Case 4.36 were selected to show the significance of the rate of loss of working fluid at the front of the current, α, at various Reynolds numbers. Case 4.37 through 4.42 were selected to study the effects of the non-dimensional outlet length, w_1*, at various Reynolds numbers. Case 4.43 through Case 4.48 were chosen to show the influence of the density ratio between the ambient fluid and the working fluid, ρ_r, at various Reynolds numbers. Finally, Case 4.49 was selected to reveal the effects of the non-dimensional length of the channel, L* + w_0*, on the solutions.

3.6.2 Estimation of errors in the computation

The accumulated volume per unit width of working fluid computed in the current again provides a measure of the error introduced by numerical dissipation. In each of the present cases, the time step and spatial resolution were carefully selected such that the error in the accumulated volume of working fluid is less than 1.5%.

3.6.3 General description of the results

The general features of the solutions for this model of viscous gravity currents in a channel of finite depth are very similar to those discussed in Section 3.5.3 for the model of viscous current in a channel of infinite depth. The bottom boundary layer of a gravity current in this model will increase with time and distance from the leading edge of the bottom wall, and the velocity of the front of the current will decelerate in the final stage. The inclusion of additional parameters in this model due to the finite channel height, such as the non-dimensional outlet length, w_1*, the non-dimensional channel height, H*, and the density ratio between the ambient fluid and the working fluid, ρ_r, will not change the general features that were associated with the model of viscous current in a channel of infinite depth. However, these factors do change the details of the

solutions. For example, the constant front speed, V_f^*, that can be achieved by a current is affected by these additional parameters.

3.6.4 Effects of the length of the inlet, w_0^*, on the solutions

The length of the inlet has a profound influence on the solutions. This is illustrated in Figure 3.45, which shows the non-dimensional constant front speed, V_f^*, as a function of Reynolds number, Re, for various non-dimensional inlet length, w_0^*. The constant front speed at a fixed Reynolds number can be seen to increase with w_0^*, and it is also observed to increase with Re for a fixed w_0^*. The difference between the constant front speeds at Re = 200 is about 20% for the range of w_0^* studied. This difference diminishes with increasing Reynolds number. The constant front speed for each w_0^* at Re = 5000 approaches that of an inviscid gravity current with the same channel height, which was shown in Section 3.4.5 to be independent of w_0^*.

3.6.5 Effects of the channel height, H*, on the solutions

Similar to the other length scales, the channel height also affects the constant front speed of a viscous gravity current. The non-dimensional constant front speed, V_f^*, as a function of Reynolds number, Re, is shown in Figure 3.46 for various channel heights. It can be seen from the figure that the limited channel height has a minimal effect on the constant front speed at low Reynolds number. However, it can also be observed that at high Reynolds number, the constant front speed increases with increasing channel height, and the effect of the channel height diminishes when $30 < H^*$. This is because when H* increases, the velocity of the excess ambient fluid being displaced from the channel decreases.

Since the experimental channel has a fixed geometry, H^*/w_0^* remains constant. As a result, a change in H* is always matched by the same percentage in w_0^*. By comparing Figure 3.45 and 3.46, it can be noticed that although V_f^* increases with H*, the reduction in V_f^* due to a change in w_0^* is larger than the increase in V_f^* due to the same percentage change in H* when H^*/w_0^* is fixed. Thus, it can be concluded that V_f^* decreases with increasing H*. This conclusion supports the experimental results shown in Figure 2.4.

3.6.6 Effects of the rate of loss of working fluid at the front of the current, α, on the solutions

In Figure 3.47, the non-dimensional constant front speed, V_f^*, as a function of Reynolds number is shown for various rates of loss of working fluid at the current front, α. By comparing the constant front speed at a fixed Reynolds number for different α, it can be concluded that α does not have a large impact on V_f^*.

3.6.7 Effects of the length of the outlet, w_1^*, on the solutions

The effect of the outlet length, w_1^*, on the solution is again found to be minimal. This is illustrated in Figure 3.48, which shows the non-dimensional constant front speed, V_f^*, as a function of Reynolds number, Re, for various non-dimensional outlet lengths, w_1^*. For the range of Reynolds numbers and outlet lengths studied, the outlet length has no apparent effect on the constant front speed.

3.6.8 Effects of the density ratio between the ambient fluid and the working fluid, ρ_r, on the solutions

Similar to the outlet length, the density ratio between the ambient fluid and the working fluid does not seem to have a major influence on the solution. Figure 3.49 shows the non-dimensional constant front speed, V_f^*, as a function of Reynolds number, Re, for various density ratios between the two fluids, ρ_r. For the range of Reynolds numbers and density ratios studied, which covers the range of parameters used in the experiments discussed in Chapter 2, there is no apparent influence of ρ_r on V_f^*.

3.7 Comparison of the model with experimental results

3.7.1 Comparison of individual features

Results obtained from the model of viscous gravity currents in a channel of finite depth are compared with experimental results to check the validity of the model. Using

that model, the time varying front position of gravity currents under various conditions were obtained. The results were compared with those obtained in the experiments as described in Chapter 2. An example is shown in Figure 3.50. The time varying front position of a gravity current at Re = 1486, d_{ref} = 1.68 cm, and t_{ref} = 0.177 s obtained from the model is compared with the experimental data in the figure. The front of the current in the model was found to spread at a faster rate than that observed in the experiment.

The non-dimensional constant front speed, V_f*, was obtained from plots similar to Figure 3.50 and the results are shown in Figure 3.51, together with the corresponding experimental data. It can be seen that the constant front speed measured in an experiment is roughly 15% lower than the corresponding value as determined by the model. It should be noted that the large variation of V_f* at low Reynolds number that was observed in the experiments is also observed in the results obtained from the model. As a result, it can be concluded that V_f*strongly depends on the inlet length, w_0*, at low Reynolds numbers. On the other hand, the value of V_f* is at best a very weak function of w_0* at high Reynolds number, since Figure 3.51 shows that there is very little variation of V_f* for 1000 < Re for the results obtained both from the model and from the experiments.

The non-dimensional depth of the current, h*, as well as the non-dimensional boundary layer thickness, δ*, at the same non-dimensional distance, x*, and the same Reynolds number, Re, as the experiment shown in Figure 2.24 were obtained. The results are compared in Figure 3.52, which shows h* and δ* as a function of t* at x* = 52 and Re = 2105. It can be observed from the figure that the current depth obtained from the model is lower than that from the experiment, while the boundary layer thickness is slightly higher than that found in the experiments. However, the rates of increase of both the current depth and the boundary layer thickness obtained from the model compare favorably with those measured in the experiment.

Figure 3.53 shows the corresponding non-dimensional time varying current velocity, U_w*, at x* = 52 and Re = 2105. The velocity obtained from the model is observed to be larger than that measured in the experiment. This observation is consistent with the observation noted above for Figures 3.50 and 3.52. On the other hand, the decreasing trend of the velocity is again captured by the model, and the

percentage difference between the result obtained from the experiments and that from the model remains roughly constant with time.

3.7.2 Discussions of possible sources for the discrepancies

The discrepancy between the results obtained from the model and those found in the experiments can be partially explained by Figure 3.54. Figure 3.54 shows the same plot as in Figure 2.13 and compares it with the corresponding result obtained from the model. It can be observed from the figure that the non-dimensional current depth, h*, decreased with distance near the source in both cases. However, an internal jump was observed in the experiment, while no internal jump was observed in the result obtained from the model. This discrepancy arises because there is no provision in the model that enforces the creation of an internal jump. Owing to the lack of the internal jump, the current depth downstream of the jump as obtained from the model is lower than that measured in the experiment, and the corresponding velocity is higher than that in the experiment. As a result, the boundary layer thickness obtained from the model is also larger than that measured in the experiment. From time varying front position measurements, the non-dimensional front position, x_f*, for the experiment at t* = 200 is at x* = 160. On the other hand, it can be observed from the figure that due to the faster front speed of the gravity current calculated in the model, the front has already hit the downstream end wall, the reflected bore is moving upstream, and the position of the reflected bore, x_r*, is already at x* = 160.

It should be noted that other shortcomings in the model might also have contributed to the discrepancy between the experimental results and the model. The most prominent effect is the three-dimensionality of the head at the current front caused by both the shear on top and the overrun ambient fluid underneath. Moreover, since the length of the channel used in the experiment is much larger than the width of the channel, viscous effects of the side walls might also be important. However, their effects on the solution should pale in comparison to the influence exerted by the internal jump.

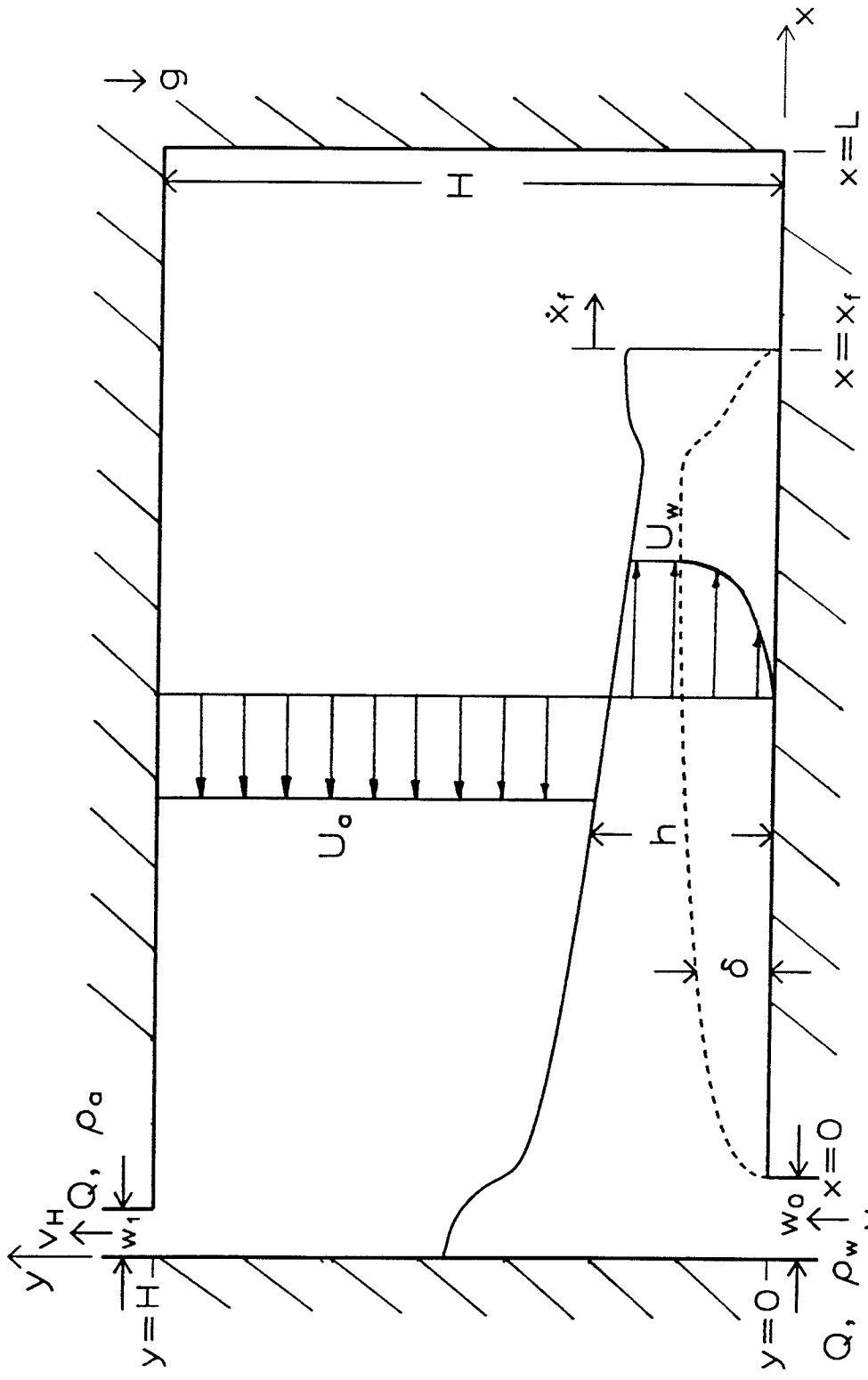

Figure 3.1 Schematic diagram of the model for adiabatic gravity currents in a horizontal channel.

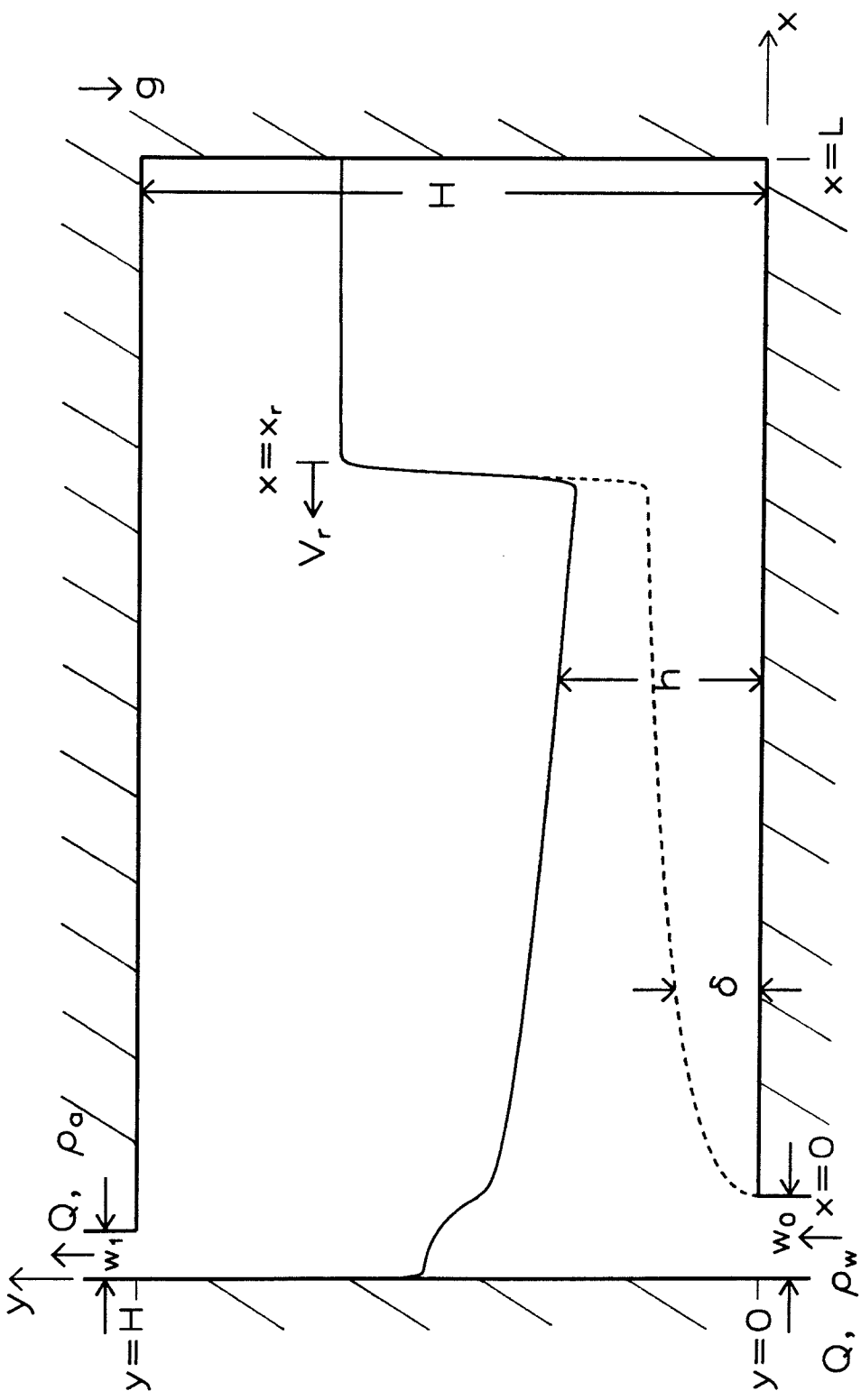

Figure 3.2 Schematic diagram of the model for the reflected bore of adiabatic gravity currents in a horizontal channel.

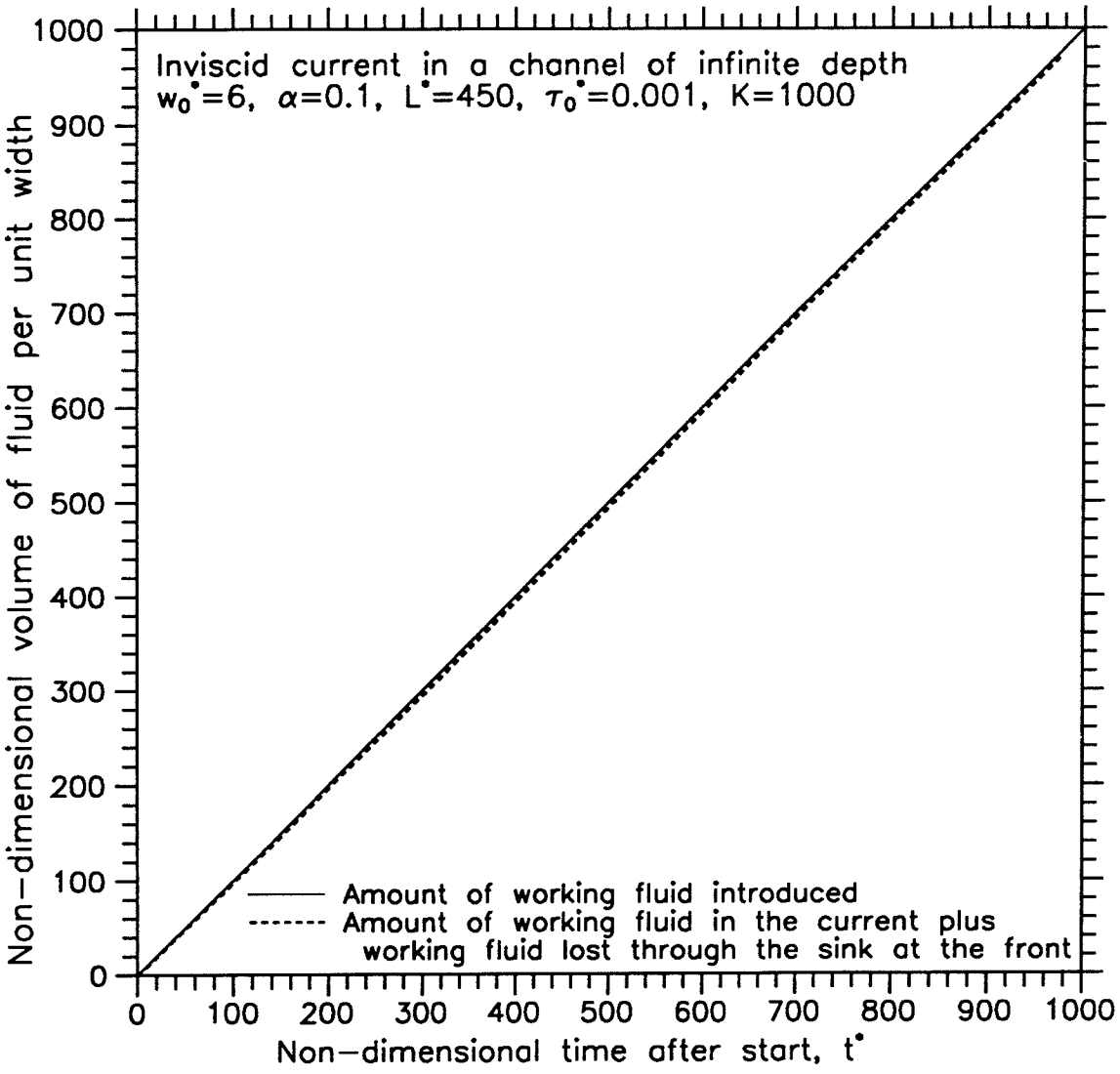

Figure 3.3 Volume of the layer of working fluid per unit width as a function of time for Case 1.7.

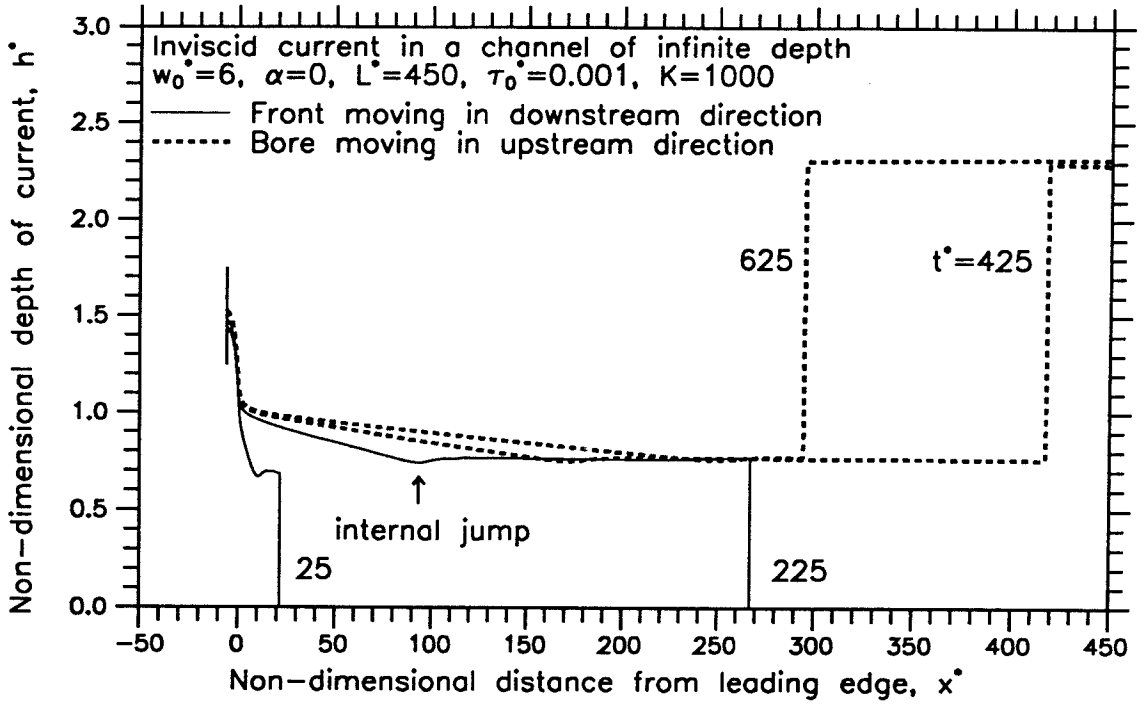

Figure 3.4a Depth of current as a function of distance from the leading edge at various times for Case 1.2.

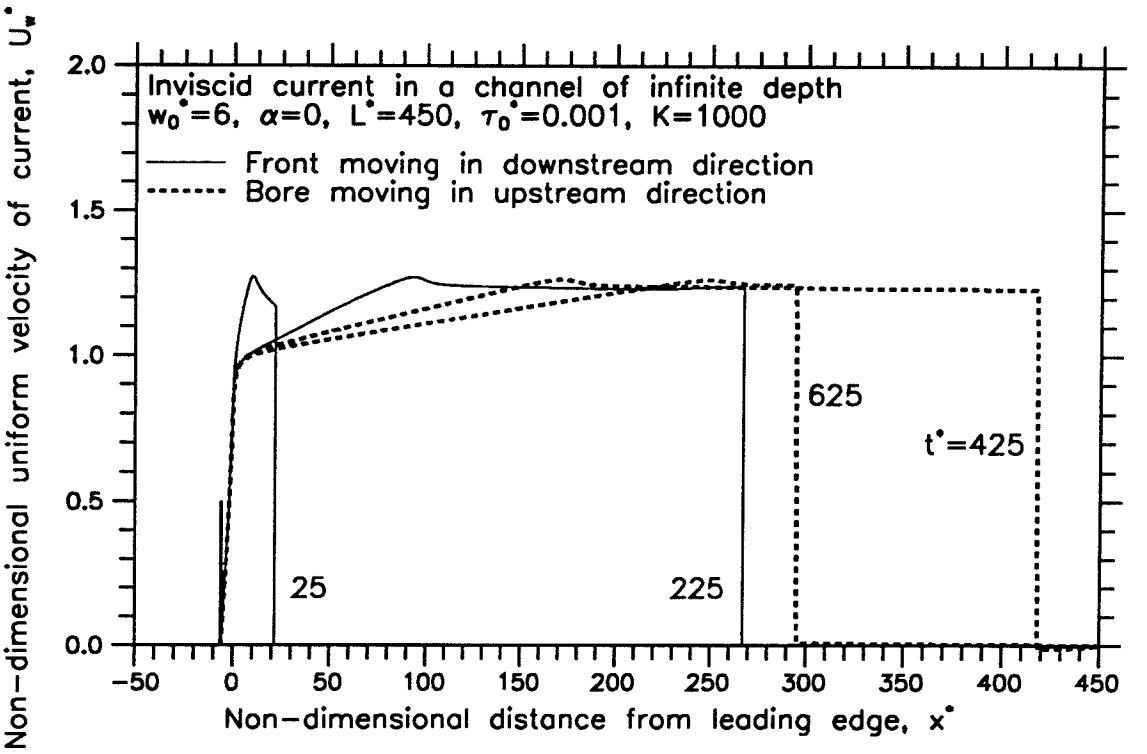

Figure 3.4b Uniform velocity of the working fluid as a function of distance from the leading edge at various times for Case 1.2.

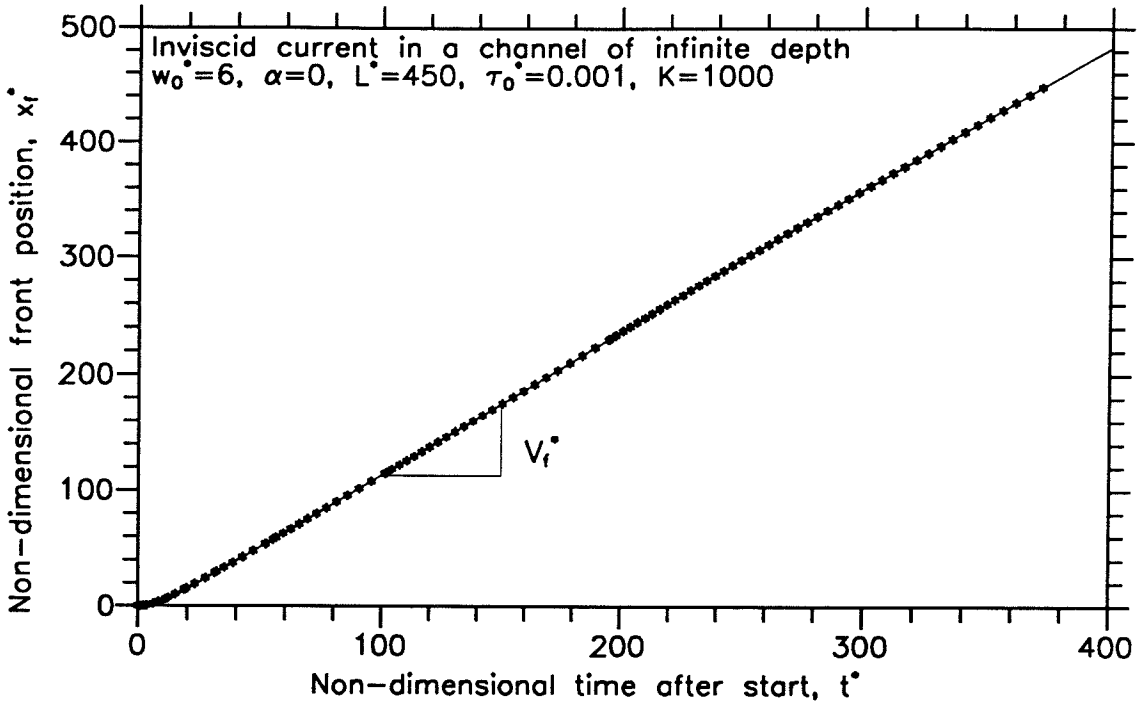

Figure 3.5a Front position as a function of time for Case 1.2.

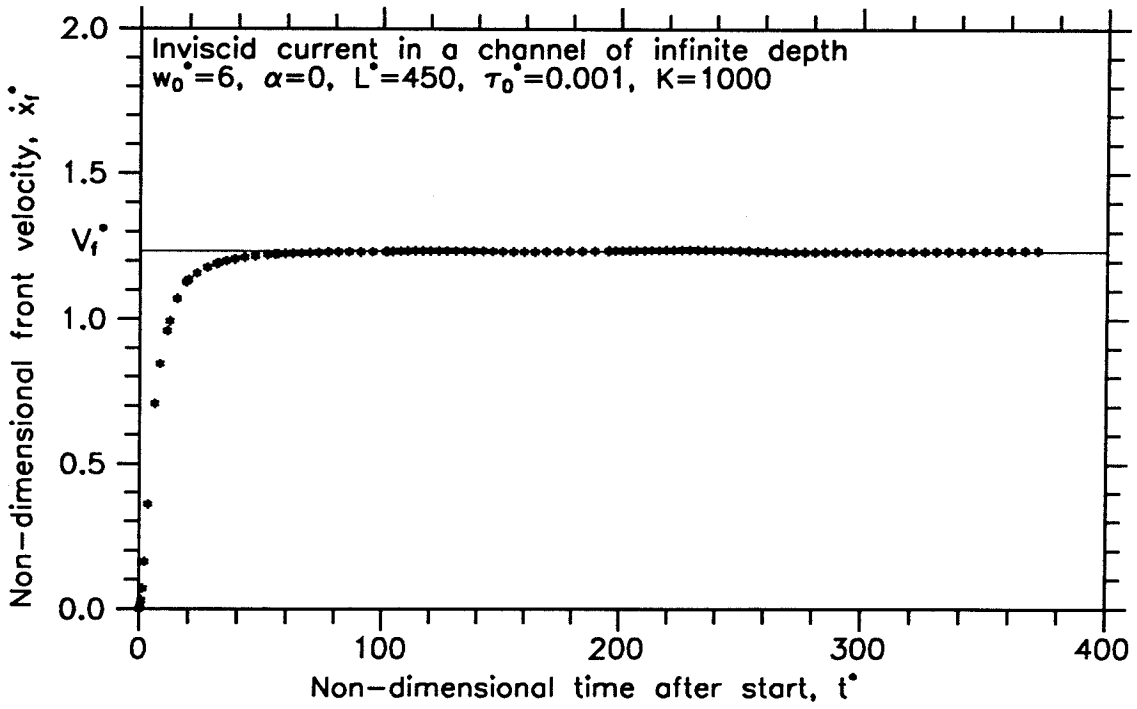

Figure 3.5b Front velocity as a function of time for Case 1.2.

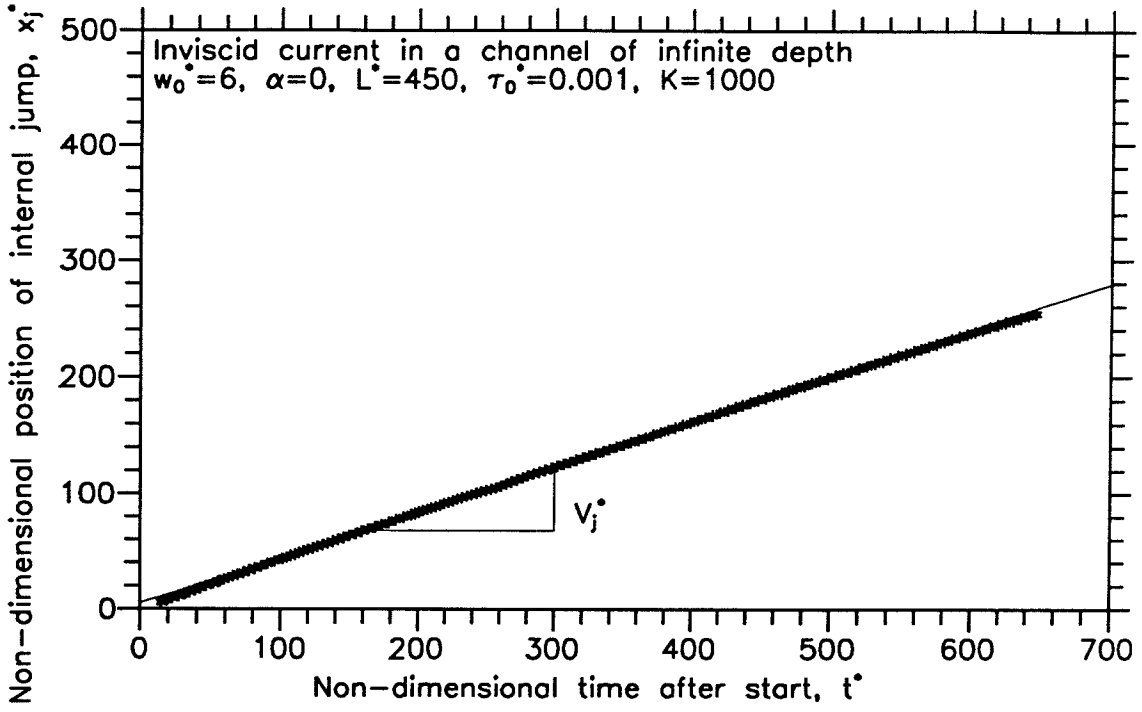

Figure 3.6a Position of the internal jump as a function of time for Case 1.2.

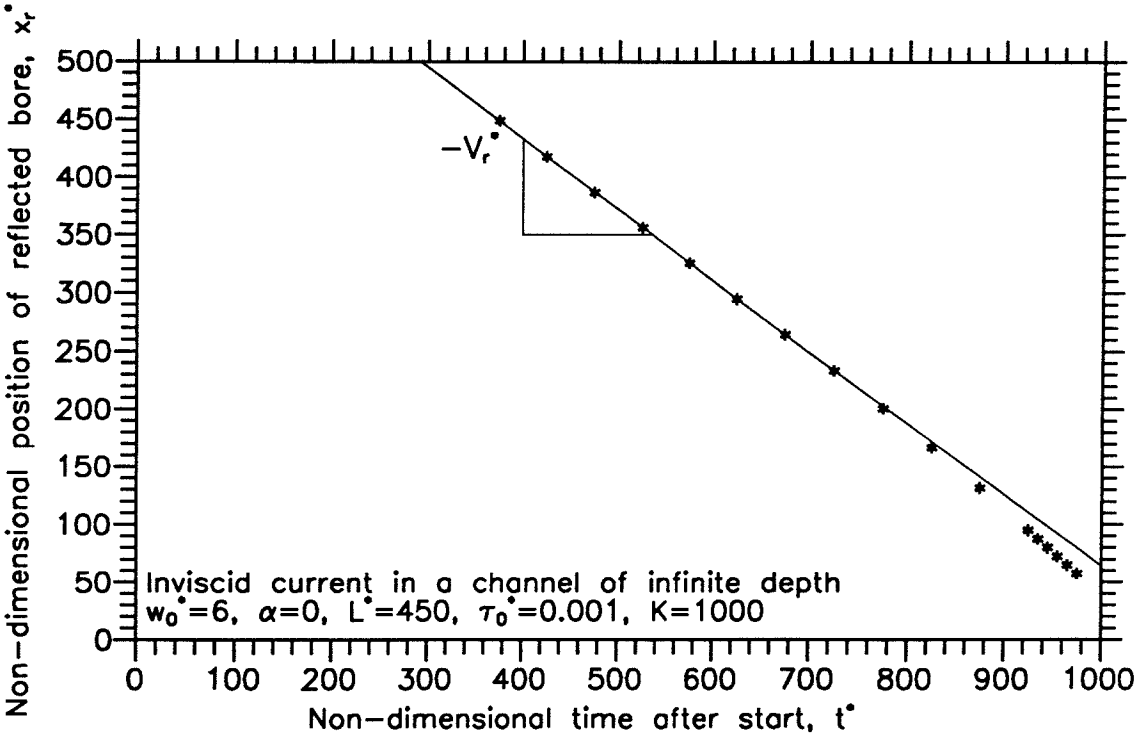

Figure 3.6b Position of the reflected bore as a function of time for Case 1.2.

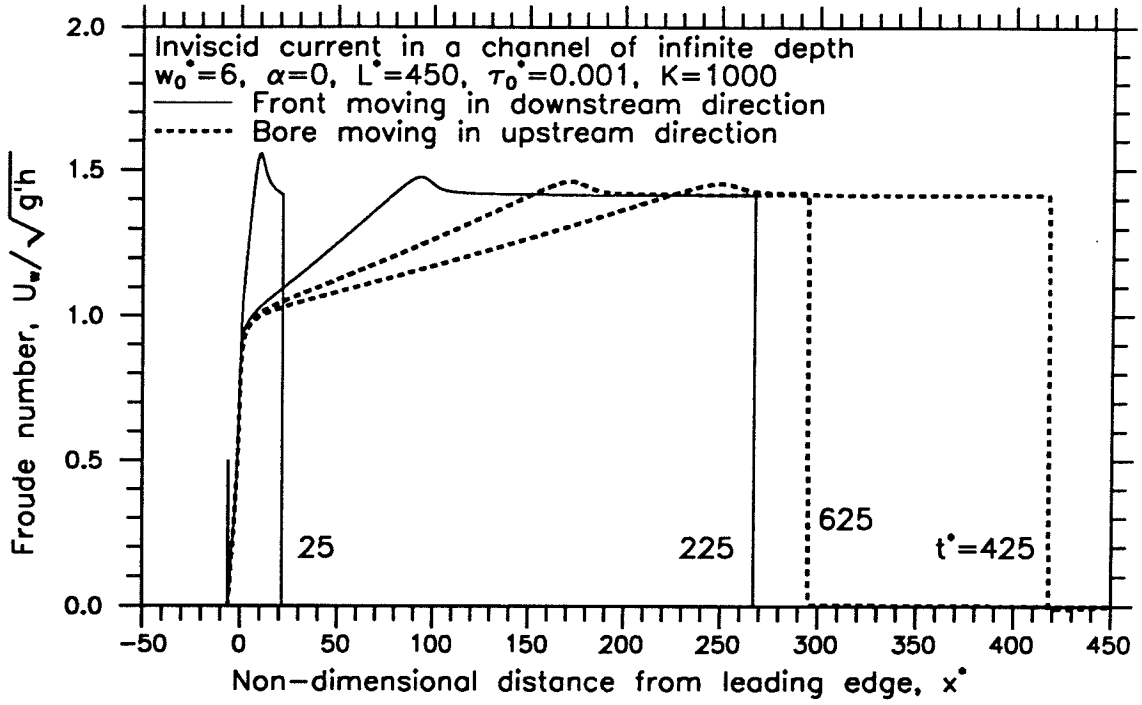

Figure 3.7a Froude number of current as a function of distance from the leading edge for Case 1.2 at various times.

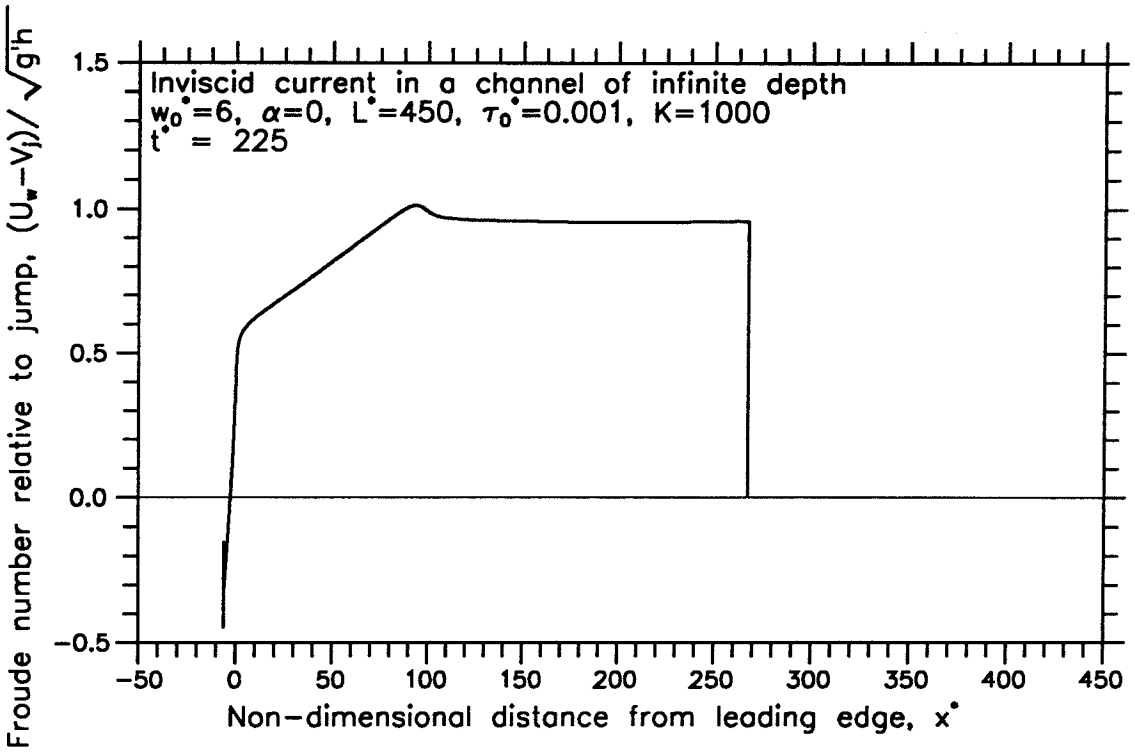

Figure 3.7b Froude number of current relative to internal jump as a function of distance from the leading edge for Case 1.2 at t^*=225.

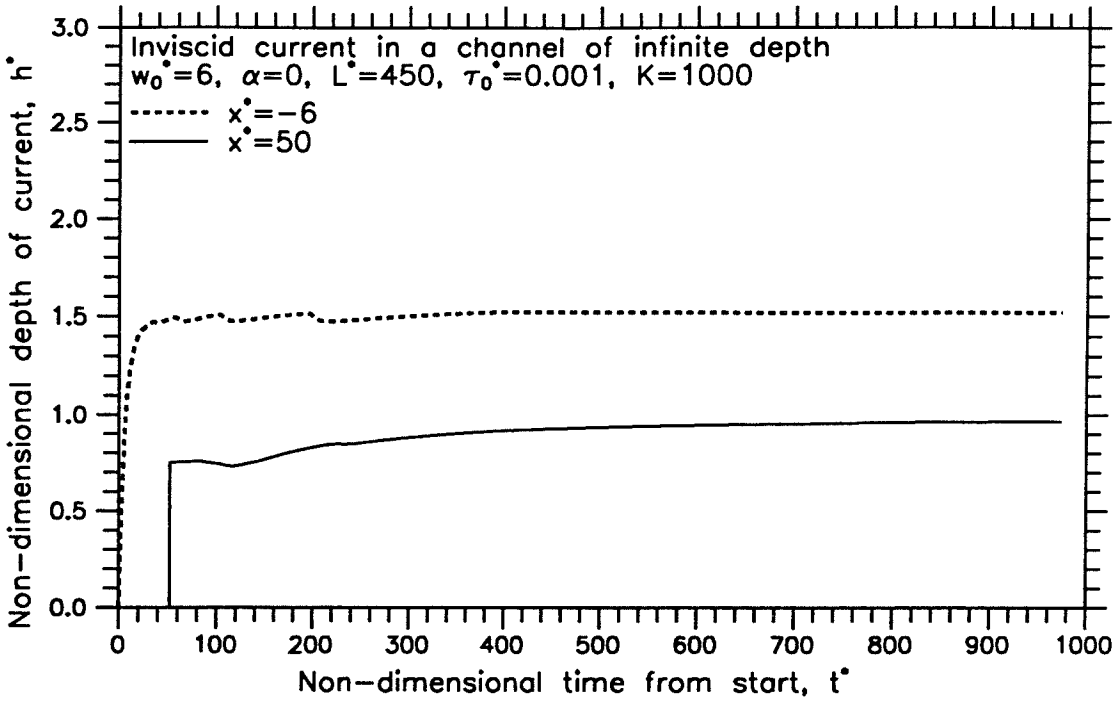

Figure 3.8a Depth of current as a function of time from start at various distances from the leading edge for Case 1.2.

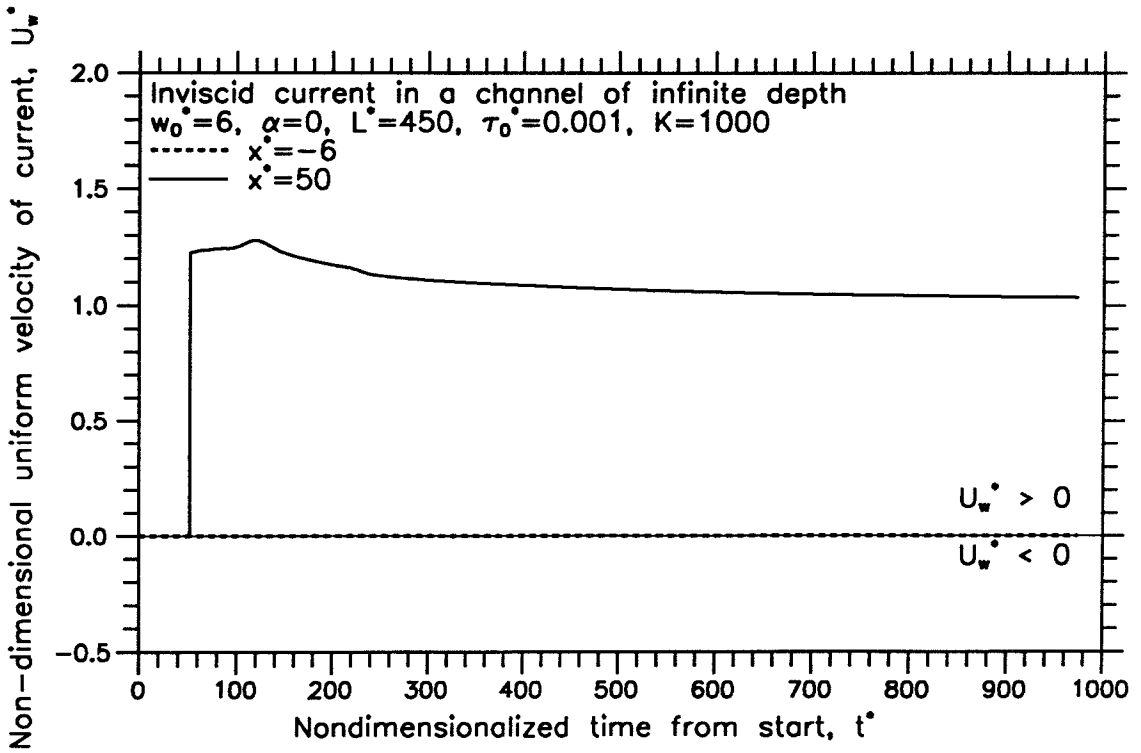

Figure 3.8b Uniform velocity of the current as a function of time from start at various distances from the leading edge for Case 1.2.

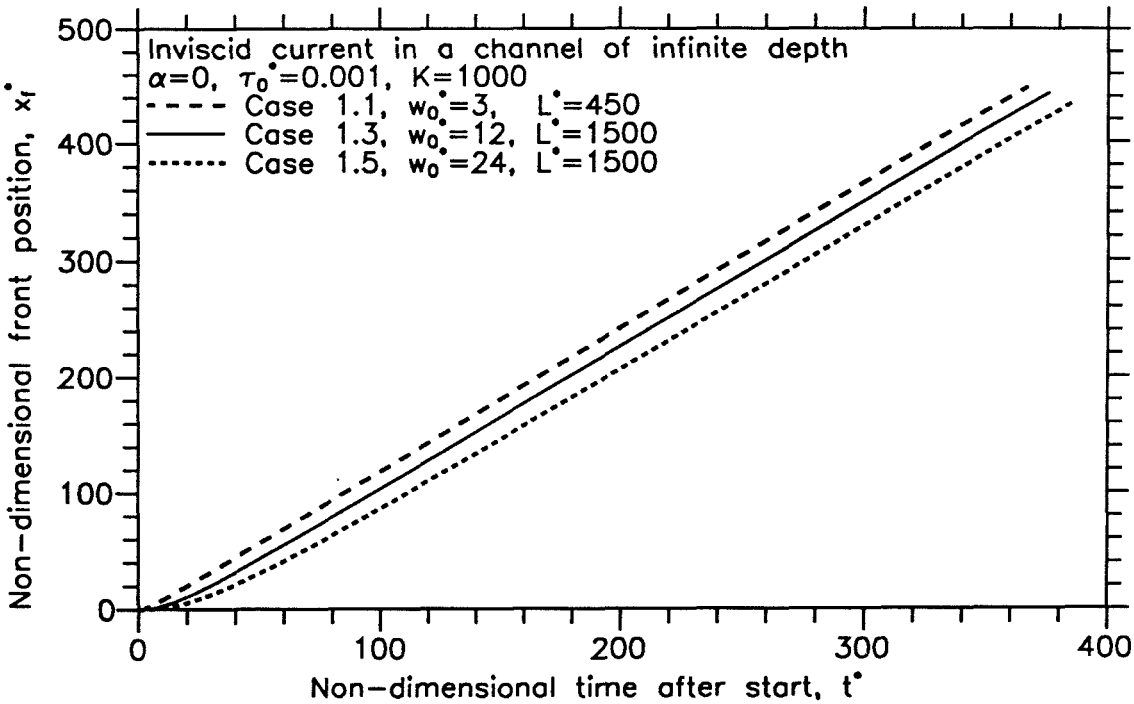

Figure 3.9a Front position as a function of time for Cases 1.1, 1.3, 1.5.

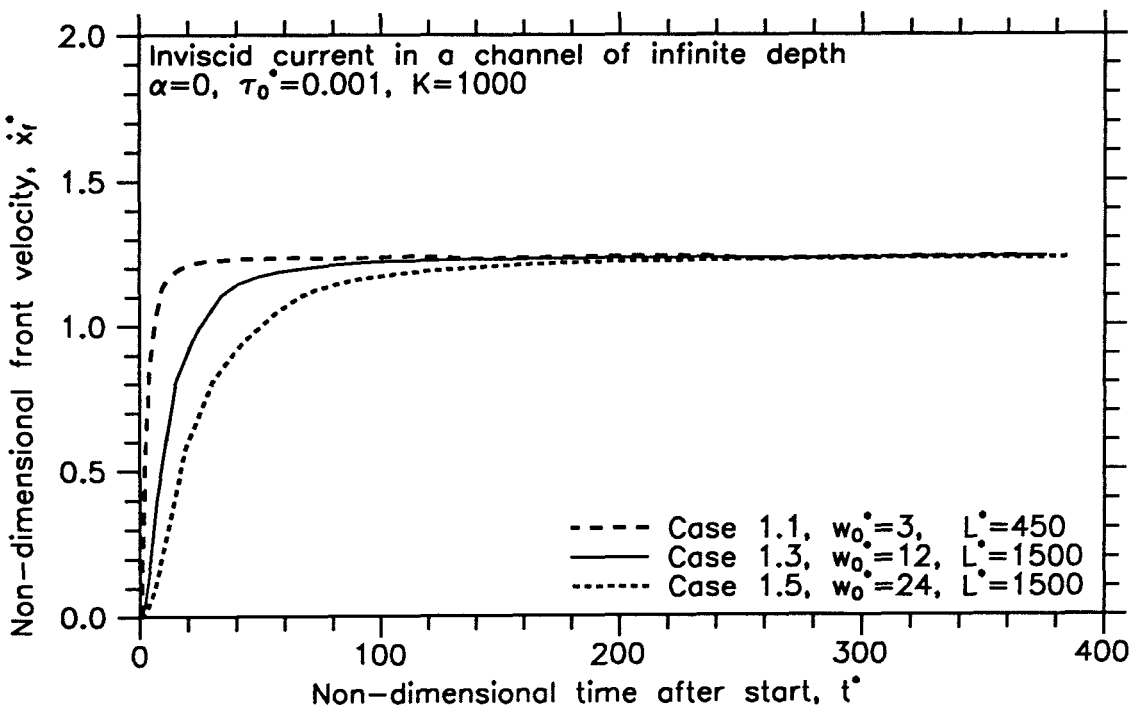

Figure 3.9b Front velocity as a function of time for Cases 1.1, 1.3, and 1.5.

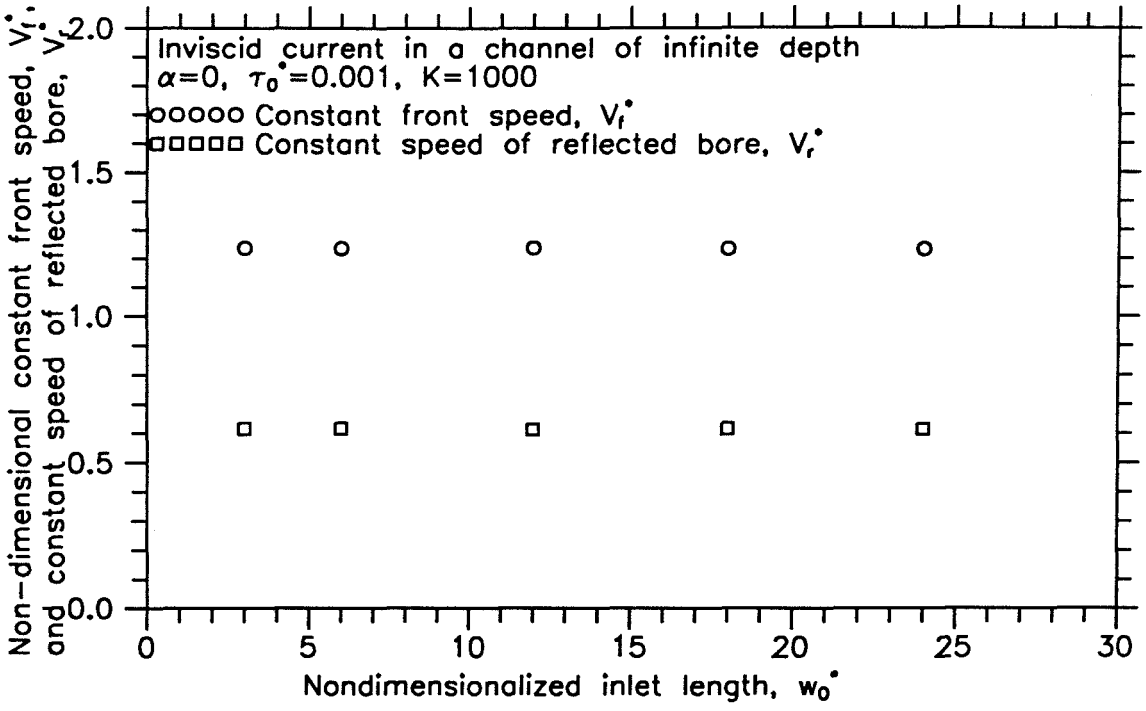

Figure 3.10a Constant front speed and constant speed of the reflected bore as a function of inlet length for cases with no loss at the front.

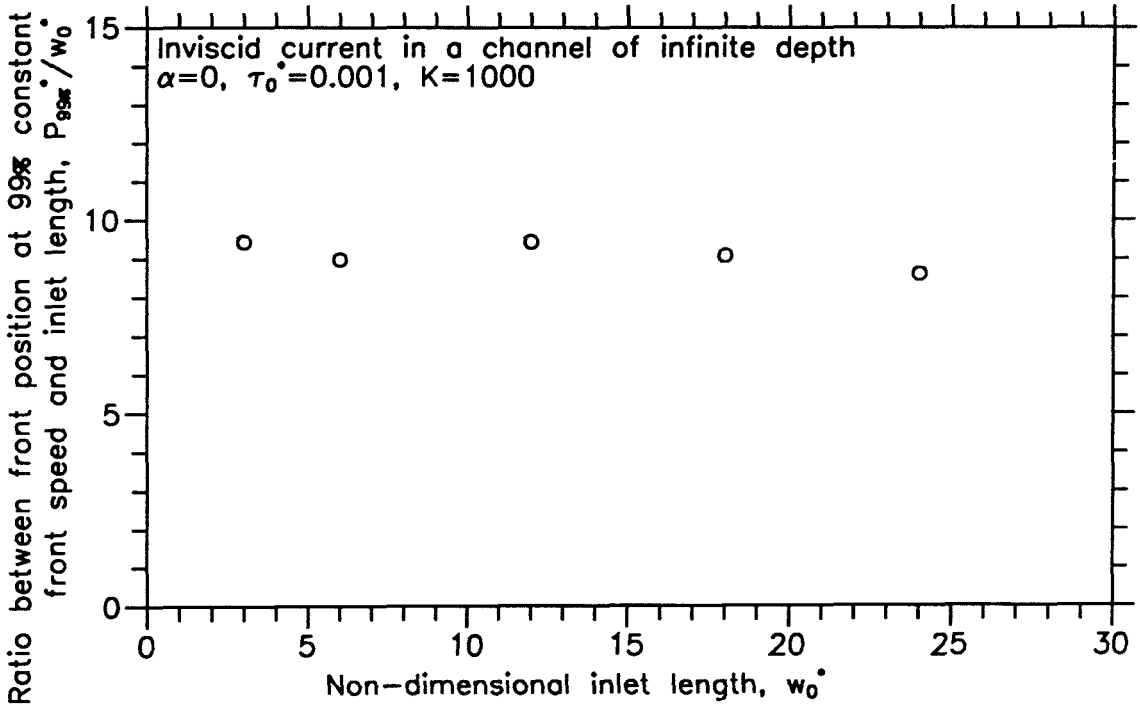

Figure 3.10b Ratio between front position at 99% constant front speed and inlet length as a function of inlet length for cases with no loss at the front.

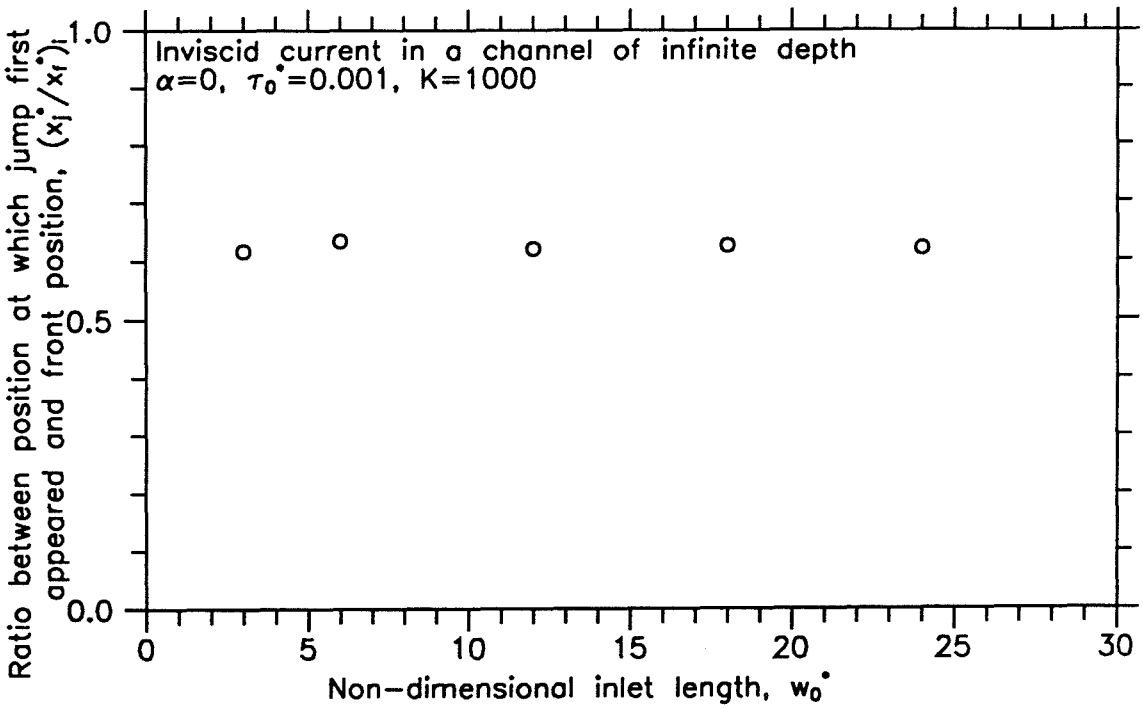

Figure 3.11a Ratio between position at which internal jump first appeared and the corresponding front position as a function of inlet length for cases with no loss of working fluid at the front.

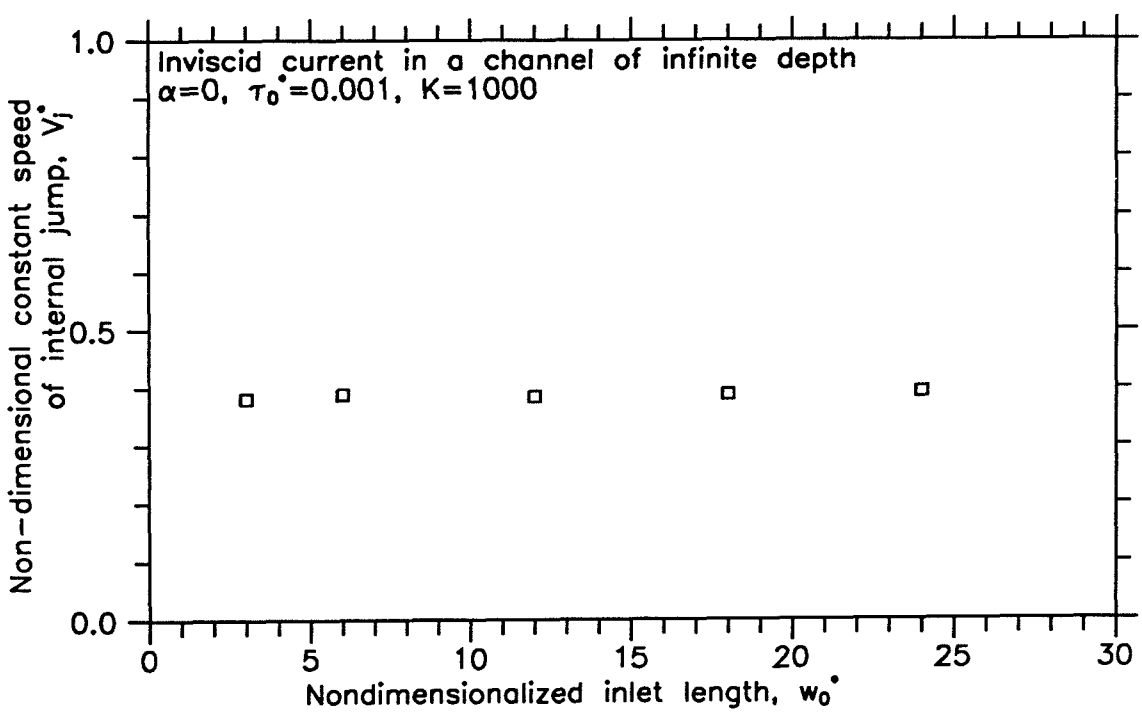

Figure 3.11b Constant speed of internal jump as a function of inlet length for cases with no loss of working fluid at the front.

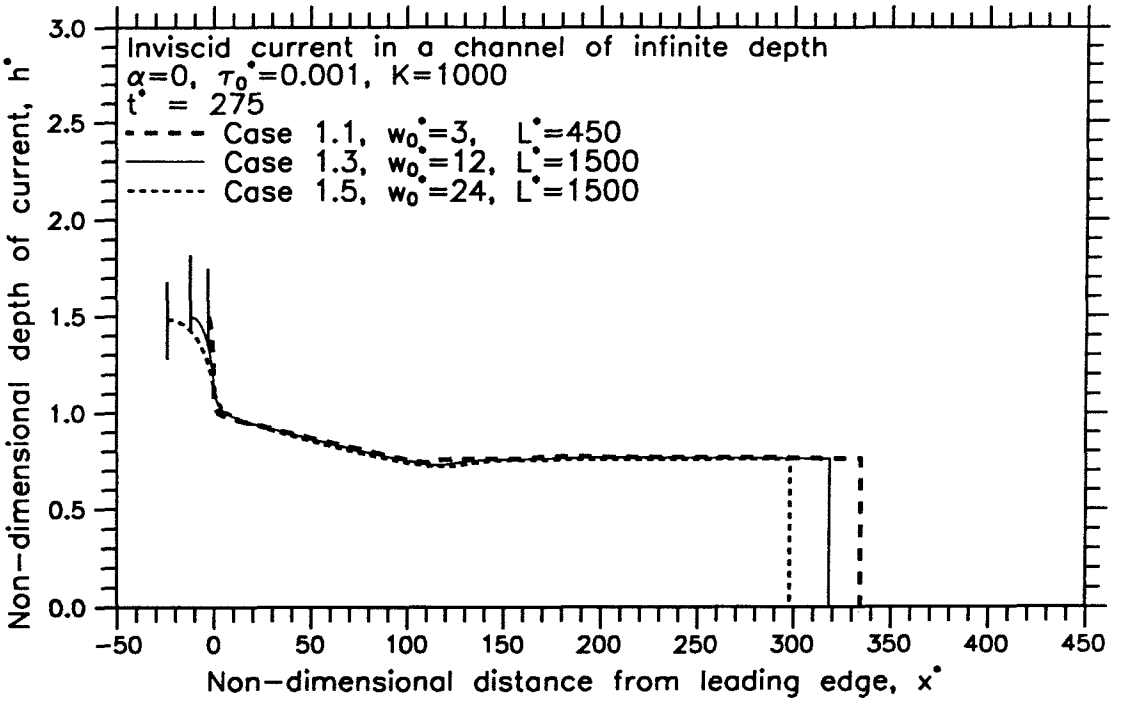

Figure 3.12a Depth of current as a function of distance from the leading edge for Cases 1.1, 1.3, and 1.5 at $t^*=275$.

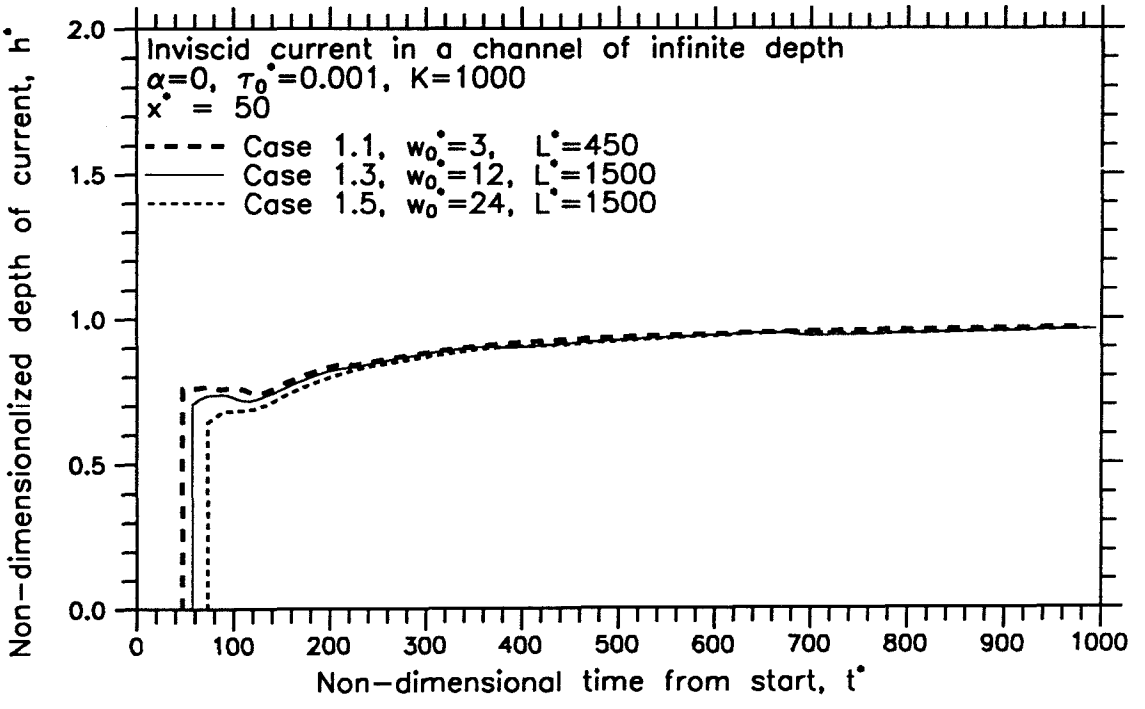

Figure 3.12b Depth of current as a function of time from start for Cases 1.1, 1.3, and 1.5 at $x^*=50$.

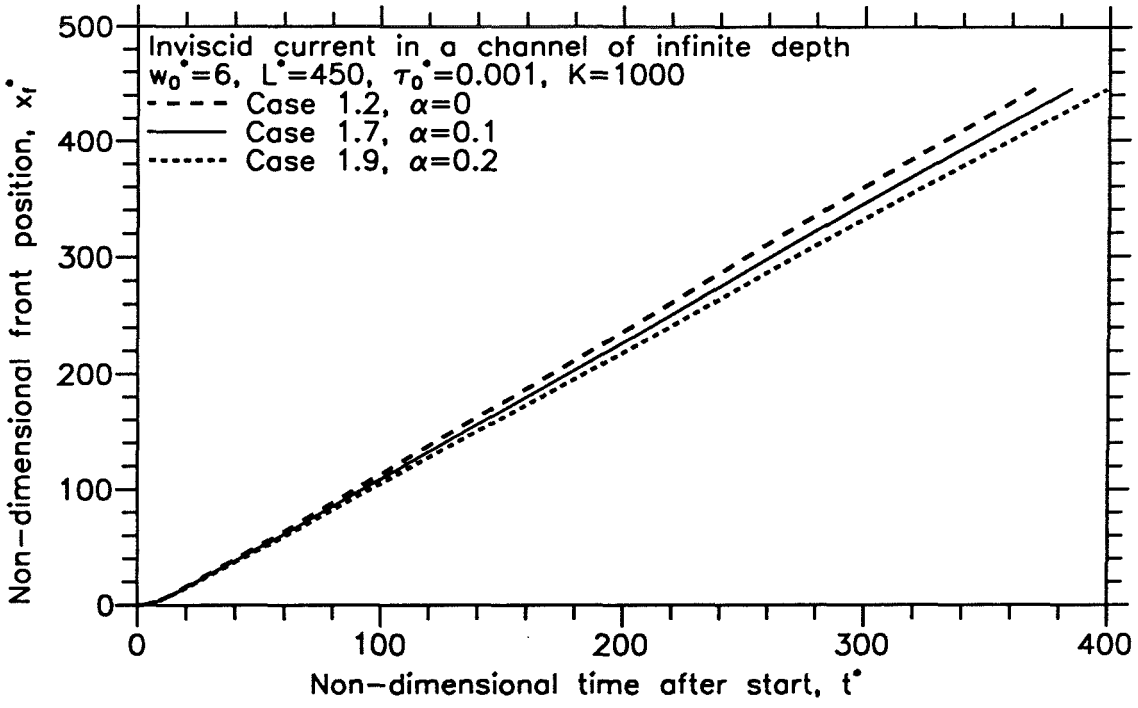

Figure 3.13a Front position as a function of time for Cases 1.2, 1.7, and 1.9.

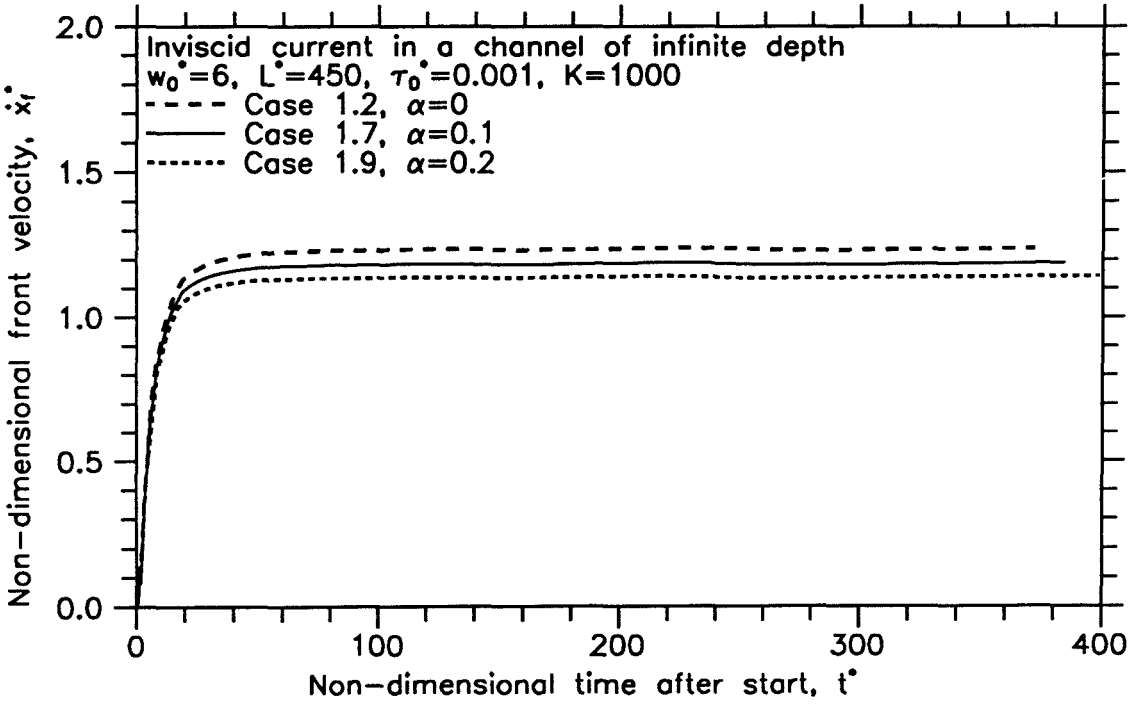

Figure 3.13b Front velocity as a function of time for Cases 1.2, 1.7, and 1.9.

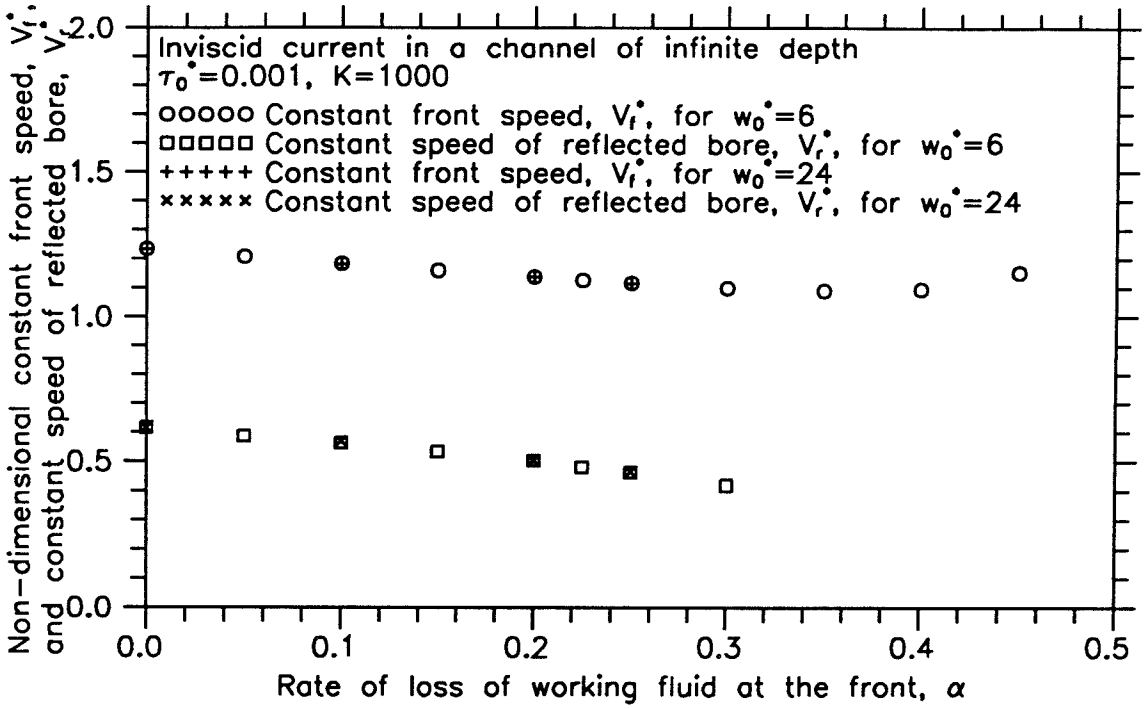

Figure 3.14a Constant front speed and constant speed of the reflected bore as a function of inlet length for cases with loss of working fluid at the front.

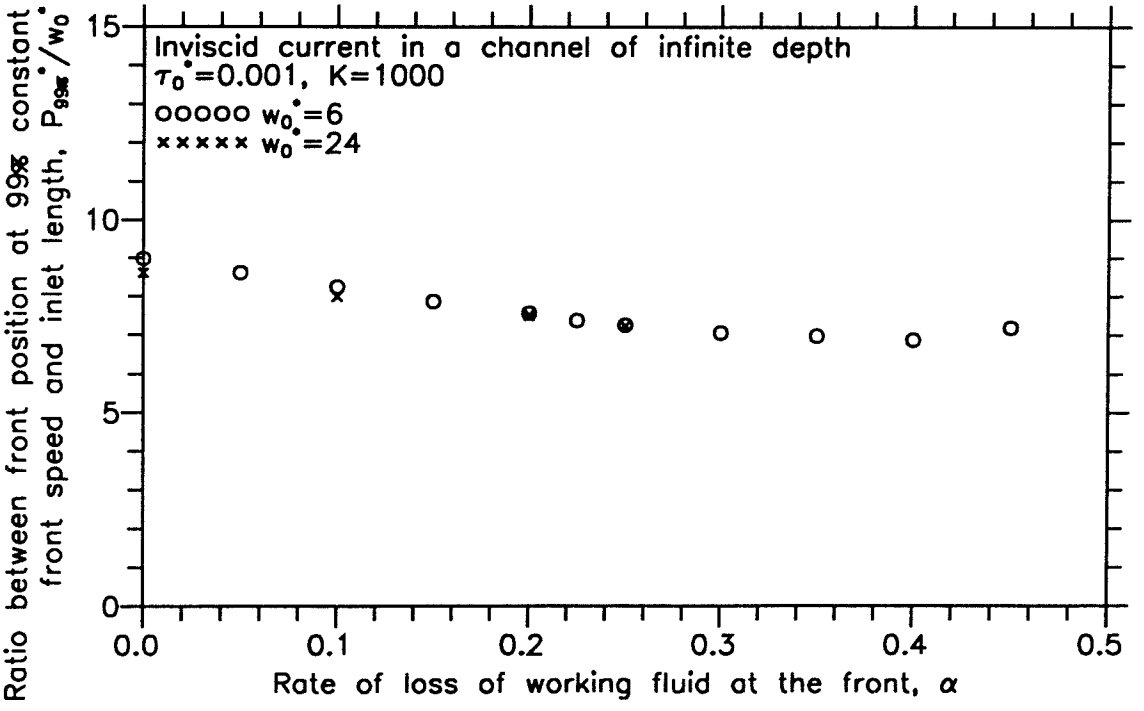

Figure 3.14b Ratio between front position at 99% constant front speed and inlet length as a function of inlet length for cases with loss at the front.

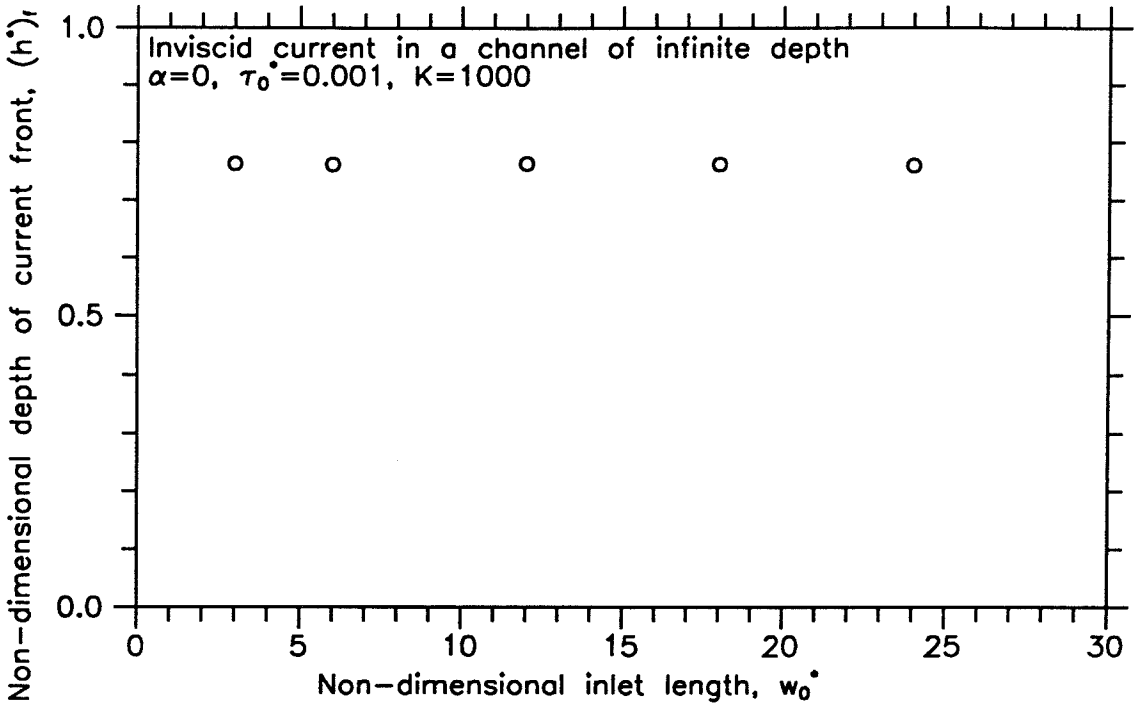

Figure 3.15a Depth of current at the front as a function of inlet length.

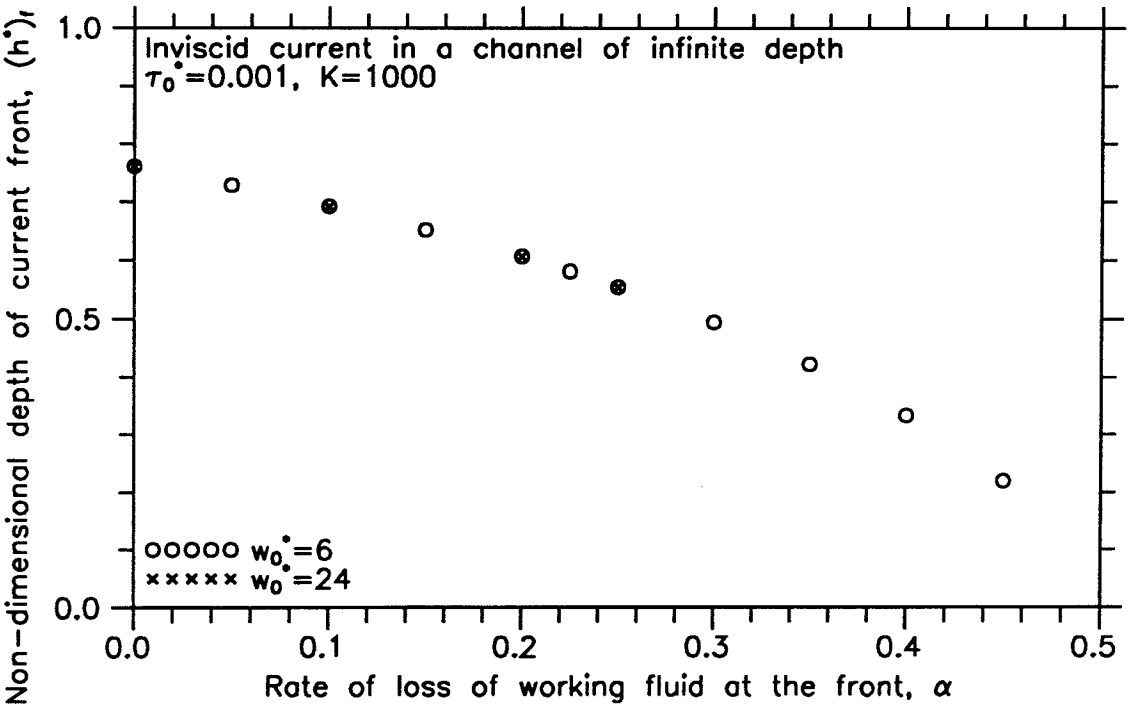

Figure 3.15b Depth of current at the front as a function of the rate of loss of working fluid through the sink at the front of the current.

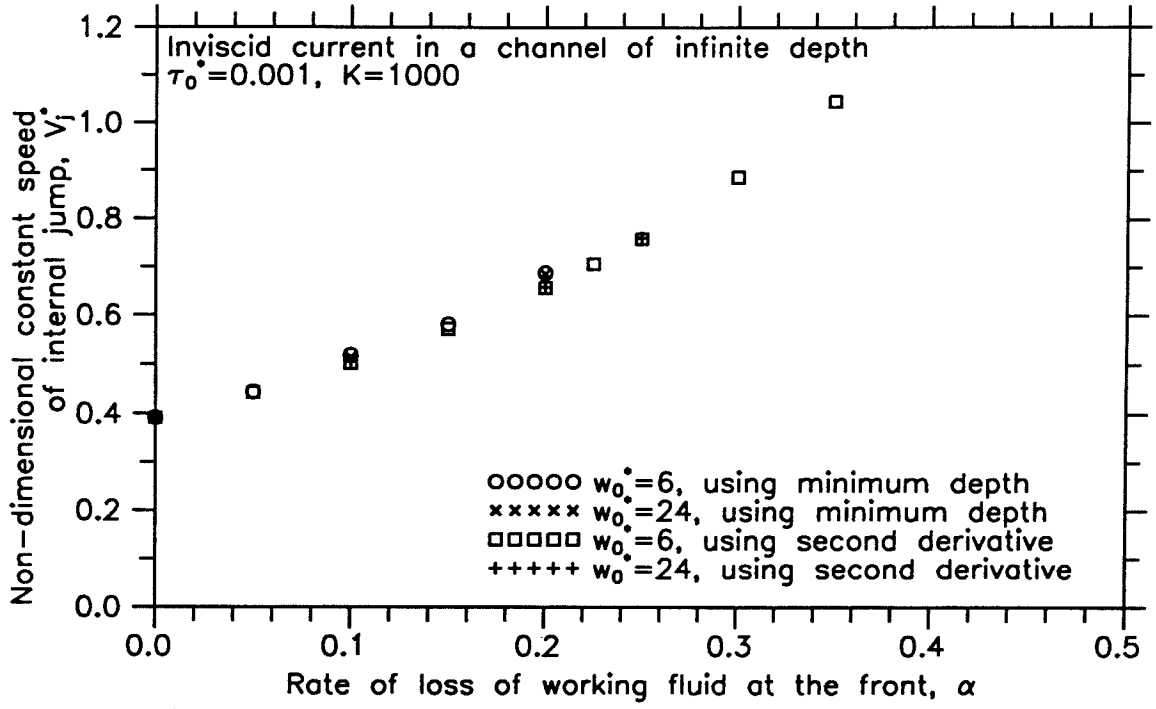

Figure 3.16a Constant speed of internal jump as a function of rate of loss of working fluid through the sink at the front of the current.

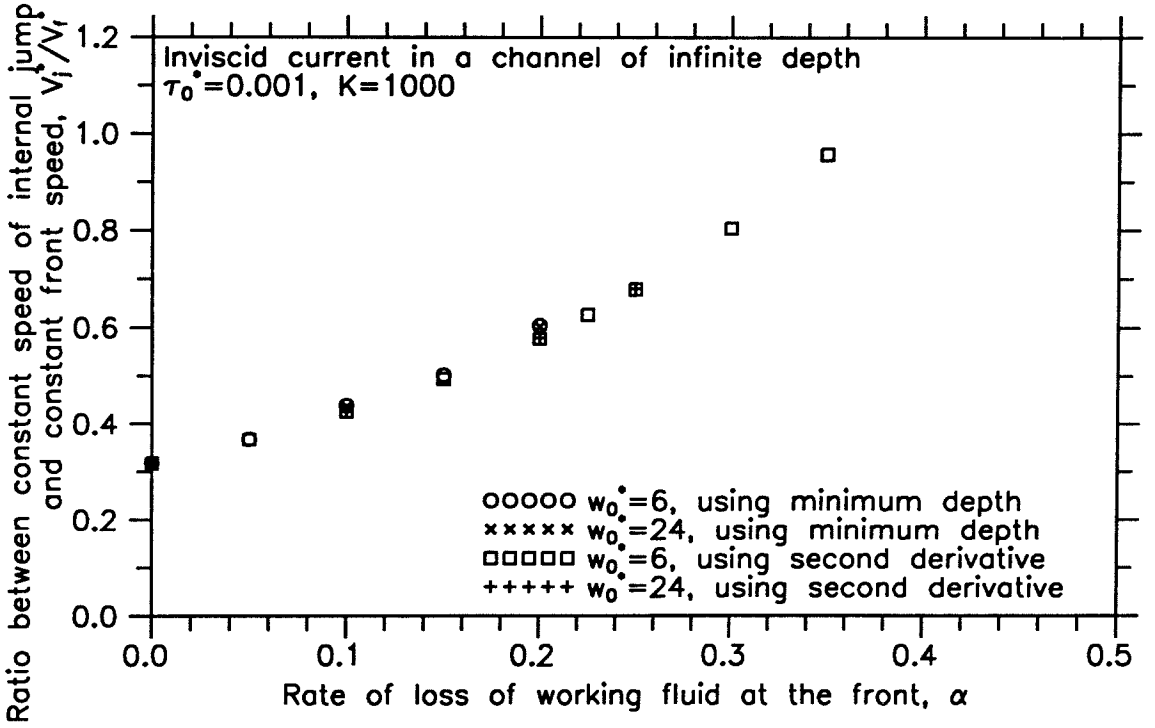

Figure 3.16b Ratio between constant speed of internal jump and constant front speed as a function of rate of loss of working fluid through the sink at the front of the current.

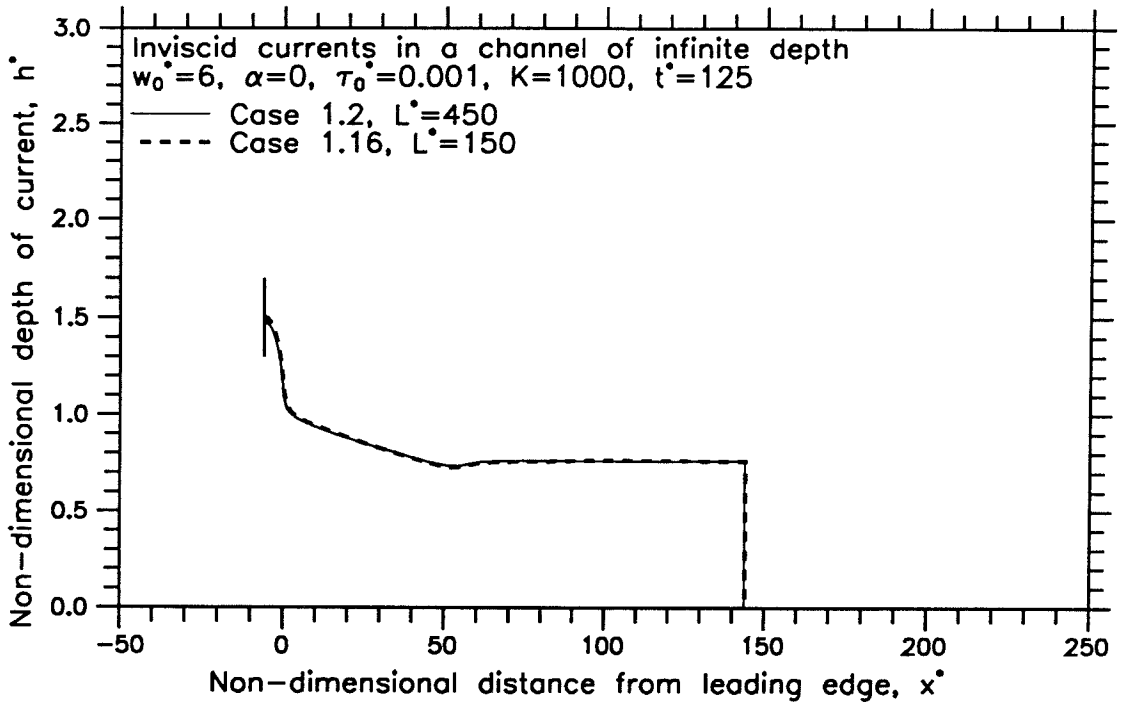

Figure 3.17a Depth of current as a function of distance from the leading edge for Cases 1.2 and 1.16 at t^*=125.

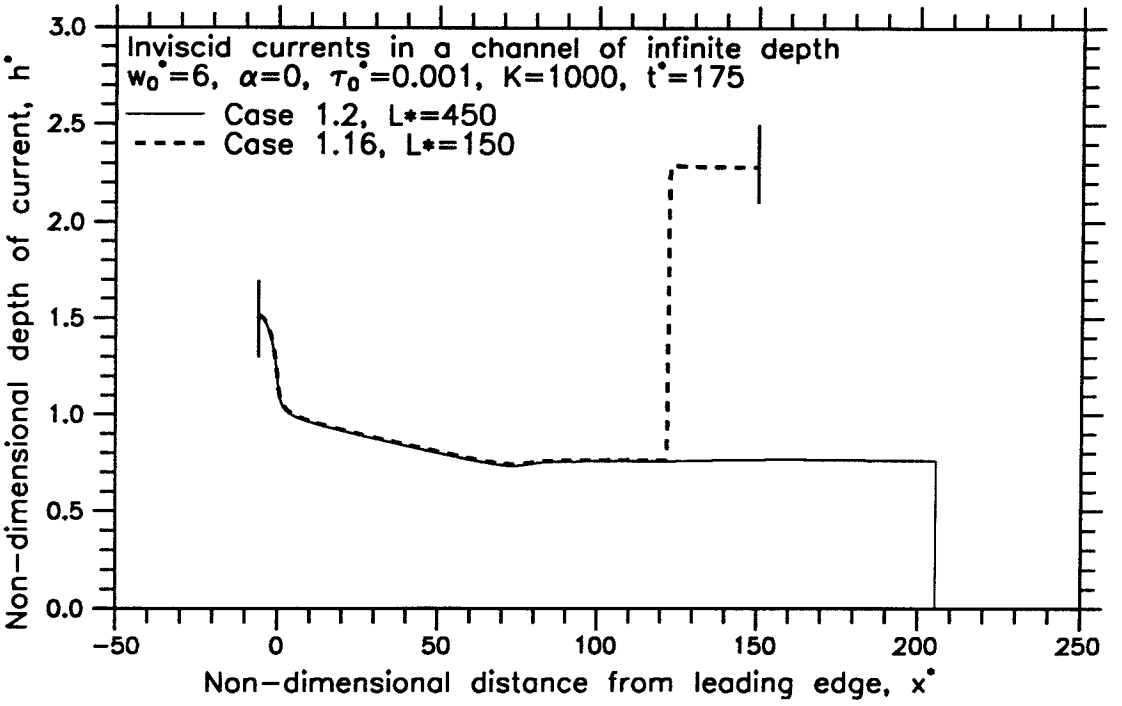

Figure 3.17b Depth of current as a function of distance from the leading edge for Cases 1.2 and 1.16 at t^*=175.

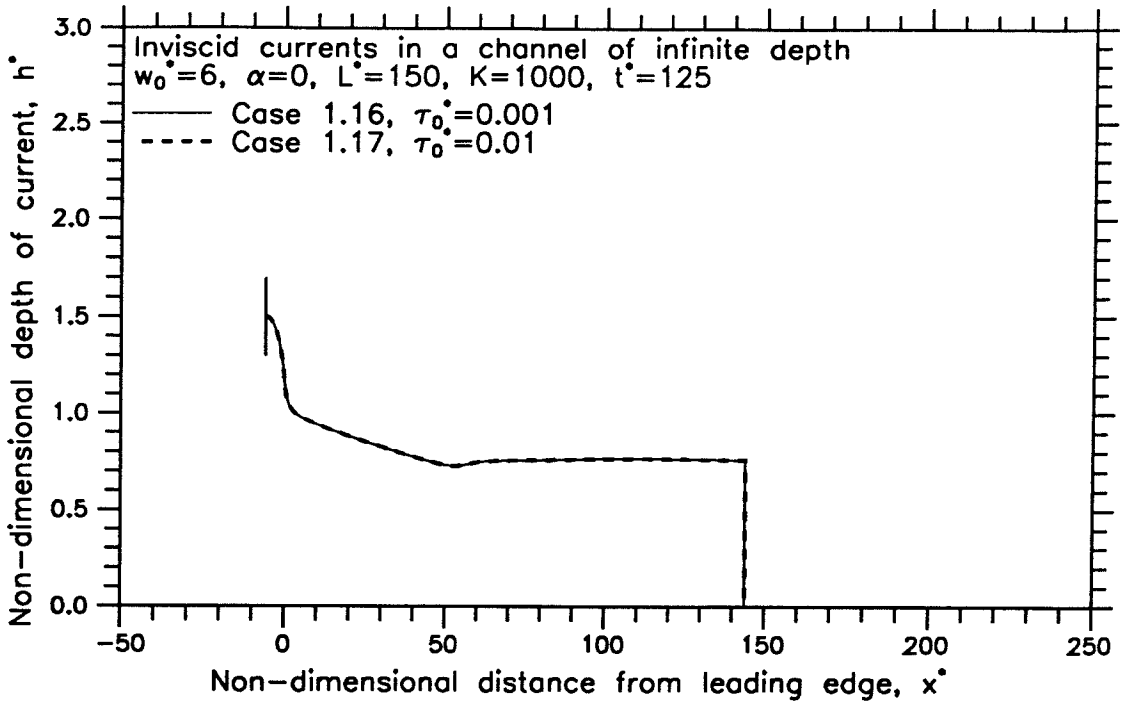

Figure 3.18a Depth of current as a function of distance from the leading edge for Cases 1.16 and 1.17 at t^*=125.

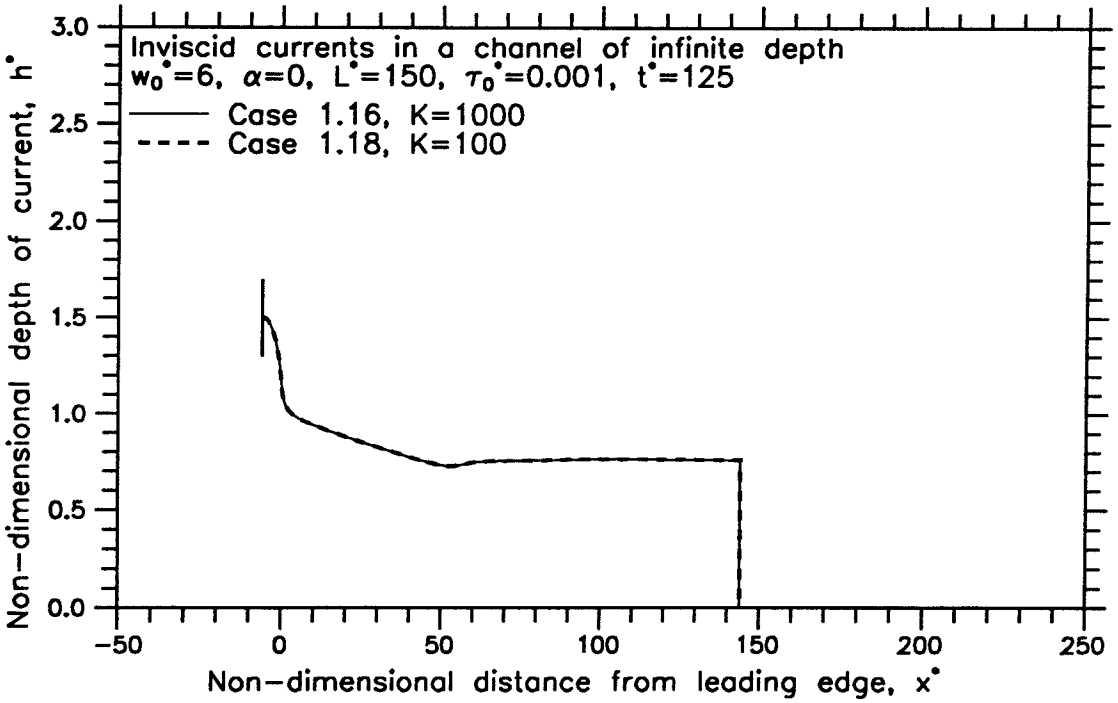

Figure 3.18b Depth of current as a function of distance from the leading edge for Cases 1.16 and 1.18 at t^*=125.

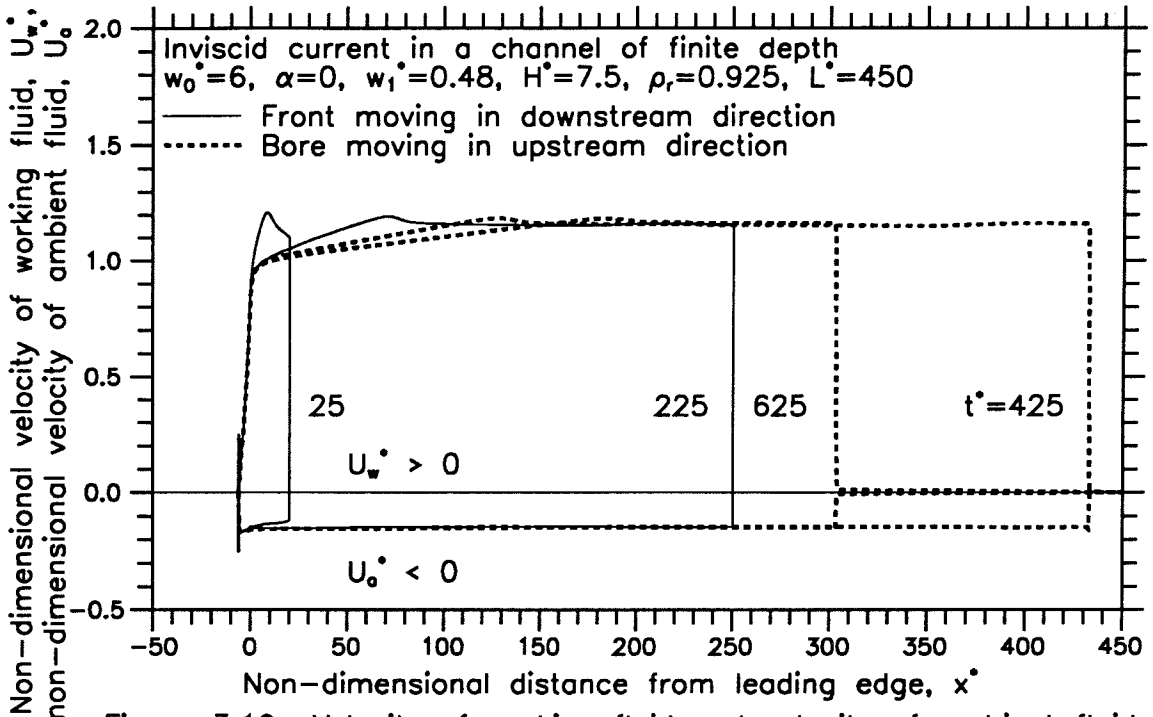

Figure 3.19a Velocity of working fluid and velocity of ambient fluid as a function of distance from the leading edge at various times for Case 2.1.

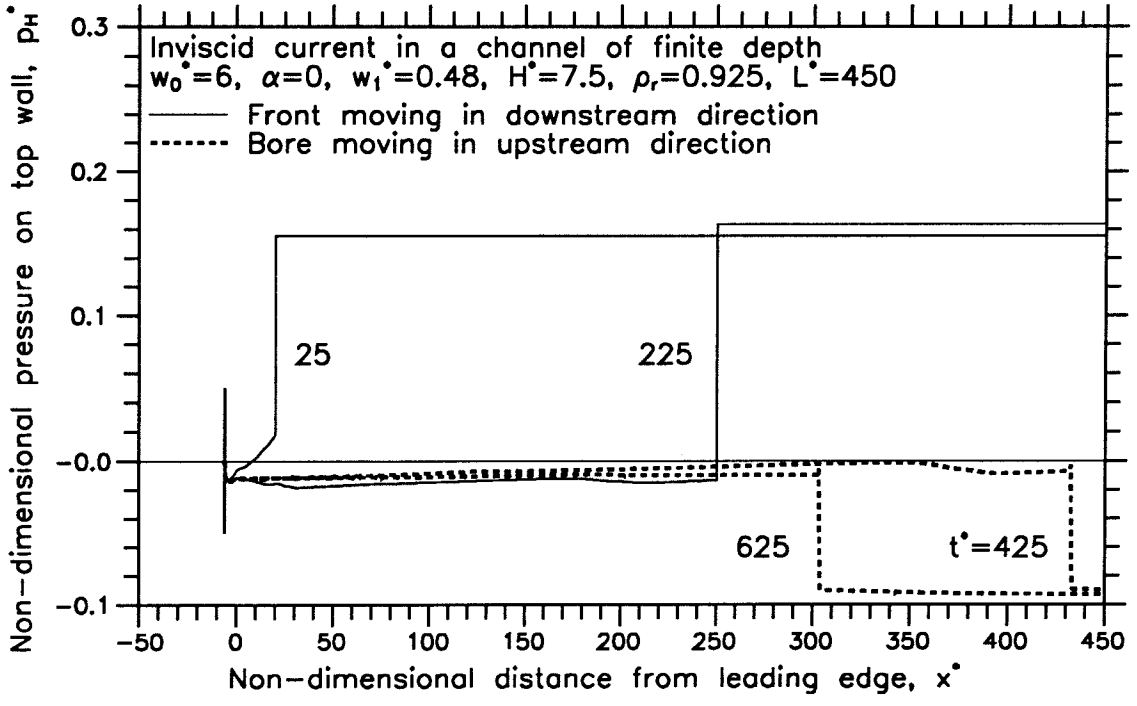

Figure 3.19b Pressure on the top wall as a function of distance from the leading edge at various times for Case 2.1.

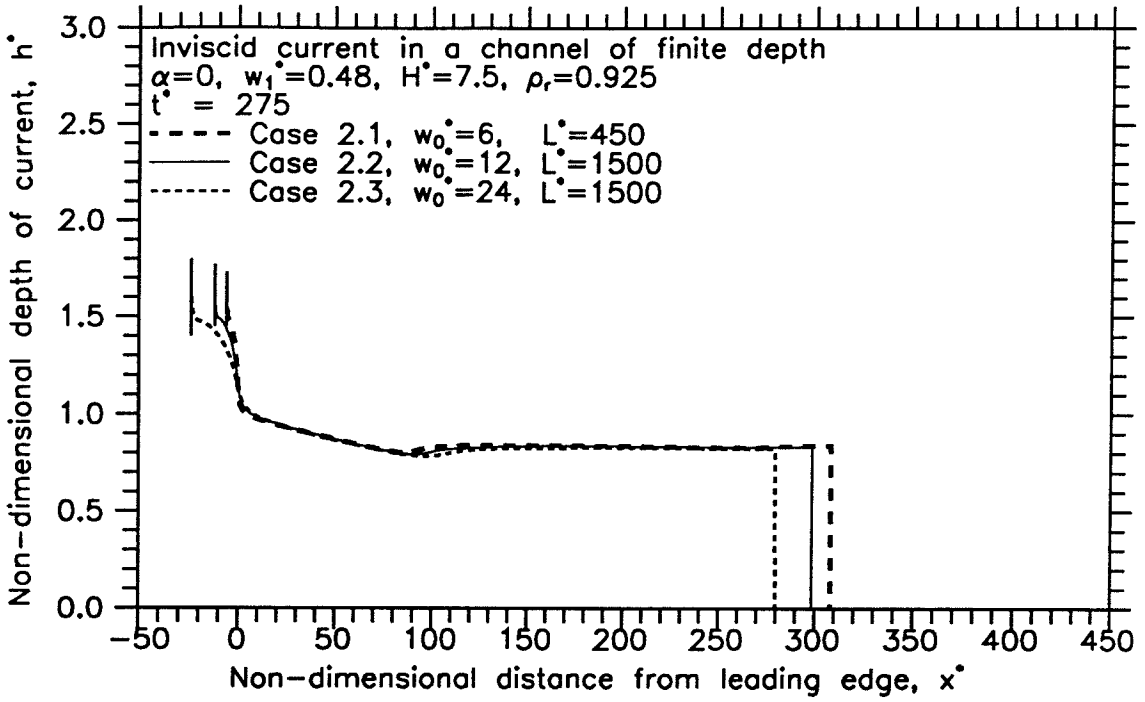

Figure 3.20a Depth of currenst as a function of distance from the leading edge at $t^*=275$ for Cases 2.1, 2.2, and 2.3.

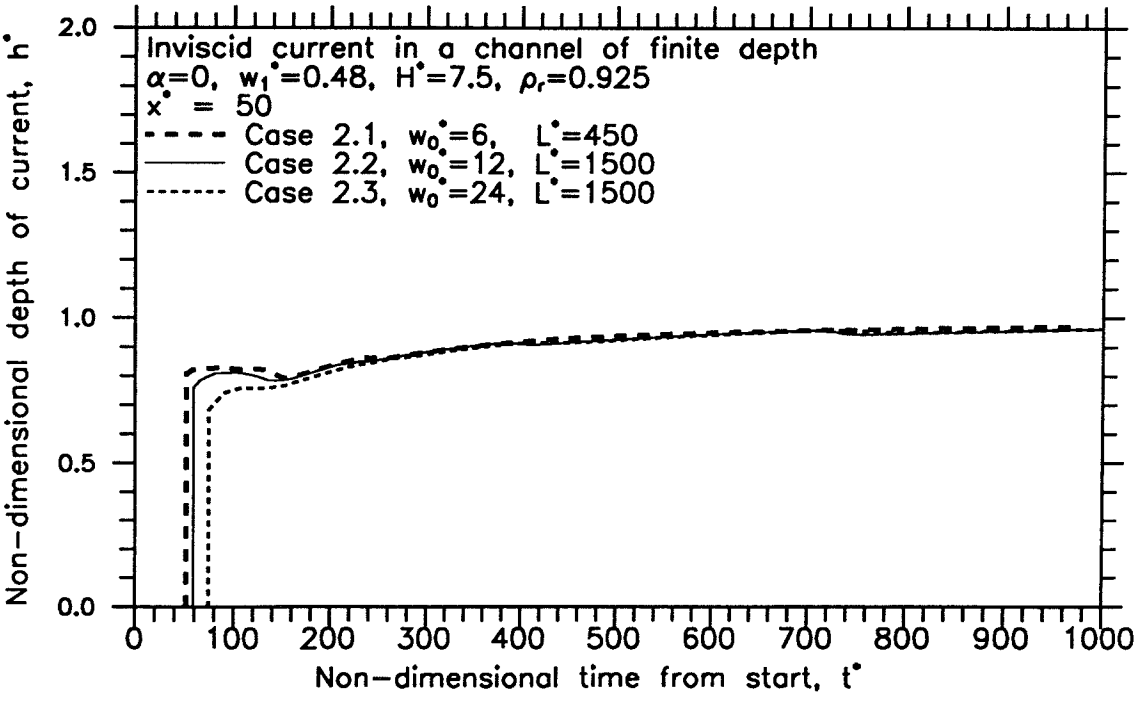

Figure 3.20b Depth of current as a function of time from start at $x^*=50$ for Cases 2.1, 2.2, and 2.3.

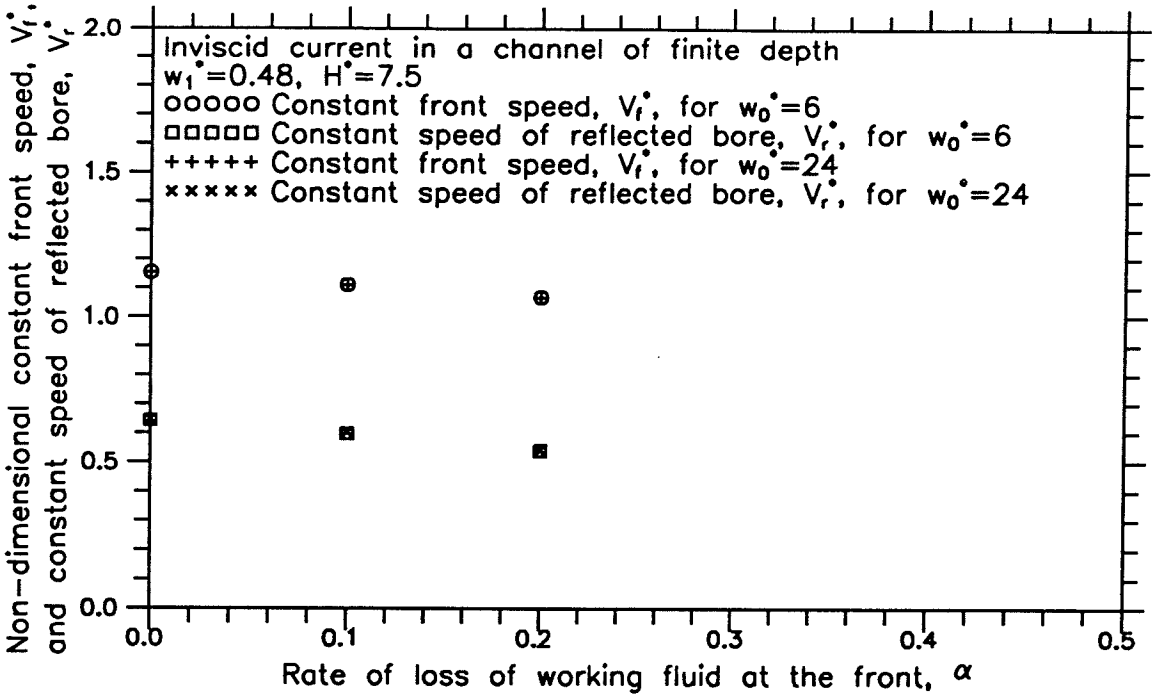

Figure 3.21a Constant front speed and constant speed of the reflected bore as a function of the rate of loss of working fluid through the sink at the front of the current.

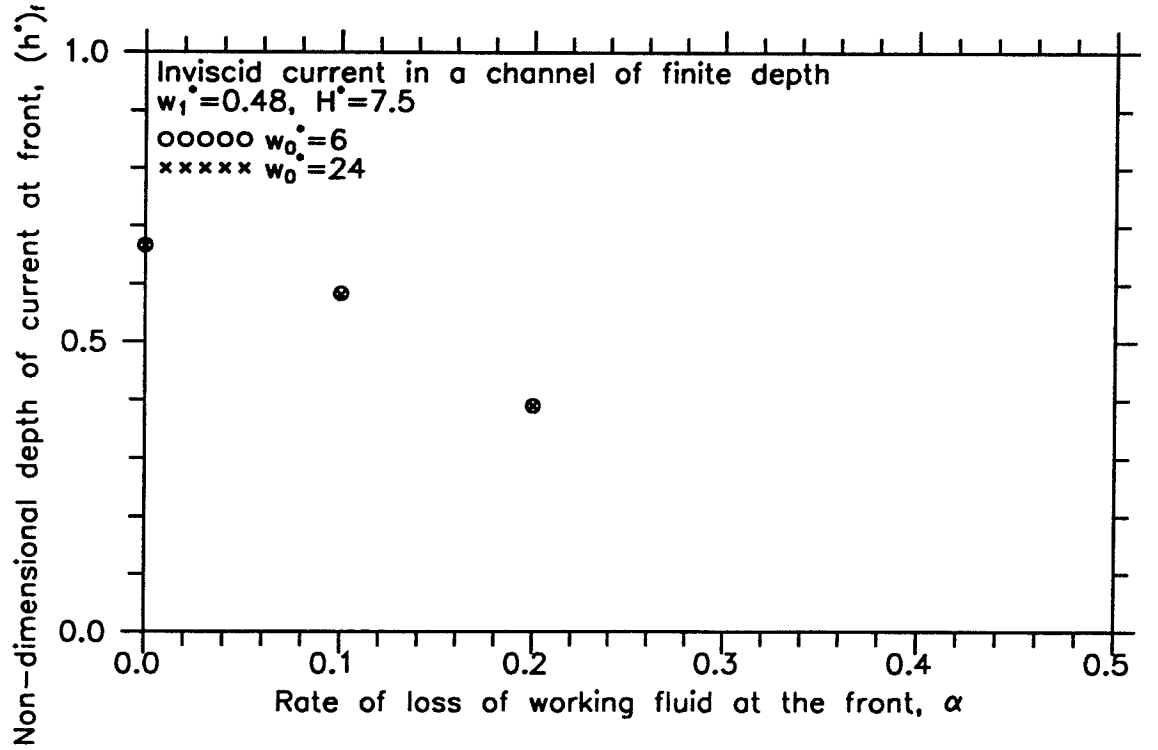

Figure 3.21b Depth of current at the front as a function of the rate of loss of working fluid through the sink at the front of the current.

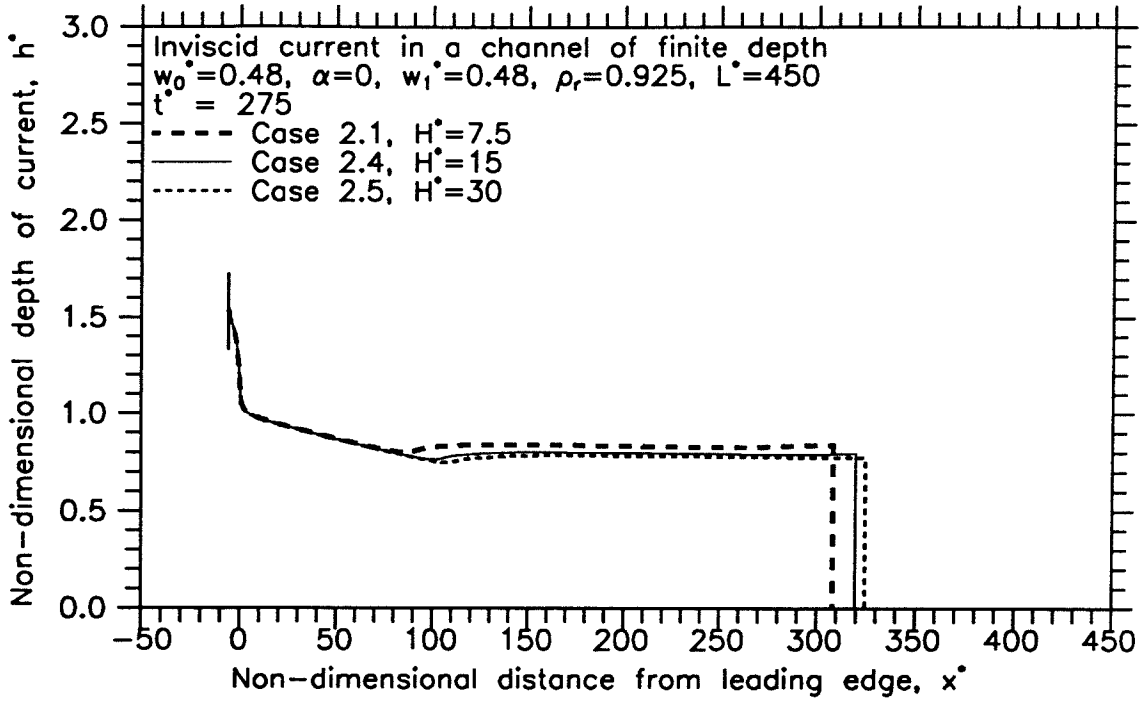

Figure 3.22a Depth of current as a function of distance from the leading edge at t^*=275 for Cases 2.1, 2.4, and 2.5.

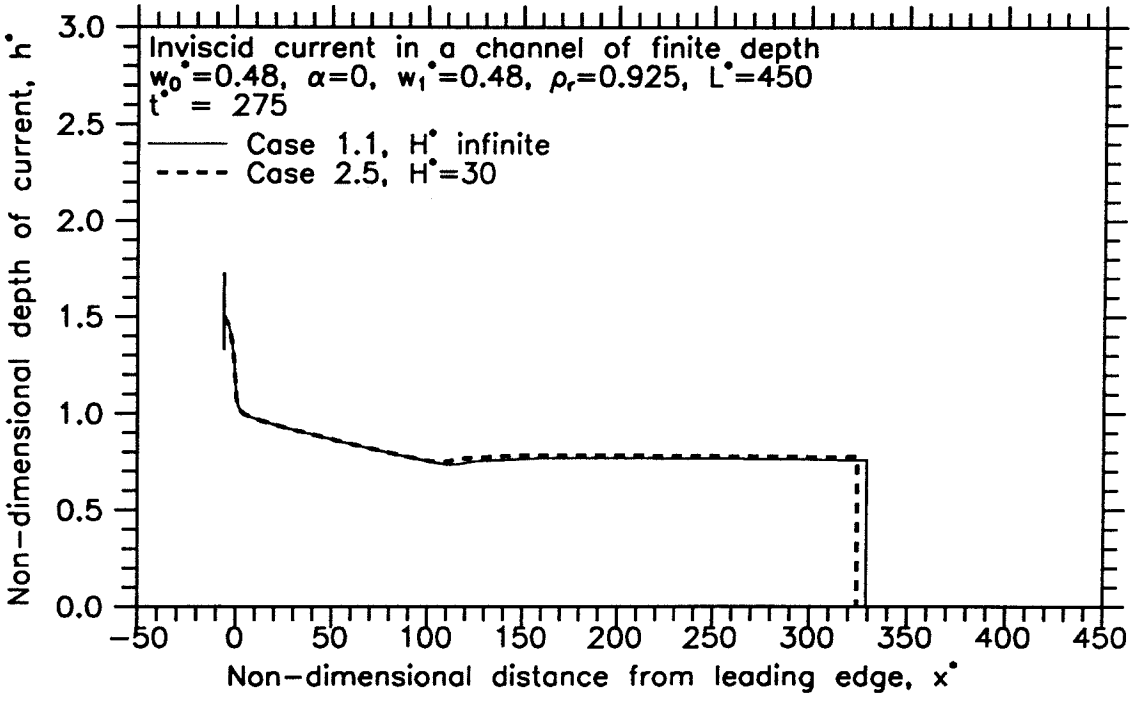

Figure 3.22b Depth of current as a function of distance from the leading edge at t^*=275 for Cases 1.1 and 2.5.

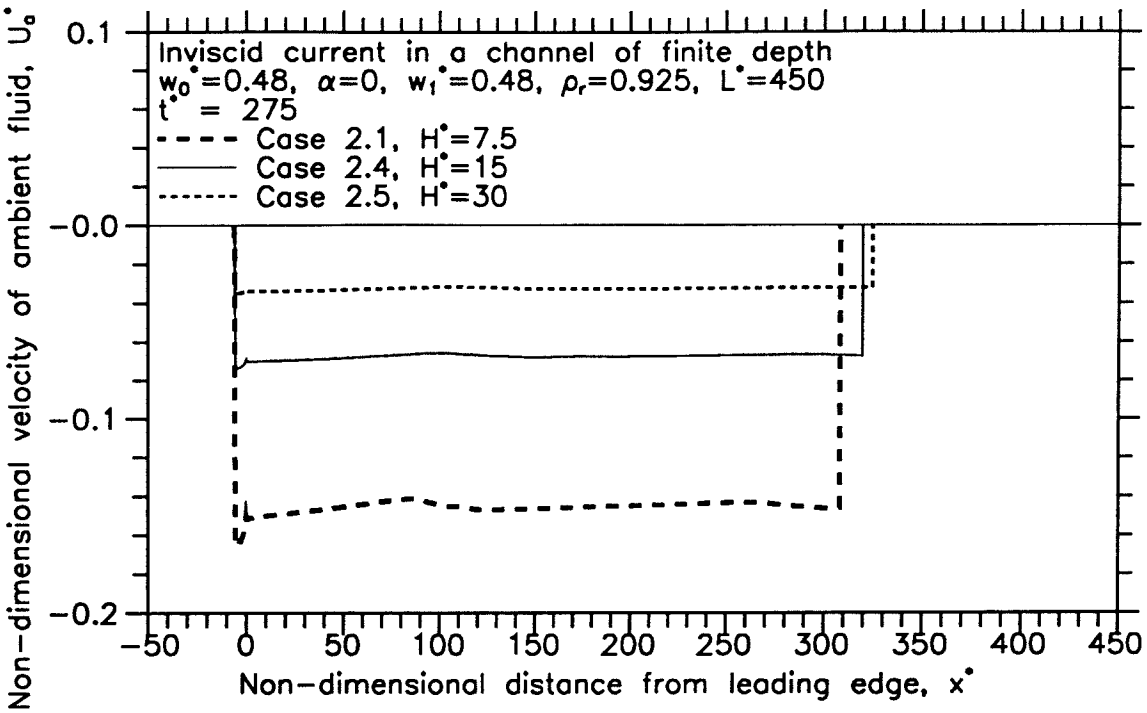

Figure 3.23a Velocity of ambient fluid as a function of distance from the leading edge at t^*=275 for Cases 2.1, 2.4, and 2.5.

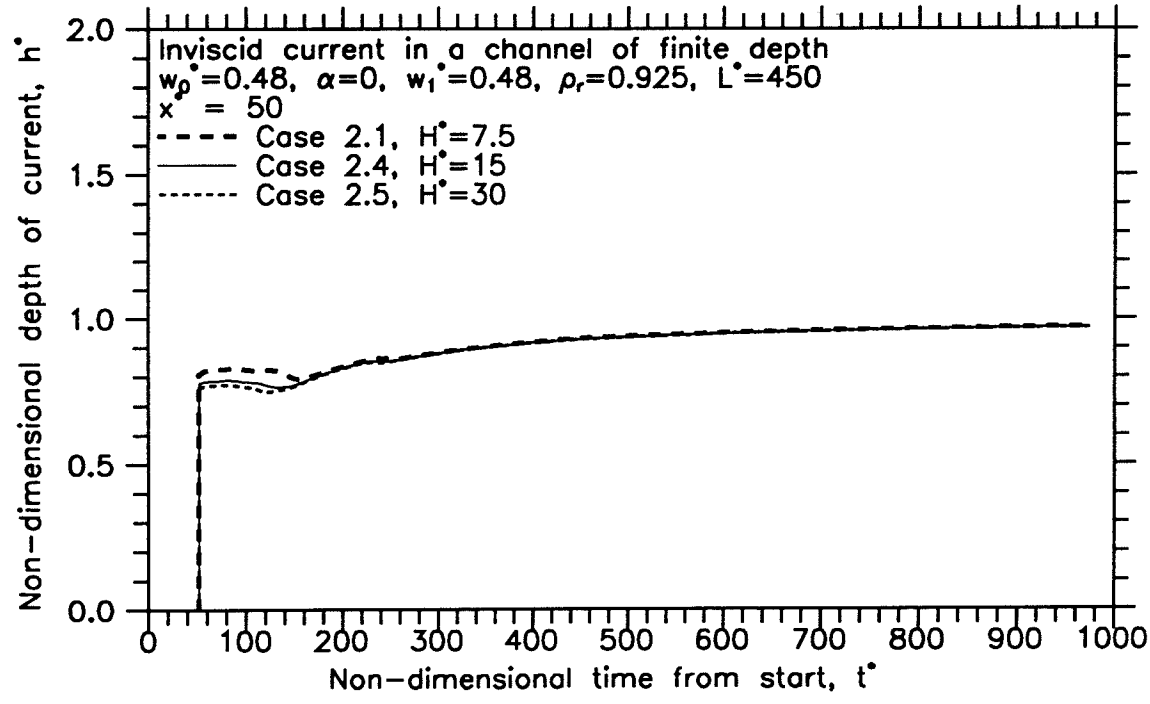

Figure 3.23b Depth of current as a function of time at x^*= 50 for Cases 2.1, 2.4, and 2.5.

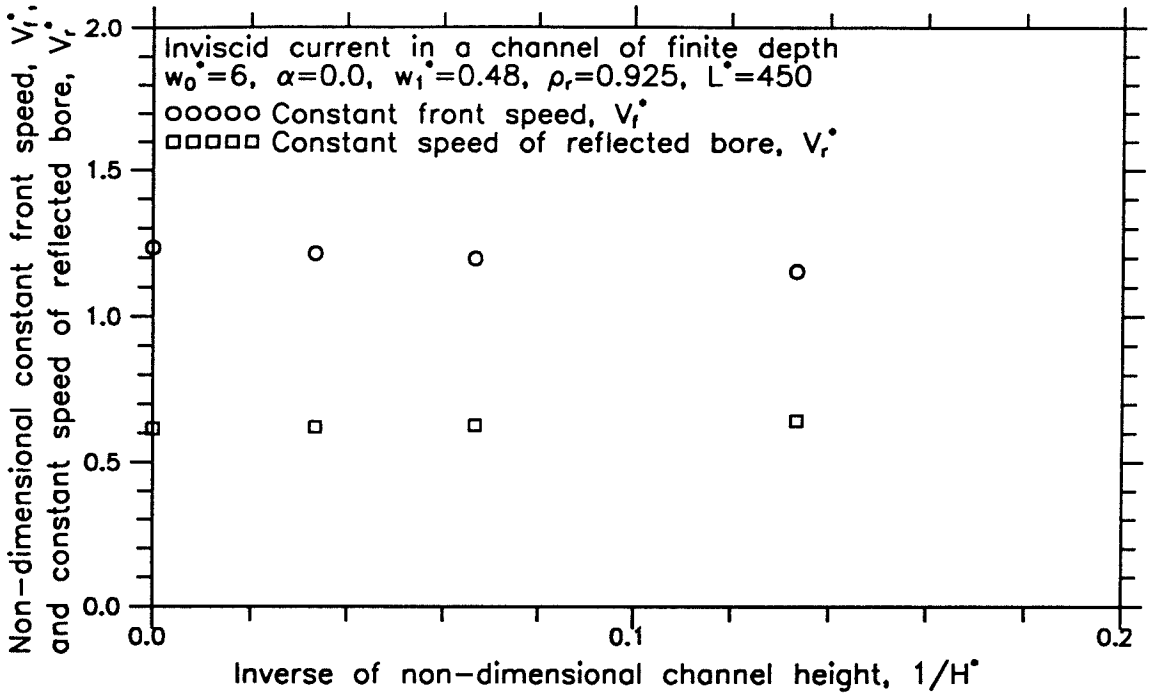

Figure 3.24a Constant front speed and constant speed of the reflected bore as functions of channel height.

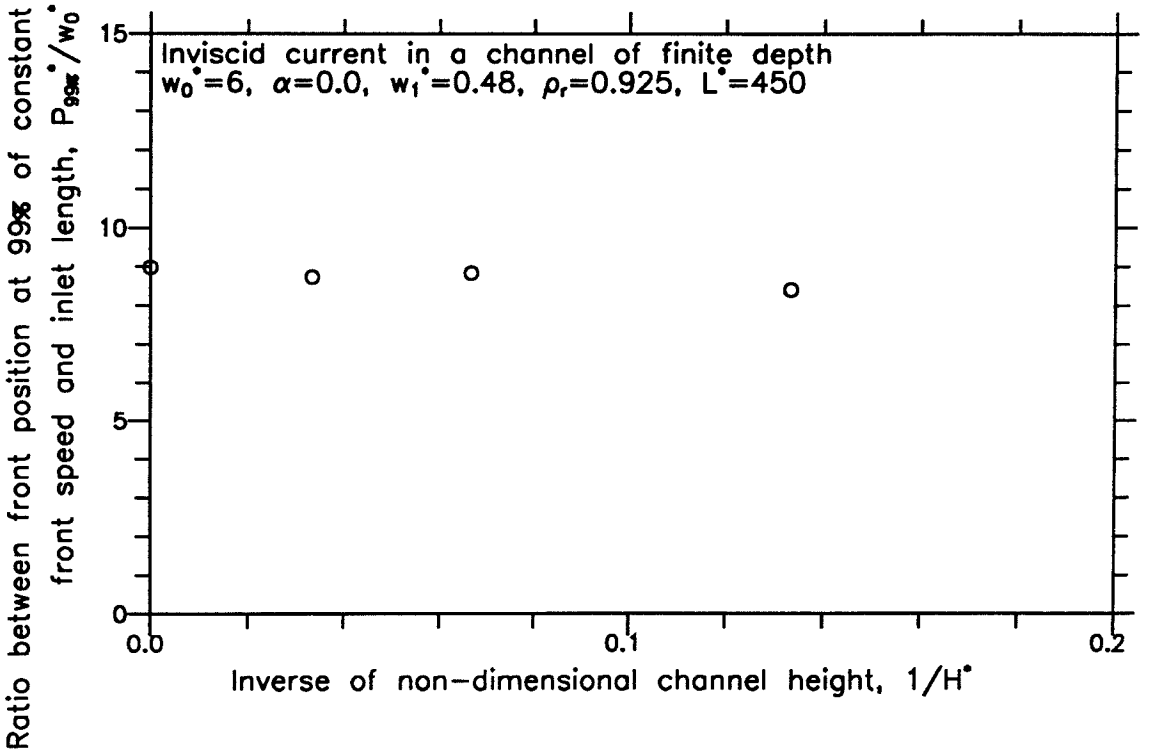

Figure 3.24b Ratio between front position at 99% constant front speed and inlet length as a function of channel height.

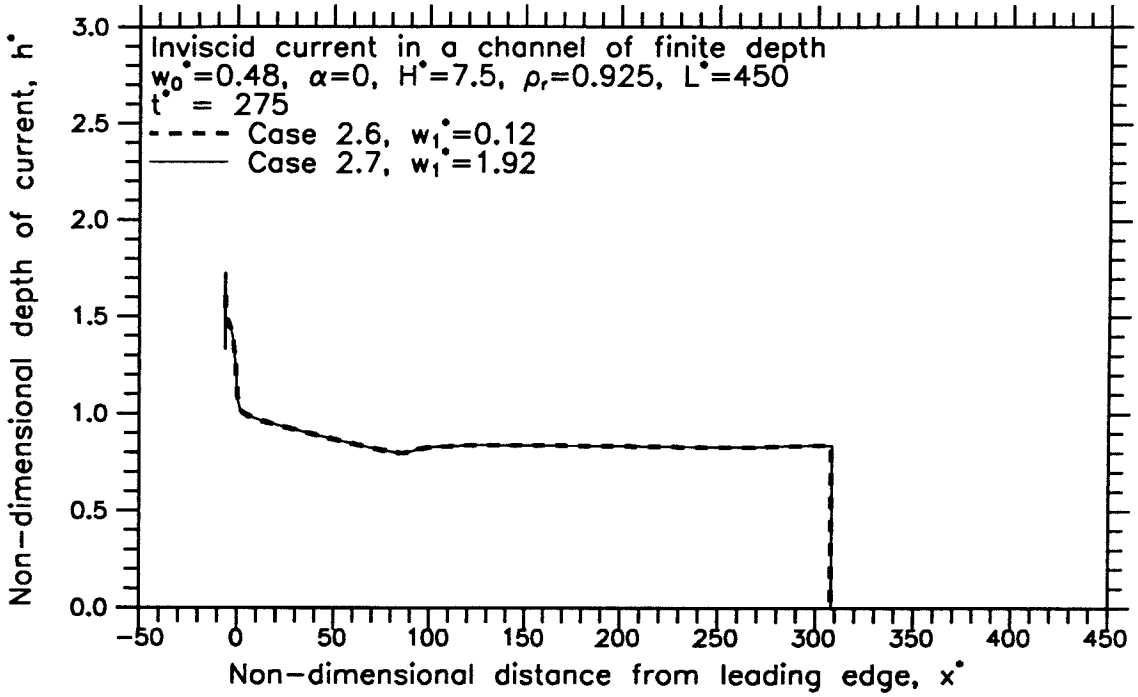

Figure 3.25a Depth of current as a function of distance from the leading edge at t^*=275 for Cases 2.6 and 2.7.

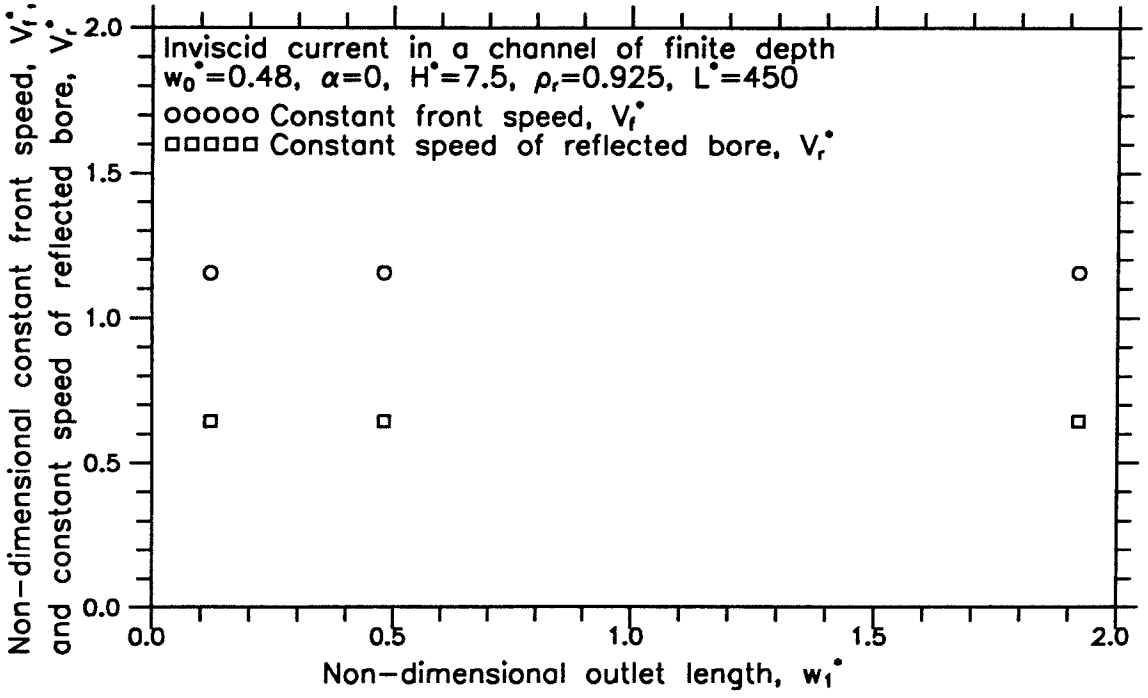

Figure 3.25b Constant front speed and constant speed of the reflected bore as functions of the outlet length.

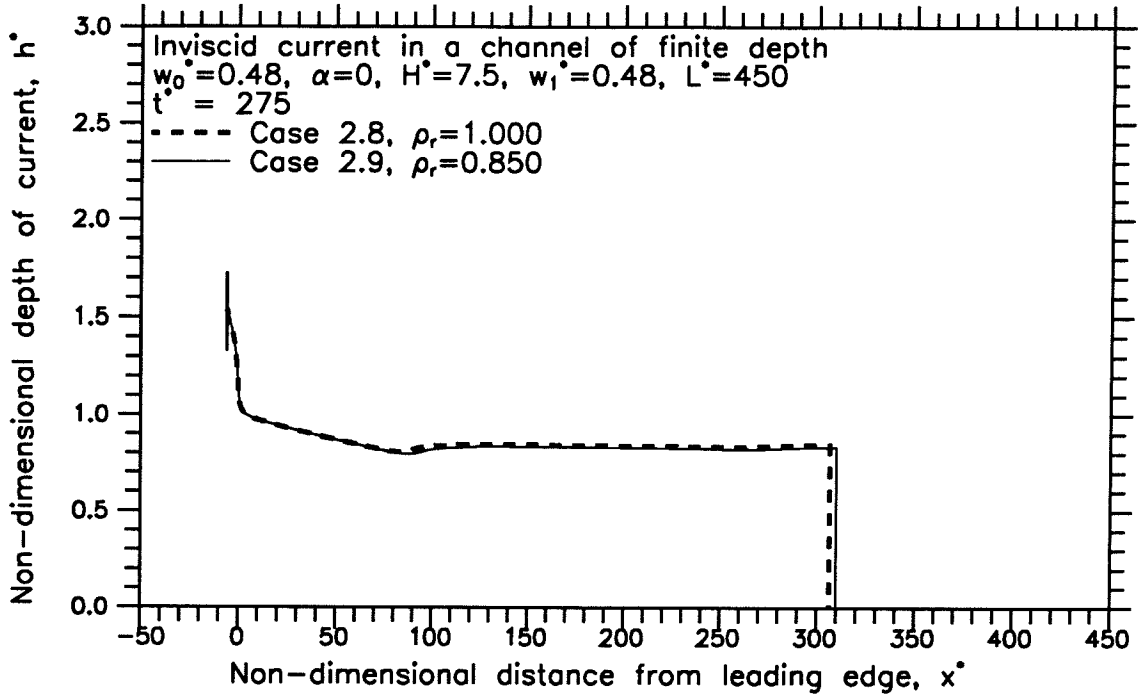

Figure 3.26a Depth of current as a function of distance from the leading edge at t^*=275 for Cases 2.8 and 2.9.

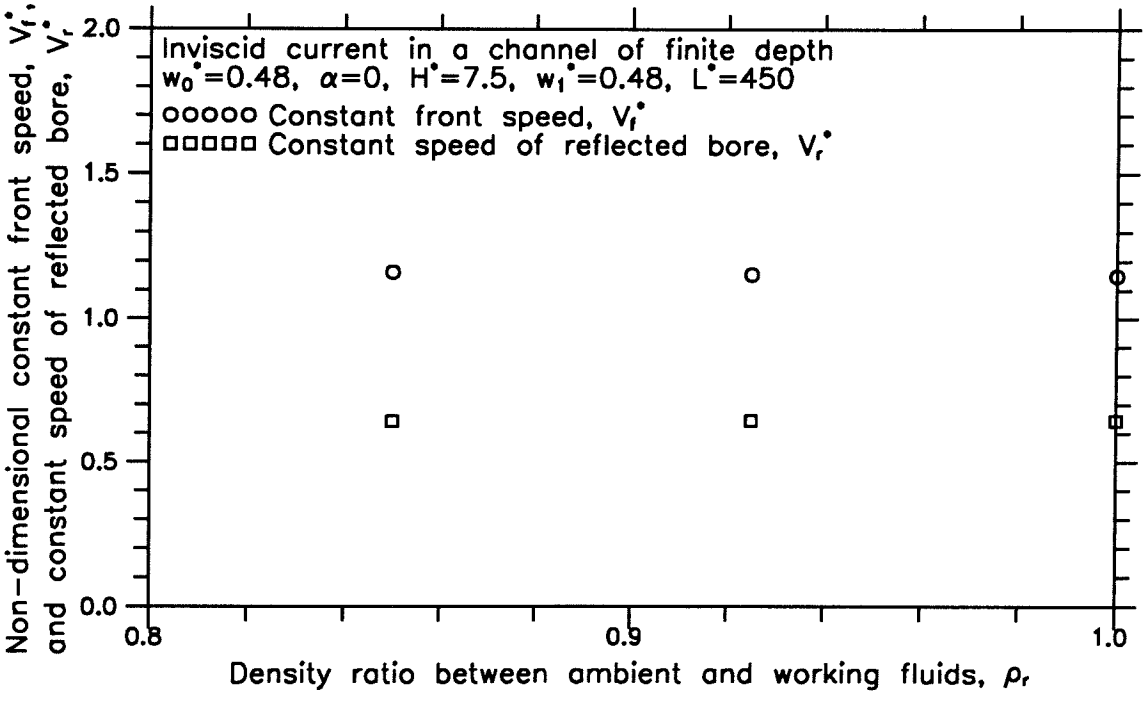

Figure 3.26b Constant front speed and constant speed of the reflected bore as functions of the density ratio between the ambient fluid and the working fluid.

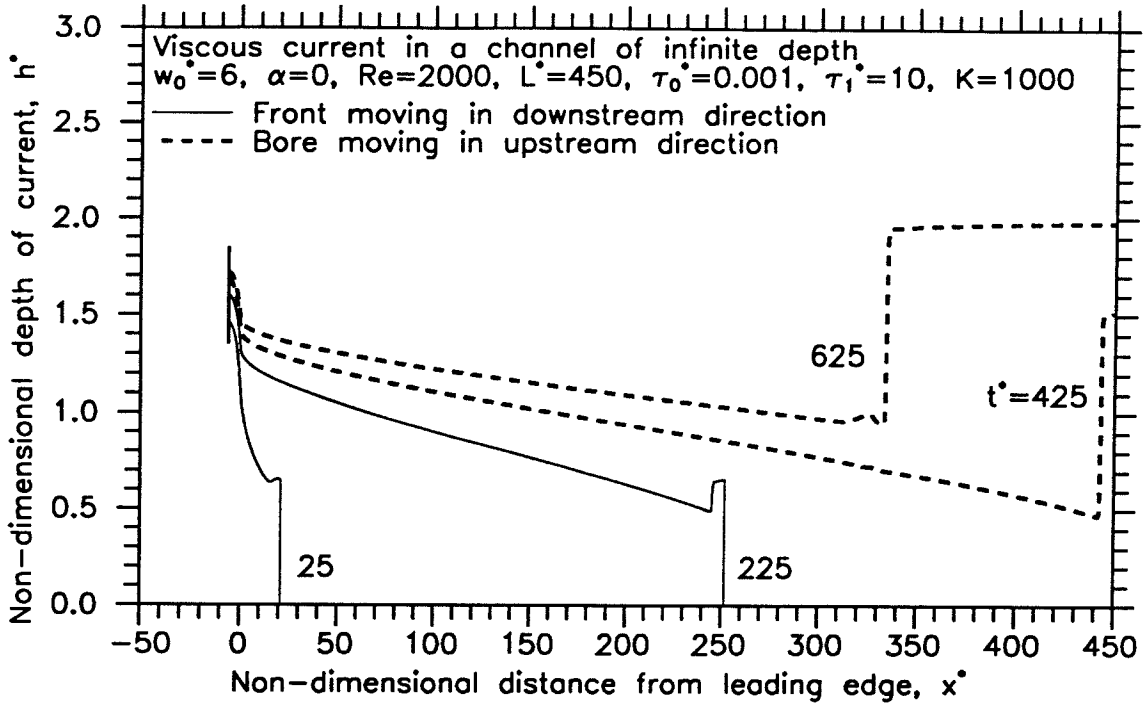

Figure 3.27a Depth of current as a function of distance from the leading edge at various times for Case 3.4.

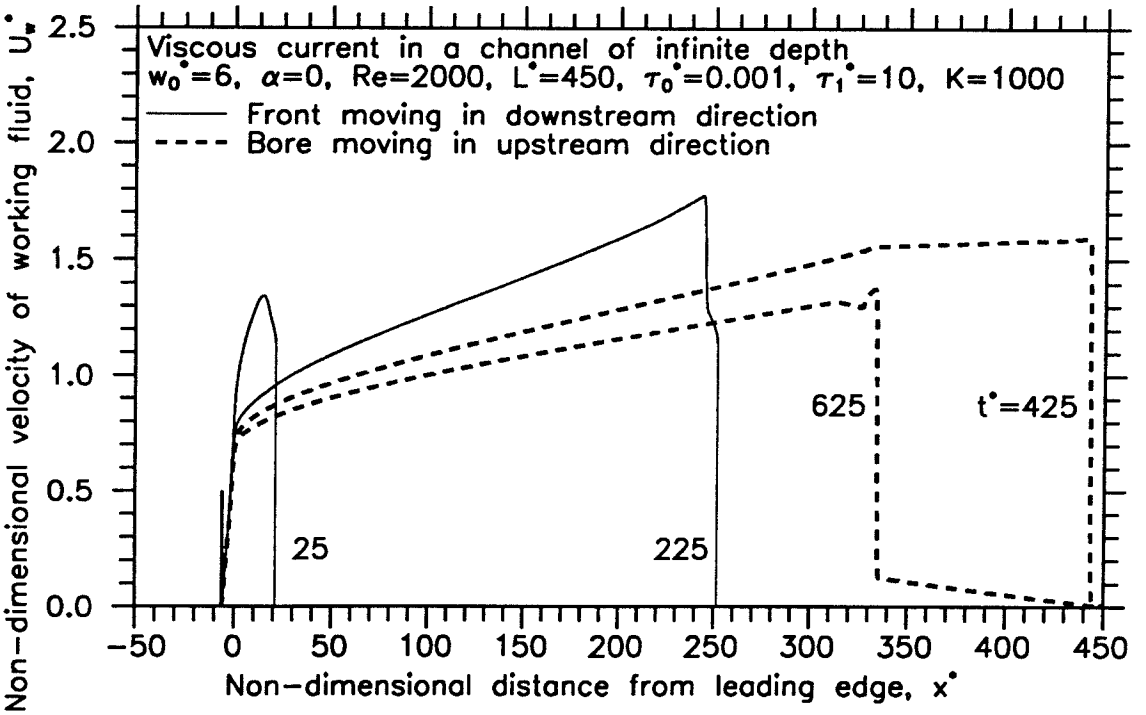

Figure 3.27b Velocity of current as a function of distance from the leading edge at various times for Case 3.4.

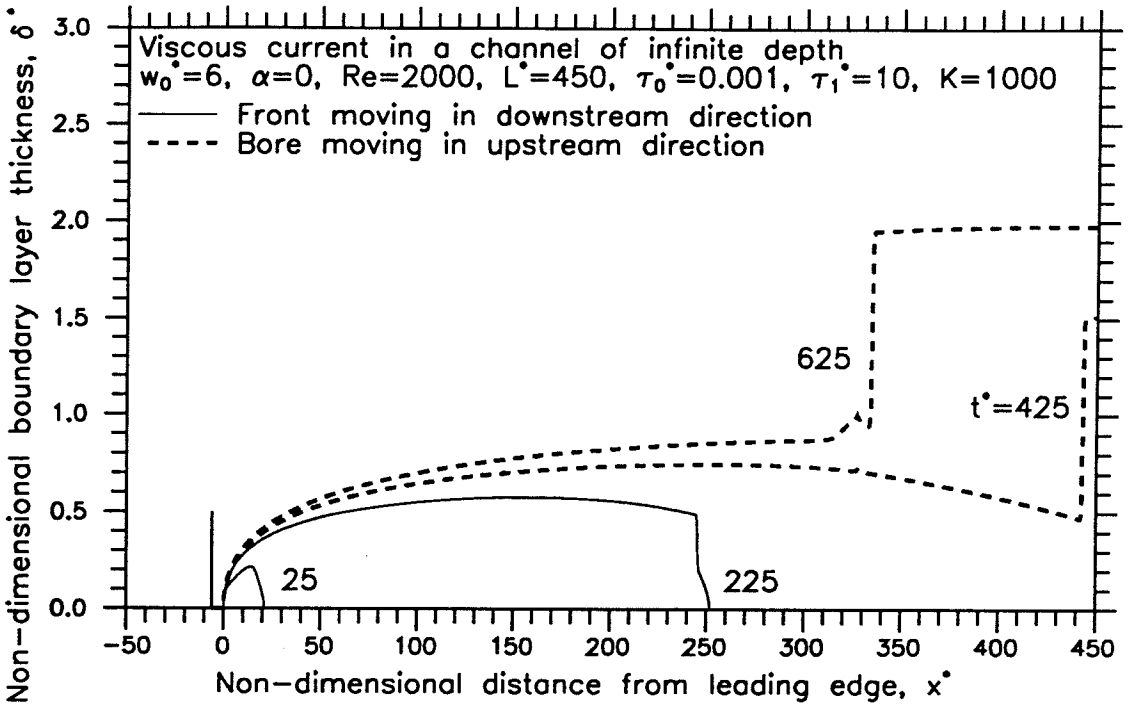

Figure 3.28a Boundary layer thickness as a function of distance from the leading edge at various times for Case 3.4.

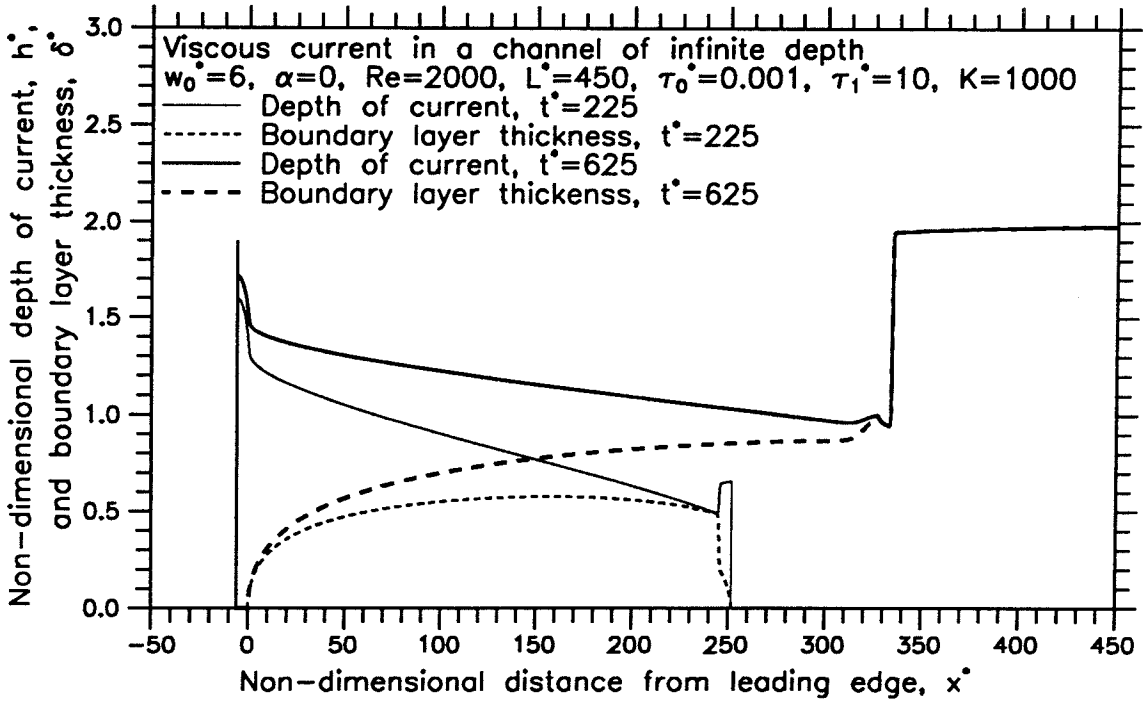

Figure 3.28b Depth of current and boundary layer thickness of working fluid as a function of distance from the leading edge at various times for Case 3.4.

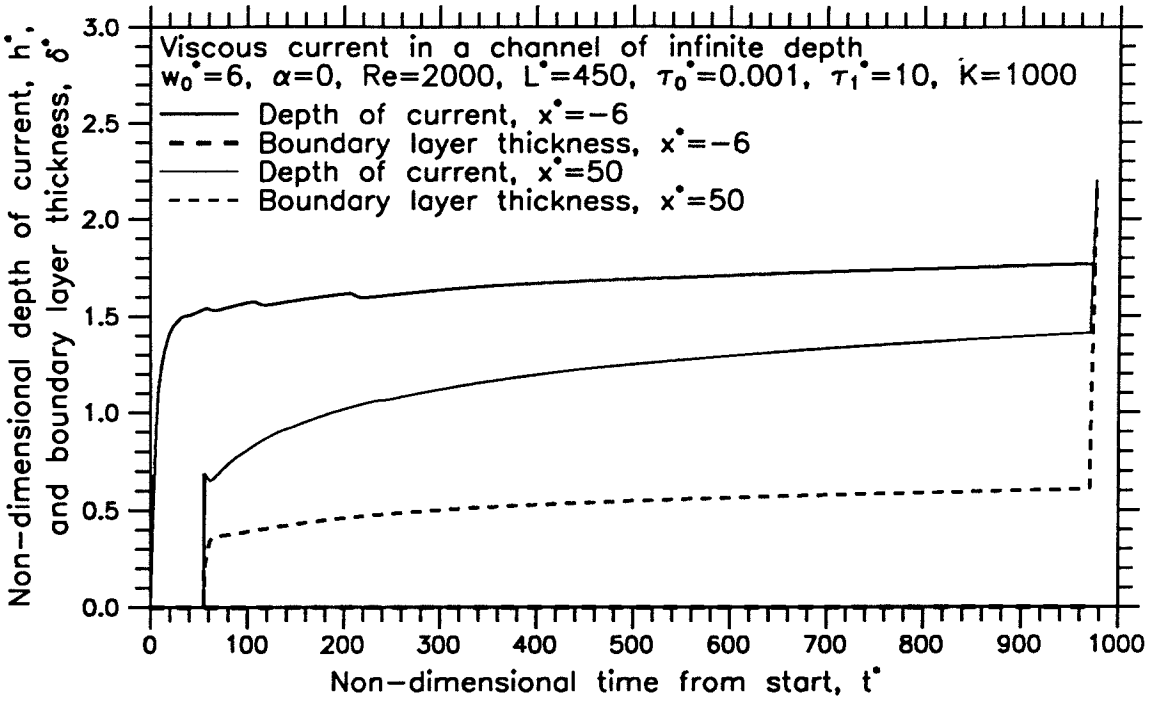

Figure 3.29a Depth of current and boundary layer thickness as a function of time at various distances from the leading edge for Case 3.4.

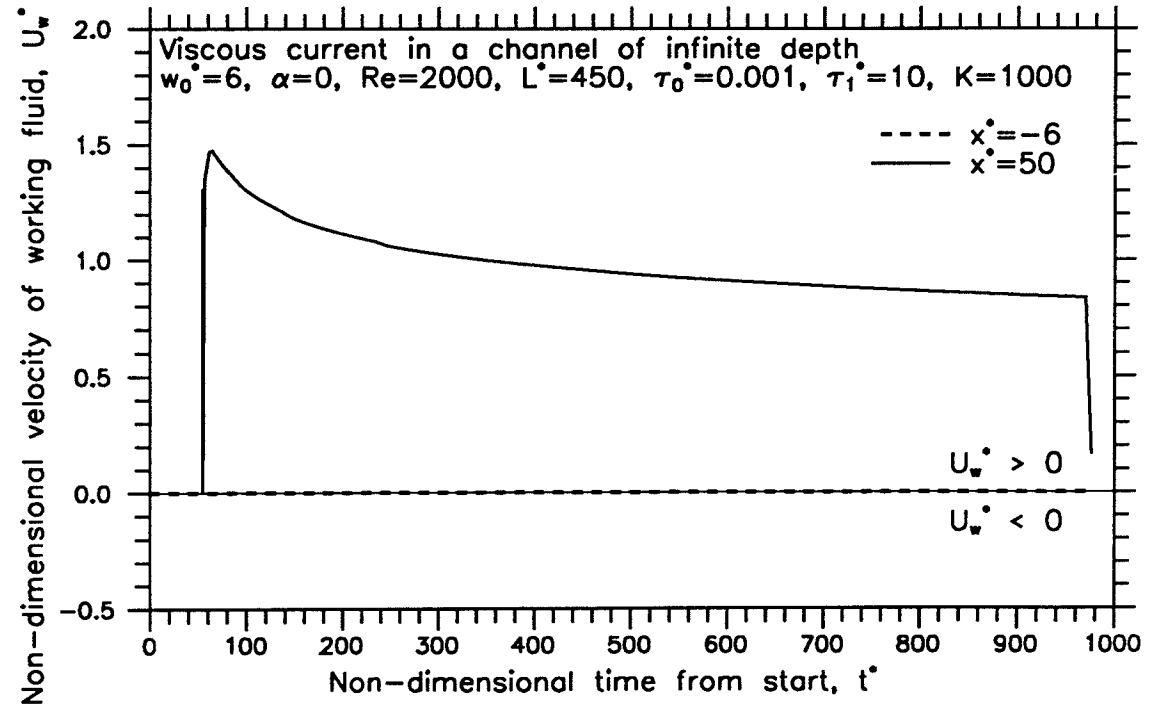

Figure 3.29b Velocity of the layer of working fluid as a function of time at various distances from the leading edge for Case 3.4.

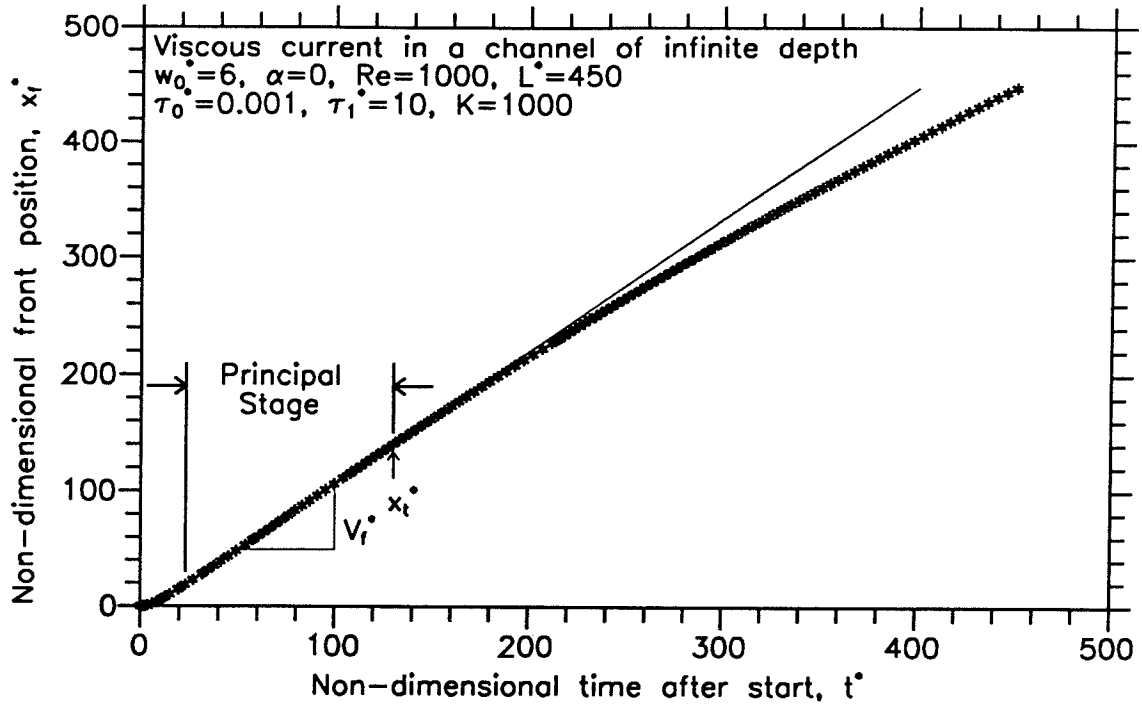

Figure 3.30a Front position as a function of time for Case 3.3.

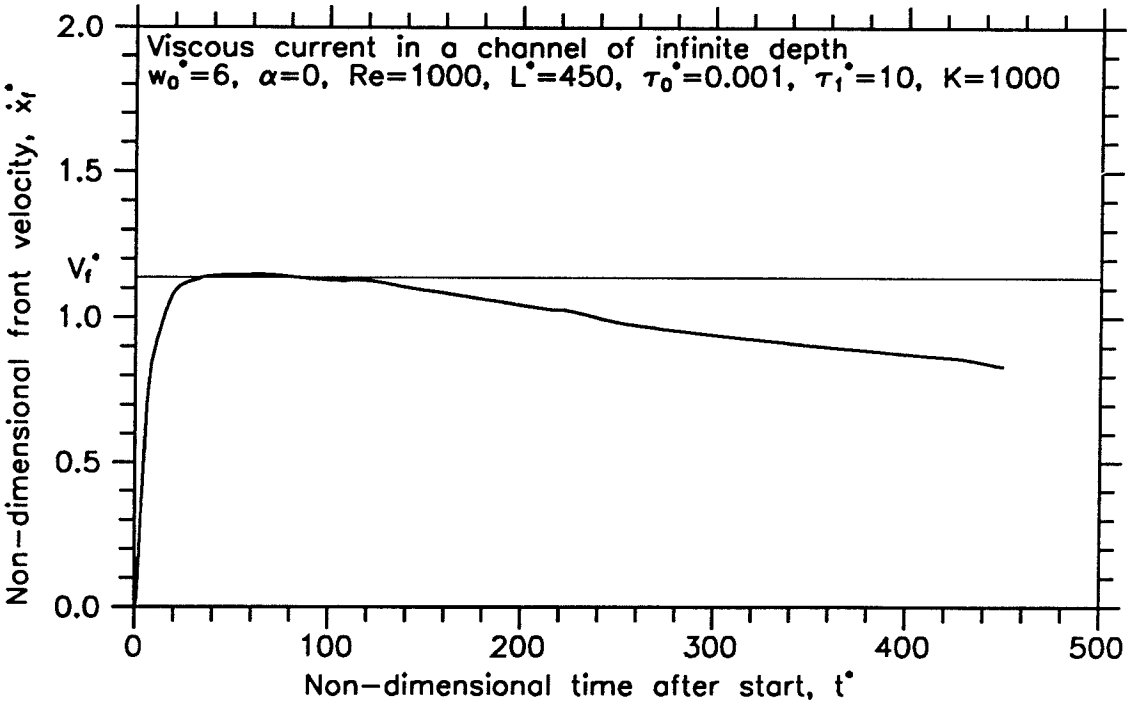

Figure 3.30b Front velocity as a function of time for Case 3.3.

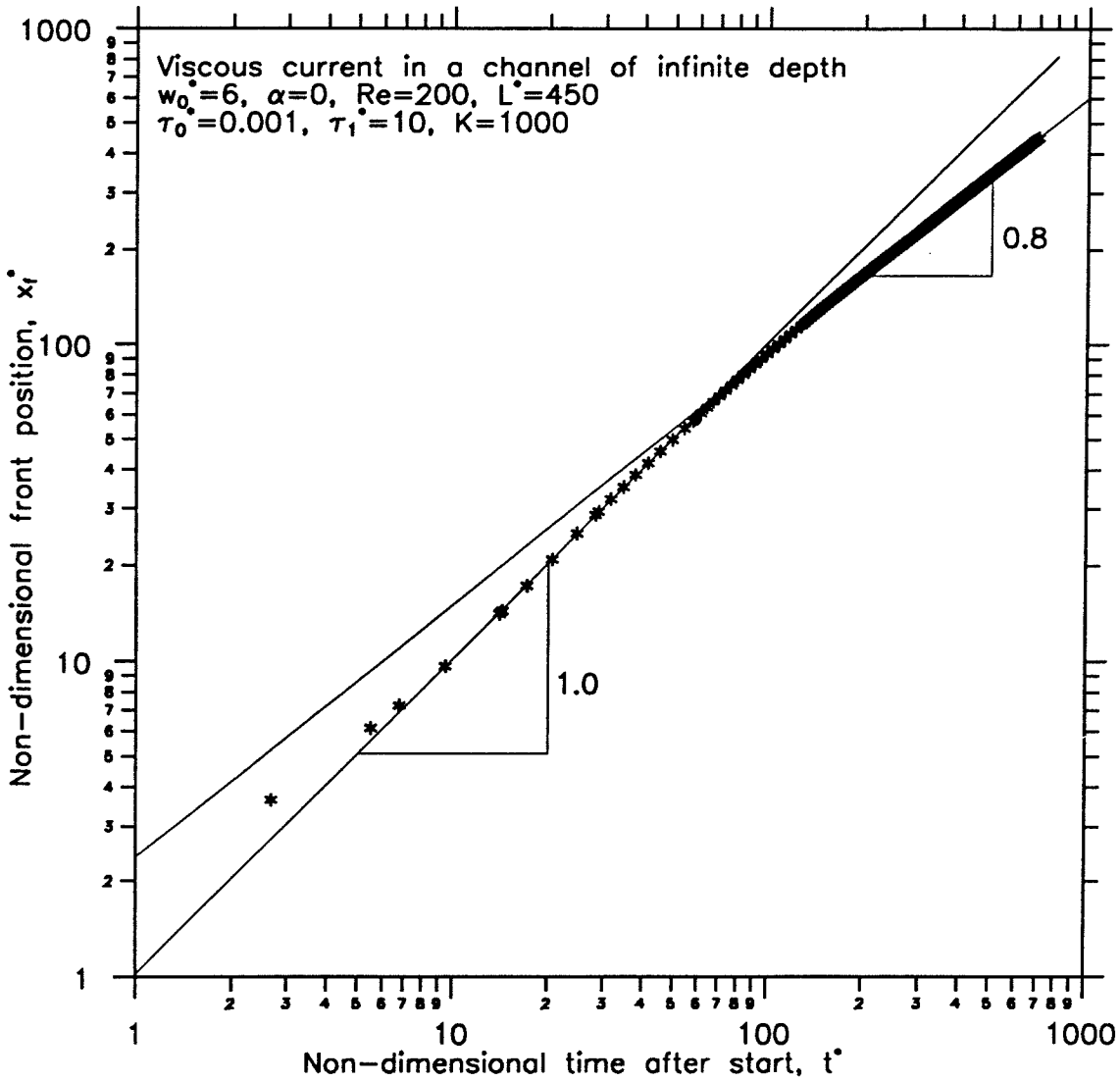

Figure 3.31 Front position as a function of time from start for Case 3.1.

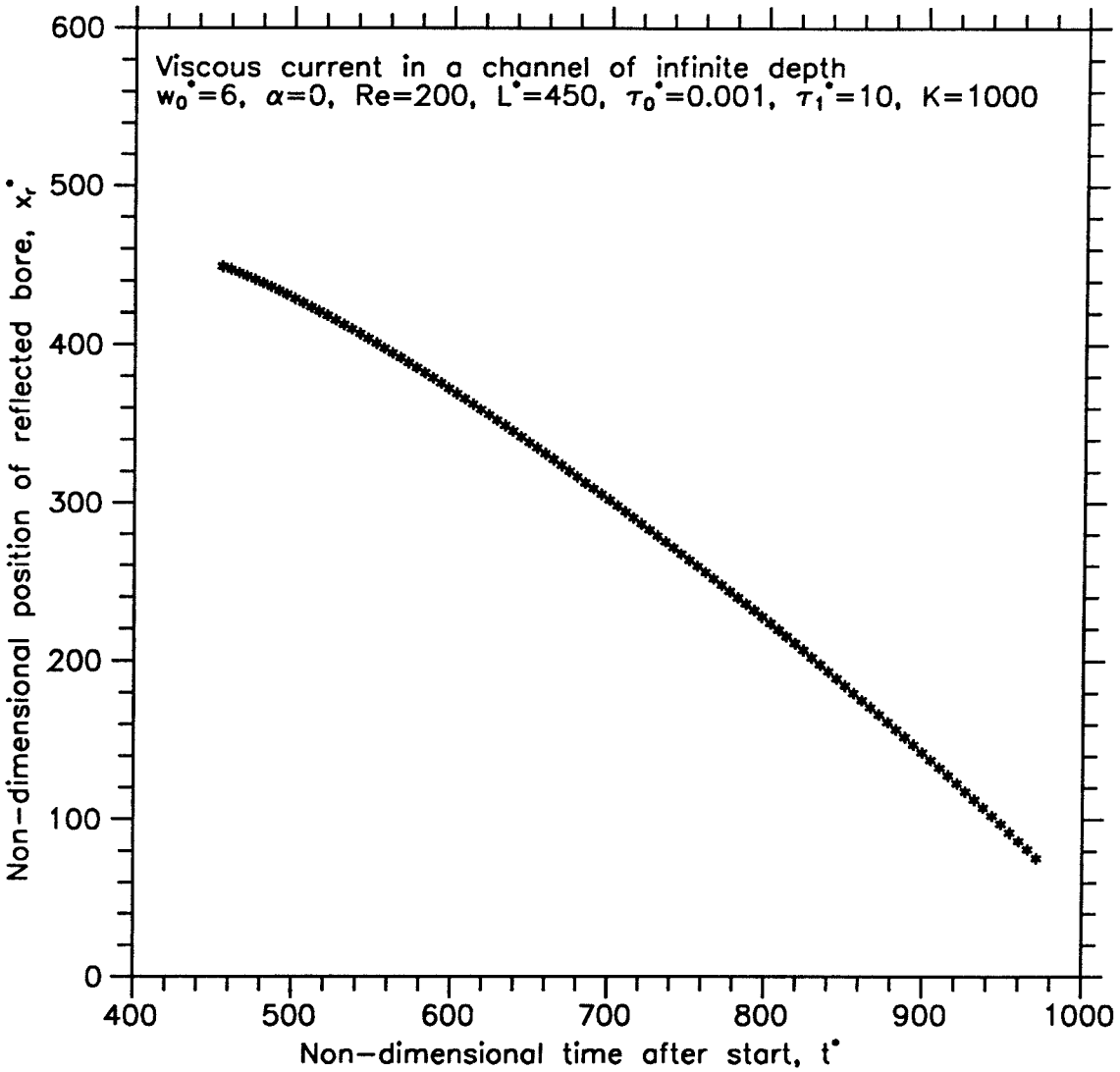

Figure 3.32 Position of the reflected bore as a function of time from start for Case 3.1.

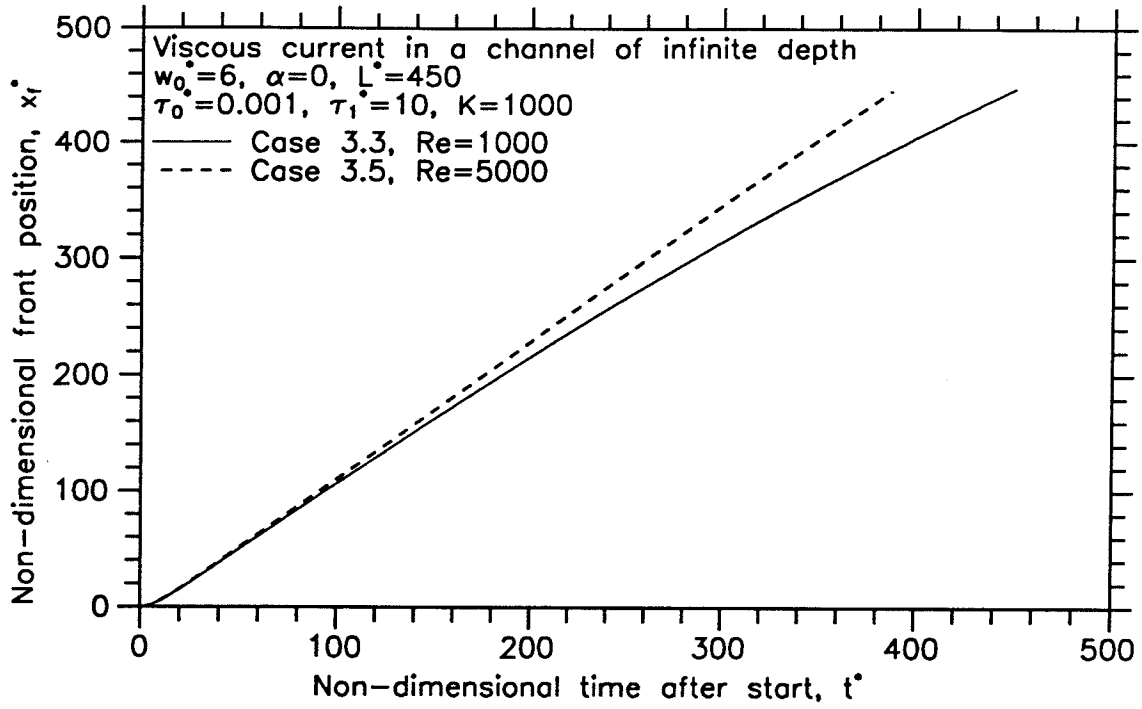

Figure 3.33a Front position as a function of time from start for Cases 3.3 and 3.5.

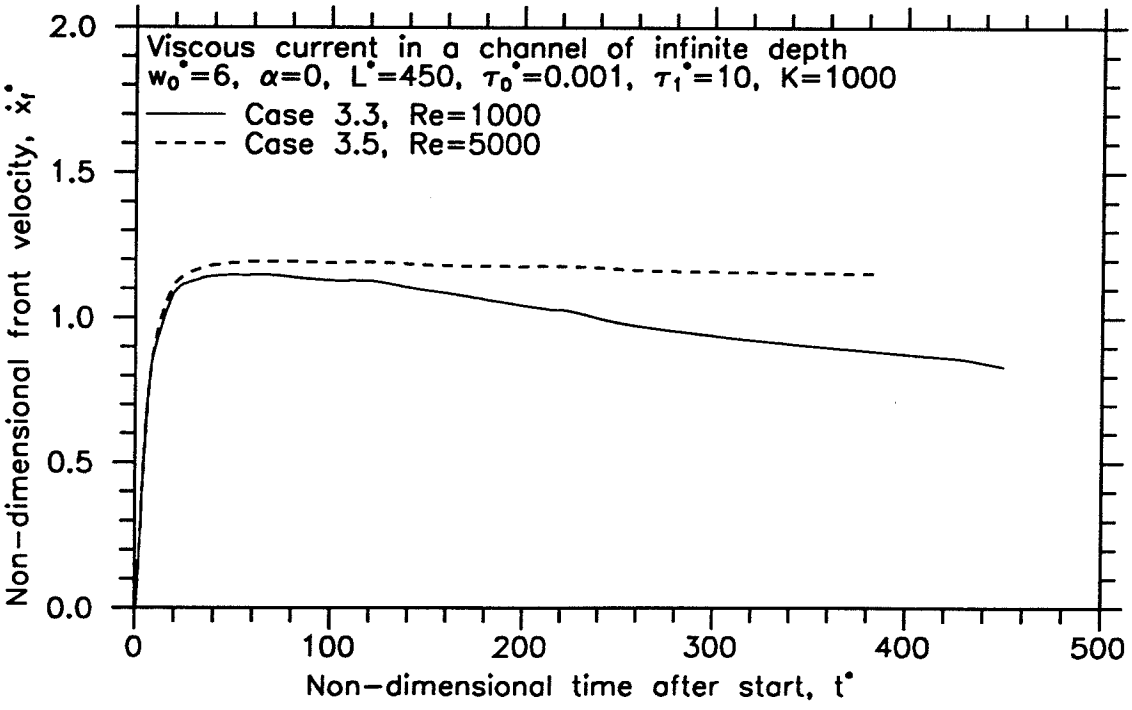

Figure 3.33b Front velocity as a function of time from start for Cases 3.3 and 3.5.

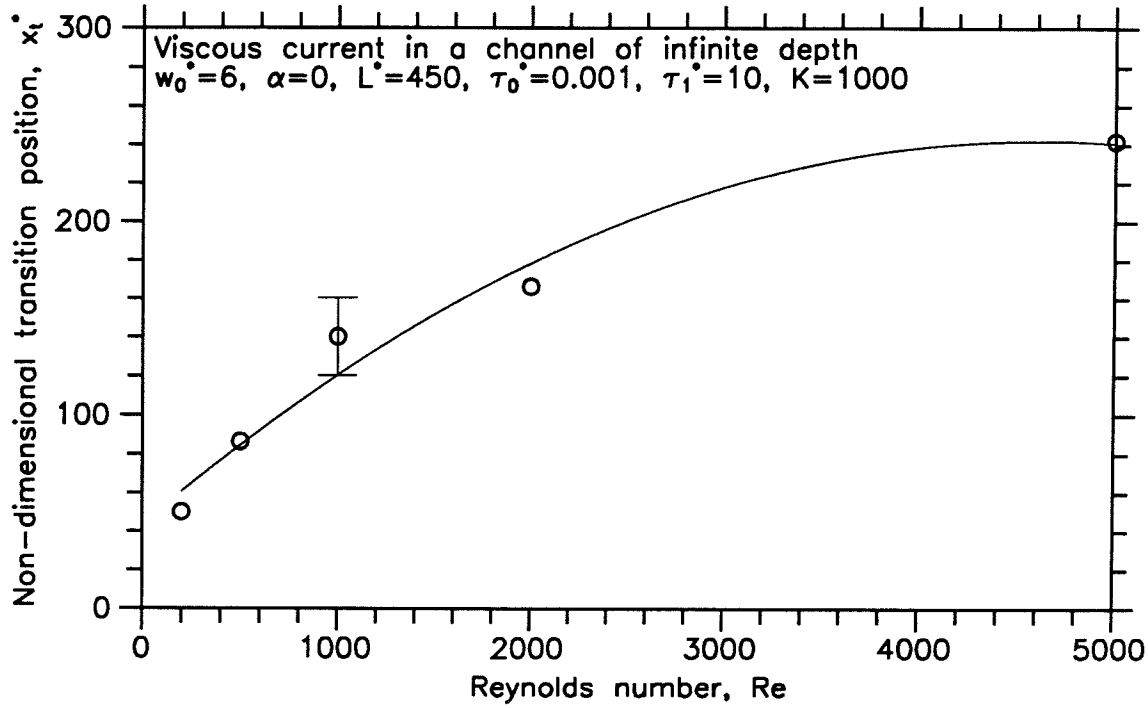

Figure 3.34a Transition position as a function of Reynolds number.

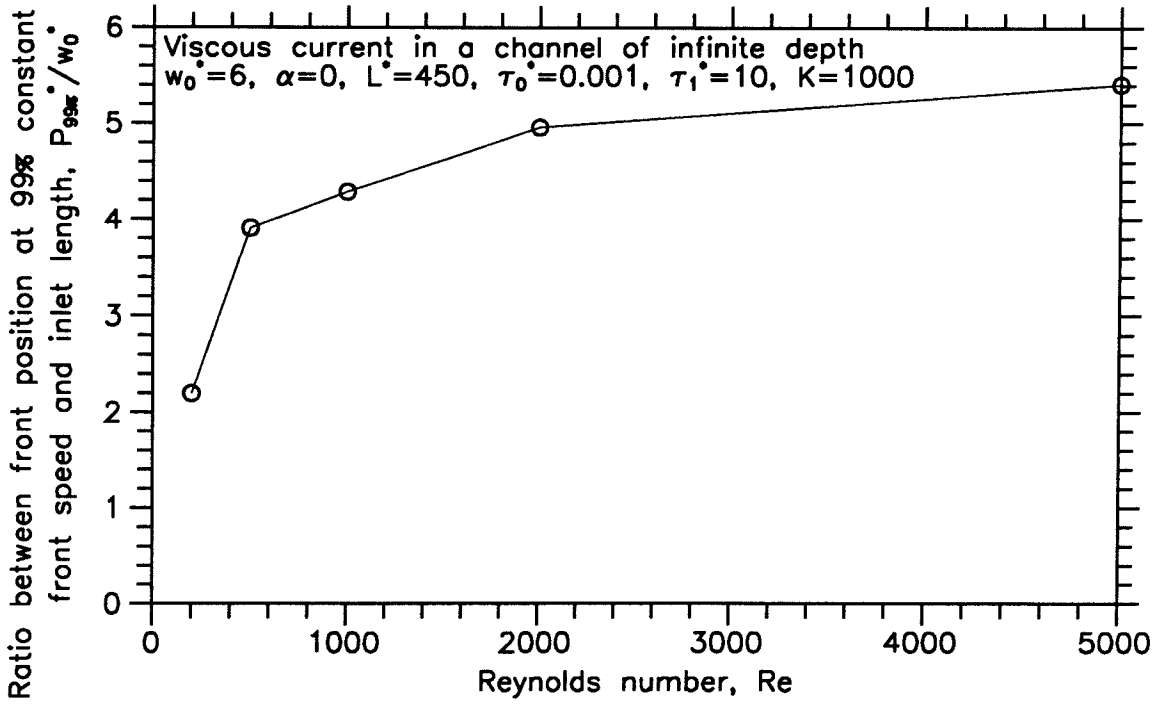

Figure 3.34b Ratio between front position at 99% constant front speed and inlet length as a function of Reynolds number.

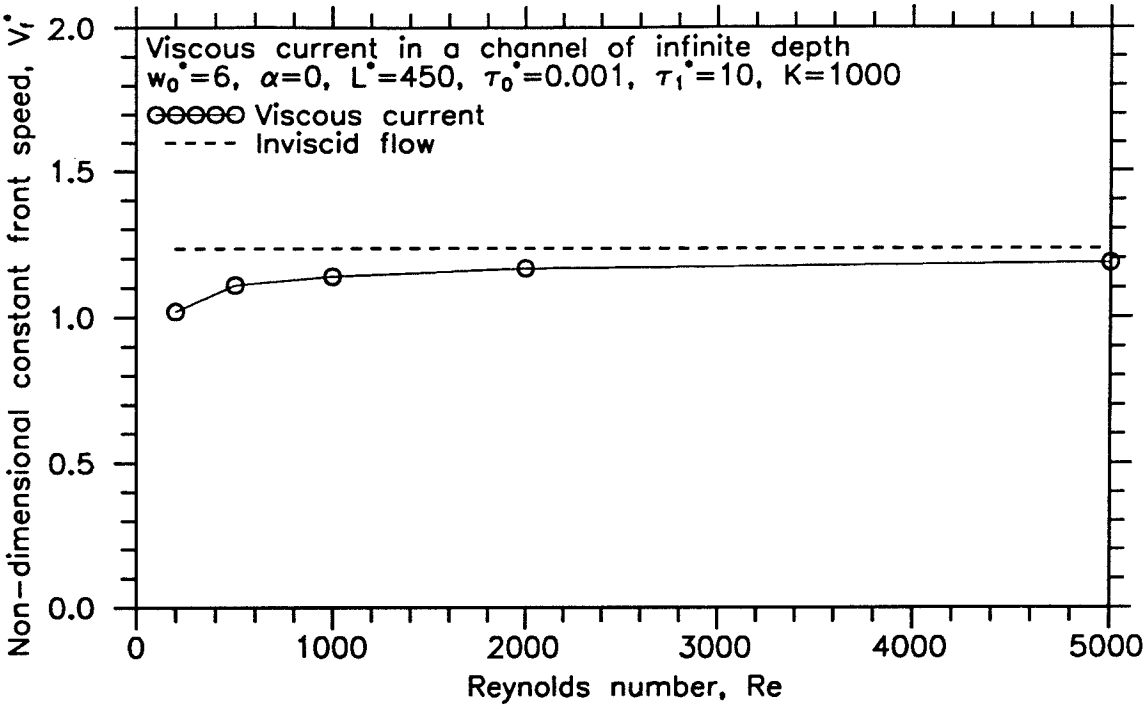

Figure 3.35a Constant front speed as a function of Reynolds number.

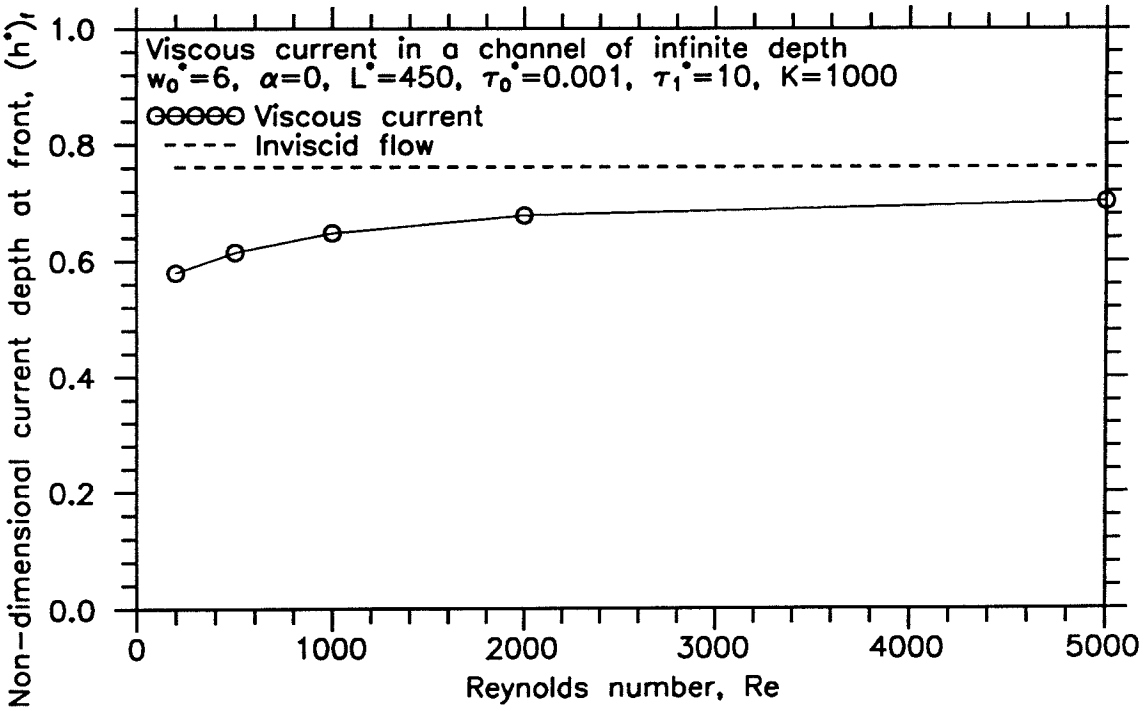

Figure 3.35b Depth of current at the front as a function of Reynolds number.

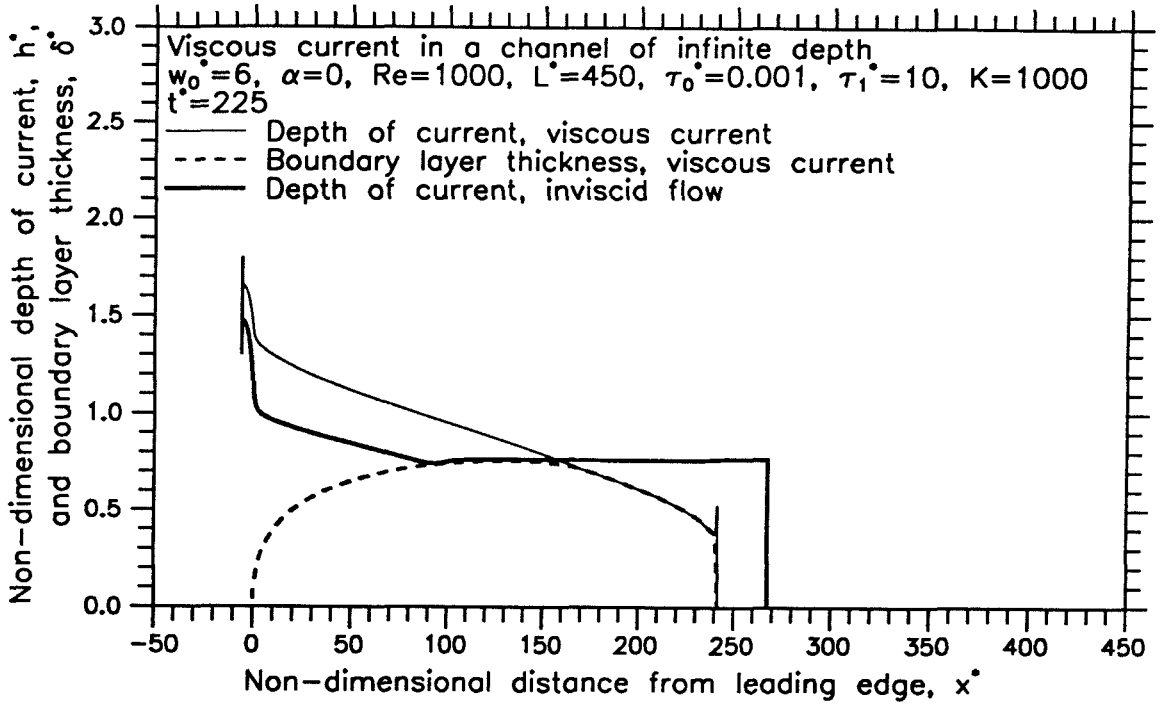

Figure 3.36a Depth of current and boundary layer thickness of the current as a function of distance from the leading edge at t^*=225 for Case 3.3.

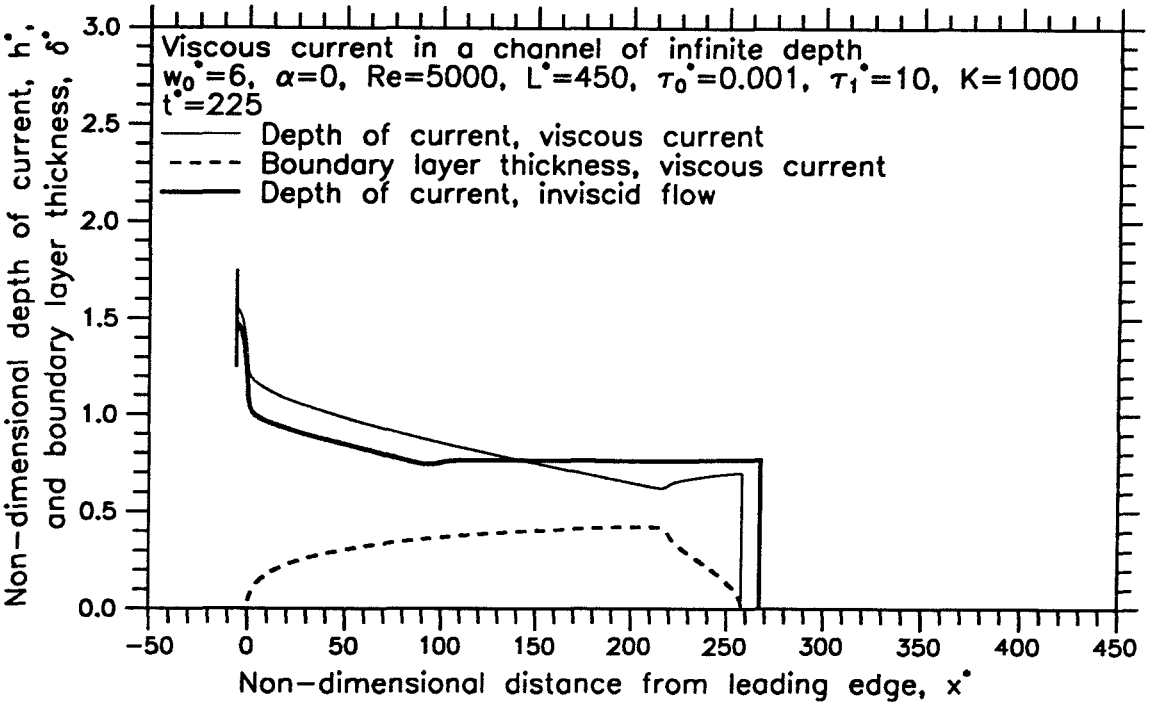

Figure 3.36b Depth of current and boundary layer thickness of the current as a function of distance from the leading edge at t^*=225 for Case 3.5.

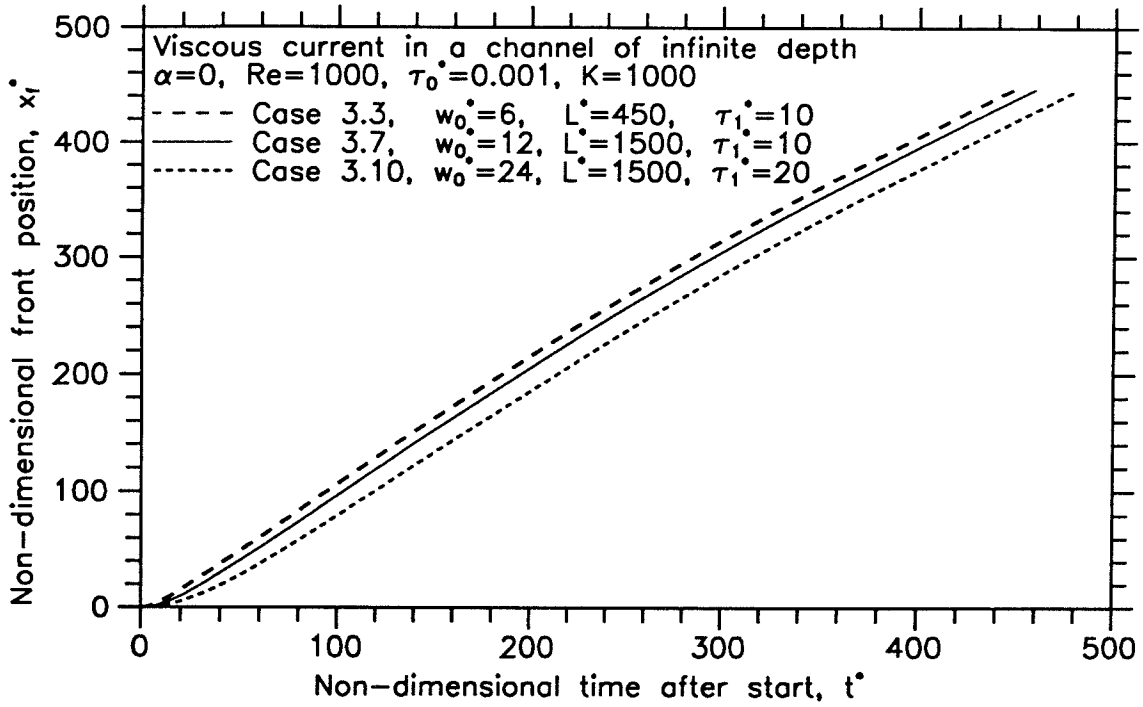

Figure 3.37a Front position as a function of time for Cases 3.3, 3.7 and 3.10.

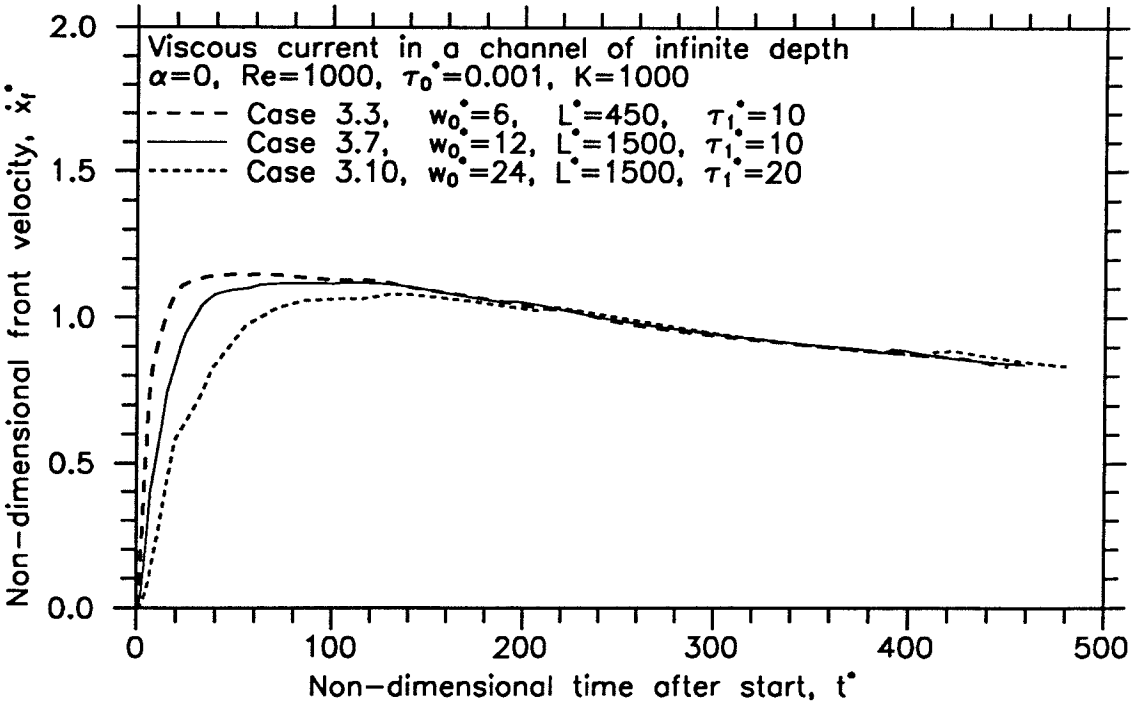

Figure 3.37b Front velocity as a function of time for Cases 3.3, 3.7 and 3.10.

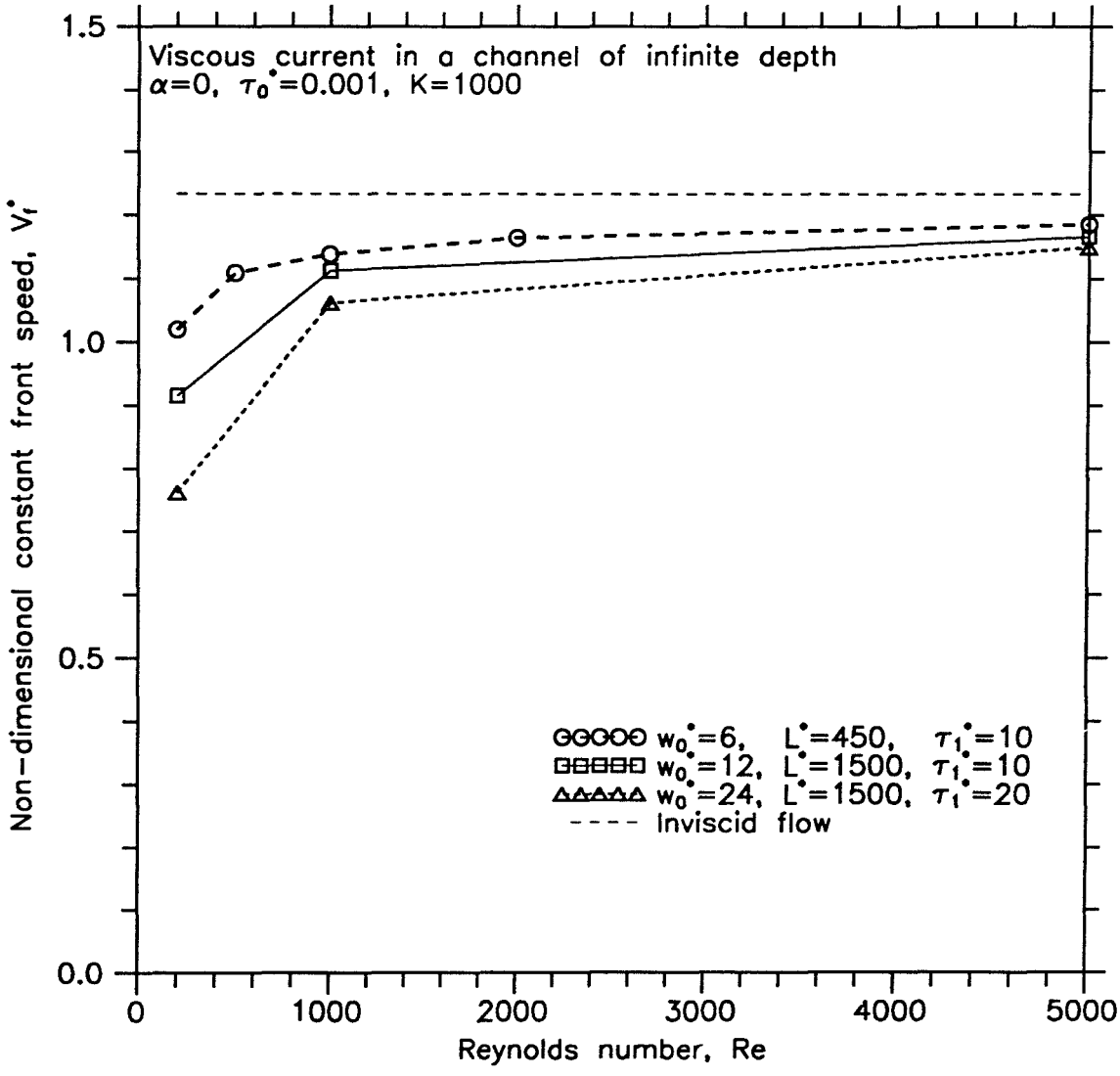

Figure 3.38 Constant front speed as a function of Reynolds number for various inlet length.

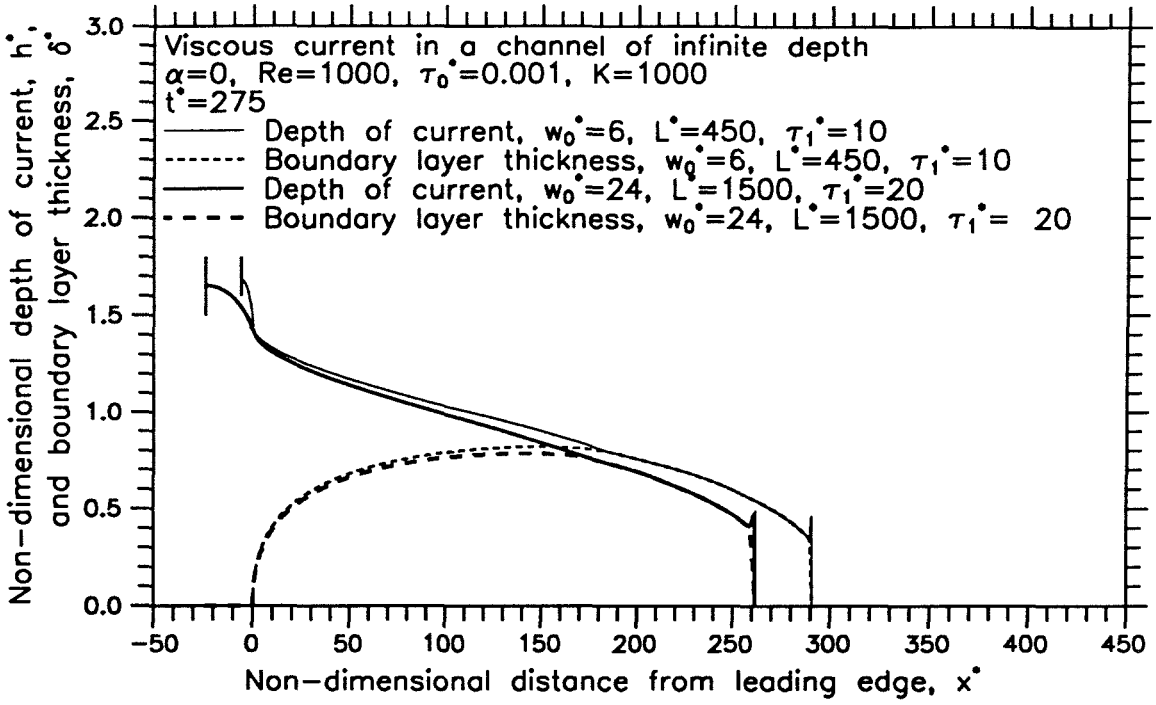

Figure 3.39a Depth of current and boundary layer thickness as a function of distance from the leading edge at $t^*=275$ for Cases 3.3 and 3.10.

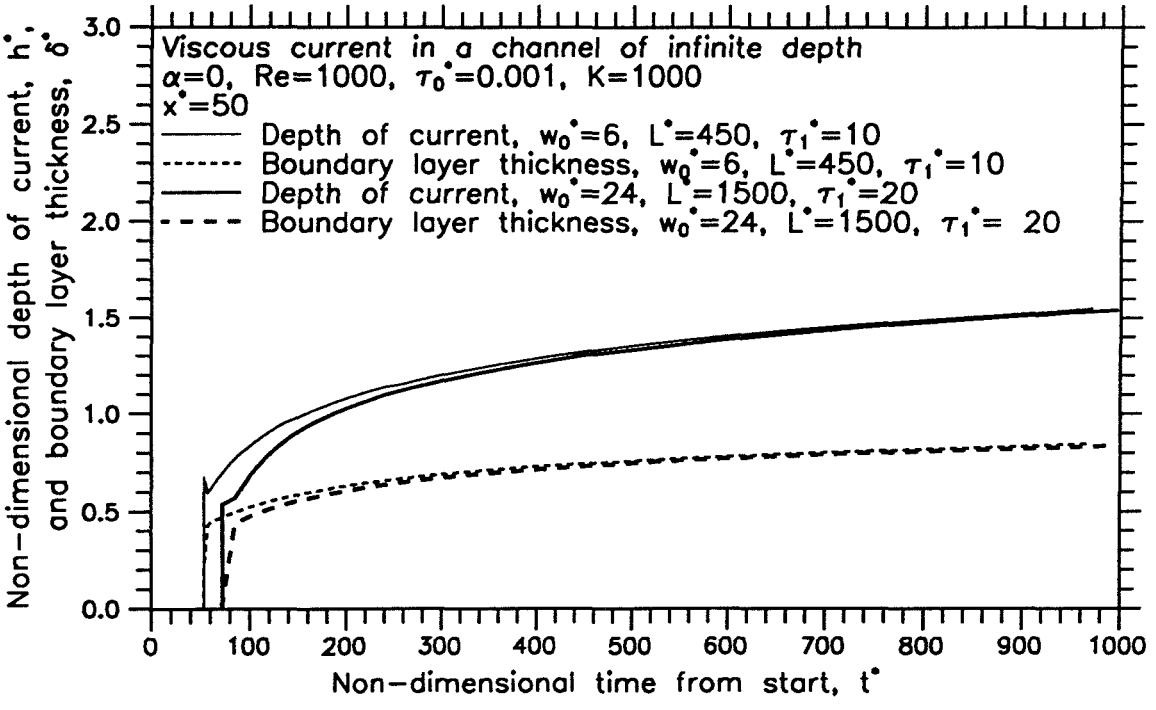

Figure 3.39b Depth of current and boundary layer thickness as a function of time from start at $x^*=50$ for Cases 3.3 and 3.10.

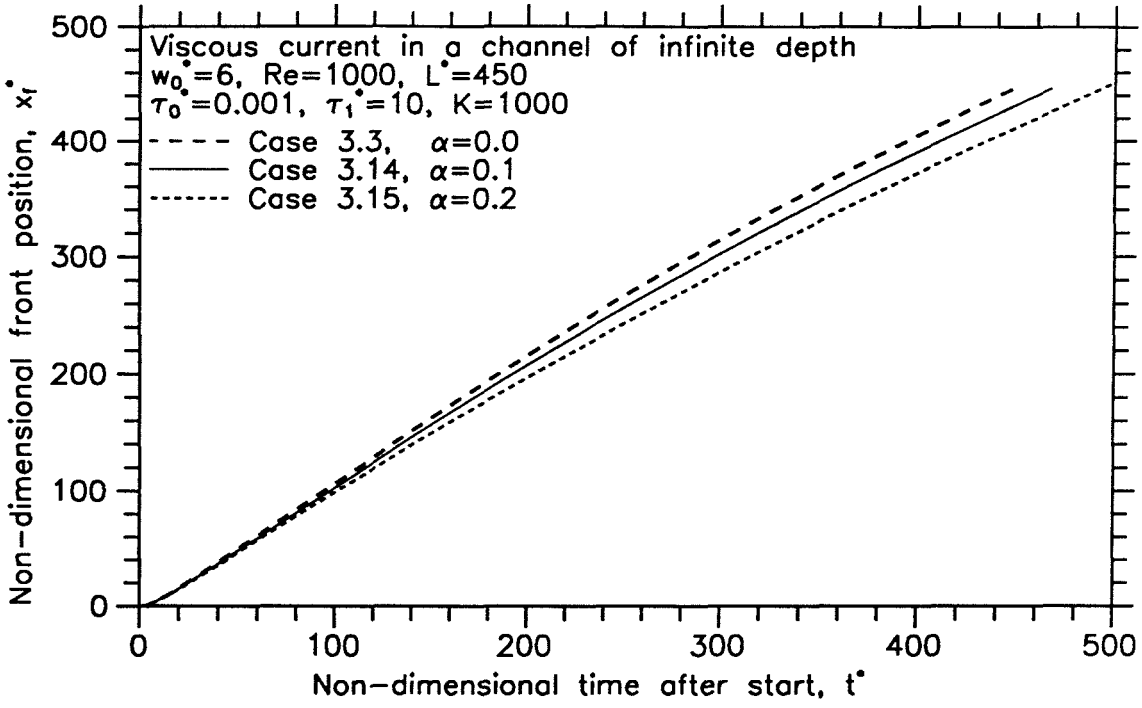

Figure 3.40a Front position as a function of time for Cases 3.3, 3.14 and 3.15.

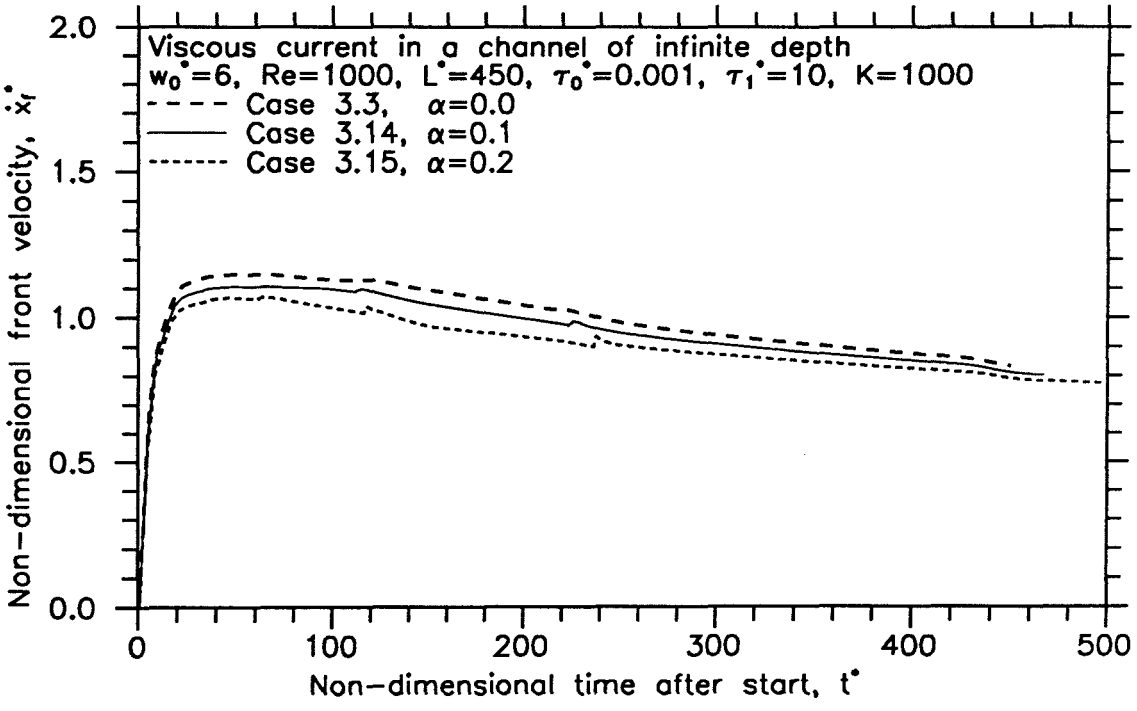

Figure 3.40b Front velocity as a function of time for Cases 3.3, 3.14 and 3.15.

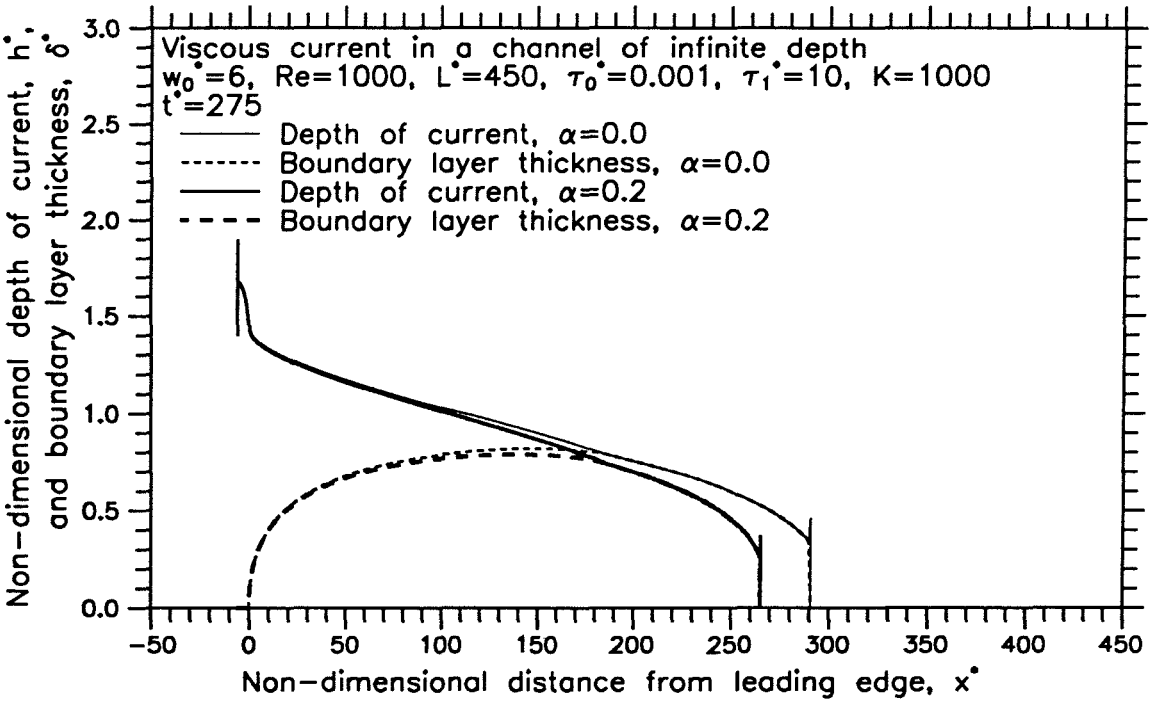

Figure 3.41a Depth of current and boundary layer thickness as a function of distance from the leading edge at t^*=275 for Cases 3.3 and 3.15.

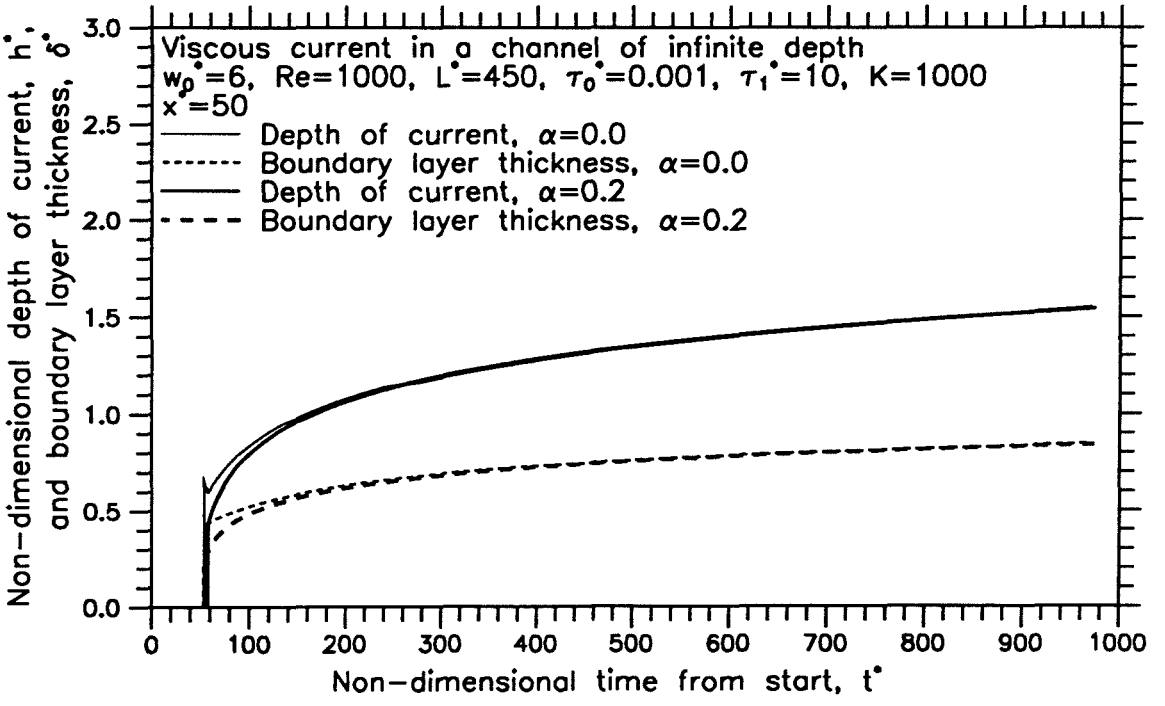

Figure 3.41b Depth of current and boundary layer thickness as a function of time from start at x^*=50 for Cases 3.3 and 3.15.

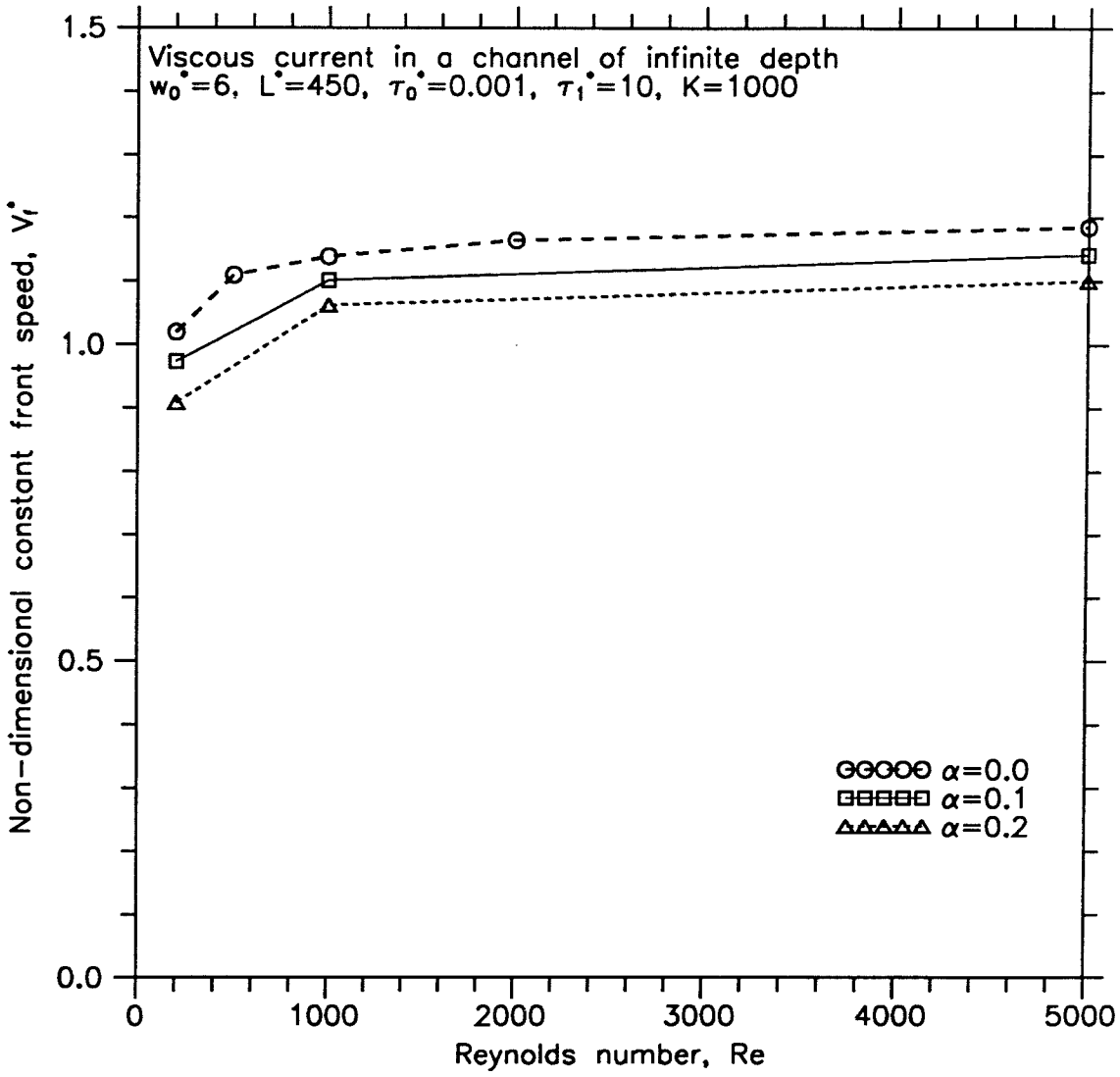

Figure 3.42 Constant front speed as a function of Reynolds number for various rate of loss of working fluid.

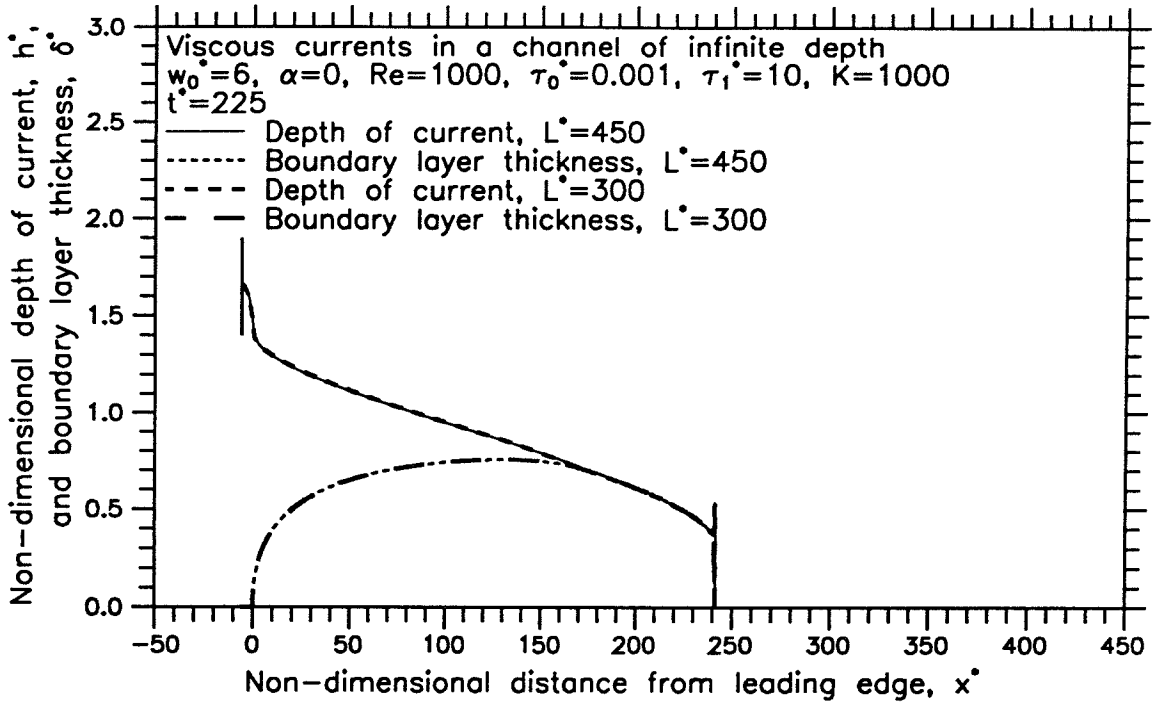

Figure 3.43a Depth of current as a function of distance from the leading edge at t^*=225 for Cases 3.3 and 3.18.

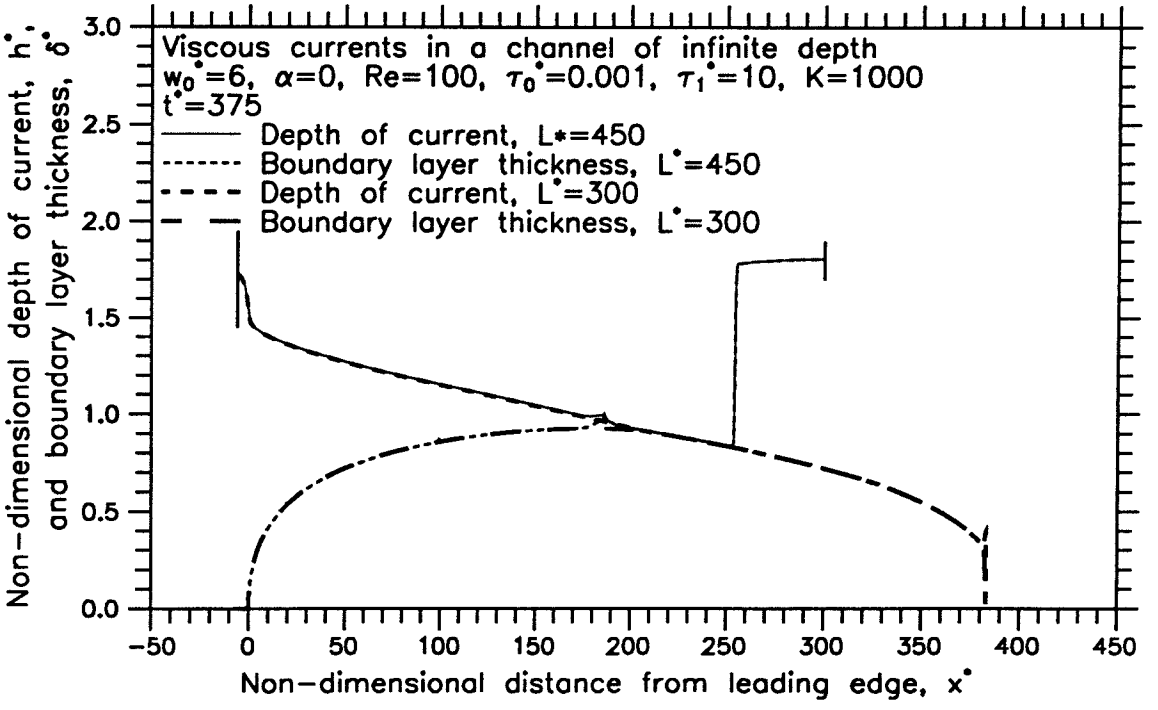

Figure 3.43b Depth of current as a function of distance from the leading edge at t^*=375 for Cases 3.3 and 3.18.

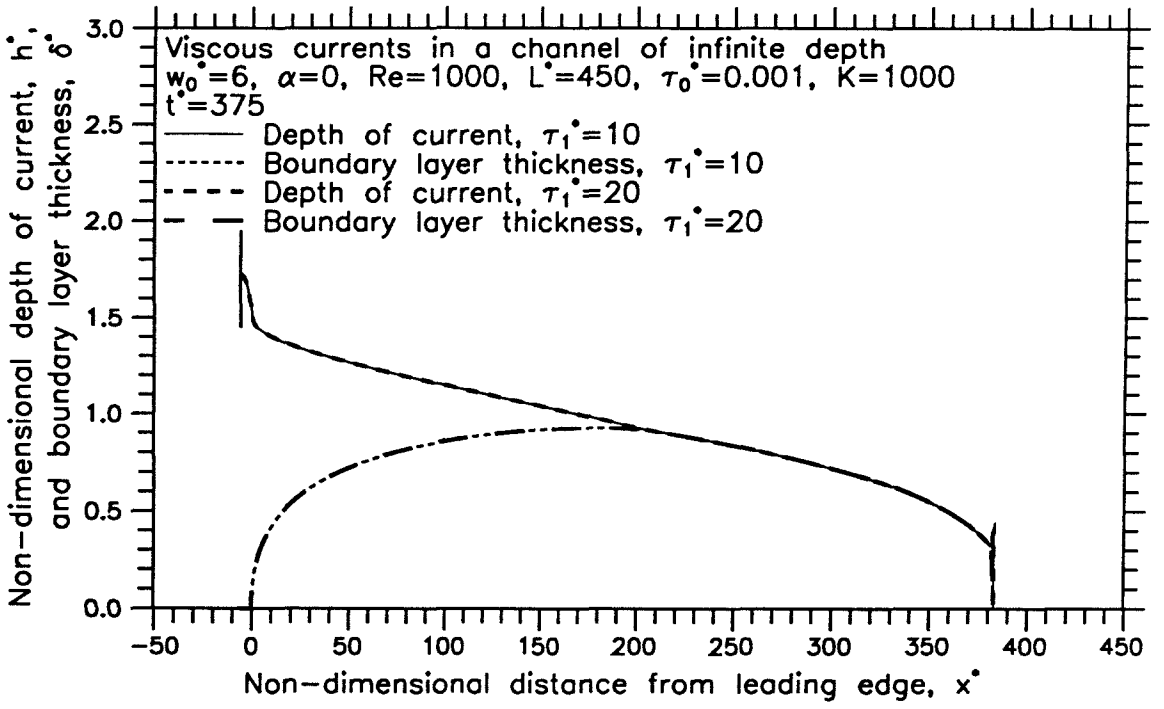

Figure 3.44a Depth of current as a function of distance from the leading edge at t^*=375 for Cases 3.3 and 3.19.

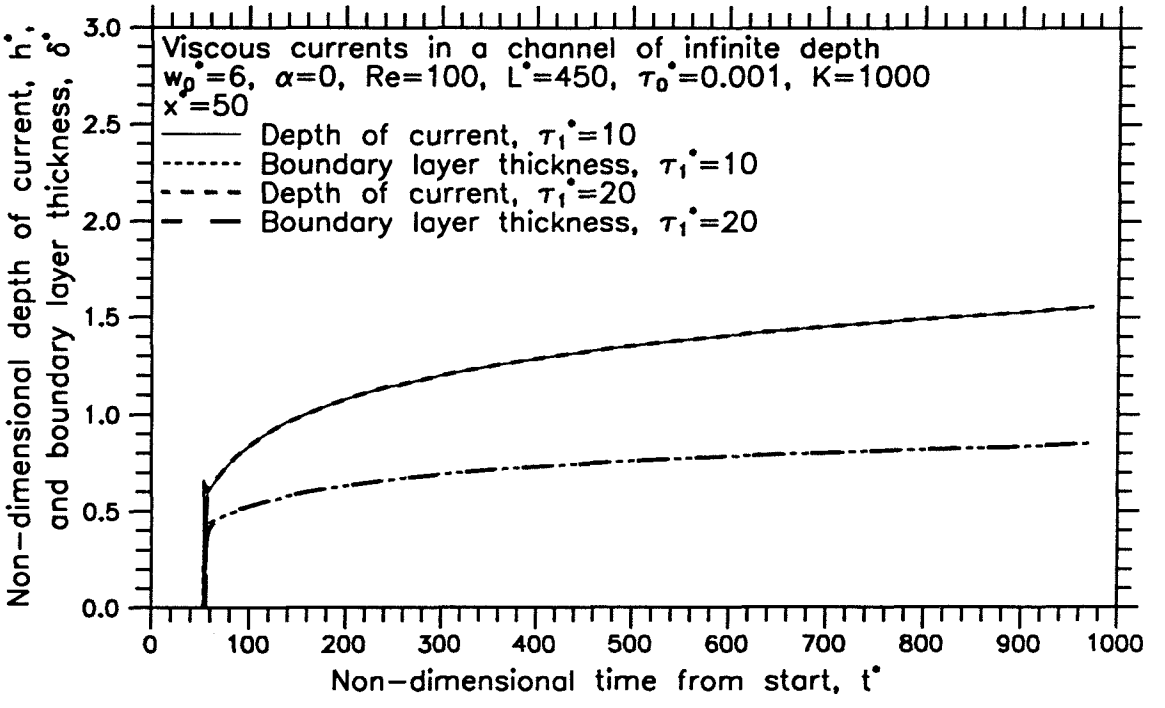

Figure 3.44b Depth of current as a function of time from start at x^*=50 for Cases 3.3 and 3.19.

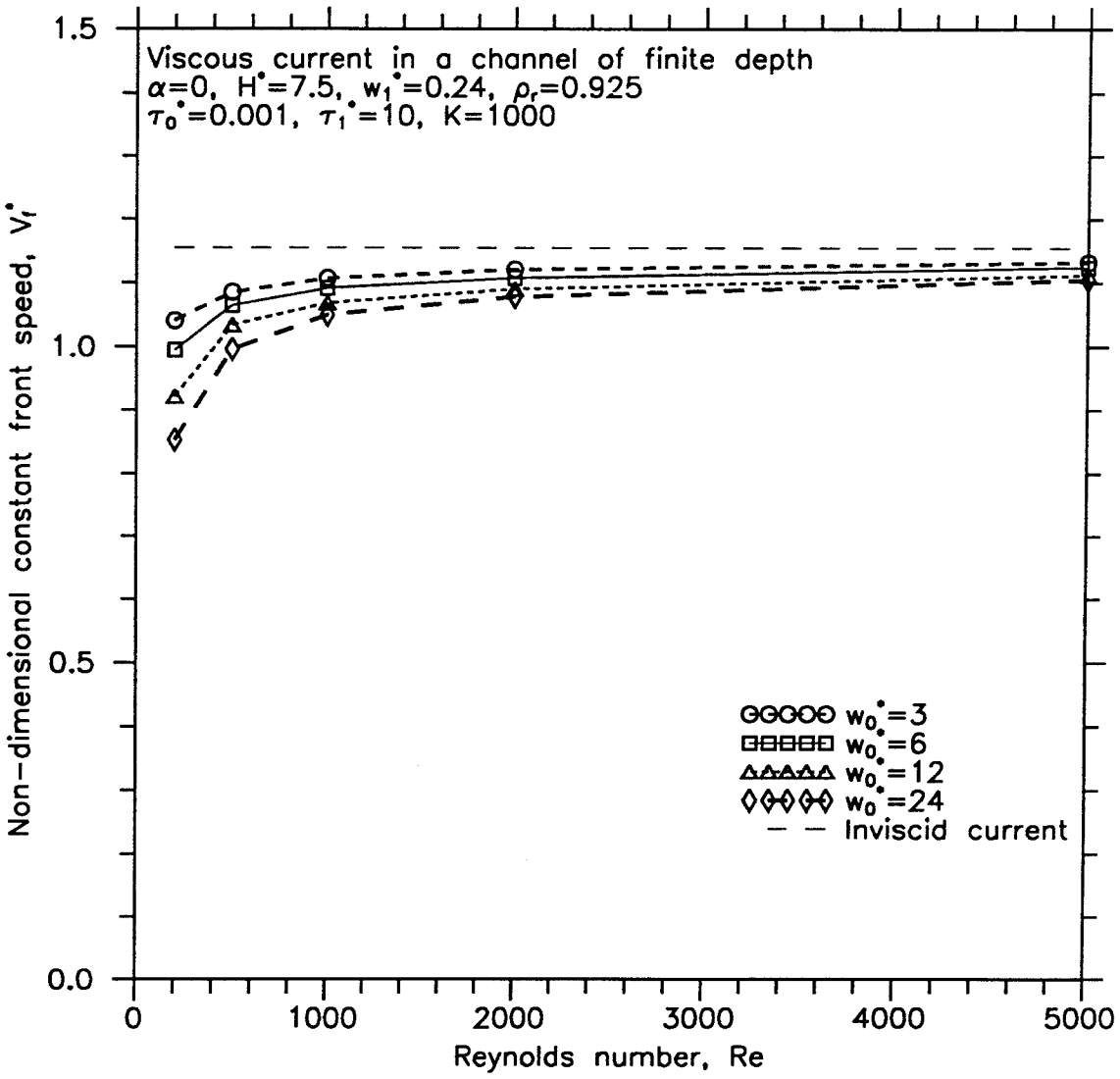

Figure 3.45 Constant front speed as a function of Reynolds number for various inlet lengths.

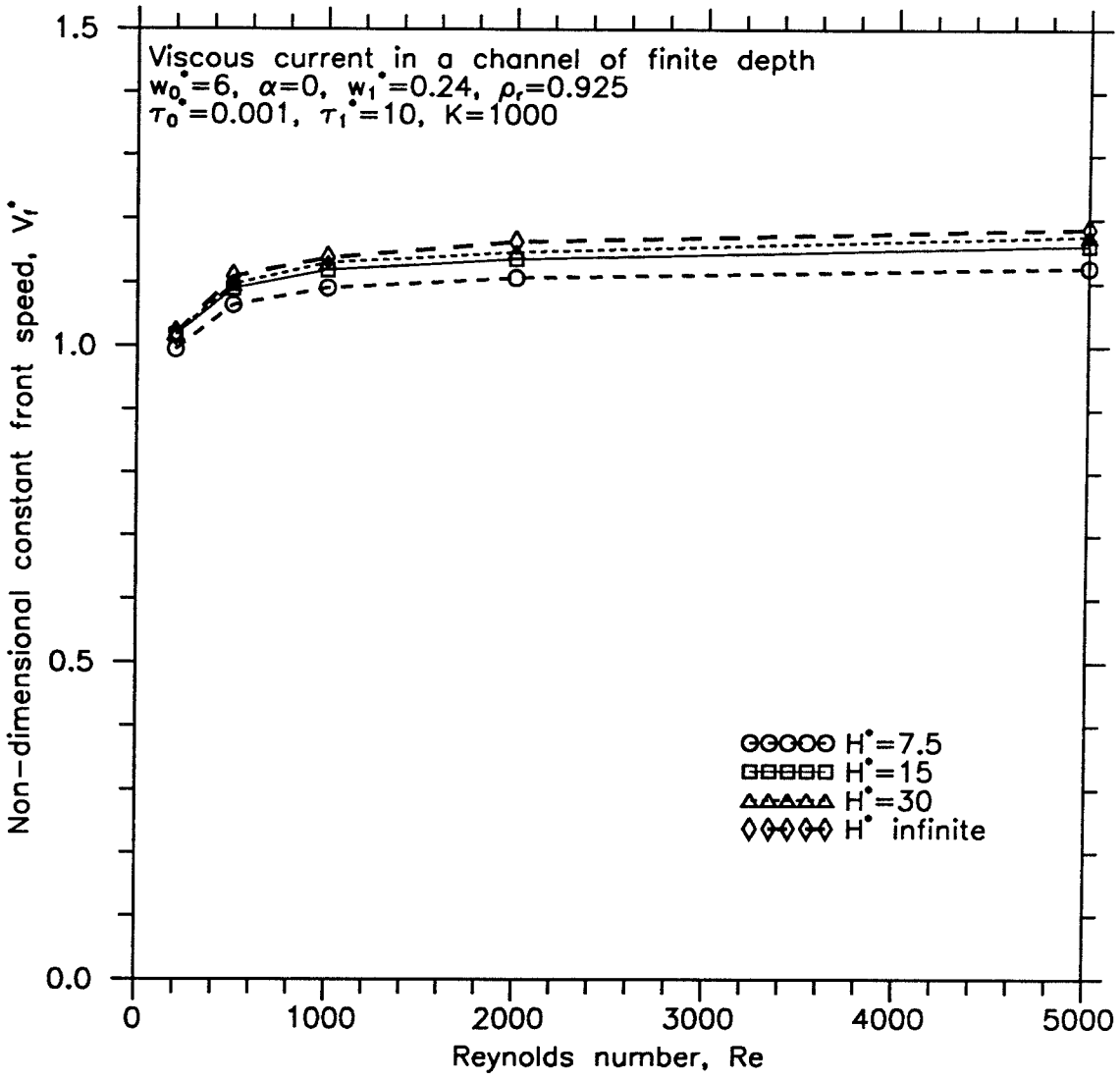

Figure 3.46 Constant front speed as a function of Reynolds number for various channel heights.

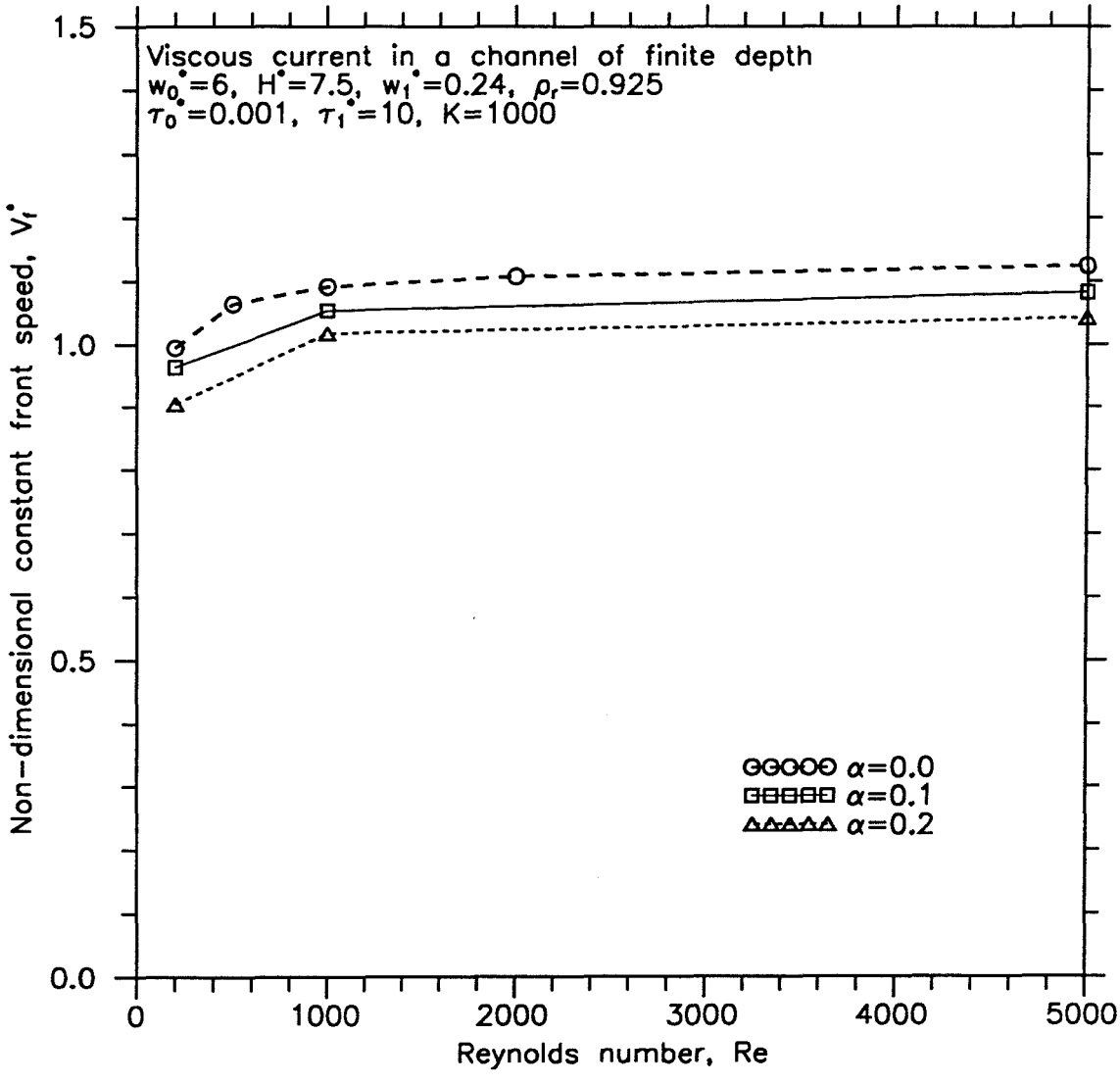

Figure 3.47 Constant front speed as a function of Reynolds number for various rates of loss of working fluid.

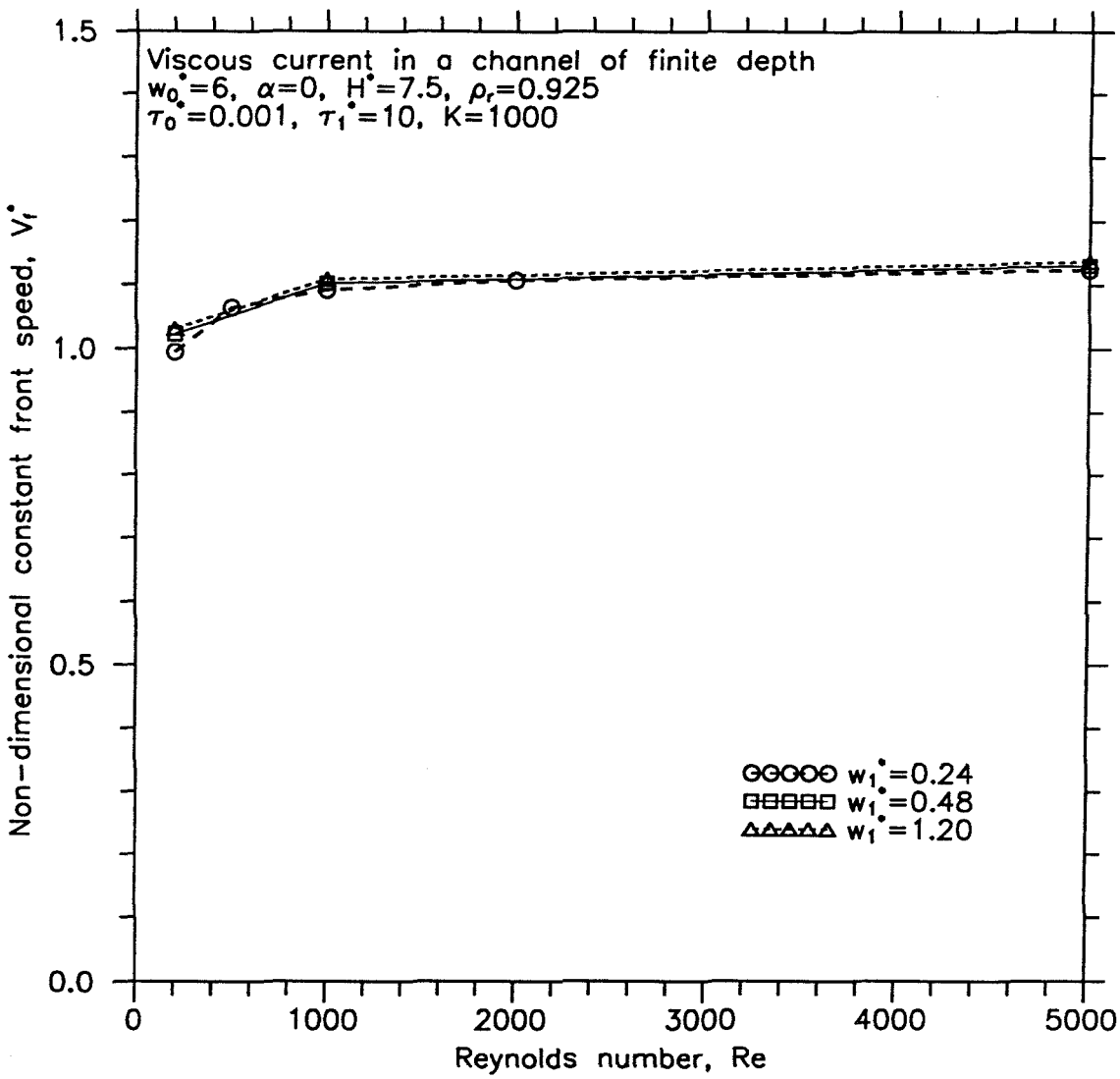

Figure 3.48 Constant front speed as a function of Reynolds number for various outlet lengths.

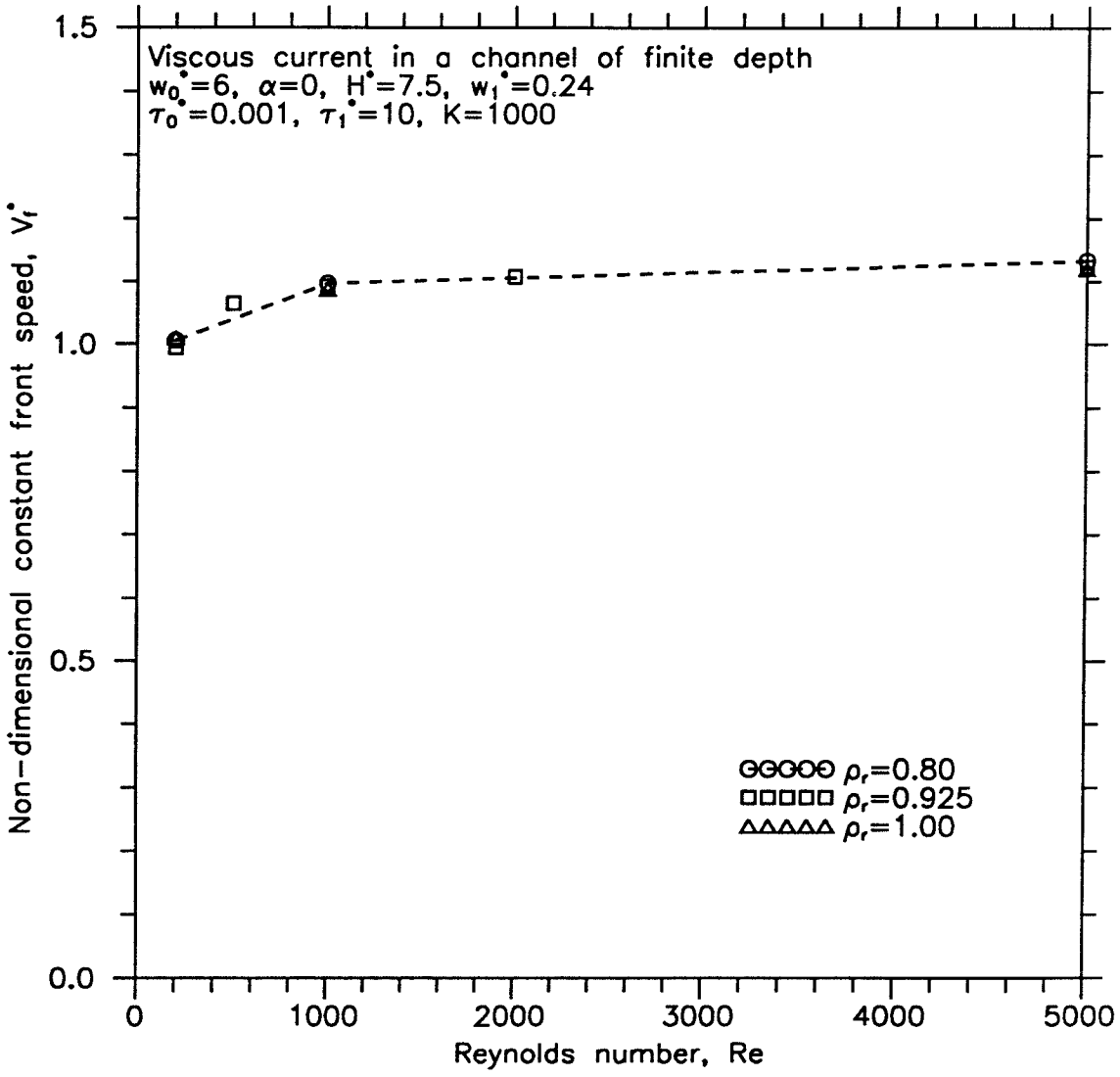

Figure 3.49 Constant front speed as a function of Reynolds number for various density ratio between ambient and working fluids.

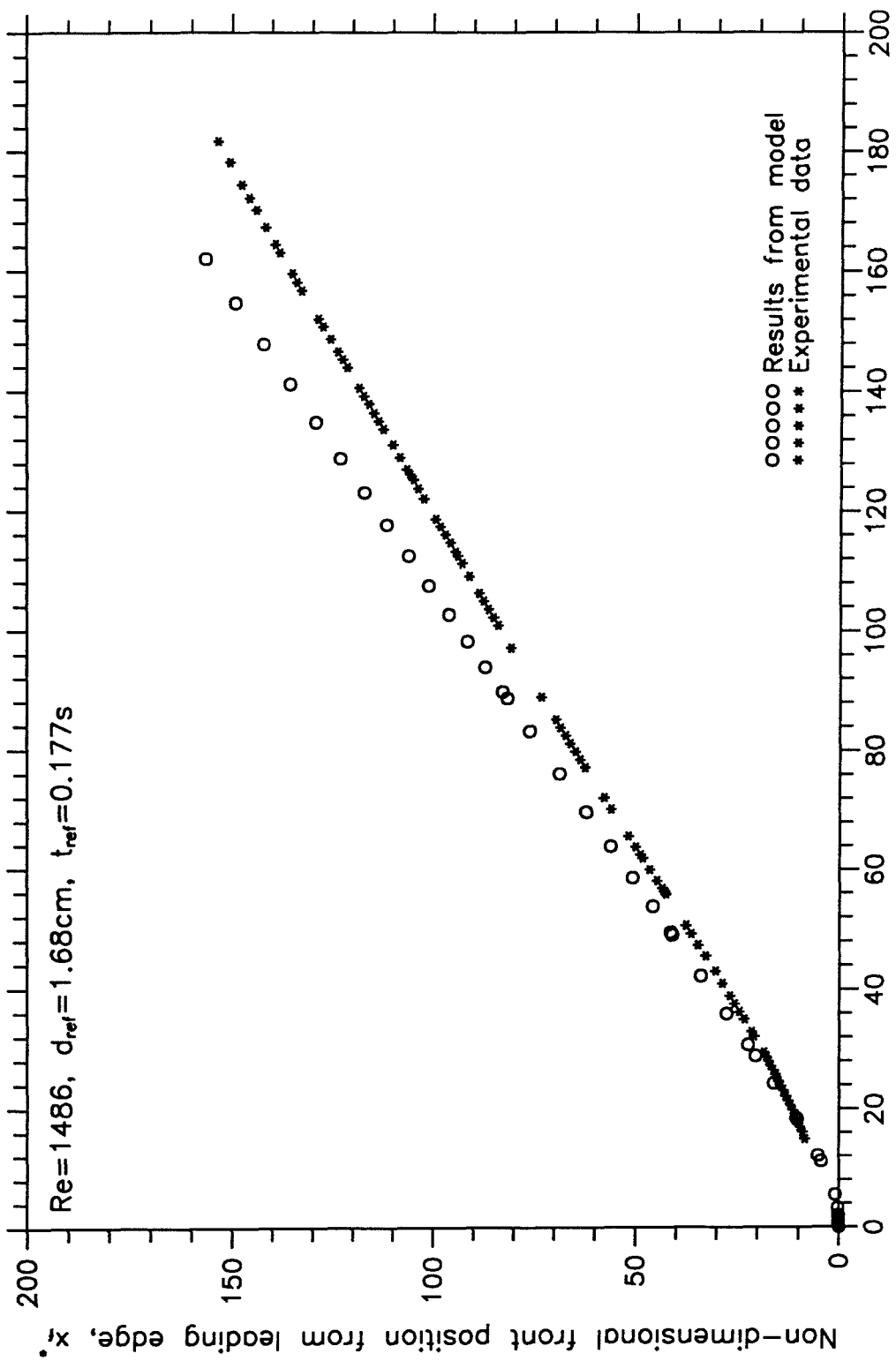

Figure 3.50 Front position from the leading edge as a function of time.

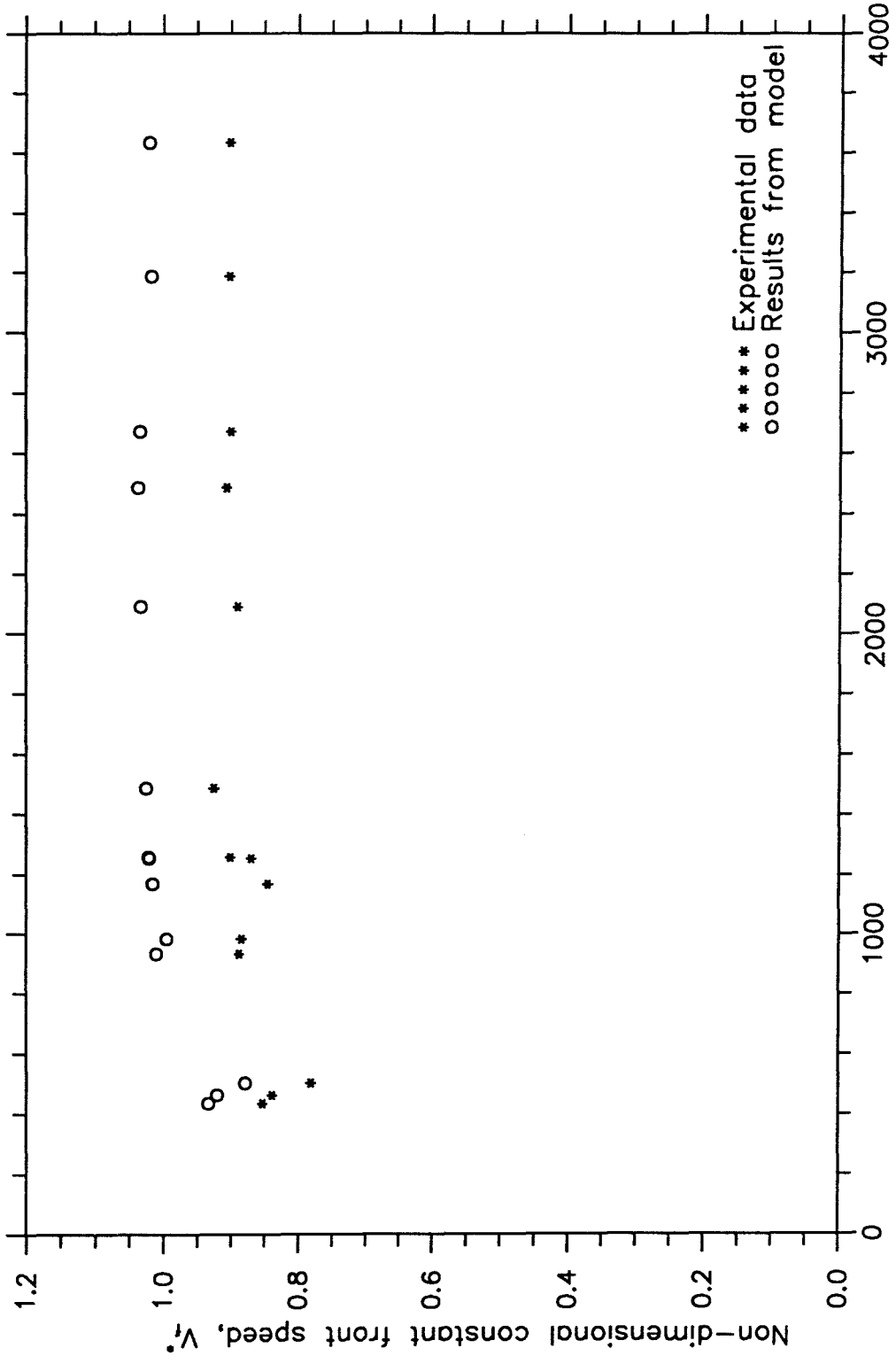

Figure 3.51 Constant front speed in a horizontal duct as a function of Reynolds number.

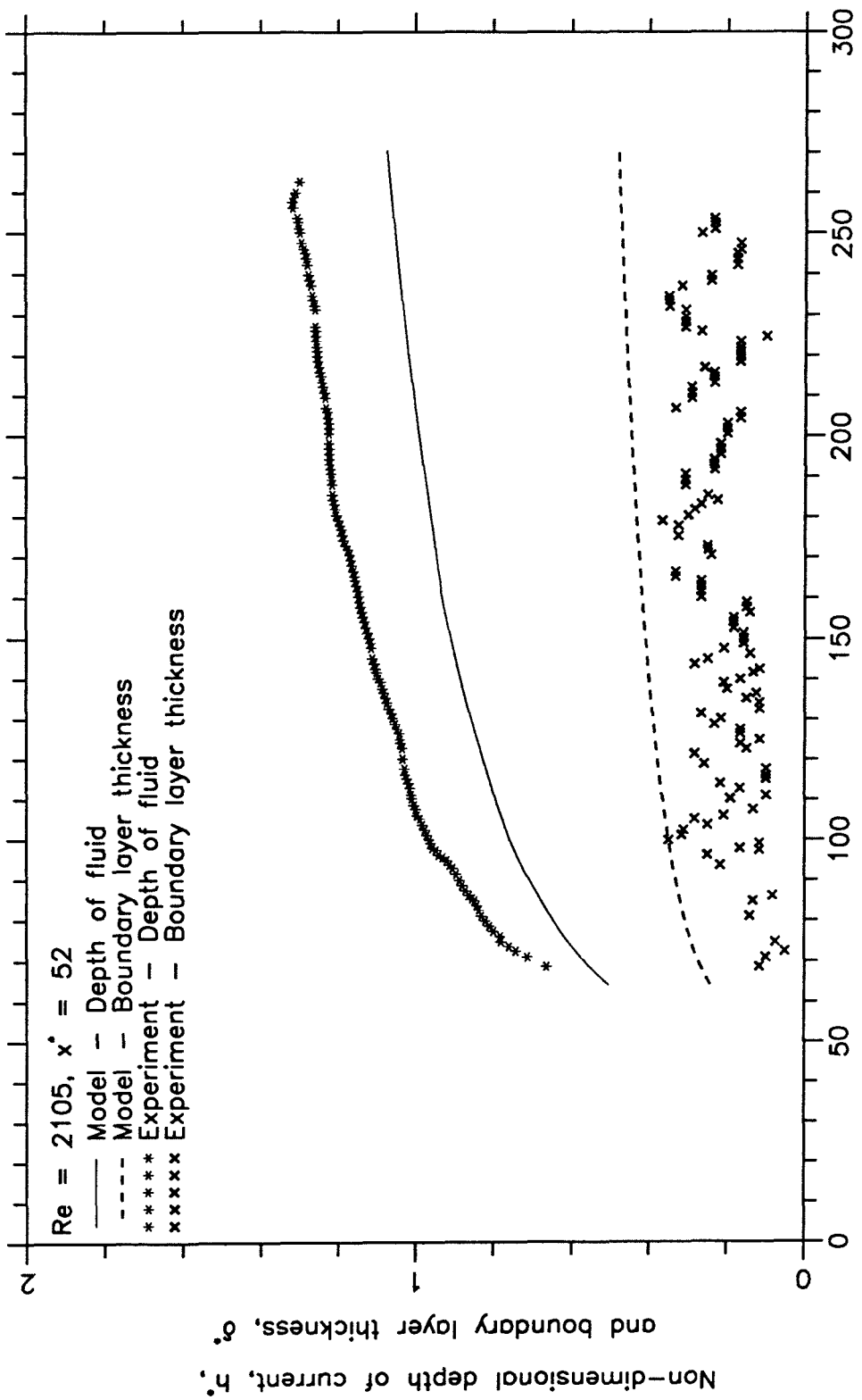

Figure 3.52 Time varying depth of current and boundary layer thickness.

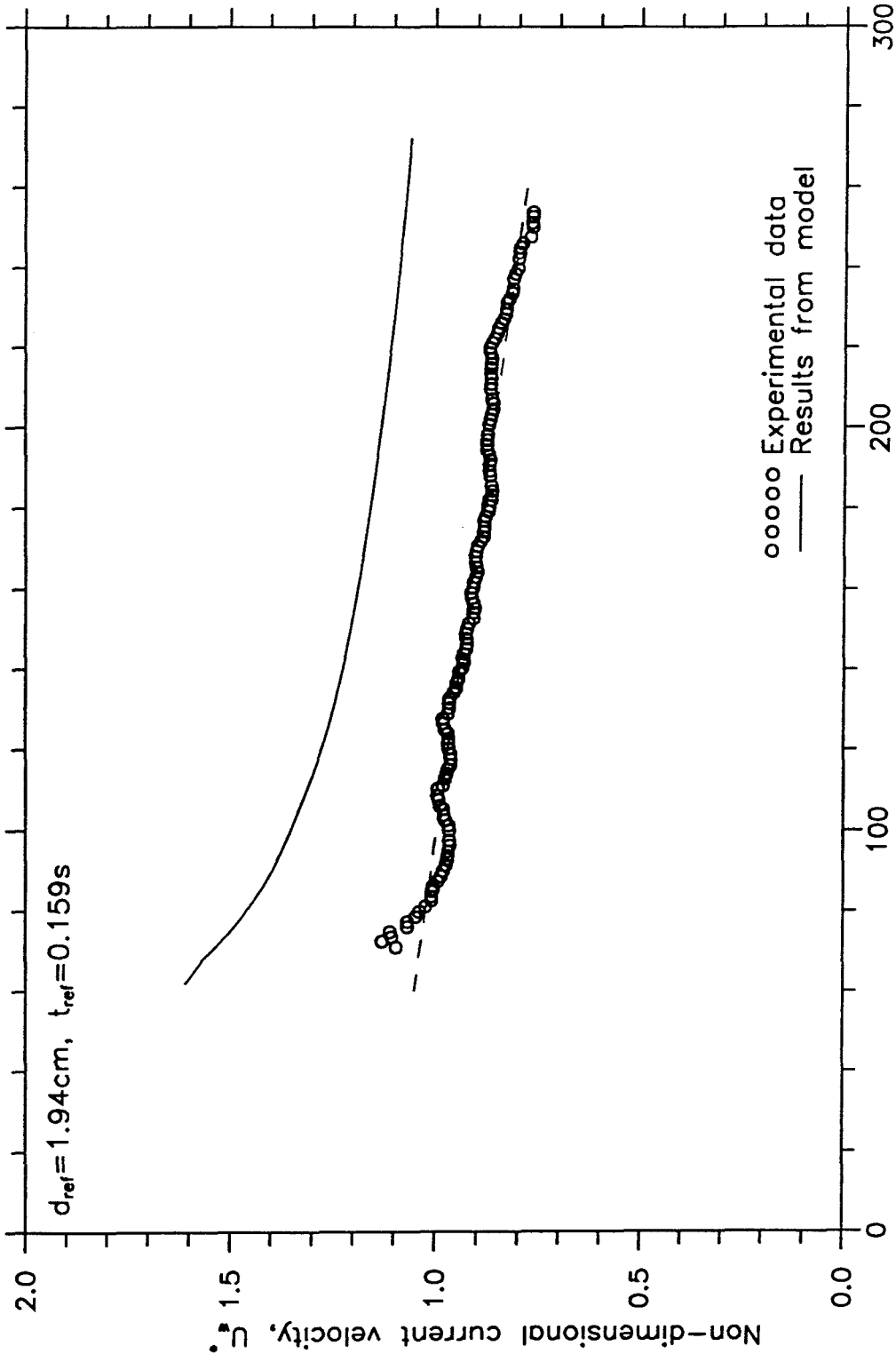

Figure 3.53 Time varying velocity of current at x^*=52 with Re=2105.

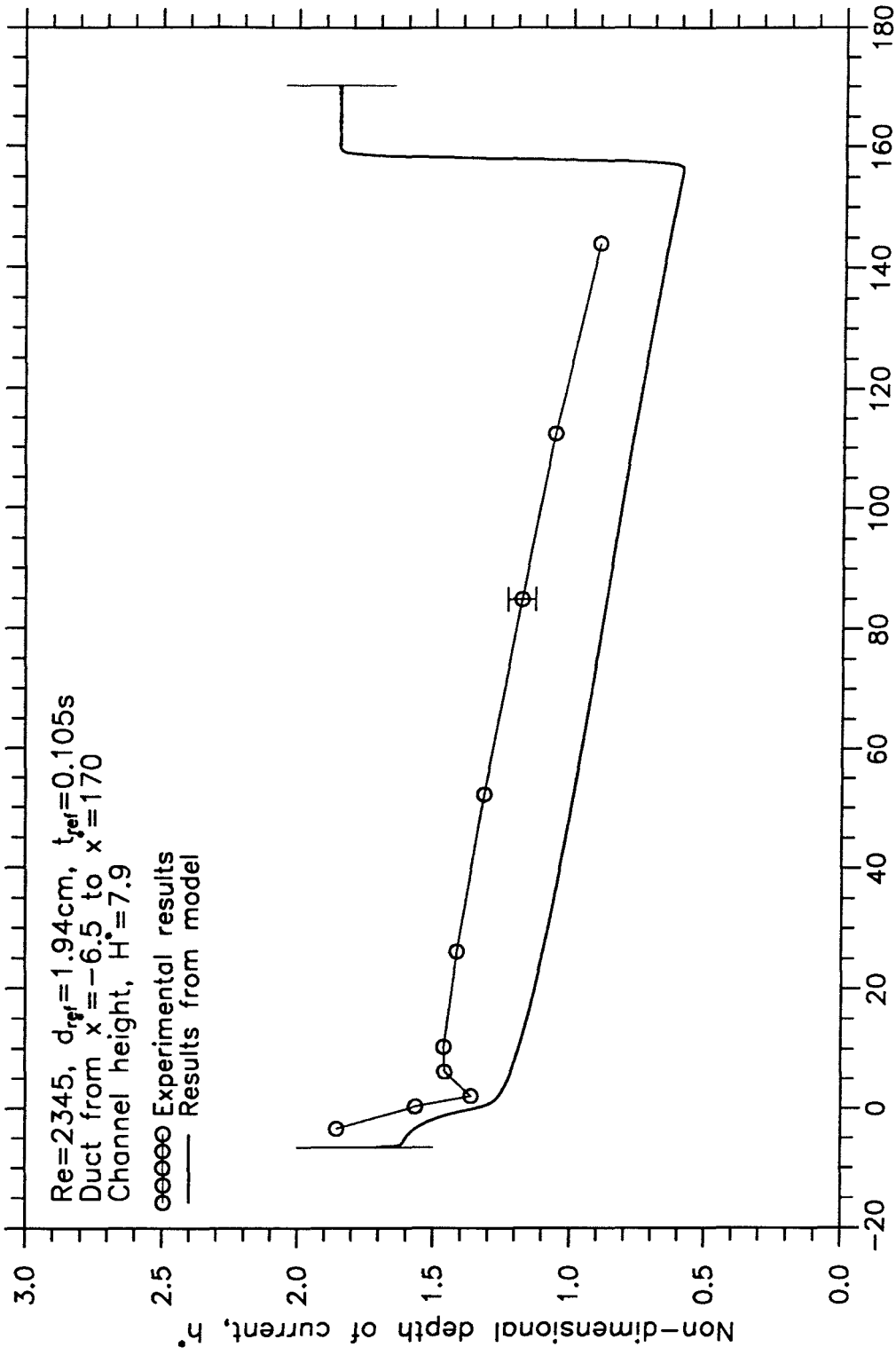

Figure 3.54 Depth of current as a function of distance from the leading edge, t^*=200.

CHAPTER 4

EXPERIMENTAL STUDIES ON GRAVITY CURRENTS IN AN INCLINED CHANNEL

4.1 Introduction

In Chapter 2, experiments conducted to study two-dimensional gravity currents with continuous discharge into a horizontal duct were discussed. In this chapter, experimental studies on two-dimensional gravity currents with continuous discharge into an inclined duct will be described.

The motion of a gravity current in an inclined duct is very different from that in a horizontal channel. It was pointed out in Chapter 2 that the current behind the nose of a gravity current in a horizontal channel remains laminar with a sharp interface and there is no mixing with the ambient fluid. The depth of the following current increases continually as the front spreads downstream.

On the other hand, the head becomes very turbulent at slopes of larger than a few degrees, and its size continues to increase as the front spreads. The whole following current becomes turbulent, and the turbulent region grows in thickness with distance downstream as the ambient fluid becomes entrained into it. Moreover, the velocity of the following current is larger than that of the front, and the difference in the two velocities increases with the angle of inclination. For a sufficiently large Reynolds number, Re, the normalized rate of entrainment, E, was found to decrease with increasing Richardson number, $Ri = \frac{g' h}{U_w^2}$, while the Richardson number was found to increase with decreasing angle of inclination. Ellison and Turner (1959) found that when Ri is larger than 0.8, entrainment is negligible regardless of the angle of inclination of the duct. In addition, when the angle of inclination increases, the head tends to have a steeper leading edge and the length of the head tends to shorten (Wood 1965). As a result, the aspect ratio of the head was found to increase with slope from 0.25 at $\theta = 5^o$ to about 0.5 at $\theta = 90^o$ (Britter and Linden 1980).

In the case of smoke movement in a long corridor, if the length of the corridor is 20 m, a 0.3 m difference in height at the two ends of the corridor would constitute an angle of inclination of 1^{o} on the ceiling. It is thus beneficial to obtain experimental results in nearly horizontal channel and to lay the ground work for future modeling efforts. As a result, Section 4.2 will be devoted to the discussion of experiments on gravity currents conducted in an inclined channel with an angle of inclination, θ, of 1^{o}. In Section 4.3, experimental results for gravity currents conducted in a channel inclined at either 9^{o} or 22^{o} will be described to reveal the difference between gravity currents in nearly horizontal channels and those in channels inclined at more than a few degrees. Finally, experiments on gravity currents with similar discharge rate and reduced gravity but slowly increasing inclination angle of the duct to the horizontal plane will be discussed in Section 4.4, so that a better picture can be obtained for flows in nearly horizontal channels.

4.2 Gravity currents in a duct inclined at 1 degree

4.2.1 Front measurements

Experiments were conducted to determine the time varying front position of gravity currents in a duct inclined at an angle of 1^{o}. The experimental procedures were the same as those used to determine the time varying front position of gravity currents in a horizontal duct, as discussed in Section 2.3.1. Figure 4.1 shows the non-dimensional time varying front position of a gravity current with Re = 2080 in an inclined duct with $\theta = 1^{o}$. The non-dimensional time varying front position of a gravity current with the same input conditions in a horizontal duct is also shown in the figure for comparison. Although both gravity currents experienced a similar initial acceleration stage, it took longer for the gravity current in the inclined duct to enter the principal stage, during which the front speed became constant. Moreover, while the front speed of the gravity current in a horizontal duct continually decreased after it entered the final stage, the front speed of the gravity current in the inclined duct remained constant throughout the time span observed as it spread downstream. None of the experiments carried out during this investigation showed a decline in the front speed for a gravity current in a duct inclined at 1^{o}. Middleton (1966) suggested that in an inclined channel, an equilibrium was set up among the rate of supply of working fluid, the rate of loss of current fluid from the head,

and the rate of dilution due to mixing. As a result, the Froude number of the head remained nearly constant, and the thickness of the following current was less than that in a horizontal channel but the average velocity in the current was larger than that in a horizontal channel. Furthermore, Britter and Linden (1980) indicated that the steady front velocity was produced by a balance between the gravitational force down the slope and the frictional and entrainment drag. It was also found that considerably more mixed fluid was left behind the head as the current advanced downstream in an inclined duct than in a horizontal duct, as more current fluid was supplied and mixed into the head and the mixed fluid was then left behind the head. After the front of the current had hit the downstream end wall, the reflected bore advanced upstream, similar to the case of a gravity current in a horizontal duct. However, the constant speed of the reflected bore decreased continually because it was running up a slope. As a result, a constant return speed could not be determined for the reflected bore.

The non-dimensional constant front speed, V_f^*, of gravity currents in a duct inclined at 1^o was determined for $200 < Re < 4200$. The value of V_f^* as a function of Re is shown in Figure 4.2. For $Re < 600$, V_f^* appeared to be significantly lower than that for $600 < Re$. The average value of V_f^* for the experiments conducted in an inclined channel with an upstream exit was 1.07 ± 0.05 for $600 < Re$. This average value is shown as the dashed line in the figure, and is 20% higher than the corresponding value for gravity currents in a horizontal channel. For the experiments conducted in a channel with a downstream exit, the value of V_f^* was almost constant at 1.11 ± 0.01 for $600 < Re$. Although this value is slightly larger than the corresponding value for the experiments conducted in a channel with the same angle of inclination and with an upstream exit, it is within one standard deviation of that value and the two values can be considered as similar. Using the average value of V_f^* together with the average value of the non-dimensional head height, h_1^*, to be shown in Section 4.2.2, the average Froude number, $Fr = \frac{V_f}{\sqrt{g' h_1}}$, obtained in a 1^o duct in the present study has a value of 0.76, which is in excellent agreement with that found by Middleton (1966), which has a value of 0.76 ± 0.05.

4.2.2 Measurements of the depth of the gravity current

A gravity current in an inclined duct, similar to a gravity current in a horizontal duct, also has a raised head with a shallower following current. However, contrary to the case of a horizontal duct, the depth of the following current, h_c, at a particular location in an inclined duct does not increase continuously with time. Instead, it reached a constant value quickly and maintained that value until the arrival of the reflected bore. This is revealed in Figure 4.3, which shows the depth of the gravity current in Test 335, with Re = 2255, at x* = 22 and x* = 72. It was found that the non-dimensional head height, h_1*, increased slightly with the distance from the leading edge of the bottom wall, x*. On the other hand, there is no evidence that the non-dimensional depth of the following current in an inclined duct, h_c*, changed with x*. The amplitude and the wavelength of the reflected bore were not found to be constant, as in the case of a gravity current in a horizontal duct. It was also observed during the experiment that the mixed layer of fluid left behind by the head in an inclined duct was deeper than that in a horizontal duct. The interface between the current and the mixed layer in an inclined duct did not appear as sharp and distinctive as in the case of a gravity current in a horizontal duct. As a result, the uncertainty in the measurement of the current depth in an inclined duct was larger than that in a horizontal duct. It also appeared that some fluid in the mixed layer was entrained across the interface and into the layer of ambient fluid. However, the amount of this entrainment is small, since the rate of entrainment, E, found by Ellison and Turner (1959), can be given by $E = 1.75 \times 10^{-5}$.

Figure 4.4 shows the non-dimensional head height, h_1*, as a function of the distance from the leading edge of the bottom wall, x*. Experiments were only carried out in a duct with an upstream exit and an angle of inclination of 1^o. For 600 < Re, the value of h_1* increased from 1.64 at x* = 20 to 2.27 at x* = 110, with a weak dependence on Re. Thus, the rate of change of h_1 with respect to x, dh_1/dx, is 7×10^{-3}. This increase in head height with respect to downstream distance is due to the continuous supply of working fluid from the following current into the head. Bitter and Linden (1980) also conducted experimental measurements of dh_1/dx, but only for $5^o < \theta$. According to extrapolation of the data presented in Figure 8 of that paper, the value of dh_1/dx would be 4×10^{-3}, which is in good agreement with the present data since, due to the small value of dh_1/dx, a small error in measurement could lead to a large difference in dh_1/dx.

On the other hand, Figure 4.5 shows the corresponding non-dimensional depth of current, h_c^*, as a function of distance from the source, x^*. It can be seen that the value of h_c^* was independent of Re, and it can be shown to have at most a very weak dependence on x^*. For practical purposes, h_c^* is assumed to be independent of x^*. For $600 < Re$, the value of h_c^* was found to be 0.81 ± 0.05 for $20 < x^* < 110$. Although it was found that in an inclined duct $dh_c/dx > 0$ (Ellison and Turner, 1959) due to increased entrainment of the ambient fluid into the following current, the rate of entrainment at 1^o was found to be negligibly small.

4.3 Gravity currents in a duct inclined at a higher angle of inclination

4.3.1 Front measurements

Britter and Linden (1980) suggested that at large Reynolds numbers, the constant front speed, V_f^*, is only a function of the slope angle. Experimental results of the time varying front position were also obtained for a duct inclined at 10^o and at 22^o. It was noticed that the shape of the front differs slightly from those seen in a horizontal duct. The nose was less pointed and the ratio of the head height to the head length was larger than those found in a horizontal duct. The following current was visibly more turbulent, and the interface between the current and the ambient fluid was no longer clearly defined. The amount of entrainment from the ambient fluid into the current increased with the angle of inclination, as judged by the color of the current. As the head of the current advanced downstream, the size of the head as well as those of the vortices shed behind the head continued to increase until they nearly filled the height of the whole channel.

Figure 4.6 shows the non-dimensional time varying front position of Test 469, with Re = 1613 and $\theta = 10^o$. It can be seen that after an initial acceleration period, the front then propagated at a non-dimensional constant speed, V_f^*. However, at $x^* \cong 120$, the front slowed down and from then on it propagated at a slower but still constant speed. This position of transition from one constant speed to another is denoted by $x_t'^*$, and is shown as a function of the channel height, H^*, in Figure 4.7. It is obvious from the figure that this transition position increases monotonically with respect to H^* and is not a function of Re. The value of $x_t'^*$ increased from 73 when $H^* = 7$ to 169 when $H^* = 14$.

No dependence of $x_t'^*$ on the exit condition was detected. For a gravity current in a channel which is much deeper than the current and the head, Britter and Linden (1980) found that the front speed would remain constant regardless of the front position. Therefore, it is concluded that the front slowed down when the head height increased to a point that it was no longer small when compared to the total channel height. The buoyancy force and the gravitational component could no longer compensate the increased retarding forces due to the increased blockage ratio. As a result, the front speed slowed down, and a new steady state was reached in which the head height remained constant. Thus, the cause of this transition position, $x_t'^*$, is different from the cause of the transition position in a horizontal channel, x_t^*, which is due to viscous effects on the bottom wall. Due to the large fluctuation of the shape of the head, no precise measurement of the blockage ratio was taken at the time of the transition, $x_t'^*$. However, it was noticed that the head height was always larger than half the channel height when transition occurred.

The non-dimensional constant front speed, V_f^*, in a channel inclined at 10^o was shown as a function of Reynolds number, Re, in Figure 4.8, while Figure 4.9 showed the corresponding plot for a channel inclined at 22^o. When $600 < Re$, V_f^* was found to be constant at both $\theta = 10^o$ and 22^o. The average value of V_f^* for $600 < Re < 2100$ at $\theta = 10^o$ was 1.34 ± 0.05, while the average value of V_f^* for $600 < Re < 1800$ at $\theta = 22^o$ was found to be 1.32 ± 0.09. By comparing Figures 4.2, 4.8 and 4.9, it is obvious that the average value of V_f^* increased with the angle of inclination when θ increased from 1^o to 10^o, but the value of V_f^* did not change significantly between $\theta = 10^o$ and $\theta = 22^o$. Moreover, the amount of scattering of the data increased significantly with the increase in θ, though no dependence on the exit condition or Reynolds number was apparent.

For large Reynolds numbers, Britter and Linden (1980) obtained an expression that describes the non-dimensional constant front speed, V_f^*, as a function of a shape factor, S_2, the angle of inclination, θ, the rate of entrainment, E, the drag coefficient due to stress at the lower boundary, C_D, and γ, the ratio of the velocity of the fluid on the streamline that stagnates at the front of the current to the mean velocity of the following flow. This expression is given as Equation (4.4) in Britter and Linden, and is reproduced below:

$$V_f^* = S_2^{1/3} \left(\frac{\cos\theta}{\gamma} + \frac{\gamma \sin\theta}{2\,(E + C_D)}\right) \left(\frac{\sin\theta}{E + C_D}\right)^{-2/3}.$$

It was proposed that $E = 1.75 \times 10^{-5}\,\theta$, $\gamma \cong 1.2$, $C_D \cong 3 \times 10^{-3}$, and $S_2 \cong 0.75$. Using these values in the expression, the calculated value of V_f^* would be 1.43 for $\theta = 10^o$ and 1.46 for $\theta = 22^o$. Although the values of V_f^* found in the present investigation are up to 10% lower than those found in Britter and Linden, they are well within one standard deviation of the data as reported by Britter and Linden, which was ±0.2.

Similarly, Wood (1965) obtained average experimental values of $V_f^* = 1.24 \pm 0.08$ at $\theta = 6^o$ and $V_f^* = 1.51 \pm 0.17$ at $\theta = 28^o$. If it is assumed that the change in V_f^* with respect to θ is monotonic in Wood's experiments within this range of θ, then the experimental results obtained in the present study for $\theta = 10^o$ and $\theta = 22^o$ are within one standard deviation of the results obtained by Wood.

4.3.2 Measurements on the depth of the current

Experimental results of the non-dimensional time varying head height of gravity currents, h_1^*, in a 10^o duct is shown as a function of the non-dimensional distance from the leading edge of the bottom plate, x^* in Figure 4.10. Experiments were only conducted in a channel with an upstream exit. It is obvious from Figure 4.10 that the head height increased with downstream distance. This agrees with the observation of Britter and Linden (1980), who reported that the nose became very turbulent and built up continually to many times the thickness of the following layer. The velocity of the front was smaller than that of the following layer. Moreover, none of the fluid in the following layer escaped, and transfer was always into the current. As a result, the value of h_1^* increased from 2.74 at $x^* = 30$ to 3.23 at $x^* = 100$. It is concluded that the rate of change of h_1 with respect to x, dh_1/dx, is equal to 7×10^{-3}, which is the slope of the dashed line. This is much smaller than that found by Britter and Linden, who obtained a value of roughly 0.04. There are two explanations for this discrepancy. First of all, all the experiments reported here were conducted with $g' > 20$ cm/s^2, since Middleton (1966) reported the tendency of the head being diluted by the mixing in of water at the back of the head at low values of g'. While Britter and Linden did not report explicitly

the values of g' used in their experiments, it was deduced from their reported values of (g' Q) that, in order to obtain a reasonably large value of Reynolds number, $g' < 20$ cm/s^2 in most of their experiments. The second explanation is that the head height as reported in the present study was taken as the maximum depth of the current before the visible breaking of the first vortex, while Britter and Linden used the maximum depth of the head structure, possibly including the shed vortices. The difference between the values of the two depths is not trivial, and might have contributed to the discrepancy.

Due to the turbulent nature of the following current, the interface between the following current and the ambient fluid was fluctuating as well as ill-defined. As a result, any measurement of the depth of the following current, h_c^*, was subject to large error. Experimental data obtained on the depth of the following current in a 10^o duct is shown as a function of distance from the leading edge in Figure 4.11. According to Britter and Linden, the measured value of dh_c^*/dx^* in a 10^o duct by Ellison and Turner (1959) was between $5x10^{-3}$ and $1.1x10^{-2}$, with the average value at roughly $8x10^{-3}$. Since Ellison and Turner reported a non-dimensional mean velocity of 1.49 in a 10^o duct, the non-dimensional depth of the current at $x^* = 0$ is $h_c^* = 0.67$. This result is shown as the dashed line in Figure 4.11, and it falls well between the experimental data in the present investigation. Since the measurement error as described above is apparently large, no definitive and quantitative conclusion about dh_c^*/dx^* can be drawn from this figure.

4.4 Effects of a small angle of inclination on gravity currents

Experiments were conducted to investigate the effects of a small angle of inclination of the duct on gravity currents with a continuous discharge. The main goal of this series of experiments was to determine whether the transition from an unsteady current in a horizontal channel to a steady one in an inclined duct is a gradual transition or an abrupt one. Table 4.1 provides the conditions used in the series of experiments.

Test number	Q (cm^2/s)	g' (cm/s^2)	θ (deg.)	V_f*	V_r*
482	23.6	93.3	-0.2	0.87	0.84
483	23.5	100.7	0.0	0.89	0.76
484	23.5	99.2	0.3	0.94	0.72
485	23.5	99.2	0.6	0.94	0.65
486	23.6	95.3	0.8	0.99	0.58

Table 4.1 Experiments conducted to investigate the effects of a small angle of inclination on gravity currents.

It can be seen that the volumetric discharge rate per unit width, Q, and the reduced gravity, g', were similar for each experiment. On the other hand, the angle of inclination, θ, increased from -0.2^o in Test 482 to 0.8^o in Test 486. In Test 482 through Test 484, the transition from an inertia-buoyancy regime to a viscous-buoyancy regime was clearly observed with $x_t^* < 90$. However, the speed of the front of the gravity current in Tests 485 and 486 did not change within the non-dimensional length of the duct, $L^* = 148$. Figure 4.12 shows graphically both the non-dimensional constant front speed, V_f^*, and the non-dimensional constant speed of the reflected bore, V_r^*, as functions of the angle of inclination, θ. Experimental data by Middleton (1966) is also shown in the figure assuming a value of non-dimensional head height $h_1^* = 1.7$ at $\theta = 0.3^o$ and $h_1^* = 1.8$ at $\theta = 0.6^o$. The non-dimensional constant front speed gradually increased from 0.87 to 0.99 when θ was increased from -0.2^o to 0.8^o, while the non-dimensional constant speed of the reflected bore decreased from 0.84 to 0.58 within the same range of θ. The dashed lines are linear least square fits to the two sets of data, and they are represented by $V_f^* = 0.11\,\theta + 0.89$ and $V_r^* = -0.24\,\theta + 0.78$, respectively. These expressions yield $V_f^* = 0.89$ and $V_r^* = 0.78$ at $\theta = 0$, which agree excellently with the average experimental values obtained in Chapter 2.

More illustrative observations can be made when the depths of the gravity currents are compared for the above tests at the same distance downstream from the leading edge of the bottom wall. Figure 4.13 shows the non-dimensional depth of the

current, h*, at a non-dimensional distance x* = 29 from the source for each of the five tests listed in Table 4.1. In the figure, it is clear that since x* is not large, the front of each gravity current arrived at roughly the same non-dimensional time with a similar head height and a similar initial depth of the current. However, each gravity current displayed a different rate of increase for its depth with time. The rate of increase in the depth of a gravity current decreased when the angle of inclination increased.

When the angle of inclination was equal to or larger than 0.6^{o}, as in Test 485 and Test 486, the depth of a gravity current experienced a short period of growth immediately after the passage of the front of the current, but it remained constant thereafter until the arrival of the reflected bore. Moreover, it was observed in each of these two tests that there was entrainment of ambient fluid into the gravity current. As a result, it is concluded that in the present investigation the transition from an unsteady, non-entraining current to a steady, entraining current is gradual. Although the critical angle, θ_c, which separates the two phenomena was not specifically identified, it was found to lie between 0.3^{o} and 0.6^{o}. These observations are in agreement with Britter and Linden (1980), who suggested that a gravity current is steady and the current depth of a gravity current at a specific location will remain constant when the angle of inclination is larger than the critical angle, θ_c, because the frictional forces are balanced by both the buoyancy force and the component of the gravitational force in the streamwise direction. Assuming a constant coefficient of friction, C_D, the critical angle was found to be roughly $\theta_c \cong 2\ C_D$. Britter and Linden obtained a value of $C_D \cong 3 \times 10^{-3}$ for their channel and thus a value of $\theta_c \cong 0.34^{o}$, which is in good agreement with the present results. Note that in the case of a gravity current in a horizontal duct, the gravitational force is normal to the direction of flow, and thus the frictional forces cannot be partially balanced by a component of the gravitational force and must be completely balanced by the buoyancy force. As a result, the depth of a gravity current in a horizontal duct had to increase with time to provide the pressure head needed to overcome the frictional forces and so that the current can propagate downstream. However, since there is no such need for a gravity current in an inclined duct, as the frictional forces are partially balanced by a component of the gravitational force, the depth of the gravity current in such a channel at a particular location remains constant.

To summarize, Figure 4.14a shows the depth of a gravity current in Test 539 at x* = 26 in a horizontal duct, while Figure 4.14b shows the depth of a gravity current in

Test 340 with similar conditions and at the same x*, but the experiment was conducted in a duct inclined at 1^{o}. It can be seen in Figure 4.14a that for a current in a horizontal duct, the depth of the current at a particular position continually increased with time after the passage of the head until the arrival of the reflected bore. No visible entrainment of ambient fluid into the gravity current was observed. On the other hand, it is clear in Figure 4.14b that the depth of the current in an inclined duct had a small increase immediately after the head had passed. However, the depth of the current reached a steady state very quickly and would not increase until the arrival of the reflected bore. It was visibly observed that some ambient fluid was entrained into the gravity current in this case.

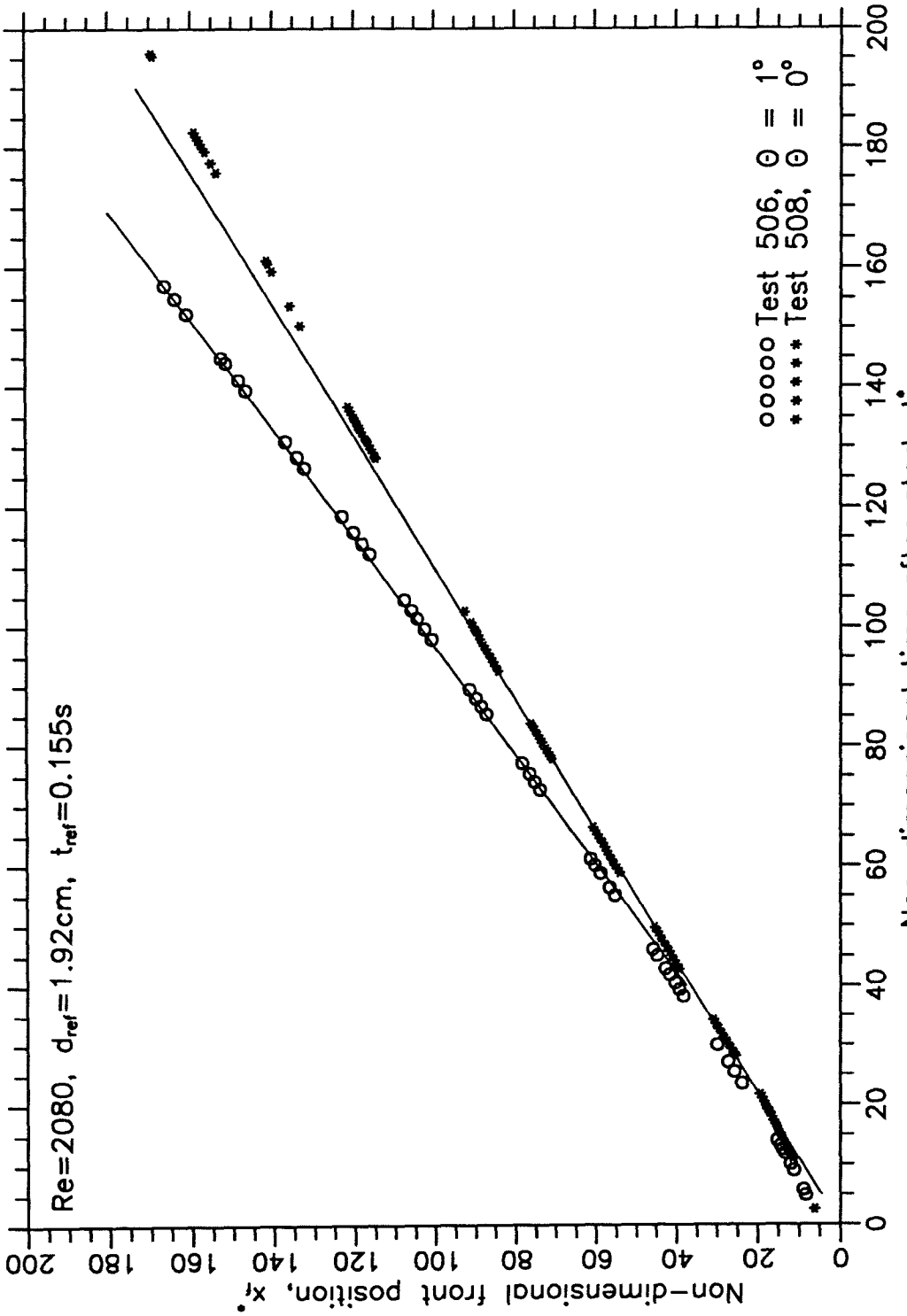

Figure 4.1 Front position in a 1° duct as a function of time.

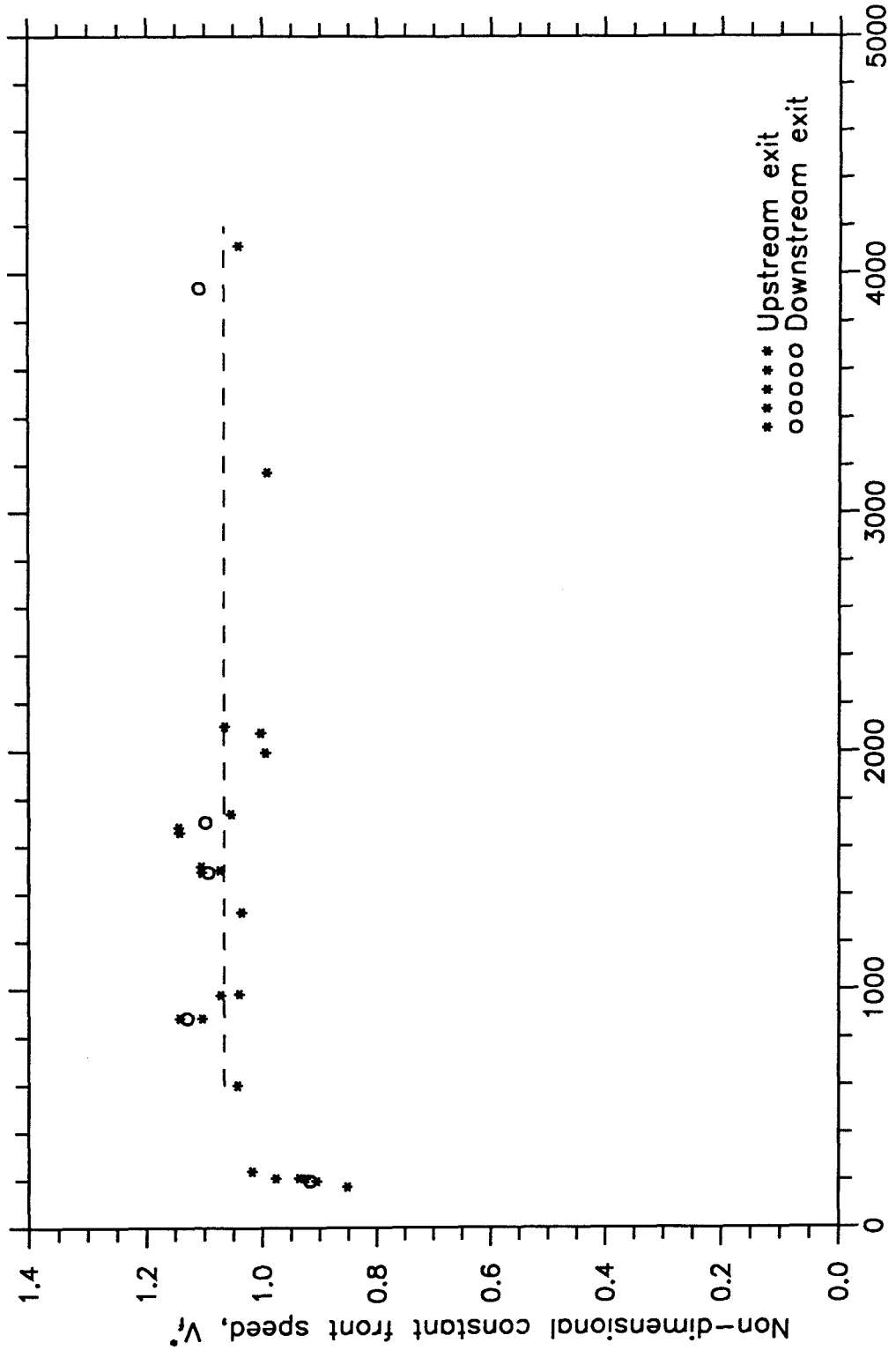

Figure 4.2 Constant front speed in a 1° duct as a function of Reynolds number.

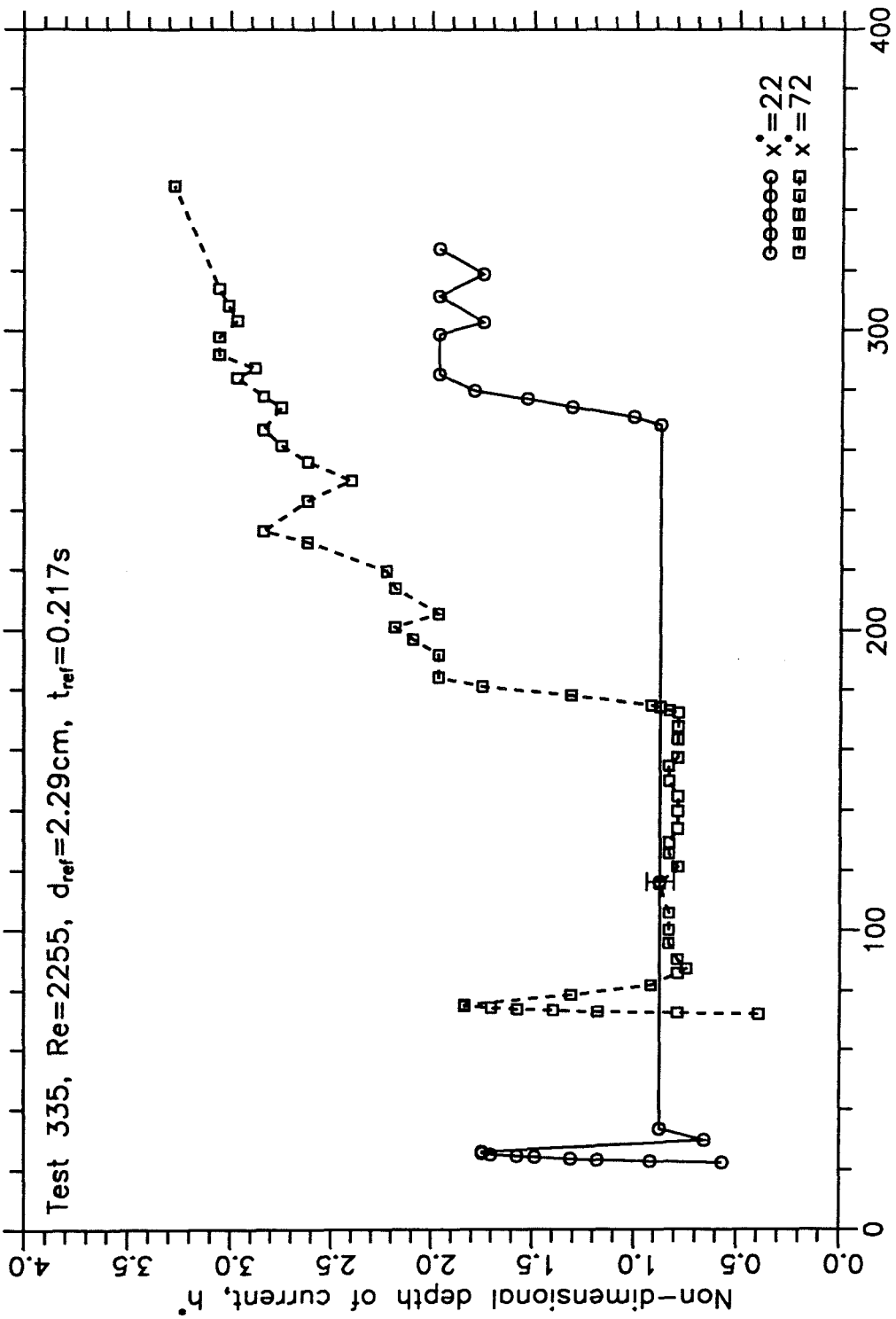

Figure 4.3 Depth of current in a 1° duct as a function of time.

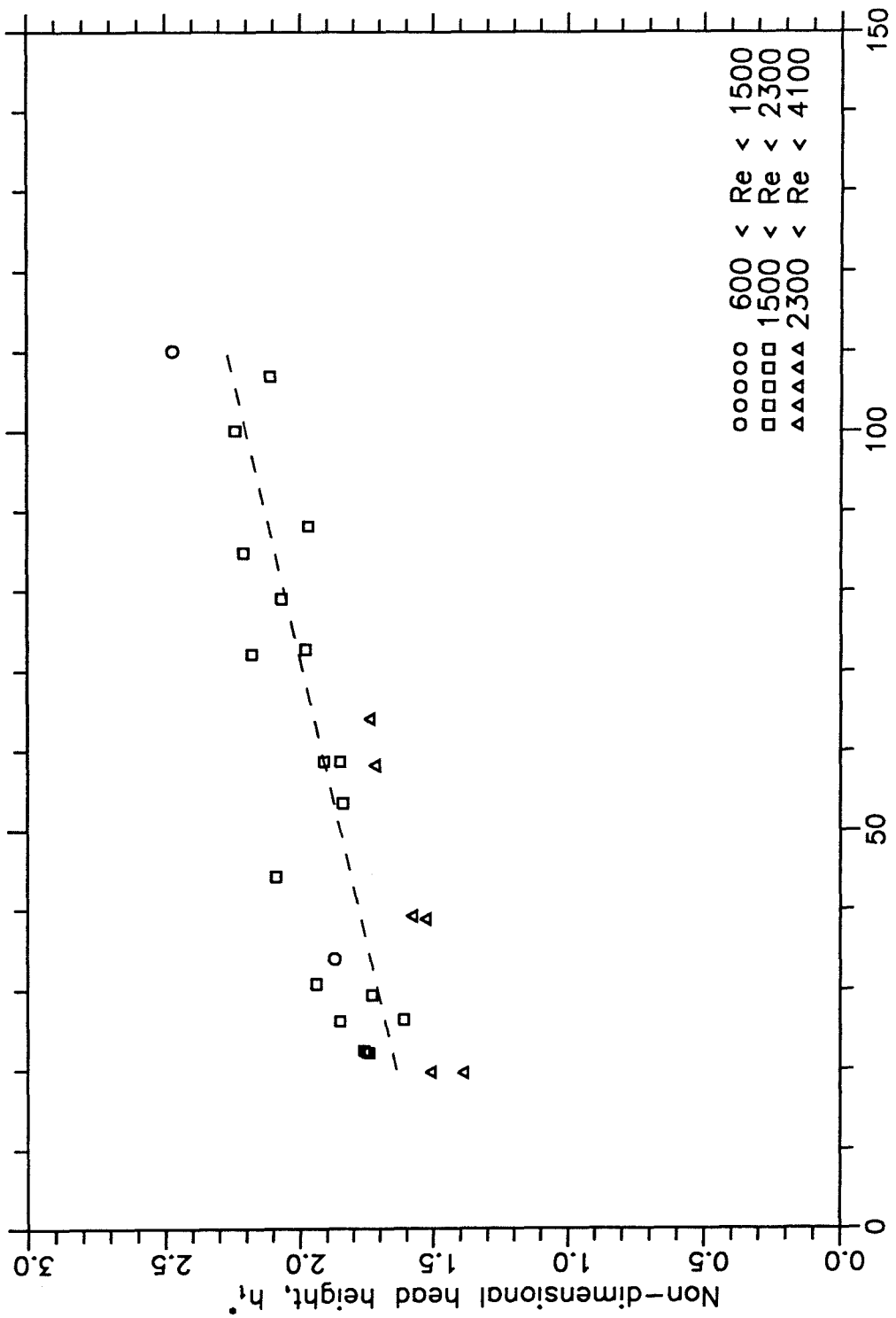

Figure 4.4 Head height in a 1° duct as a function of distance from source.

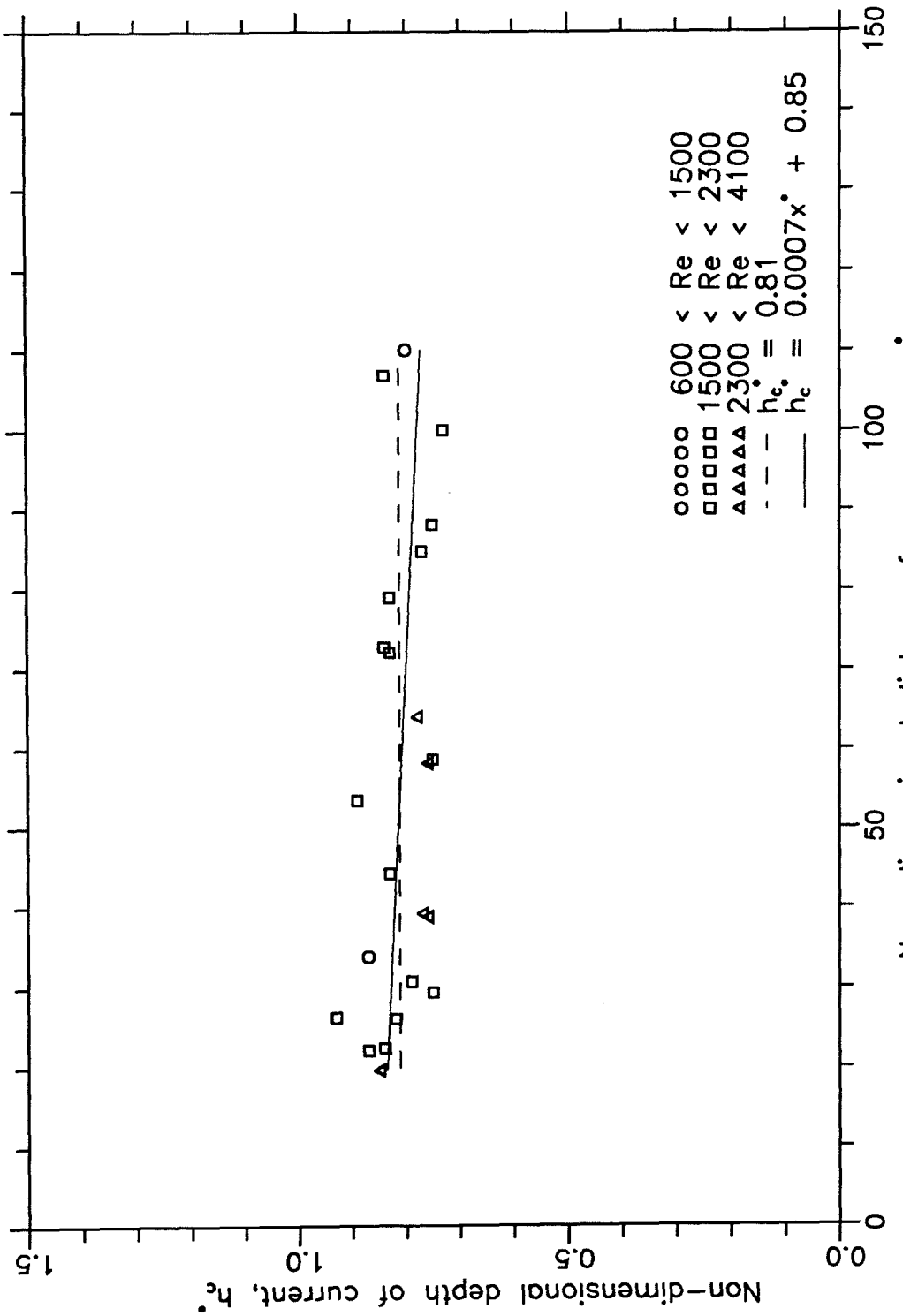

Figure 4.5 Depth of current in a 1° duct as a function of distance from source.

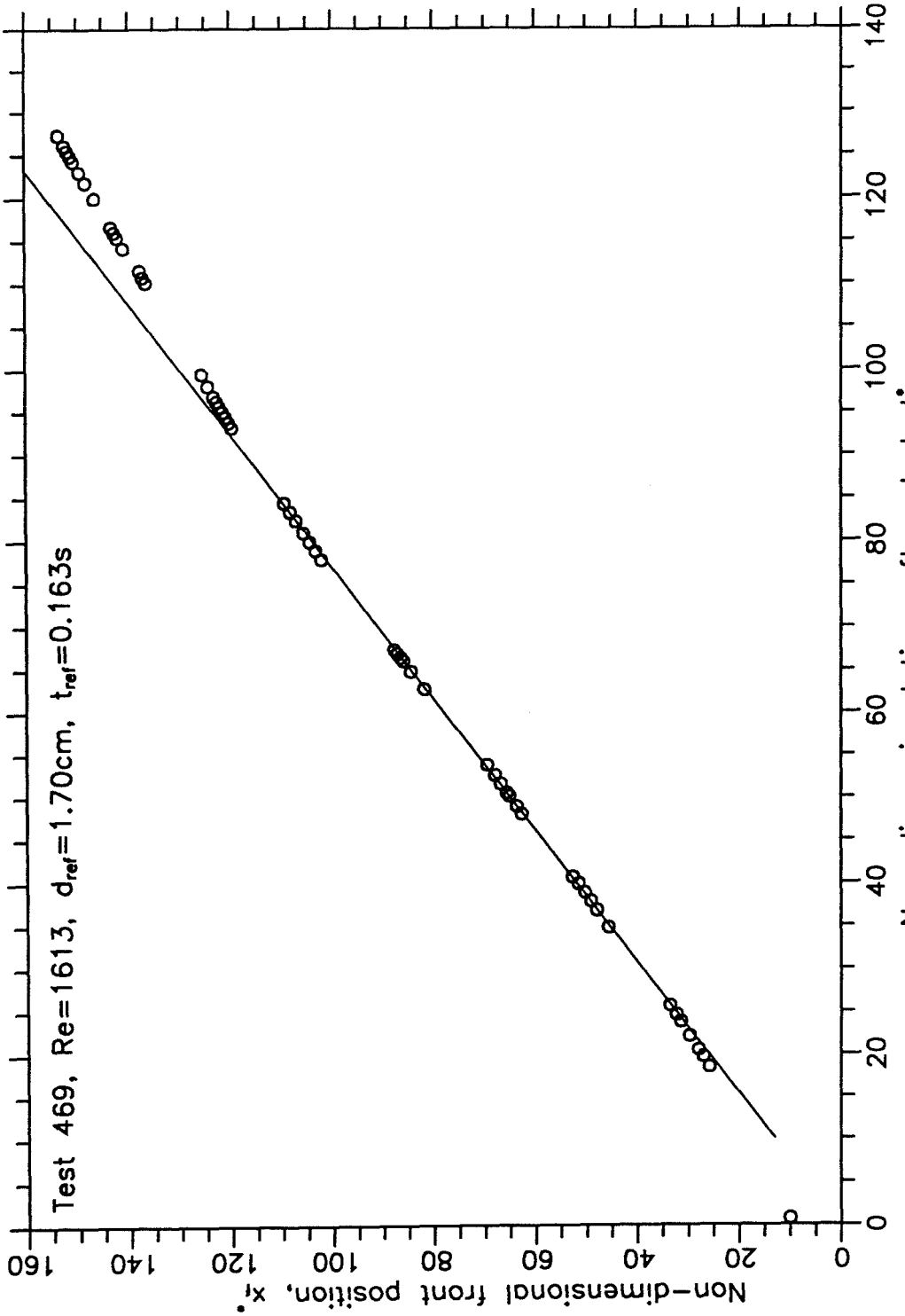

Figure 4.6 Front position in a 10° duct as a function of time.

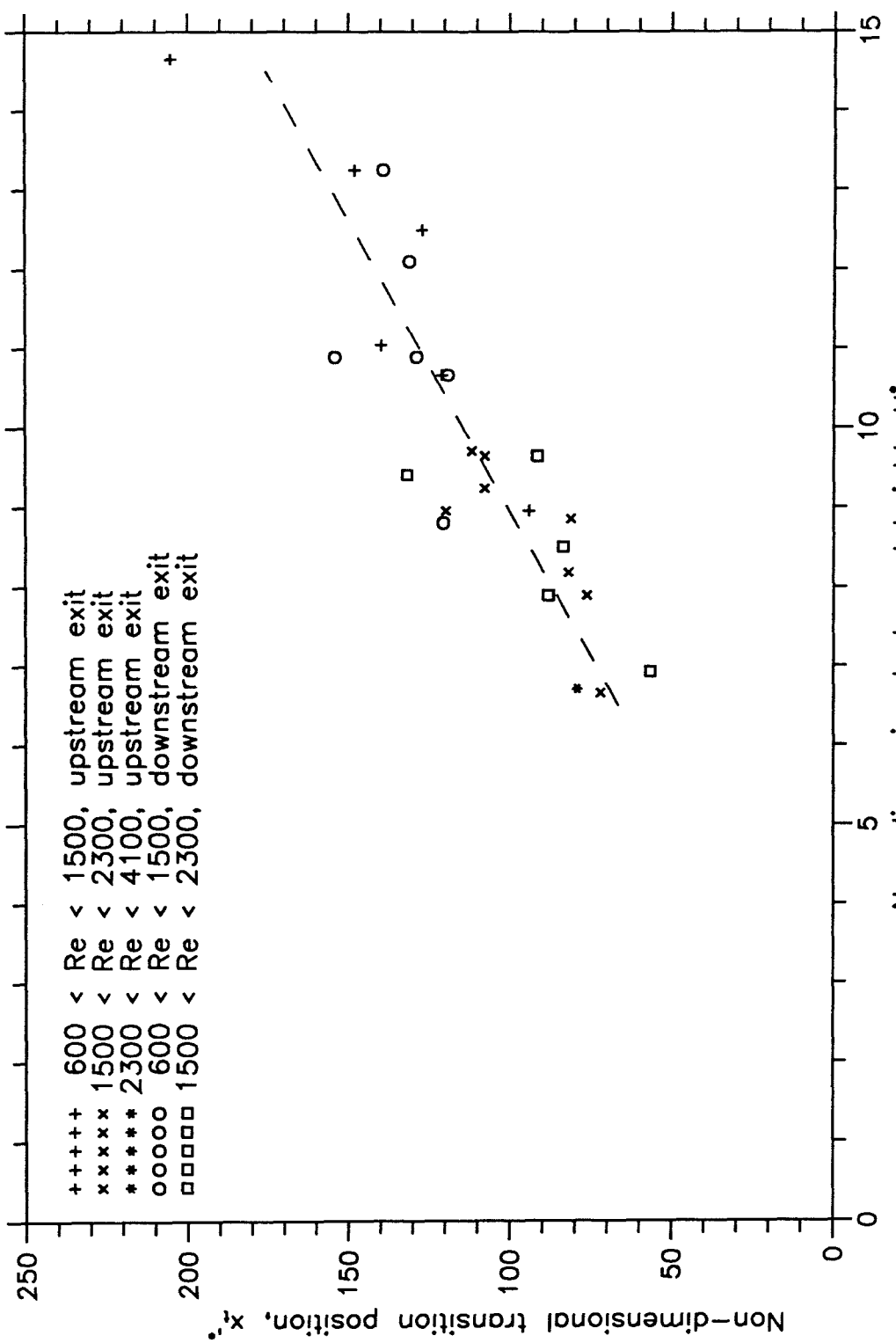

Figure 4.7 Transition position in a 10° duct as a function of channel height.

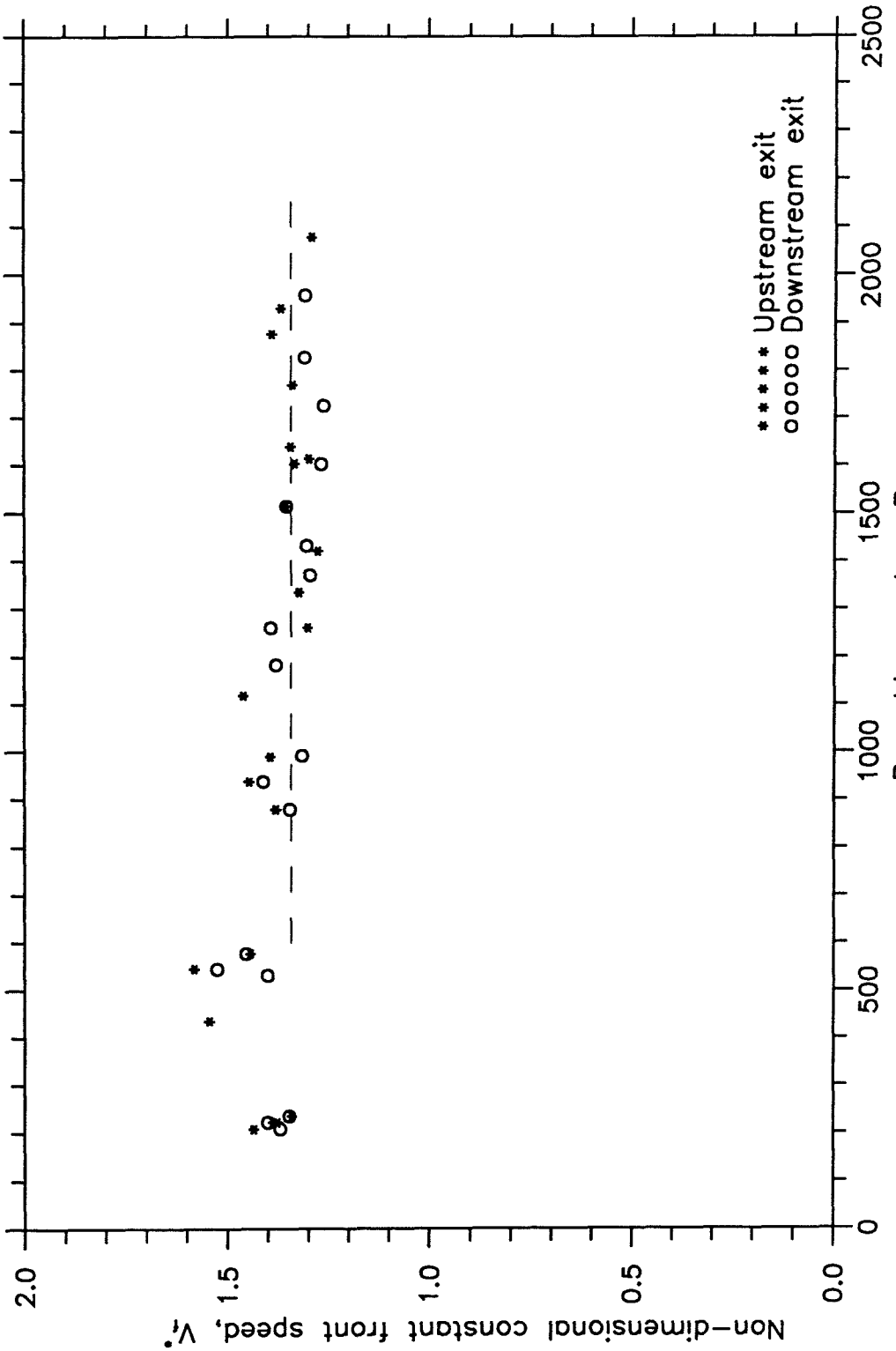

Figure 4.8 Constant front speed in a 10° duct as a function of Reynolds number.

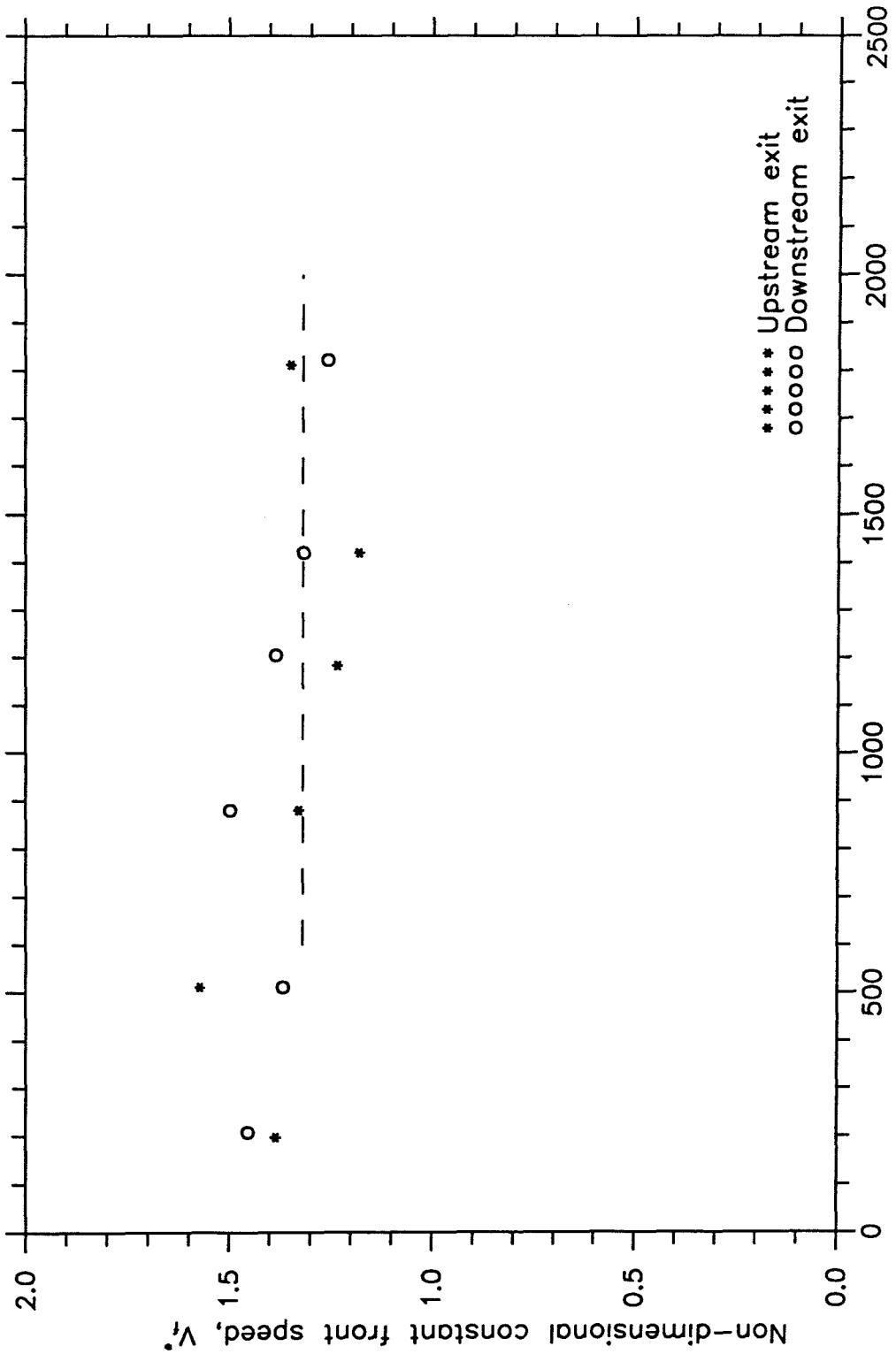

Figure 4.9 Constant front speed in a 22° duct as a function of Reynolds number.

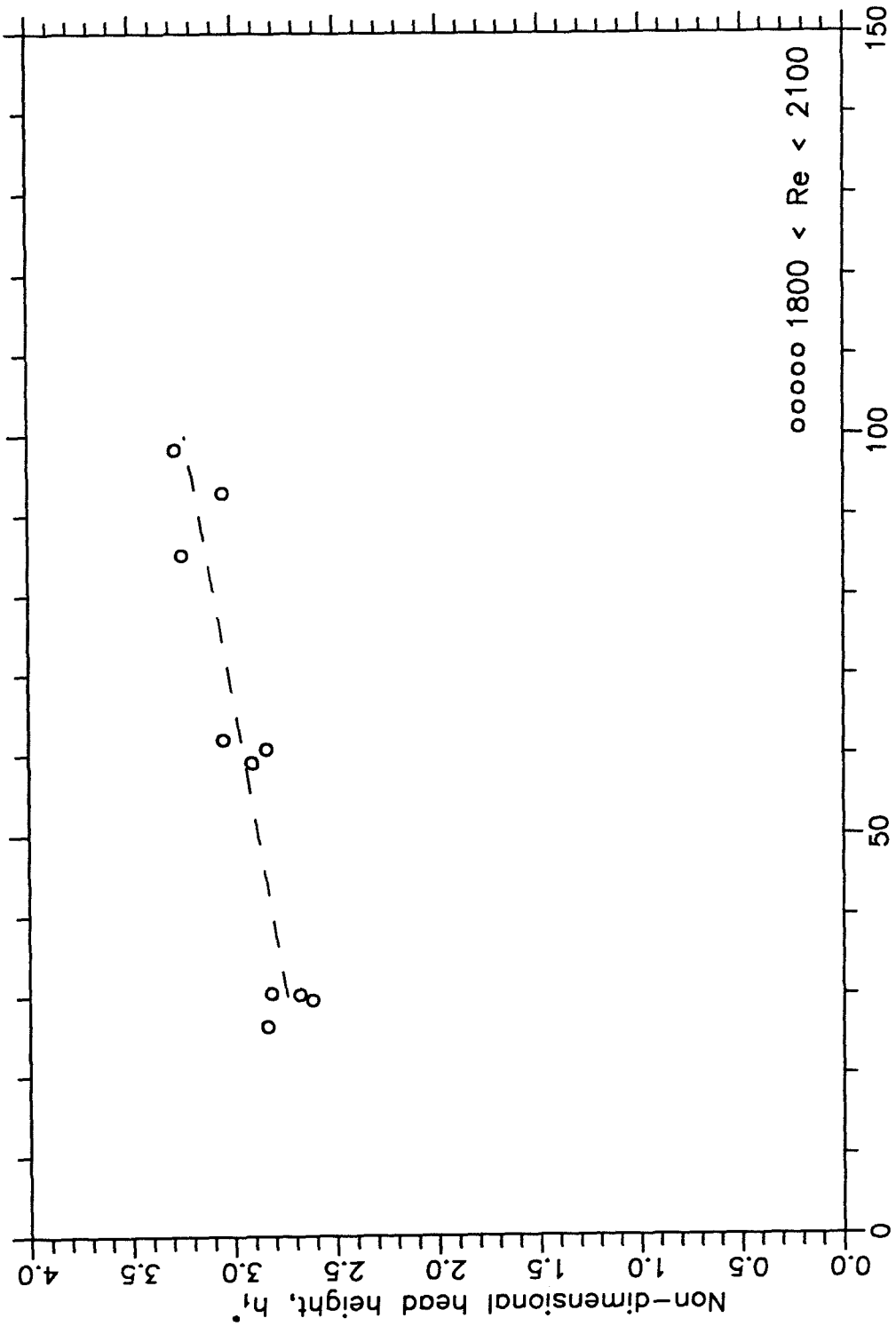

Figure 4.10 Head height in a 10° duct as a function of distance from source.

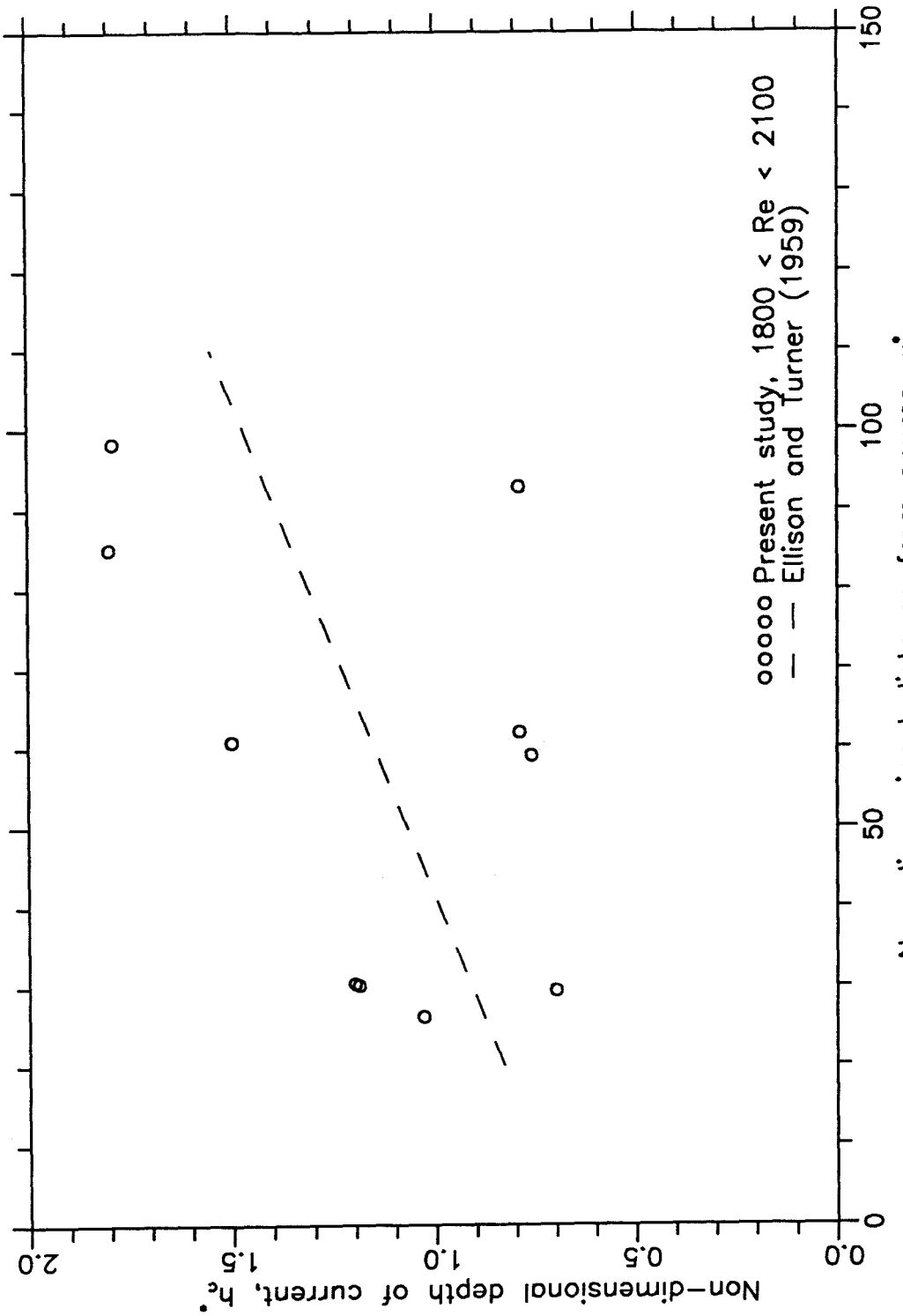

Figure 4.11 Depth of current in a 10° duct as a function of distance from source.

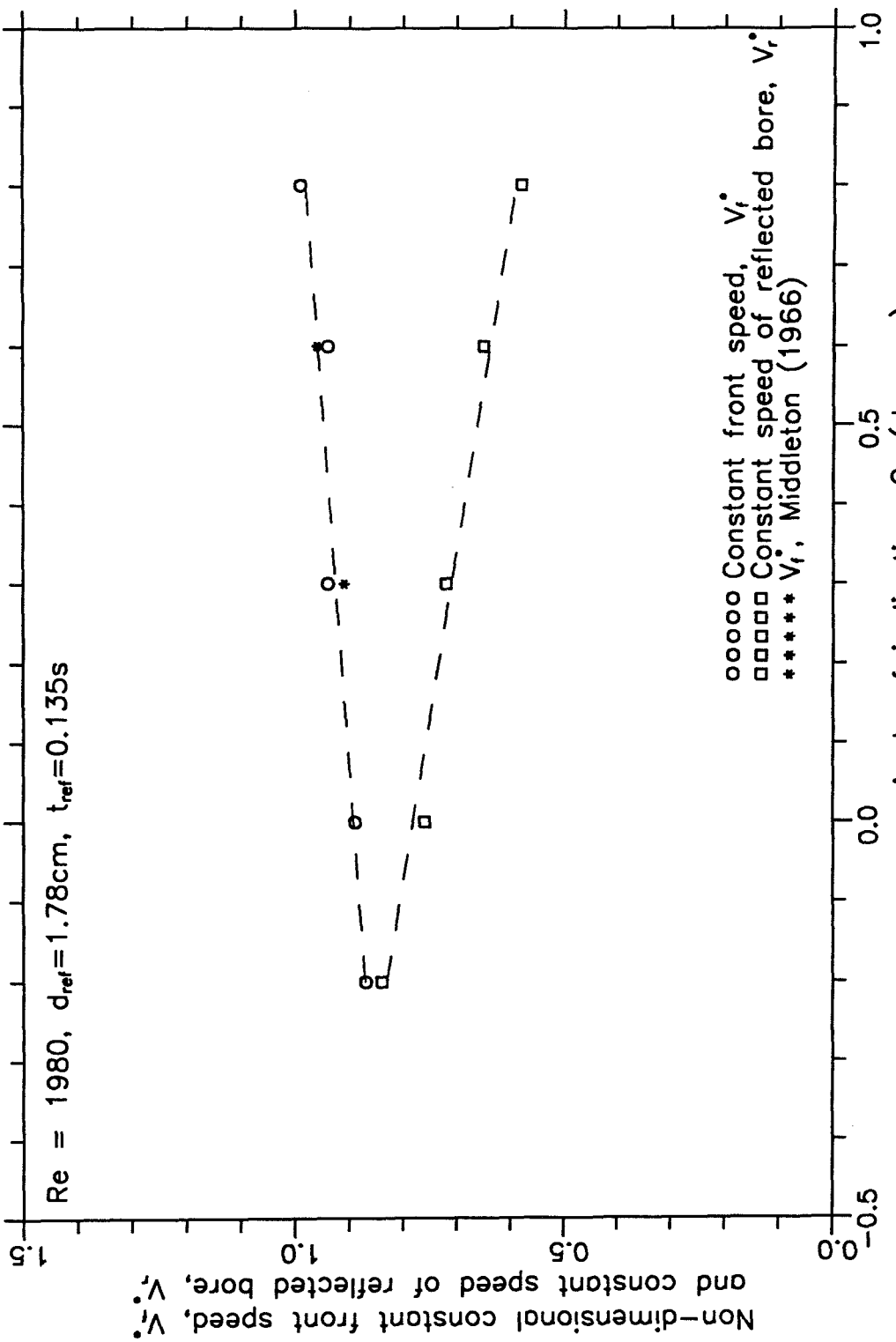

Figure 4.12 Constant front speed and constant speed of the reflected bore as a function of angle of inclination.

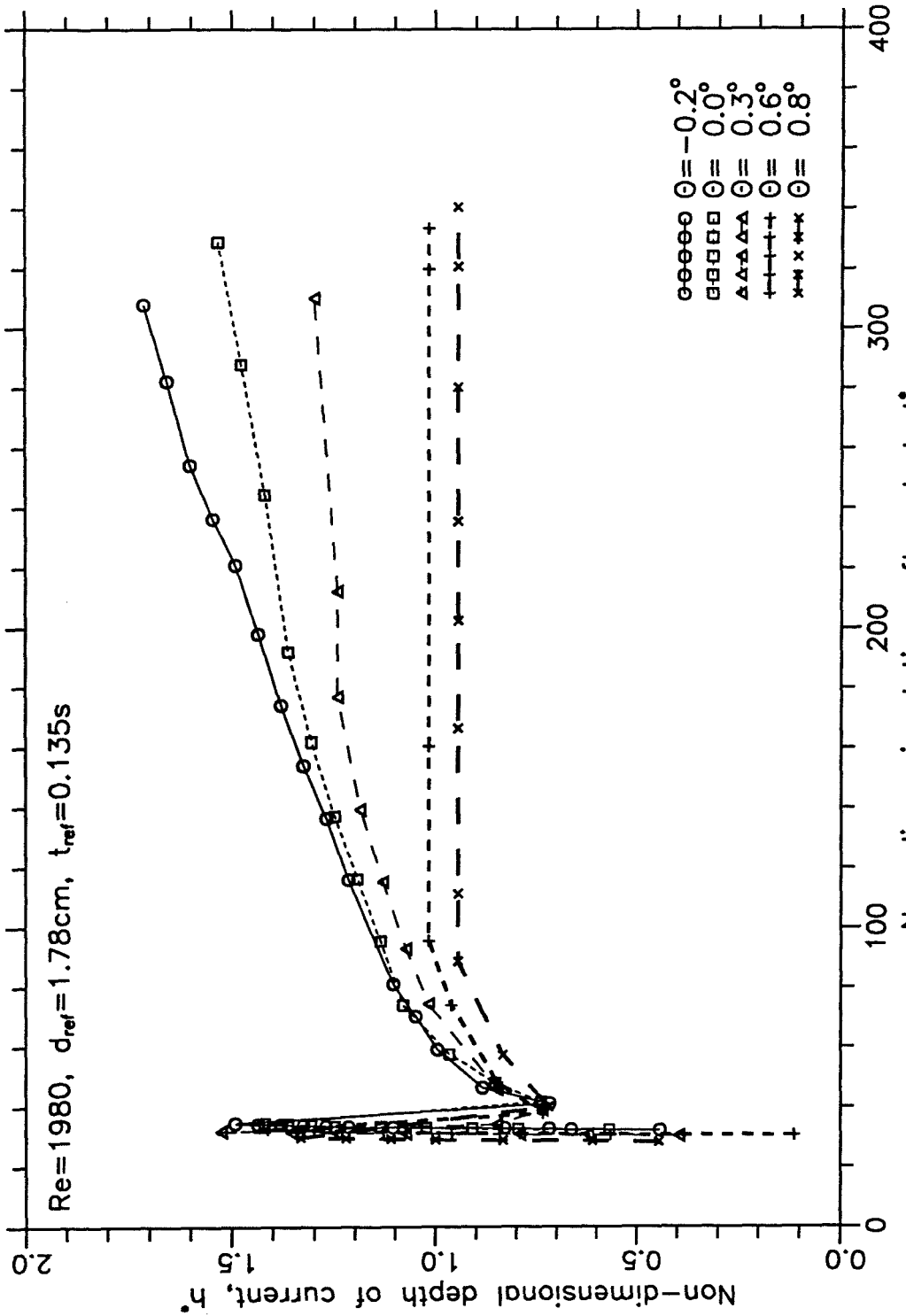

Figure 4.13 Depth of current at $x^* = 29$ as a function of time for various Θ.

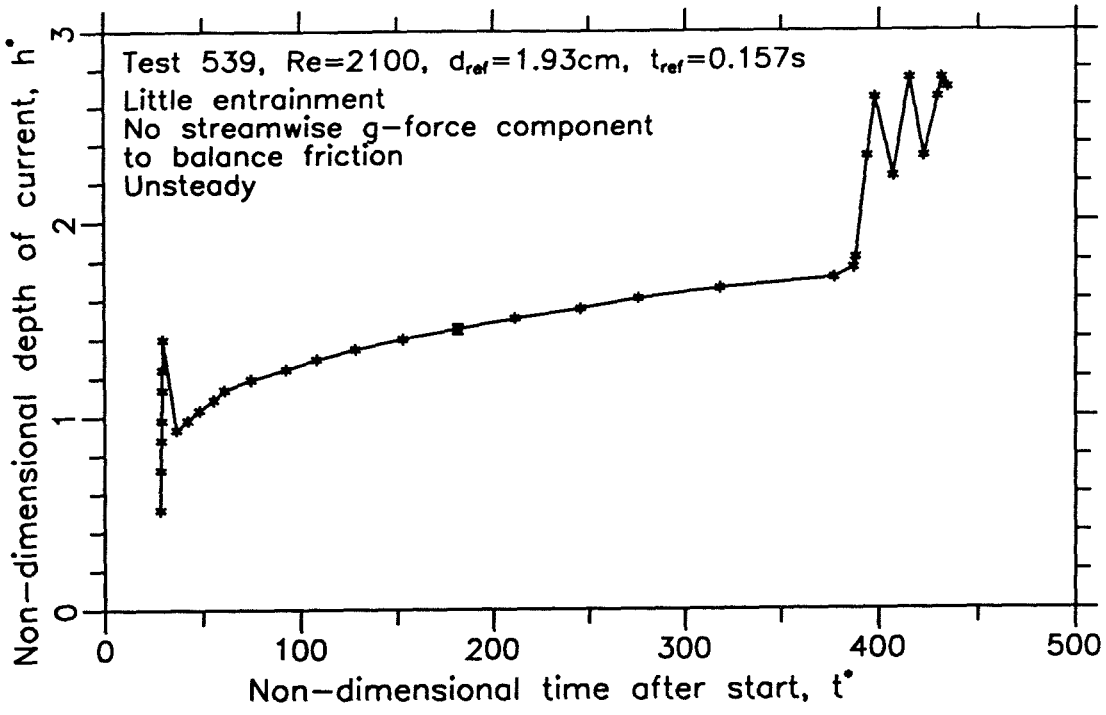

Figure 14a Depth of current as a function of time at x^*=26, Θ=0°

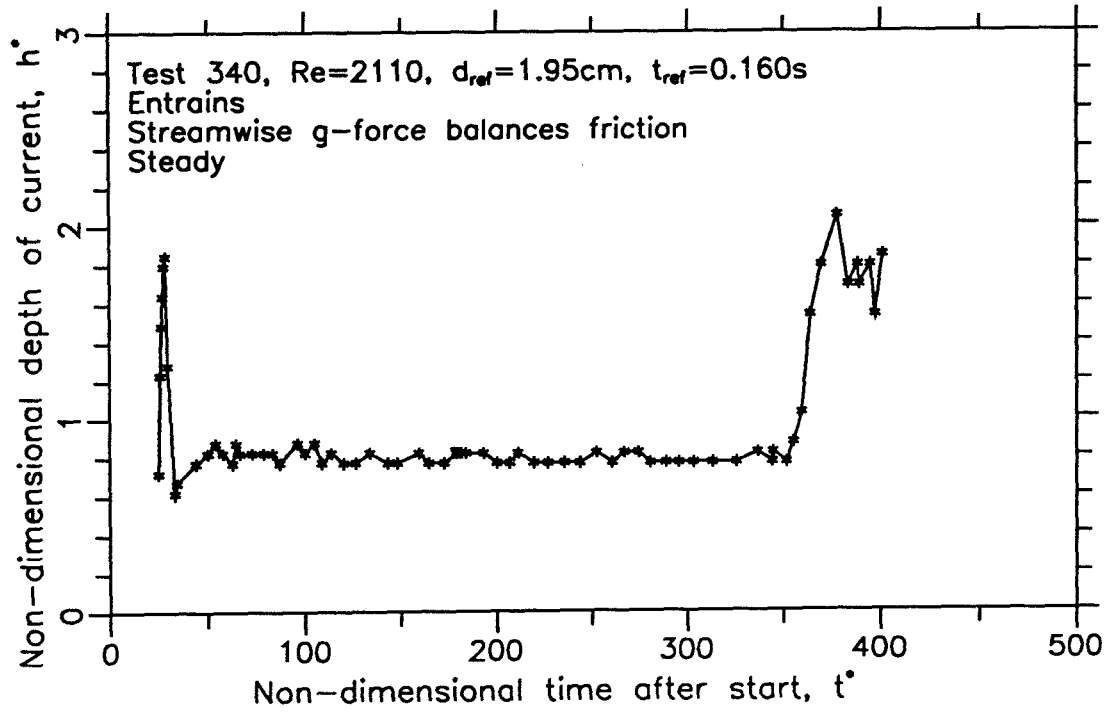

Figure 4.14b Depth of current as a function time at x^*=26, Θ=1°

CHAPTER 5

CONCLUSIONS

An experimental study on two-dimensional adiabatic gravity currents has been performed. The characteristics of gravity currents, notably the velocity of the advancing front and the depth of the following current, in a horizontal channel and also those in an inclined duct were examined. While video photography was used as the primary technique in data gathering, both Kriegrocine blue dye and hydrogen bubbles were used as flow visualization aids. A series of models was developed to examine both inviscid and viscous adiabatic gravity currents. Numerical technique was used to obtain quantitative information from the models, and the results were compared with the experimental results. The major qualitative characteristics of the gravity currents were also reviewed.

5.1 Adiabatic gravity currents in a horizontal channel

Two-dimensional gravity currents spreading in a horizontal channel comprise of a raised head followed by a shallower current. The current front was found to undergo a short accelerating stage during experiments in the present study. When there is a balance between inertia and buoyancy forces during the principal stage of a gravity current, the current advances with a constant front velocity, V_f, until viscous drag on the bottom wall is no longer negligible. The non-dimensional constant front speed in this stage was observed to be an increasing function of Reynolds number at low Reynolds numbers. It was also found that $V_f^* = 0.89 \pm 0.02$ for $1000 < Re$. The current then enters the final stage during which the front velocity continues to decrease. When the viscous forces become much larger than the inertia forces, the front position will advance at a rate of $x_f \sim t^{4/5}$. The transition position between the inertia-buoyancy regime and the viscous-buoyancy regime, x_t, was found to decrease with Reynolds number at low Reynolds numbers. On the other hand, when Reynolds number is sufficiently large, it was noticed that $x_t^* = 88 \pm 11$ for $1000 < Re$.

The head height, h_1, of a gravity current does not change significantly during an experiment. The non-dimensional head height was found to be $h_1^* = 1.59 \pm 0.19$. On the other hand, the non-dimensional depth of the following current just behind the head was observed to decrease with distance travelled according to the expression $h_0^* = -1.4 \times 10^{-3} x^* + 0.85$. This is due to the increase in boundary layer thickness which causes the supply of fluid to the front to decrease with time.

The current depth, h, of a gravity current at a fixed position was found to increase with time. It can be described by a curve fit of the form

$$h^* \cong h_0^* + c_1 \sqrt{t^* - t_0^*}$$

in which c_1 was found to increase with Reynolds number at a rate $c_1 = 5.9 \times 10^{-4}$ Re + 0.91. Initially, this can be attributed to the increase in the boundary layer thickness at the location of interest. However, it was deduced from velocity profile measurements that the boundary layer thickness at a fixed position attains a constant value rather rapidly. As a result, it is concluded that the continuous increase in current depth arises from the need of an increasing pressure head to overcome the growing boundary layer downstream of the location of interest.

By measuring the current depth at various positions, it was determined that the current depth decreases rapidly with distance near the inlet. It then undergoes a weak internal jump. The current depth again decreases downstream of the jump.

Owing to this continuous increase in current depth, the velocity in the following current at a fixed position must decrease with time to satisfy the mass conservation. It was found in an experiment that $U_w^* = -1.3 \times 10^{-3} t^* + 1.13$ at $x^* = 52$. It can be deduced that the current velocity just behind the head is roughly 20% large than the front velocity.

Moreover, no significant entrainment through the interface was observed in the experiments using hydrogen bubbles as the flow visualization aid.

After the current front reaches the downstream end wall, it will be reflected in the form of a bore. The reflected bore was observed to advance upstream at a relatively constant speed which can be expressed as $V_r^* = 0.74 \pm 0.04$.

The non-dimensional mean height of the reflected bore displayed a decreasing trend with respect to distance from the source. This can be expressed as $h_2^* = -3.4 \times 10^{-3} x^* + 2.43$.

The model developed for a viscous adiabatic gravity current in a channel of finite depth was found to be able to capture the essence of the phenomenon. Solutions obtained from the model show the same three stages of advancement at the front as in the experiments. The continuous increase in current depth and the corresponding decrease in current velocity were also observed in the solution obtained from the model. Except for the region close to the advancing front, the boundary layer thickness was found to be due to the leading edge of the bottom wall. It was also observed to increase very rapidly at a fixed position just after the head had passed, but then remained relatively constant. This is in good agreement with the experimental results.

However, the model is unable to handle the three-dimensional and complicated features of the head of a gravity current. It did not take into account the effects of the side walls. Finally, its inability to predict the internal jump causes it to predict higher current velocities and lower current depths than observed in the experiments.

5.2 Adiabatic gravity currents in an inclined channel

When a gravity current spreads in a channel inclined at an angle of $0.6^o \leq \theta$, it exhibits different characteristics from those observed in a horizontal channel. The front of a gravity current in a two-dimensional inclined duct advances at a constant speed as long as the head height is small when compared to the channel height. This is because viscous and entrainment drag is partially balanced by the streamwise component of gravity. Both the head height and the current depth continue to increase with distance travelled, even though the depth of the following current at a fixed position does not increase with time.

The head height of a gravity current in an inclined duct was observed to increase with increasing slope, while the head height to head length ratio was observed to increase with increasing slope. The rate of entrainment was also observed to increase with the

slope. The front velocity was found to increase from a value of $V_f^* = 1.11 \pm 0.01$ at $\theta = 1^o$ to $V_f^* = 1.34 \pm 0.05$ at $\theta = 10^o$.

APPENDIX A

DERIVATION OF THE EQUATIONS FOR AN ADIABATIC, INVISCID GRAVITY CURRENT IN A CHANNEL OF INFINITE DEPTH

A.1 General description of the model

With the assumptions put forth in Section 3.2, the continuity, x-momentum and y-momentum equations in differential form for fluid motion, with boundary layer approximation, are given respectively by

$$\frac{\partial u}{\partial x} + \frac{\partial v}{\partial y} = 0 \qquad \text{(A.1a)}$$

$$\frac{\partial u}{\partial t} + u\frac{\partial u}{\partial x} + v\frac{\partial u}{\partial y} = -\frac{1}{\rho}\frac{\partial p}{\partial x} + \nu\frac{\partial^2 u}{\partial y^2} \qquad \text{(A.1b)}$$

and $$0 = -\frac{1}{\rho}\frac{\partial p}{\partial y} + g \qquad \text{(A.1c)}$$

where $u = u_{(t,x,y)}$ and $v = v_{(t,x,y)}$ are the velocities of the fluid in the x-direction and y-direction at any time t and co-ordinate (x,y), respectively, while $p = p_{(t,x,y)}$ and $\rho = \rho_{(t,x,y)}$ represent the corresponding pressure and density, respectively.

Integrating equation (A.1c) with respect to y, from y = 0 to any arbitrary y yields

$$p = p_0 - \rho_w g y \qquad \text{for } 0 \le y \le h \qquad \text{(A.2a)}$$

and $$p = p_0 - \rho_w g h - \rho_a g(y - h) \qquad \text{for } h \le y \le H \qquad \text{(A.2b)}$$

where $h = h_{(t,x)}$ and $p_0 = p_{0(t,x)}$ are the depth of the working fluid at any time t and position x and the corresponding pressure of the fluid on the bottom wall of the channel, respectively. Since mixing is assumed to be negligible, $h_{(t,x)}$ also represents the position

of the interface between the two fluids. When the pressure on the top wall is evaluated, equation (A.2b), with y = H, yields

$$p_0 = p_H + \rho_w g h + \rho_a g (H - h) \qquad (A.3)$$

where $p_H = p_{H(t,x)}$ is the pressure of the fluid on the top wall of the channel at any time t and position x. Replacing p_0 in favour of p_H in equations (A.2a) and (A.2b) using equation (A.3) gives

$$p = p_H + \rho_a g (H - h) + \rho_w g (h - y) \qquad \text{for } 0 \le y \le h \qquad (A.4a)$$

and

$$p = p_H + \rho_a g (H - y) \qquad \text{for } h \le y \le H. \qquad (A.4b)$$

Therefore, the partial derivative of p with respect to x can be written as

$$\frac{\partial p}{\partial x} = \frac{\partial p_H}{\partial x} + (\rho_w - \rho_a)\, g \frac{\partial h}{\partial x} \qquad \text{for } 0 \le y \le h \qquad (A.5a)$$

and

$$\frac{\partial p}{\partial x} = \frac{\partial p_H}{\partial x} \qquad \text{for } h \le y \le H. \qquad (A.5b)$$

Equation (A.5a) is significant since the pressure gradient, which partially arises from the density difference between the two fluids, is the primary driving force of the flow.

Since the flow spreads horizontally, the changes in the y-direction are not of primary interest. As a result, an integral approach can be used to obtain a set of unsteady quasi-one-dimensional equations. Integrating equation (A.1a) from y = 0 to y = h yields

$$v_h = v_0 + u_h \frac{\partial h}{\partial x} - \frac{\partial}{\partial x} \int_0^h u \, dy \qquad (A.6)$$

where $v_h = v_{h(t,x)}$ and $v_0 = v_{0(t,x)}$ are the vertical velocity components of the fluid at $y = h_{(t,x)}$ and y = 0, respectively, and $u_h = u_{h(t,x)}$ is the horizontal velocity component of the fluid at $y = h_{(t,x)}$. In addition, the partition between the ambient fluid and the working fluid at the front of the current is assumed to be sharp and vertical, as indicated in Figure

3.1. The position of that partition is denoted by $x_{f(t)}$, also known as the front position of the current. The velocity of this partition moving in the downstream direction is known as the front velocity, and is denoted by $\dot{x}_{f(t)}$. Furthermore, the ambient fluid downstream of the front of the current is assumed to be quiescent.

Since the total influx of working fluid is steady, v_0 is also steady, and thus $v_{0(t,x)} = v_{0(x)}$. In addition, there is a solid boundary at $y = 0$ for $x > 0$. As a result, $v_{0(x>0)} = 0$. Finally, integrating v_0 with respect to x from $x = -w_0$ to $x = 0$ must equal to the influx of working fluid Q in order to satisfy the conservation equation of mass. Assuming a constant value of v_0 for all x in this region will give rise to difficulties in an effort to obtain a solution for this model with the help of computational methods. These difficulties are beyond the scope of this investigation. As a result, for computational purposes, the profile of $v_{0(x)}$ is assumed to be of the form

$$v_{0(x)} = \frac{1}{(1-\frac{1}{2}k)}\frac{Q}{w_0} \qquad \text{for } -w_0 \le x \le -kw_0 \qquad \text{(A.7a)}$$

$$v_{0(x)} = \frac{1}{(1-\frac{1}{2}k)}\frac{Q}{w_0}\left(\frac{x}{-kw_0}\right) \qquad \text{for } -kw_0 \le x \le 0 \qquad \text{(A.7b)}$$

and $$v_{0(x)} = 0 \qquad \text{for } 0 \le x \le L \qquad \text{(A.7c)}$$

where $0 < k < 1$, and $k \cong 0$. It was found that the solution does not depend on k for a small k.

Since $y = h_{(t,x)}$ is a streamline, in addition to equation (A.6), v_h and u_h are also related by

$$v_h = \frac{\partial h}{\partial t} + u_h\frac{\partial h}{\partial x}. \qquad \text{(A.8)}$$

Combining equations (A.6) and (A.8) to eliminate v_h yields

$$\frac{\partial h}{\partial t} + \frac{\partial}{\partial x}\int_0^h u\,dy = v_0. \qquad \text{(A.9)}$$

Equations (A.1) through (A.9) do not depend on the flow being inviscid or the channel being infinitely deep, except that the interface is sharp so that the top of the layer of working fluid coincides with the interface. Therefore, these equations can, and also will, be used in all four cases.

A.2 Governing equations for the model

For an inviscid gravity current, there is no boundary or shear layer. As a result, the integral on the left-hand side of equation (A.9) can be written as

$$\int_0^h u\, dy = U_w h \tag{A.10}$$

where $U_w = U_{w(t,x)}$ represents the free-stream velocity in the layer of working fluid. As a result, equation (A.9) can then be written as

$$\frac{\partial h}{\partial t} + \frac{\partial}{\partial x}(U_w h) = v_0 \,. \tag{A.11a}$$

Since there is no variation of U_w in the y-direction, equation (A.1b) can also be written as

$$\frac{\partial U_w}{\partial t} + U_w \frac{\partial U_w}{\partial x} = -\frac{1}{\rho_w}\frac{\partial p}{\partial x} \,. \tag{A.11b}$$

In addition, for an infinitely deep channel, the pressure distribution on the top wall is constant, that is, $\partial p_H/\partial x = 0$. As a result, using equation (A.5a), equation (A.11b) can be written as

$$\frac{\partial U_w}{\partial t} + U_w \frac{\partial U_w}{\partial x} = -\frac{1}{\rho_w}(\rho_w - \rho_a)\, g \frac{\partial h}{\partial x} \,. \tag{A.11c}$$

By using the length scale, d_{ref}, the time scale, t_{ref}, and the velocity scale, U_{ref}, shown in Section 1.2, equations (A.11a) and (A.11c) can be rewritten in the following non-dimensional forms

$$\frac{\partial h^*}{\partial t^*} + \frac{\partial}{\partial x^*}(U_w^* h^*) = v_0^* \qquad \text{(A.12a)}$$

$$\frac{\partial U_w^*}{\partial t^*} + \frac{\partial}{\partial x^*}\left[\frac{1}{2}(U_w^*)^2 + h^*\right] = 0 \qquad \text{(A.12b)}$$

where ( )* quantities are the non-dimensional quantities normalized by the appropriate combinations of length, time, and velocity scales. Equations (A.12a) and (A.12b) are the governing partial differential equations for $-w_0^* \leq x^* \leq L^*$. These two equations constitute a system of unsteady quasi-one-dimensional equations which was applied by Grundy and Rottman (1985, 1986) to both constant-volume gravity currents and gravity currents with a steady and continuous discharge.

A.3 Boundary conditions for the model

To solve the above differential equations, boundary conditions are needed. The boundary conditions in this model are:

At $x^* = -w_0^*$, $\frac{\partial h^*}{\partial x^*} = 0$ (A.13a)

and $U_w^* = 0$. (A.13b)

At $x^* = 0$, $h^*_{(x^*=0^-)} = h^*_{(x^*=0^+)}$ (A.13c)

$$\frac{\partial h^*}{\partial x^*}(x^*=0^-) = \frac{\partial h^*}{\partial x^*}(x^*=0^+) \qquad \text{(A.13d)}$$

$$U_w^*{}_{(x^*=0^-)} = U_w^*{}_{(x^*=0^+)} \qquad \text{(A.13e)}$$

and $$\frac{\partial U_w^*}{\partial x^*}(x^*=0^-) = \frac{\partial U_w^*}{\partial x^*}(x^*=0^+) . \qquad (A.13f)$$

At $x^* = x_f^*$, $\dot{x}_f^* = (1 - \alpha)U_w^*$ (A.13g)

and $$U_w^* = \sqrt{\frac{h^*}{\frac{1}{2} - \alpha}} \qquad (A.13h)$$

where α is a constant, and $\alpha U_w^* h^*$ is the rate of volumetric loss of working fluid per unit width at the front of the current. This is achieved by putting a sink of strength $\alpha U_w^* h^*$ at the front of the current.

Note that equations (A.13a) and (A.13b) are deduced from physical considerations at the upstream end wall. Equations (A.13c) to (A.13f) state that both the values and the gradients of h and U_w are continuous. Equations (A.13g) and (A.13h) were obtained by integrating equations (A.12a) and (A.12b) across the front of the current, keeping in mind that no working fluid moves farther downstream than the front and that working fluid is lost at a rate of $\alpha U_w^* h^*$ at the front of the current. They are the same as the conditions cited by Grundy and Rottman (1986), with β^2 in equation (2.5) of that paper equals to the inverse of $(1/2 - \alpha)$ in equation (A.13h). As a result, when there is no loss of fluid mass or momentum at the front, $\beta^2 = 2$ in Grundy and Rottman as well as in Benjamin (1968), while $\alpha = 0$ in this model. On the other hand, $\beta^2 < 2$ and $\alpha > 0$ represents a case when there is loss of fluid at the front of the current. In addition, the position of the front can be found simply by integrating the velocity of the front over time

$$x_f^* = \int_0^{t^*} \dot{x}_f^* \, dt^* . \qquad (A.13i)$$

A.4 Transformation of the independent variables

In this model, the distance between $x^* = -w_0^*$ and $x^* = 0$ is constant, but the distance between $x^* = 0$ and $x^* = x_f^*$ is increasing with time. As a result, new variables

τ and z are introduced to replace the variables t and x in order to minimize the computational efforts. This new set of variables is defined as follows

For $-w_0^* \le x^* \le 0$, $\tau^* = t^*$ (A.14a)

and $$z^* = \frac{x^*}{w_0^*} .$$ (A.14b)

For $0 \le x^* \le x_f^*$, $\tau^* = t^*$ (A.14c)

and $$z^* = \frac{x^*}{x_f^*_{(t^*)}} .$$ (A.14d)

Thus, the partial differential equations (A.12a) and (A.12b) can be rewritten as

For $-1 \le z^* \le 0$, $$\frac{\partial h^*}{\partial \tau^*} + \frac{1}{w_0^*}\frac{\partial}{\partial z^*}(U_w^* h^*) = v_0^*$$ (A.15a)

and $$\frac{\partial U_w^*}{\partial \tau^*} + \frac{1}{w_0^*}\frac{\partial}{\partial z^*}[\tfrac{1}{2}(U_w^*)^2 + h^*] = 0 .$$ (A.15b)

For $0 \le z^* \le 1$, $$\frac{\partial h^*}{\partial \tau^*} - \frac{z^* \dot{x}_f^*}{x_f^*}\frac{\partial h^*}{\partial z^*} + \frac{1}{x_f^*}\frac{\partial}{\partial z^*}(U_w^* h^*) = v_0^*$$ (A.15c)

and $$\frac{\partial U_w^*}{\partial \tau^*} - \frac{z^* \dot{x}_f^*}{x_f^*}\frac{\partial U_w^*}{\partial z^*} + \frac{1}{x_f^*}\frac{\partial}{\partial z^*}[\tfrac{1}{2}(U_w^*)^2 + h^*] = 0 .$$ (A.15d)

Equations (A.15a) through (A.15d) are the governing partial differential equations for $-1 \le z^* \le 1$, or equivalently, $-w_0^* \le x^* \le x_f^*$. The influx velocity v_0^* can be defined as a function of the co-ordinate z*, and is given by

$$v_0^*_{(z^*)} = \frac{1}{(1-\frac{1}{2}k)}\frac{1}{w_0^*} \qquad \text{for } -1 \le z^* \le -k$$ (A.16a)

$$v_0^*(z^*) = \frac{1}{(1-\frac{1}{2}k)} \frac{1}{w_0^*} \left(\frac{z^*}{-k}\right) \qquad \text{for } -k \le z^* \le 0 \qquad \text{(A.16b)}$$

and $$v_0^*(z^*) = 0 \qquad \text{for } 0 \le z^* \le \frac{L^*}{w_0^*} \qquad \text{(A.16c)}$$

where $0 < k < 1$, and $k \cong 0$. In addition, the boundary conditions (A.13a) through (A.13i) become

At $x^* = -w_0^*$, $z^* = -1$, $$\frac{\partial h^*}{\partial z^*} = 0 \qquad \text{(A.17a)}$$

and $$U_w^* = 0 \,. \qquad \text{(A.17b)}$$

At $x^* = 0$, $z^* = 0$, $$h^*_{(z^*=0^-)} = h^*_{(z^*=0^+)} \qquad \text{(A.17c)}$$

$$\frac{1}{w_0^*} \frac{\partial h^*}{\partial z^*}(z^*=0^-) = \frac{1}{x_f^*} \frac{\partial h^*}{\partial z^*}(z^*=0^+) \qquad \text{(A.17d)}$$

$$U_w^*{}_{(z^*=0^-)} = U_w^*{}_{(z^*=0^+)} \qquad \text{(A.17e)}$$

and $$\frac{1}{w_0^*} \frac{\partial U_w^*}{\partial z^*}(z^*=0^-) = \frac{1}{x_f^*} \frac{\partial U_w^*}{\partial z^*}(z^*=0^+) \,. \qquad \text{(A.17f)}$$

At $x^* = x_f^*$, $z^* = 1$, $$\dot{x}_f^* = (1 - \alpha) U_w^* \qquad \text{(A.17g)}$$

and $$U_w^* = \sqrt{\frac{h^*}{\frac{1}{2} - \alpha}} \,. \qquad \text{(A.17h)}$$

Also, $$x_f^* = \int_0^{\tau^*} \dot{x}_f^* \, d\tau^* \,. \qquad \text{(A.17i)}$$

Finally, an additional boundary condition is required at the front of the current. Since this condition involves the specifics of the numerical scheme being used, its introduction

and discussion will be postponed until the computational scheme is introduced in Section A.7.

A.5 Boundary conditions at the end wall of the channel

When the layer of working fluid is allowed to spread for a long time, the front will hit the end wall of the channel. When this occurs, the layer of working fluid reflects from the wall, and the reflected bore moves in the upstream direction. This is schematically shown in Figure 3.2. Since a distinct front no longer exists, a different set of boundary conditions are needed at the downstream end wall of the channel to replace those conditions represented by equations (A.17g), (A.17h), (A.17i) and the additional boundary condition mentioned in the last section. The new boundary conditions are

At $z^* = 1$, $$\frac{\partial h^*}{\partial z^*} = 0 \qquad \text{(A.17j)}$$

$$U_w^* = 0 \,. \qquad \text{(A.17k)}$$

Also, $$\dot{x}_f^* = 0 \qquad \text{(A.17l)}$$

and $$x_f^* = L^* \,. \qquad \text{(A.17m)}$$

A.6 Initial conditions for the model

Finally, initial conditions are needed to start the computation. Assuming the flow started at $\tau^* = 0$, at time $\tau^* = \tau_0^* > 0$, where $\tau_0^* \cong 0$, it can be deduced from equations (A.15a) and (A.15b), as a first approximation, that:

For $-1 \le z^* < 0$, $$h^* = v_0^*{}_{(z^*)}\, \tau_0^* \qquad \text{(A.18a)}$$

and $$U_w^* = 0 \,. \qquad \text{(A.18b)}$$

In addition, a small amount of working fluid has already spread in the streamwise direction. Therefore, the front of the layer of working fluid is at $z^* = 1$. However, it is difficult to determine the precise depth and velocity distribution of the layer. As a result, the following assumptions are used:

For $0 \le z^* \le 1$, $\quad h^* = v_0^*{}_{(z^* = -k)}\, \tau_0^*/K$ (A.18c)

and $$U_w^* = \sqrt{\frac{h^*}{\frac{1}{2} - \alpha}} \tag{A.18d}$$

where K is an arbitrarily large number. For large τ^* compared to τ_0^*, the solution was found to be independent of K and τ_0^*. Using equations (A.17g) and (A.17i), the velocity and position of the front at $\tau^* = \tau_0^*$ can then be found.

A.7 Description of the computational method

Numerical method is needed to help solve the system of equations described above. After many methods were tried, the Lax method (Press et al. 1986) was chosen because it provides stable solutions in spite of the fact that it is numerically dissipative. In addition, the errors introduced by the numerical dissipation can be minimized by carefully selecting the time step and the spatial resolution used throughout the computation. The Lax method can be described in the following way. If i denotes the local spatial node, and j denotes the present time, the Lax method discretizes the spatial and temporal gradients of an arbitrary variable R* as follows

$$\frac{\partial R^*}{\partial z^*} = \frac{R^*_{i+1,j} - R^*_{i-1,j}}{z^*_{i+1} - z^*_{i-1}} \tag{A.19a}$$

$$\frac{\partial R^*}{\partial \tau^*} = \frac{R^*_{i,j+1} - \frac{1}{2}(R^*_{i+1,j} - R^*_{i-1,j})}{\tau^*_{j+1} - \tau^*_{j}}. \tag{A.19b}$$

Finally, as mentioned in Section A.5, an additional boundary condition is needed at the front of the current before it reaches the downstream end wall. For the present

model for inviscid flow in a channel of infinite depth, this condition can be readily found by utilizing the method of characteristics. However, if that method is employed for the case of viscous flow in a channel of finite depth, it was found that difficulties which are beyond the scope of the present investigation will arise. As a result, an approximation was instead introduced as the additional boundary condition in the estimation of h* at the front. If the present time is again denoted by j, and the spatial node at $z^* = 1$ is denoted by i_K, this approximation is given by

$$h^*_{i_K,j+1} = h^*_{i_K,j} + \frac{\tau^*_{j+1} - \tau^*_j}{\tau^*_j - \tau^*_{j-1}} (2h^*_{i_K-1,j} - h^*_{i_K-2,j-1} - h^*_{i_K,j}) \,. \qquad \text{(A.20)}$$

Equation (A.20) represents a linear extrapolation scheme. It was found that the solution thus obtained for inviscid flow in a channel of infinite depth does not deviate from that found by the method of characteristics. The same extrapolation scheme will be used in all the models presented in this study.

APPENDIX B

DERIVATION OF THE EQUATIONS FOR AN INVISCID GRAVITY CURRENT IN A CHANNEL OF FINITE DEPTH

B.1 General description of the model

As mentioned in Section A.1, equations (A.1) through (A.9) are valid for both the last and the present models. In addition, equations (A.10) and (A.11a) are also applicable for this model because the conditions required for their validity are satisfied. However, the motion of the layer of ambient fluid is not negligible any more. Since the channel depth is fixed at H, the depth of the layer of ambient fluid is only the difference between the channel depth, H, and the depth of the gravity current, h. It can be thus obtained by inspection once h is found. On the other hand, the velocity of the fluid in this layer, U_a, cannot be found by inspection. Furthermore, when U_a is not identically zero, the pressure gradient on the top wall, $\partial p_H/\partial x$ does not vanish. As a result, the conservation equations for mass and momentum for the layer of ambient fluid must also be used.

B.2 Governing equations for the model

To obtain the governing equations of motion, the same approach in Appendix A is used. Integrating equation (A.1a) from y = 0 to y = H yields

$$\frac{\partial}{\partial x}\int_0^H u\,dy = v_0 - v_H \qquad \text{(B.1)}$$

where $v_H = v_{H(t,x)}$ and $v_0 = v_{0(t,x)}$ are the vertical velocity components of the fluid at y = H and y = 0, respectively, as shown in Figure 3.1. The influx velocity, v_0, was defined in equations (A.7a) through (A.7c) in Appendix A. Using similar arguments for v_0, the outflow velocity, v_H, can be defined as

$$v_{H(x)} = \frac{Q}{w_1} \qquad \text{for } -w_0 \le x \le -(w_0-w_1) \qquad \text{(B.2a)}$$

and $v_{H(x)} = 0$ for $-(w_0-w_1) \le x \le L$. (B.2b)

Similar to equation (A.11a), equation (B.1) can be rewritten as

$$\frac{\partial}{\partial x}[U_w h + U_a(H - h)] = v_0 - v_H . \tag{B.3}$$

For the inviscid part of the flow, keeping in mind that the pressure gradient on the top wall does not vanish, equation (A.1b) can be written for the layers of ambient and working fluids, respectively, as

$$\frac{\partial U_a}{\partial t} + U_a \frac{\partial U_a}{\partial x} = -\frac{1}{\rho_a}\frac{\partial p_H}{\partial x} \tag{B.4a}$$

$$\frac{\partial U_w}{\partial t} + U_w \frac{\partial U_w}{\partial x} = -\frac{1}{\rho_w}\left[\frac{\partial p_H}{\partial x} + (\rho_w-\rho_a)\, g \frac{\partial h}{\partial x}\right] . \tag{B.4b}$$

The reference length, time, and velocity scales shown in Section 1.2 can be used to rewrite equations (A.11a), and (B.3) through (B.4b) in non-dimensional forms. Due to the presence of the term p_H in equations (B.4a) and (B.4b), a reference pressure is required. This reference pressure can be defined as

$$P_{ref} = \rho_a U_{ref}^2 . \tag{B.5}$$

Note that the definition of the reference pressure will not affect the solutions. As a result, the equations (A.11a), and (B.3) through (B.4b) can be rewritten as

$$\frac{\partial h^*}{\partial t^*} + \frac{\partial}{\partial x^*}(U_w^* h^*) = v_0^* \tag{B.6a}$$

$$\frac{\partial}{\partial x^*}[U_w^* h^* + U_a^*(H^* - h^*)] = v_0^* - v_H^* \tag{B.6b}$$

$$\frac{\partial U_a^*}{\partial t^*} + \frac{\partial}{\partial x^*}\left[\frac{1}{2}(U_a^*)^2 + p_H^*\right] = 0 \qquad \text{(B.6c)}$$

and $$\frac{\partial U_w^*}{\partial t^*} + \frac{\partial}{\partial x^*}\left[\frac{1}{2}(U_w^*)^2 + \rho_r p_H^* + h^*\right] = 0 \qquad \text{(B.6d)}$$

where ( )* quantities are the non-dimensional quantities normalized by the appropriate combinations of length, time, velocity and pressure scales. Equations (B.6a) through (B.6d) are the governing partial differential equations for inviscid gravity currents in a channel of finite depth in the region $-w_0^* < x^* < L^*$. It should be noted that there is no time rate of change of pressure on the top wall in the equations (B.6a) through (B.6d). As a result, this pressure can be found only relative to a reference pressure. The pressure on the top wall at the upstream end wall is picked as this reference pressure. Equations (B.6c) and (B.6d) can then be combined to eliminate the pressure gradient on the top wall. The resulting equation is

$$\frac{\partial}{\partial t^*}(U_w^* - \rho_r U_a^*) + \frac{\partial}{\partial x^*}\left[\frac{1}{2}(U_w^*)^2 - \frac{1}{2}\rho_r (U_a^*)^2 + h^*\right] = 0 \qquad \text{(B.6e)}$$

Equations (B.6a), (B.6b) and (B.6e) now form the set of partial differential equations that governs the behavior of the gravity currents in this model.

If the transformation of the independent variables as described by equations (A.14a) through (A.14d) is employed, the system of equations becomes

For $-1 \le z^* \le 0$, $$\frac{\partial h^*}{\partial \tau^*} + \frac{1}{w_0^*}\frac{\partial}{\partial z^*}(U_w^* h^*) = v_0^* \qquad \text{(B.7a)}$$

$$\frac{1}{w_0^*}\frac{\partial}{\partial z^*}\left[U_w^* h^* + U_a^*(H^* - h^*)\right] = v_0^* - v_H^* \qquad \text{(B.7b)}$$

and $$\frac{\partial}{\partial \tau^*}(U_w^* - \rho_r U_a^*)$$

$$+ \frac{1}{w_0^*}\frac{\partial}{\partial z^*}\left[\frac{1}{2}(U_w^*)^2 - \frac{1}{2}\rho_r (U_a^*)^2 + h^*\right] = 0\,. \qquad \text{(B.7c)}$$

For $0 \le z^* \le 1$,
$$\frac{\partial h^*}{\partial \tau^*} - \frac{z^* \dot{x}_f^*}{x_f^*} \frac{\partial h^*}{\partial z^*} + \frac{1}{x_f^*} \frac{\partial}{\partial z^*} (U_w^* h^*) = v_0^* \qquad \text{(B.7d)}$$

$$\frac{1}{x_f^*} \frac{\partial}{\partial z^*} [U_w^* h^* + U_a^* (H^* - h^*)] = v_0^* - v_H^* \qquad \text{(B.7e)}$$

and
$$\frac{\partial}{\partial \tau^*} (U_w^* - \rho_r U_a^*) - \frac{z^* \dot{x}_f^*}{x_f^*} \frac{\partial}{\partial z^*} (U_w^* - \rho_r U_a^*)$$
$$+ \frac{1}{x_f^*} \frac{\partial}{\partial z^*} [\tfrac{1}{2} (U_w^*)^2 - \tfrac{1}{2} \rho_r (U_a^*)^2 + h^*] = 0 . \qquad \text{(B.7f)}$$

Equations (B.7a) through (B.7f) are the governing partial differential equations for the region $-1 \le z^* \le 1$. The influx velocity, v_0^*, was defined in equations (A.16a) through (A.16c) in Section A.4. The outflow velocity, v_H^*, defined in equations (B.2) can now be written in terms of the new independent variables as

$$v_H^*{}_{(z^*)} = \frac{1}{w_1^*} \qquad \text{for } -1 \le z^* \le -(1 - \frac{w_1^*}{w_0^*}) \qquad \text{(B.8a)}$$

and
$$v_H^*{}_{(z^*)} = 0 \qquad \text{for } -(1 - \frac{w_1^*}{w_0^*}) \le z^* \le \frac{L^*}{w_0^*} . \qquad \text{(B.8b)}$$

B.3 Boundary Conditions for the model

Similar to the model for inviscid gravity currents in a channel of infinite depth, the boundary conditions for the present model can be expressed as

At $z^* = -1$,
$$\frac{\partial h^*}{\partial z^*} = 0 \qquad \text{(B.9a)}$$

$$U_w^* = 0 \qquad \text{(B.9b)}$$

and
$$U_a^* = 0 . \qquad \text{(B.9c)}$$

At $z^* = 0$,
$$h^*_{(z^*=0^-)} = h^*_{(z^*=0^+)} \qquad \text{(B.9d)}$$

$$\frac{1}{w_0^*}\frac{\partial h^*}{\partial z^*}(z^*=0^-) = \frac{1}{x_f^*}\frac{\partial h^*}{\partial z^*}(z^*=0^+) \qquad \text{(B.9e)}$$

$$U_w^*{}_{(z^*=0^-)} = U_w^*{}_{(z^*=0^+)} \qquad \text{(B.9f)}$$

$$\frac{1}{w_0^*}\frac{\partial U_w^*}{\partial z^*}(z^*=0^-) = \frac{1}{x_f^*}\frac{\partial U_w^*}{\partial z^*}(z^*=0^+) \qquad \text{(B.9g)}$$

and $$\frac{1}{x_f^*}\frac{\partial}{\partial z^*}[U_w^* h^* + U_a^*(H^* - h^*)]_{(z^*=0)} = v_0^*{}_{(z^*=0)} - v_H^*{}_{(z^*=0)} . \qquad \text{(B.9h)}$$

At $z^* = 1$, $$\dot{x}_f^* = (1 - \alpha)\, U_w^* \qquad \text{(B.9i)}$$

$$U_w^* = \sqrt{\frac{h^*}{(\frac{1}{2} - \alpha) + \rho_r \frac{h^*}{H^* - h^*}(1 - \alpha) + \frac{1}{2}\rho_r (\frac{h^*}{H^* - h^*})^2}} \qquad \text{(B.9j)}$$

and $$U_a^* = -\frac{h^*}{H^* - h^*} U_w^* . \qquad \text{(B.9k)}$$

As in the case of equations (A.17), equations (B.9a) through (B.9c) were deduced from physical considerations at the upstream end wall. Equations (B.9d) through (B.9g) reflect the fact that both the values and the gradients of h^* and U_w^* are continuous. Equation (B.9h) was derived from the continuity equation at $z^*=0$. Equations (B.9i) and (B.9j) were obtained by integrating equations (B.7a) and (B.7b) across the front, together with equations (A.16c) and (B.8b). Equation (B.9k) was then derived from the equation of mass conservation at $z^*=1$.

In addition, the position of the front can be found, as in equation (A.17i), by integrating the velocity of the front over time as follows:

$$x_f^* = \int_0^{\tau^*} \dot{x}_f^*\, d\tau^* . \qquad \text{(B.9l)}$$

Moreover, equation (A.20) from Section A.7 is employed to supply the last boundary condition which is needed to find h* at z* = 1, and it is repeated below:

$$h^*_{i_K,j+1} = h^*_{i_K,j} + \frac{\tau^*_{j+1} - \tau^*_j}{\tau^*_j - \tau^*_{j-1}} (2h^*_{i_K-1,j} - h^*_{i_K-2,j-1} - h^*_{i_K,j}) \,. \qquad \text{(B.9m)}$$

As described in Section A.5, after the front of the current has hit the downstream end wall, equations (B.9i) through (B.9m) must be replaced by the following equations

At z* = 1, $$\frac{\partial h^*}{\partial z^*} = 0 \qquad \text{(B.9n)}$$

$$U_w^* = 0 \qquad \text{(B.9o)}$$

$$U_a^* = 0 \qquad \text{(B.9p)}$$

Also, $$\dot{x}_f^* = 0 \qquad \text{(B.9q)}$$

and $$x_f^* = L^* \,. \qquad \text{(B.9r)}$$

Note that equations (B.9n) through (B.9r), with the exception of equation (B.9p), are identical to equations (A.17j) through (A.17m) because they are deduced from the same physical considerations at the downstream end wall of the channel. These physical conditions are not affected by changes in the models.

B.4 Initial conditions and the computational method for the model

Finally, initial conditions are needed to start the computation. As described in Section A.6, it is assumed that the flow started at $\tau^* = 0$. At time $\tau^* = \tau_0^* > 0$, where $\tau_0^* \cong 0$, it can be deduced from equations (B.7a) through (B.7c) that:

For $-1 \le z^* < 0$, $$h^* = v_0^*{}_{(z^*)}\, \tau_0^* \qquad \text{(B.10a)}$$

$$U_w^* = 0 \tag{B.10b}$$

and

$$U_a^* = 0\,. \tag{B.10c}$$

With reasons similar to those stated in Section A.6, the following assumptions are employed:

For $0 \le z^* \le 1$,

$$h^* = v_0^*{}_{(z^* = -k)}\, \tau_0^*/K \tag{B.10d}$$

$$U_w^* = \sqrt{\frac{h^*}{\frac{1}{2} - \alpha}} \tag{B.10e}$$

and

$$U_a^* = -\frac{h^*}{H^* - h^*}\, U_w^* \tag{B.10f}$$

where K is an arbitrarily large number, as mentioned before. The velocity and position of the front at $\tau^* = \tau_0^*$ can then be found using equations (B.9i) and (B.9l), respectively. For large τ^* compared to τ_0^*, the solution was again found to be independent of K.

The Lax method used to discretize the partial differential equations in Section A.7 was again used to obtain solution for this model due to the reasons stated in that section. In addition, the spatial gradient in equation (B.7b) is evaluated by

$$\frac{\partial S^*}{\partial z^*} = \frac{S^*_{i,j} - S^*_{i-1,j}}{z^*_i - z^*_{i-1}} \tag{B.11a}$$

and that in equation (B.7e) is evaluated by

$$\frac{\partial S^*}{\partial z^*} = \frac{S^*_{i+1,j} - S^*_{i,j}}{z^*_{i+1} - z^*_i}\,. \tag{B.11b}$$

APPENDIX C

DERIVATION OF THE EQUATIONS FOR A VISCOUS GRAVITY CURRENT IN A CHANNEL OF INFINITE DEPTH

C.1 General description and the governing equations for the model

In the models presented in Appendices A and B, the gravity current is assumed to be inviscid. It is certainly not the case in the experiments shown in Chapter 2. As a result, although the same approach used in Appendix A to derive governing equations and boundary conditions is also used in this appendix, the inviscid assumption is replaced by the assumption that viscous effects only take place at the bottom wall.

As mentioned in Section A.1, equations (A.1a) through (A.9) are also valid for this model. Equation (A.9) again represents the continuity equation. In the section of the channel where working fluid is introduced, the integral on the left-hand side of equation (A.9) is still given by equation (A.10). However, that integral is no longer given by equation (A.10) in the section between $x = 0$ and $x = x_f$ due to the presence of the viscous drag on the bottom wall. Using $\delta = \delta(t,x)$ to denote the boundary layer thickness due to friction on the bottom wall, and $\delta' = \delta'(t,x)$ to represent the corresponding displacement thickness, the integral on the left-hand side of equation (A.9) can be evaluated as

$$\int_0^h u \, dy = U_w (h - \delta') \tag{C.1}$$

in which the displacement thickness, δ', is defined as

$$\delta' = \int_0^\delta (1 - \frac{u}{U_w}) \, dy \, . \tag{C.2}$$

Moreover, the motion of the layer of ambient fluid in this case is negligible, as discussed in Section A.3, and thus the pressure gradient on the top wall, $\partial p_H/\partial x$, vanishes. As a result, the momentum equation in the free-stream is given by equation (A.11c) when the boundary layer thickness, δ, is smaller than the depth of the current, h. However, when δ

= h, another equation is needed in place of equation (A.11c). This will be discussed later in Section C.2.

Since the bottom wall is not present in the inlet section of the channel, there is no boundary layer in the current in that section. On the other hand, the bottom wall exerts a viscous drag on the current in the section of the channel between x = 0 and x = x_f, and thus the boundary layer thickness in that section is not zero. The equation that governs the behavior of the boundary layer thickness due to viscous effects on the bottom wall can be derived by first integrating the continuity equation (A.1a) and the momentum equation (A.1b) from y = 0 to y = δ, and then combining the resulting equations. A similar method was used by Murdock (1971) to obtain the boundary layer which grows downstream of the leading edge of a semi-infinite flat plate with a shock wave propagating over it. This equation can be written as

$$\frac{\partial}{\partial t}(U_w\delta) + \frac{\partial}{\partial x}[(U_w)^2\theta'] + U_w\delta\frac{\partial U_w}{\partial x} = \nu_w \left.\frac{\partial u}{\partial y}\right|_0 \qquad (C.3)$$

where $\theta' = \theta'(t,x)$ is the momentum thickness, and it is defined as

$$\theta' = \int_0^\delta \frac{u}{U_w}\left(1 - \frac{u}{U_w}\right) dy \,. \qquad (C.4)$$

The term on the right-hand side of equation (C.3) represents the viscous drag exerted by the bottom wall on the current. As a result, the equations (A.9), (A.11c) and (C.3) represent the governing equations for a viscous gravity current in a channel of infinite depth.

Since the velocity profile in the current, u = u(t,x,y), is not known, there are more unknowns to be solved than equations available. As a result, von Karman's momentum-integral theory is used to obtain an approximate solution. Although the result is only an approximation, White (1986) described the method as "startlingly accurate."

For the present model, the velocity profile inside the current can be assumed to have a cubic shape. The resulting velocity profile which satisfies the boundary conditions can be written as

$$\frac{u}{U_w} = \frac{3}{2}\frac{y}{\delta} - \frac{1}{2}\left(\frac{y}{\delta}\right)^3 . \qquad \text{(C.5)}$$

The displacement thickness and the momentum thickness defined in equations (C.2) and (C.4) can then be evaluated using equation (C.5). They are related to the boundary layer thickness by the following equations

$$\delta' = \frac{3}{8}\delta \qquad \text{(C.6a)}$$

$$\theta' = \frac{39}{280}\delta . \qquad \text{(C.6b)}$$

The gradient on the right-hand side of equation (C.3) can also be evaluated and was found to be

$$\left.\frac{\partial u}{\partial y}\right|_0 = \frac{3}{2}\frac{U_w}{\delta} . \qquad \text{(C.6c)}$$

Thus, using the reference length, time, and velocity scales as shown in Section 1.2, together with equations (C.6a) through (C.6c), the governing equations (A.9), (A.11c), and (C.3) can be rewritten as

$$\frac{\partial h^*}{\partial t^*} + \frac{\partial}{\partial x^*}\left[U_w^* \left(h^* - \frac{3}{8}\delta^*\right)\right] = v_0^* \qquad \text{(C.7a)}$$

and $$\frac{\partial U_w^*}{\partial t^*} + \frac{\partial}{\partial x^*}\left[\frac{1}{2}(U_w^*)^2 + h^*\right] = 0 ; \qquad \text{(C.7b)}$$

for $-w_0^* < x^* < 0$, $\delta^* = 0$; (C.7c)

for $0 < x^* < L^*$, $$\frac{\partial}{\partial t}(U_w^*\delta^*) + \frac{13}{35}\frac{\partial}{\partial x^*}[(U_w^*)^2\,\delta]$$

$$+ U_w^*\delta^*\frac{\partial U_w^*}{\partial x^*} = \frac{4}{Re}\frac{U_w^*}{\delta^*} \qquad \text{(C.7d)}$$

where Re is the Reynolds number as defined in equation (3.1f), and ( )* quantities are the non-dimensional quantities, normalized by the appropriate combinations of length, time, and velocity scales. Equations (C.7a) through (C.7d) are the governing partial differential equations for viscous gravity currents in a channel of infinite depth in the region $-w_0^* < x^* < L^*$ when $\delta^* < h^*$.

On the right-hand side of equation (C.7d), the term has a factor δ^* in the denominator. As a result, if δ^* is close to zero, the term will approach infinity, and the numerical error due to this term will be large. Therefore, equation (C.7d) is multiplied throughout by $(U_w^*\delta^*)$, and the temporal derivative of U_w^* is eliminated by using equation (C.7b). The resulting equation that replaces equation (C.7d) is:

For $0 < x^* < L^*$,

$$\frac{\partial}{\partial t^*}[(\delta^*)^2] + \frac{13}{35} U_w^* \frac{\partial}{\partial x^*}[(\delta^*)^2] + \frac{52}{35}(\delta^*)^2 \frac{\partial U_w^*}{\partial x^*} - 2\frac{(\delta^*)^2}{U_w^*}\frac{\partial h^*}{\partial x^*} = \frac{8}{Re}. \qquad \text{(C.7e)}$$

Thus, equations (C.7a) through (C.7c) and equation (C.7e) together form the set of governing equations for viscous gravity currents in a channel of infinite depth.

If the transformation of the independent variables as described by equations (A.14a) through (A.14d) is employed, the system of equations becomes:

For $-1 \le z^* \le 0$,

$$\frac{\partial h^*}{\partial \tau^*} + \frac{1}{w_0^*}\frac{\partial}{\partial z^*}[U_w^*(h^* - \tfrac{3}{8}\delta^*)] = v_0^* \qquad \text{(C.8a)}$$

$$\frac{\partial U_w^*}{\partial \tau^*} + \frac{1}{w_0^*}\frac{\partial}{\partial z^*}[\tfrac{1}{2}(U_w^*)^2 + h^*] = 0 \qquad \text{(C.8b)}$$

and

$$\delta^* = 0. \qquad \text{(C.8c)}$$

For $0 \le z^* \le 1$,

$$\frac{\partial h^*}{\partial \tau^*} - \frac{z^*\dot{x}_f^*}{x_f^*}\frac{\partial h^*}{\partial z^*} + \frac{1}{x_f^*}\frac{\partial}{\partial z^*}[U_w^*(h^* - \tfrac{3}{8}\delta^*)] = v_0^* \qquad \text{(C.8d)}$$

$$\frac{\partial U_w^*}{\partial \tau^*} - \frac{z^* \dot{x}_f^*}{x_f^*} \frac{\partial U_w^*}{\partial z^*} + \frac{1}{x_f^*} \frac{\partial}{\partial z^*} \left[\frac{1}{2} (U_w^*)^2 + h^* \right] = 0 \qquad \text{(C.8e)}$$

and

$$\frac{\partial}{\partial \tau^*} [(\delta^*)^2] - \frac{z^* \dot{x}_f^*}{x_f^*} \frac{\partial}{\partial z^*} [(\delta^*)^2] + \frac{13}{35} \frac{U_w^*}{x_f^*} \frac{\partial}{\partial z^*} [(\delta^*)^2]$$
$$+ \frac{52}{35} \frac{(\delta^*)^2}{x_f^*} \frac{\partial U_w^*}{\partial z^*} - 2 \frac{1}{x_f^*} \frac{(\delta^*)^2}{U_w^*} \frac{\partial h^*}{\partial z^*} = \frac{8}{Re} . \qquad \text{(C.8f)}$$

Equations (C.8a) through (C.8f) are the governing partial differential equations for the region $-1 \le z^* \le 1$ when $\delta^* < h^*$. The influx velocity v_0^* was defined in equations (A.16a) through (A.16c) in Section A.4.

C.2 Equations for a fully developed boundary layer

As mentioned in the last section, the set of equations (C.8a) through (C.8f) does not apply to the locations in the gravity current at which the boundary layer fills the depth of the current, that is, when $\delta^* = h^*$. Although equations (C.8a) through (C.8d) are still valid, there is no portion in the velocity profile that maintains a uniform velocity, and thus equation (C.8e) should be replaced by an equation that will reflect the status of the boundary layer. In addition, the boundary layer thickness is no longer governed by equation (C.8f) because the thickness is the same as, and cannot exceed, the depth of the current. Therefore, equations (C.8e) and (C.8f) must be replaced.

For $\delta^* = h^*$,

$$\frac{\partial U_w^*}{\partial \tau^*} - \frac{z^* \dot{x}_f^*}{x_f^*} \frac{\partial U_w^*}{\partial z^*} + \frac{1301}{2800} \frac{1}{x_f^*} \frac{\partial}{\partial z^*} [(U_w^*)^2]$$
$$+ \left[\frac{8}{5} + \frac{213}{1400} \frac{(U_w^*)^2}{h^*} \right] \frac{1}{x_f^*} \frac{\partial h^*}{\partial z^*} = - \frac{12}{5} \frac{1}{Re} \frac{(U_w^*)^2}{h^*} \qquad \text{(C.8g)}$$

and

$$\delta^* = h^* . \qquad \text{(C.8h)}$$

Equation (C.8g) is derived by integrating the momentum equation (A.1b) from $y = 0$ to $y = h$, keeping in mind that $\delta^* = h^*$, and then eliminating the temporal derivative of h^* by using equation (C.8d). Equation (C.8h) merely states the fact that $\delta^* = h^*$. Thus, equations (C.8d), (C.8g) and (C.8h) form the set of partial differential equations that

governs the behavior of a viscous gravity current in a channel of infinite depth at the locations where $\delta^* = h^*$.

C.3 Boundary conditions for the model

Similar to the model for inviscid gravity currents in a channel of infinite depth, the boundary conditions for the present model can be expressed as:

At $z^* = -1$, $$\frac{\partial h^*}{\partial z^*} = 0 \qquad \text{(C.9a)}$$

$$U_w^* = 0 \qquad \text{(C.9b)}$$

and $$\delta^* = 0 . \qquad \text{(C.9c)}$$

At $z^* = 0$, $$h^*_{(z^*=0^-)} = h^*_{(z^*=0^+)} \qquad \text{(C.9d)}$$

$$\frac{1}{w_0^*}\frac{\partial h^*}{\partial z^*}(z^*=0^-) = \frac{1}{x_f^*}\frac{\partial h^*}{\partial z^*}(z^*=0^+) \qquad \text{(C.9e)}$$

$$U_w^*{}_{(z^*=0^-)} = U_w^*{}_{(z^*=0^+)} \qquad \text{(C.9f)}$$

$$\frac{1}{w_0^*}\frac{\partial U_w^*}{\partial z^*}(z^*=0^-) = \frac{1}{x_f^*}\frac{\partial U_w^*}{\partial z^*}(z^*=0^+) \qquad \text{(C.9g)}$$

and $$\delta^* = 0 . \qquad \text{(C.9h)}$$

At $z^* = 1$, $$\delta^* = 0 \qquad \text{(C.9i)}$$

$$\dot{x}_f^* = (1 - \alpha)\, U_w^* \qquad \text{(C.9j)}$$

and $$U_w^* = \sqrt{\frac{h^*}{\frac{1}{2} - \alpha}} . \qquad \text{(C.9k)}$$

As in the case of equations (A.17), equations (C.9a) through (C.9c) were deduced from physical considerations at the upstream end wall. Equations (C.9d) through (C.9g) reflect the fact that both the values and the gradients of h^* and U_w^* are continuous. Equation (C.9h) states that the boundary layer starts at $z^*=0$. Equation (C.9i) was obtained by observing the flow phenomenon with a co-ordinate fixed at the front of the current. Equations (C.9j) and (C.9k) were obtained by integrating equations (C.8d) and (C.8e) across the front, together with equations (A.16c) and (C.9i). In addition, the position of the front can be found, as in equation (A.17i), by integrating the velocity of the front over time as follows

$$x_f^* = \int_0^{\tau^*} \dot{x}_f^* \, d\tau^* \, . \tag{C.9l}$$

Finally, equation (A.20) from Appendix A is employed to supply the last boundary condition which is needed to find h^* at $z^*=1$, and is repeated below:

$$h^*_{i_K,j+1} = h^*_{i_K,j} + \frac{\tau^*_{j+1} - \tau^*_j}{\tau^*_j - \tau^*_{j-1}} (2h^*_{i_K-1,j} - h^*_{i_K-2,j-1} - h^*_{i_K,j}) \, . \tag{C.9m}$$

As described in Appendix A, after the front of the current hits the downstream end wall, equations (C.9i) through (C.9m) must be replaced by the following equations:

At $z^* = 1$,

$$\frac{\partial h^*}{\partial z^*} = 0 \tag{C.9n}$$

$$U_w^* = 0 \tag{C.9o}$$

$$\frac{\partial \delta^*}{\partial z^*} = 0 \, . \tag{C.9p}$$

Also,

$$\dot{x}_f^* = 0 \tag{C.9q}$$

and

$$x_f^* = L^* \, . \tag{C.9r}$$

Note that the boundary conditions stated in equations (C.9n) through (C.9r) do not depend on whether the boundary layer is fully developed or not at various locations in the gravity current.

C.4 Initial conditions and the computational method for the model

Initial conditions are needed to start the computation. As described in Appendix A, it is assumed here that the flow started at $\tau^* = 0$. At time $\tau^* = \tau_0^* > 0$, where $\tau_0^* \cong 0$, it can be deduced from equations (C.8a) through (C.8c) that:

For $-1 \le z^* < 0$, $\quad h^* = v_0^*{}_{(z^*)}\, \tau_0^*$ (C.10a)

$$U_w^* = 0 \qquad \text{(C.10b)}$$

and $\quad \delta^* = 0\,.$ (C.10c)

With reasons similar to those stated in Appendix A, the following assumptions are employed:

For $0 \le z^* \le 1$, $\quad h^* = v_0^*{}_{(z^* = -k)}\, \tau_0^*/K$ (C.10d)

$$U_w^* = \sqrt{\frac{h^*}{\frac{1}{2} - \alpha}} \qquad \text{(C.10e)}$$

and $\quad \delta^* = 0$ (C.10f)

where K is an arbitrarily large number, as mentioned before. The velocity and position of the front at $\tau^* = \tau_0^*$ can then be found using equations (C.9j) and (C.9l). In addition, it was found that equation (C.8f) will give rise to numerical instability when τ^* is not large when compared to τ_0^*. However, if equation (C.10f) was used in place of equation (C.8f) until $\tau^* = \tau_1^*$, where $\tau_1^* \gg \tau_0^*$, then the solution was found to be stable. For

large τ^* compared to τ_0^* and τ_1^*, the solution was found to be independent of K, τ_0^* and τ_1^*.

The Lax method used to discretize the partial differential equations in Appendix A was again used to obtain solution for this model due to the reasons stated in that section. The spatial and temporal gradients of an arbitrary variable R* are given by Equations (A.19a) and (A.19b), respectively.

APPENDIX D

DERIVATION OF THE EQUATIONS FOR A VISCOUS GRAVITY CURRENT IN A CHANNEL OF FINITE DEPTH

D.1 General description of the model

In this appendix, the derivation of the equations of a model that describes the behavior of a viscous gravity current in a channel of finite depth will be shown. Unlike the models presented in Appendices B and C, in which new features were added to the model presented in Appendix A, the model to be presented in this appendix is merely a collection of the features already presented in the previous models.

D.2 Governing equations for the model

Equations (A.1a) through (A.9) are again valid for this model. As discussed in Appendix C, the integral on the left-hand side of the continuity equation for the layer of working fluid, equation (A.9), can be evaluated as shown in equation (C.1). Furthermore, the continuity equation for the layer of ambient fluid is given by equation (B.3).

In addition, as described in Appendices B and C, the momentum equations for the layer of working fluid are represented by equations (B.4b) and (C.3) when $\delta < h$, while the corresponding momentum equation for the layer of ambient fluid is identical to that given by equation (B.4a). However, when $\delta = h$, the boundary layer is fully developed. Although equation (B.4a) can still be used as the momentum equation for the layer of ambient fluid, the momentum equations for the layer of working fluid can no longer be represented by equations (B.4b) and (C.3). Instead, in non-dimensional form, the correct momentum equations for the layer of working fluid will resemble equations (C.8g) and (C.8h). Since the development of the governing partial differential equations was described in detail in Appendix A through Appendix C, the governing continuity and momentum equations to be used in this model for a viscous gravity current in a horizontal channel of finite depth are simply stated below in non-dimensional form and in the transformed z^*-τ^* co-ordinates:

For $-1 \le z^* \le 0$,

$$\frac{\partial h^*}{\partial \tau^*} + \frac{1}{w_0^*}\frac{\partial}{\partial z^*}(U_w^* h^*) = v_0^* \tag{D.1a}$$

$$\frac{1}{w_0^*}\frac{\partial}{\partial z^*}[U_w^* h^* + U_a^*(H^* - h^*)] = v_0^* - v_H^* \tag{D.1b}$$

$$\frac{\partial}{\partial \tau^*}(U_w^* - \rho_r U_a^*) + \frac{1}{w_0^*}\frac{\partial}{\partial z^*}[\frac{1}{2}(U_w^*)^2 - \frac{1}{2}\rho_r(U_a^*)^2 + h^*] = 0 \tag{D.1c}$$

and $$\delta^* = 0\,. \tag{D.1d}$$

For $0 \le z^* \le 1$,

when $\delta^* < h^*$,

$$\frac{\partial h^*}{\partial \tau^*} - \frac{z^*\dot{x}_f^*}{x_f^*}\frac{\partial h^*}{\partial z^*} + \frac{1}{x_f^*}\frac{\partial}{\partial z^*}[U_w^*(h^* - \frac{3}{8}\delta^*)] = v_0^* \tag{D.1e}$$

$$\frac{1}{x_f^*}\frac{\partial}{\partial z^*}[U_w^*(h^* - \frac{3}{8}\delta^*) + U_a^*(H^* - h^*)] = v_0^* - v_H^* \tag{D.1f}$$

$$\frac{\partial}{\partial \tau^*}(U_w^* - \rho_r U_a^*) - \frac{z^*\dot{x}_f^*}{x_f^*}\frac{\partial}{\partial z^*}(U_w^* - \rho_r U_a^*) + \frac{1}{x_f^*}\frac{\partial}{\partial z^*}[\frac{1}{2}(U_w^*)^2 - \frac{1}{2}\rho_r(U_a^*)^2 + h^*] = 0 \tag{D.1g}$$

and

$$\frac{\partial}{\partial \tau^*}[(\delta^*)^2] - \frac{z^*\dot{x}_f^*}{x_f^*}\frac{\partial}{\partial z^*}[(\delta^*)^2] + \frac{13}{35}\frac{U_w^*}{x_f^*}\frac{\partial}{\partial z^*}[(\delta^*)^2] + 2\frac{(\delta^*)^2}{U_w^*}\frac{\partial U_w^*}{\partial \tau^*} - 2\frac{(\delta^*)^2}{U_w^*}\frac{z^*\dot{x}_f^*}{x_f^*}\frac{\partial U_w^*}{\partial z^*} + \frac{122}{35}\frac{(\delta^*)^2}{x_f^*}\frac{\partial U_w^*}{\partial z^*} = \frac{8}{Re}\,; \tag{D.1h}$$

when $\delta^* = h^*$,

$$\frac{\partial h^*}{\partial \tau^*} - \frac{z^*\dot{x}_f^*}{x_f^*}\frac{\partial h^*}{\partial z^*} + \frac{1}{x_f^*}\frac{\partial}{\partial z^*}[U_w^*(h^* - \frac{3}{8}\delta^*)] = v_0^* \tag{D.1i}$$

$$\frac{1}{x_f^*}\frac{\partial}{\partial z^*}\left[U_w^*\left(h^* - \frac{3}{8}\delta^*\right) + U_a^*\left(H^* - h^*\right)\right] = v_0^* - v_H^* \qquad \text{(D.1j)}$$

$$\frac{\partial}{\partial \tau^*}\left[U_w^*\left(h^* - \frac{3}{8}\delta^*\right) - \rho_r U_a^* h^*\right]$$

$$- \frac{z^* \dot{x}_f^*}{x_f^*}\frac{\partial}{\partial z^*}\left[U_w^*\left(h^* - \frac{3}{8}\delta^*\right) - \rho_r U_a^* h^*\right]$$

$$+ \frac{1}{x_f^*}\frac{\partial}{\partial z^*}\left[(U_w^*)^2\left(h^* - \frac{18}{35}\delta^*\right)\right] - \frac{\rho_r U_a^* h^*}{x_f^*}\frac{\partial U_a^*}{\partial z^*}$$

$$- \frac{\rho_r U_a^*}{x_f^*}\frac{\partial}{\partial z^*}\left[U_w^*\left(h^* - \frac{3}{8}\delta^*\right)\right] + \frac{h^*}{x_f^*}\frac{\partial h^*}{\partial z^*} = \frac{3}{2}\frac{1}{\mathrm{Re}}\frac{U_w^*}{\delta^*} \qquad \text{(D.1k)}$$

and $$\delta^* = h^* . \qquad \text{(D.1l)}$$

Equations (D.1a) through (D.1l) are the governing partial differential equations for the region $-1 \le z^* \le 1$. The influx velocity v_0^* was defined in equations (A.16a) through (A.16c) in Appendix A, and the outflow velocity v_h^* was defined in equations (B.8a) and (B.8b) in Appendix B.

D.3 Boundary conditions for the model

Similar to the previous models, the boundary conditions for the present model are given by:

At $z^* = -1$, $$\frac{\partial h^*}{\partial z^*} = 0 \qquad \text{(D.2a)}$$

$$U_w^* = 0 \qquad \text{(D.2b)}$$

$$U_a^* = 0 \qquad \text{(D.2c)}$$

and $$\delta^* = 0 . \qquad \text{(D.2d)}$$

At $z^* = 0$, $h^*_{(z^*=0^-)} = h^*_{(z^*=0^+)}$ (D.2e)

$$\frac{1}{w_0^*}\frac{\partial h^*}{\partial z^*}(z^*=0^-) = \frac{1}{x_f^*}\frac{\partial h^*}{\partial z^*}(z^*=0^+) \tag{D.2f}$$

$$U_w^*{}_{(z^*=0^-)} = U_w^*{}_{(z^*=0^+)} \tag{D.2g}$$

$$\frac{1}{w_0^*}\frac{\partial U_w^*}{\partial z^*}(z^*=0^-) = \frac{1}{x_f^*}\frac{\partial U_w^*}{\partial z^*}(z^*=0^+) \tag{D.2h}$$

$$\frac{1}{x_f^*}\frac{\partial}{\partial z^*}[U_w^*\,(h^* - \tfrac{3}{8}\delta^*) + U_a^*\,(H^*-h^*)]_{(z^*=0)} = v_0^*{}_{(z^*=0)} - v_H^*{}_{(z^*=0)} \tag{D.2i}$$

and $\delta^* = 0$. (D.2j)

At $z^* = 1$, $\delta^* = 0$ (D.2k)

$$\dot{x}_f^* = (1 - \alpha)U_w^* \tag{D.2l}$$

$$U_w^* = \sqrt{\frac{h^*}{(\frac{1}{2} - \alpha) + \rho_r \frac{h^*}{H^* - h^*}(1 - \alpha) + \frac{1}{2}\rho_r (\frac{h^*}{H^* - h^*})^2}} \tag{D.2m}$$

and $U_a^* = -\frac{h^*}{H^*-h^*}U_w^*$. (D.2n)

Similar to the previous models, equations (D.2a) through (D.2d) were deduced from physical considerations at the upstream end wall. Equations (D.2e) through (D.2h) reflect the fact that both the values and the gradients of h^* and U_w^* are continuous. Equation (D.2i) was derived from the continuity equation at $z^* = 0$, while equation (D.2j) states that the boundary layer starts at $z^* = 0$. Equation (D.2k) was obtained by observing the flow phenomenon with a co-ordinate fixed at the front of the current. Equations (D.2l) and (D.2m) were obtained by evaluating the governing partial differential equations across the front of the current. Equation (D.2n) was derived from mass conservation at $z^* = 1$. In addition, equation (A.20) from Appendix A is employed

to supply the last boundary condition which is needed to find h* at z* = 1, and is repeated below:

$$h^*_{i_K,j+1} = h^*_{i_K,j} + \frac{\tau^*_{j+1} - \tau^*_j}{\tau^*_j - \tau^*_{j-1}} (2h^*_{i_K-1,j} - h^*_{i_K-2,j-1} - h^*_{i_K,j}) . \qquad (D.2o)$$

Finally, the position of the front can be found by integrating the velocity of the front over time as follows:

$$x_f^* = \int_0^{\tau^*} \dot{x}_f^* \, d\tau^* . \qquad (D.2p)$$

As in all three previous models, after the front of the current hits the downstream end wall, equations (D.2k) through (D.2p) must be replaced by the following equations:

At z* = 1,
$$\frac{\partial h^*}{\partial z^*} = 0 \qquad (D.2q)$$

$$U_w^* = 0 \qquad (D.2r)$$

$$U_a^* = 0 \qquad (D.2s)$$

$$\frac{\partial \delta^*}{\partial z^*} = 0 . \qquad (D.2t)$$

Also,
$$\dot{x}_f^* = 0 \qquad (D.2u)$$

and
$$x_f^* = L^* . \qquad (D.2v)$$

These boundary conditions are a combination of those used in the previous models.

D.4 Initial conditions and the computational method for the model

As in the previous models, it is assumed here that the flow started at $\tau^* = 0$. At time $\tau^* = \tau_0^* > 0$, where $\tau_0^* \equiv 0$, it can be deduced from equations (D.1a) through (D.1d) that:

For $-1 \leq z^* < 0$, $h^* = v_0^*{}_{(z^*)}\, \tau_0^*$ (D.3a)

$U_w^* = 0$ (D.3b)

$U_a^* = 0$ (D.3c)

and $\delta^* = 0$. (D.3d)

In addition, the following assumptions are employed:

For $0 \leq z^* \leq 1$, $h^* = v_0^*{}_{(z^* = -k)}\, \tau_0^*/K$ (D.3e)

$$U_w^* = \sqrt{\frac{h^*}{(\frac{1}{2} - \alpha) + \rho_r \frac{h^*}{H^* - h^*}(1 - \alpha) + \frac{1}{2}\rho_r (\frac{h^*}{H^* - h^*})^2}} \qquad \text{(D.3f)}$$

$$U_a^* = -\frac{h^*}{H^* - h^*} U_w^* \qquad \text{(D.3g)}$$

and $\delta^* = 0$ (D.3h)

where K is an arbitrarily large number as discussed in the previous models. The velocity and position of the front at $\tau^* = \tau_0^*$ can then be found using equations (D.2l) and (D.2p). In addition, it was found that equation (D.1h) will give rise to numerical instability when τ^* is not large when compared to τ_0^*. However, if equation (D.3h) was used in place of equation (D.1h) until $\tau^* = \tau_1^*$, where $\tau_1^* \gg \tau_0^*$, then the solution was found to be stable. This was discussed earlier in Appendix C for the model of viscous gravity currents in a channel of infinite depth. For large τ^* compared to τ_0^* and τ_1^*, the solution was found to be independent of K, τ_0^* and τ_1^*.

The Lax method used to discretize the partial differential equations in the previous models was again used to obtain solutions for this model due to the reasons previously stated in Appendix A. The spatial and temporal gradients of an arbitrary variable R* are given by Equations (A.19a) and (A.19b), respectively.

REFERENCES

Alavian, V. (1986), "Behavior of Density Currents on an Incline," *J. of Hydraul. Engr.*, **112(1)**, 27-42.

Benjamin, T. B. (1968), "Gravity Currents and Related Phenomena," *J. Fluid Mech.*, **31**, 209-248.

Britter, R. E., and Linden, P. F. (1980), "The Motion of the Front of a Gravity Current Travelling Down an Incline," *J. Fluid Mech.*, **99**, 531-543.

Britter, R. E., and Simpson, J. E. (1978), "Experiments on the Dynamics of a Gravity Current Head," *J. Fluid Mech.*, **88**, 223-240.

Chen, J.-C. (1980), "Studies on Gravitational Spreading Currents," Report No. KH-R-40, W. M. Keck Laboratory of Hydraulics and Water Resources, California Institute of Technology, Pasadena, California.

Chobotov, M. V. (1987), "Gravity Currents with Heat Transfer Effects," Ph.D. thesis, California Institute of Technology, Pasadena, California.

Delichatsios, M. A. (1988), "The Outflow of Buoyant Releases Including Fire Gases from a Long Corridor Closed at One End," *J. Fluids Engr.*, **112**, 28-32.

Didden, N., and Maxworthy, T. (1982), "The Viscous Spreading of Plane and Axisymmetric Gravity Currents," *J. Fluid Mech.*, **121**, 27-42.

Ellison, T. H., and Turner, J. S. (1959), "Turbulent Entrainment in Stratified Flows," *J. Fluid Mech.*, **6**, 423-448.

Grundy, R. E., and Rottman, J. W. (1985), "The Approach to Self-Similarity of the Solutions of the Shallow-Water Equations Representing Gravity-Current Releases," *J. Fluid Mech.*, **156**, 39-53.

Grundy, R. E., and Rottman, J. W. (1986), "Self-Similar Solutions of the Shallow-Water Equations Representing Gravity Currents with Variable Inflow," *J. Fluid Mech.*, **169**, 337-351.

Heskestad, G., and Hill, J. P. (1987), "Propagation of Fire Smoke in a Corridor," 2nd ASME-JSME Thermal Engineering Joint Conference, Honolulu, Hawaii.

Huppert, H. E. (1982), "The Propagation of Two-Dimensional and Axisymmetric Viscous Gravity Currents Over a Rigid Horizontal Surface," *J. Fluid Mech.*, **121**, 43-58.

Karman, T. von (1940), "The Engineer Grapples with Nonlinear Problems," *Bull. Am. Math. Soc.*, **46**, 615-683.

Keulegan, G. H. (1946), "Model Laws for Density Currents," First Progress Report, to Chief of Engineers, U. S. Army.

Keulegan, G. H. (1958), "Model Laws for Density Currents: The Motion of Saline Fronts in Still Water," Twelfth Progress Report, to Director, Waterways Experiment Station, Corps of Engineers, Department of the Army, Nat. Bur. Stand. Rept. 5831.

Lock, R. C. (1951), "The Velocity Distribution in the Laminar Boundary Layer between Parallel Streams," *Quart. J. Mech. Applied Mach.*, **IV(1)**, 42-63.

Middleton, G. V. (1966), "Experiments on Density and Turbidity Currents. I: Motion of the Head," *Can. J. Earth Sci.*, **3**, 523-546.

Miller, G. D. (1987), "Hydrogen Bubble Wire Technique," Laboratory Report for AE104, California Institute of Technology, Pasadena, California.

Murdock, J. W. (1971), "A Solution of Shock-Induced Boundary-Layer Interaction Problems by an Integral Method," *J. Applied Mech.*, **1-8**, Paper No. 71-APM-21.

Oh, S., and Sun, B. K. H. (1983), "Prediction of the Transit Time of a Stably Stratified Flow in a Channel with Inclined Surface," *J. Heat Trans.*, **105**, 666-667.

Press, W. H., Flannery, B. P., Teukolsky, S. A., and Vetterling, W. T. (1986), *Numerical Recipes*, Cambridge University Press, New York, pp. 626-635.

Schlichting, H. (1968), *Boundary-Layer Theory*, McGraw-Hill, Inc., New York, pp. 452-455.

Schraub, F. A., Kline, S. J., Henry, J., Runstadler, P. W., Jr., and Littell, A. (1965), "Use of Hydrogen Bubbles for Quantitative Determination of Time-Dependent Velocity Fields in Low-Speed Water Flows," *J. Basic Engr.*, 429-444, Paper No. 64-WA/FE-20.

Simpson, J. E. (1969), "A Comparison between Laboratory and Atmospheric Density Currents," *Quart. J. R. Met. Soc.*, **95**, 758-765.

Simpson, J. E. (1972), "Effects of the Lower Boundary on the Head of a Gravity Current," *J. Fluid Mech.*, **53**, 759-768.

Simpson, J. E. (1982), "Gravity Currents in the Laboratory, Atmosphere, and Ocean," *Ann. Rev. Fluid Mech.*, **14**, 213-234.

Simpson, J. E. (1987), *Gravity Currents: In the Environment and the Laboratory*, John Wiley and Sons, New York.

Simpson, J. E., and Britter, R. E. (1979), "The Dynamics of the Head of a Gravity Current Advancing Over a Horizontal Surface," *J. Fluid Mech.*, **94**, 477-495.

White, F. M. (1986), *Fluid Mechanics*, McGraw-Hill, Inc., New York, pp. 387-392.

Wilkinson, D. L. (1970), "Studies in Density Stratified Flows," Water Research Laboratory, The Univ. N. S. Wales, Manly Vale, N. S. W., Australia, Rept. 118.

Wood, I. R. (1965), "Studies in Unsteady Self Preserving Turbulent Flows," Water Research Laboratory, The Univ. N. S. Wales, Manly Vale, N. S. W., Australia, Rept. 81.

Zukoski, E. E. (1966), "Influence of Viscosity, Surface Tension, and Inclination Angle on Motion of Long Bubbles in Closed Tubes," *J. Fluid Mech.*, **25**, 821-837.